Development of Magnetic Resonance Guided Functional and Anatomical Markers for the Brain

Entwicklung von Markierungssubstanzen für die funktionelle und anatomische Kernspinresonanztomografie des Gehirns

DISSERTATION

der Fakultät für Chemie und Pharmazie
der Eberhard-Karls-Universität Tübingen

zur Erlangung des Grades eines Doktors
der Naturwissenschaften

2009

vorgelegt von

Kirti Dhingra

Tag der mündlichen Prüfung: 4. Februar 2009

Dekan: Prof. Dr. Lars Wesemann

1. Berichterstatter: Prof. Dr. Martin E. Maier

2. Berichterstatter: Prof. Dr. Karl-Heinz Wiesmüller

This doctoral thesis was carried out at the Dept. of Physiology of Cognitive Processes of the Max Planck Institute for Biological Cybernetics under the supervision of Prof. Dr. Nikos K. Logothetis and in collaboration with the Institute for Organic Chemistry, Eberhard-Karls-University, Tübingen under the guidance of Prof. Dr. Martin E. Maier during the period from September 2004 to January 2009.

I would like to thank Max Planck Society and Hertie Foundation for the financial support to carry out this work

Tübingen, Januar 2009

Acknowledgement

I would like to express my heartfelt gratitude to all who gave me possibilities to complete this thesis.

I would like to thank Prof. Nikos K. Logothetis who gave me an opportunity to pursue my Ph.D in his esteemed research group. His constant support, encouragment and trust kept me moving with great enthusiasm through out my doctoral work. He gave me the confidence and freedom to expand my theories and ideas.

I would like to thank Prof. Martin E. Maier who constantly supervised my work. His suggestions, ideas, and valuable comments significantly helped me understanding the chemistry in various facets.

I am very thankful to Prof. Karl-Heinz Wiesmüller for reviewing my doctoral thesis and giving valuable comments.

My sincere thanks go to Dr. Santiago Canals and Dr. Joern Engelmann for all the helpful discussions on the problems I faced during my research work.

I express my special thanks to Dipl. –Ing. Michael Beyerlein. Without his help in performing the measurements in the University of Tuebingen and in Max Planck Institute, I would not have been able to finish this thesis in time.

I am thankful to Prof. Almut Schüz for doing the histology experiments and Dr. Rolf Pohmann for performing the MR experiments at different magnetic field.

I owe a sincere thanks to Prof. Anil K. Mishra who guided me in the beginning of my research career and showed me the right way to realize my research ambitions

I also thank Dr. Éva Jakab Tóth and Dr. Petra Fousková, Centre de Biophysique Moléculaire, CNRS, France for performing the physicochemical characterization of the synthesized agents and helped me in learning the project from an inorganic chemist point of view.

I thank Dr. Klaus Eichele, Dr. Caecilia Maichle-Moessmer and Ms. Elke Niquet for doing the X-ray crystallography. I would also thank Graeme Nicholson for doing the high resolution MS.

I would like to thank Dr. Goran Angelovski, Dr. Jozien Goense, and Dr. Anurag Mishra for reviewing my thesis and giving the useful comments. I thank all the members of bioconjugate chemistry group: Dr. Anurag Mishra, Dr. Ilgar Mamedov, Dr. Goran Angelovski, Dr. Jörn Engelmann, Dr. Rajendra Joshi, Aneta Brud, Deepti Jha, Ritu Mishra, and Hildegard Schülz for creating a good working atmosphere.

I am very thankful to Aneta Brud, Vishal Kapoor, Vishnudev, Vikram, Anurag Mishra, Ritu Mishra, and Deepti Jha. Their help, optimism, and energy made my stay in Tuebingen cheerful.

Finally I would like to thank my dear brother, Ashwini. Without his constant support and care throughout my education, I would not have been able to explore this part of the world outside my home country, India. I would also thank my sis-in-law and my sisters for their support and optimism.

I would pay tribute to my parents who taught me that hard work is the key to success. I thank them for nurturing and educating me. Thank you is not sufficient but it is said with great appreciation and respect.

Abbreviations

ACSF	Artificial cerebrospinal fluid
AECM	Artificial extracellular matrix
APTRA	*o*-aminophenol-N,N,O-triacetate
Boc	*tert*-Butoxy carbonyl
BOLD	Blood oxygenation level dependent
BAPTA	1,2-bis(o-aminophenoxy)ethane-N,N,N’,N’-teteracetic acid
tert-Bu	*tert*-butyl
Cbz	Chlorobenzoformate
$CDCl_3$	Chloroform-deuterated
CEST	Chemical exchange saturation transfer
CLIO	Cross linked nanoparticle
DMF	Dimethyl formamide
DCC	Dicyclohexylcarbodiimide
D_2O	Deuteriumoxide
DTPA	Diethylenetriaminepentaacetic acid
EDTA	ethylenediaminetetracetic acid
ECM	Extracellular matrix
DOTA	1,4,7,10-tetraazacyclododecane-1,4,7,10-tetracetic acid
DO3A	1,4,7,10-tetraazacyclododecane-1,4,7-tetracetic acid

Abbreviations

DMAP	4-Dimethylaminopyridine
DIEA	Diisopropylethylamine
ECM	Extracellular matrix
EDC	1-Ethyl-3-(3’-dimethylaminopropyl)carbodiimide
ESI-MS	Electron Spray Ionization – Mass Spectrometry
equiv	Equivalents
eq	Equation
FT	Fourier Transform
h	Hour (s)
Hz	Hertz
HATU	2-(1H-7-Azabenzotriazol-1-yl)--1,1,3,3-tetramethyl uronium hexafluorophosphate Methanaminium
HOBt	Hydroxybenzotriazole
HPLC	High performance liquid chromatography
ICP-OES	Inductively Coupled Plasma Optical Emission Spectrometry
i-Bu	Isobutyl
J	Coupling constant
Ln	Lanthanide
LiOH	Lithium hydroxide
MeCN	Acetonitrile
MeOD-*d4*	Methanol-deuterated
m/z	Mass to charge ratio

Abbreviations

mmol	millimole
mM	Millimolar
mAb	monoclonal antibody
MRI	Magnetic resonance imaging
fMRI	Functional magnetic resonance imaging
NMP	N-methylpyrolidinone
NMRD	Nuclear magnetic resonance dispersion
NMM	N-methylmorpholine
Pd-C	Palladium on activated carbon
PyBrop	Bromo-trispyrrolidino-phosphonium hexafluorophosphate
R_f	Retention factor
RT	Room temperature
RM	Reaction mixture
RIME	Receptor induced magentisation enhancement
RP-HPLC	Reversed phase high performance liquid chromatography
SPIO	superparamagnetic iron oxide
TBAF	Tetrabutylammoniumfluoride
TBDMS	Tert-Butyldimethylsilylether
TFA	Trifluoroacetic acid
THF	Tetrahydrofuran

Table of Contents

A. Section A: Introduction

B. Section B: Development of magnetic resonance guided functional markers

C. Section C: Development of magnetic resonance guided anatomical markers

D. Section D: Materials and Methods

E. Appendix 1: NMR of final ligands and important intermediates

F. Appendix 2: Data of fitting analysis

G. Appendix 3: X-ray Crystallography

H. References

Section A

Introduction

CHAPTER 1

1. MAGNETIC RESONANCE IMAGING

1.1 Basic principle

Magnetic resonance imaging (MRI) is a powerful imaging modality based on the principle of nuclear magnetic resonance (NMR). It reveals the fine details of anatomy without the use of ionizing radiations such as x-rays. The noninvasive nature of MRI coupled with the relative safety of magnetic field employed has made it the most indispensable imaging tool in understanding the structure as well as the function of human body.

The basic concept of MRI is the NMR phenomenon exhibited by atomic nuclei containing odd number of protons or neutrons. The protons and neutrons possess an intrinsic angular momentum called spin. As they pair together in a nucleus with oppositely oriented spin, the nuclei containing an odd number of them e.g. ^{1}H, ^{13}C etc possess a net spin and an associated magnetic dipole moment. For example, the hydrogen atom contains a single proton in the nucleus and thus has a net magnetic moment.

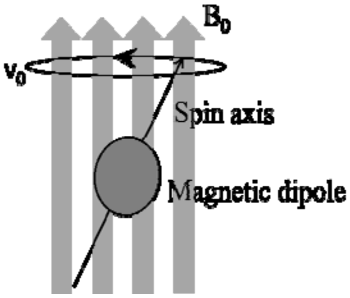

Figure 1: A precessing magnetic dipole in an external magnetic field. The external magnetic field exerts a torque on magnetic dipole causing it to precess about B_0. The precessional frequency ν_0 is the resonant frequency of NMR.

As MRI is a bulk phenomenon, the signal is recorded from an ensemble of nuclei. The hydrogen nuclei present in the form of water in the human body is the main focus of MRI. In the absence of a magnetic field, these nuclei are randomly oriented and thus have no net magnetization. When placed in an external magnetic field, they experience a torque and tend to align with it. However because of the magnetic dipole moment, they do not only align but starts to precess as well around the field axis (Figure 1).

The frequency of precession is resonant frequency of nuclear magnetic resonance and is called Larmor frequency (ν_o) (eq 1.1.)

$$\nu_0 = \gamma B_0 \qquad \text{eq (1.1)}$$

where B_0 is the magnetic field strength and γ is a constant called gyromagnetic ratio. γ has a fixed value for each nucleus and is expressed in MHz/T units.

At equilibrium the net magnetization (M_0) is in the direction of the field ($M_0 = M_Z$, M_X, $M_Y = 0$) and is due to the small difference in the number of spins precessing with the field and opposite to it. This local equilibrium magnetization is very small as compared to the applied field B_0 and therefore cannot be observed directly. However, if the M_Z flipped off the z-axis, a measurable transient signal is observed. Such a flipping is done by a short application (pulse) of magnetic field B_1 perpendicular to B_0 and is created by an oscillating radiofrequency (RF) current coil. This causes the net magnetization to split into two components, a longitudinal component M_Z and a transverse component M_{XY}. The precession of M_{XY} generates a measurable MR signal (called as free induction decay, FID) in the receiver coil. The angle with which the magnetization is flipped (flip angle, α) can be increased by increasing the magnitude of B_1 or by increasing the duration of application of the RF pulse [1].

1.2 Relaxation times [2]

Immediately after the RF field is turned off, the M_Z component starts to grow back to its initial value and M_{XY} component gradually shrink back. The M_{XY} shrink faster than the M_Z re-growth. The time required for the z-component of M_0 to return to the equilibrium value is the T_1 relaxation time. It is also called longitudinal relaxation time or spin-lattice relaxation. This relaxation is due to the energy transfer from an excited spin to its surrounding (lattice) and follows the following exponential equation:

$$M_z(t) = M_0\left(1 - e^{-t/T_1}\right) \qquad \text{eq(1.2)}$$

The relaxation time T_2 is the time required for the transverse component of the M_0 to decay to the equilibrium value. It is also called transverse relaxation time or spin-spin relaxation. The loss of phase coherence between different spin corresponds to spin-spin decay and arises due to the variation in the local precessional frequency. The decay of transverse magnetization follows the following equation:

$$M_{XY}(t) = M_0\left(1 - e^{-TR/T_1}\right)e^{-t/T_2} \qquad \text{eq (1.3)}$$

where TR is the repetition time of the pulse and e^{-t/T_2} is the spin-spin decay factor characterized by the time constant T_2.

The dephasing between different spins could also occur due to inhomogeneities in the external field and is termed as T_2*. The inhomogeneities causes the spin coherence to fall out faster than what the T_2 process alone would cause ($T_2^* < T_2$).

Thus, the MR signal produced by a particular tissue is dependent on M_0 which is directly proportional to the spin density (SD), and the relaxation times T_1 and T_2.

1.3 Measuring relaxation times and constructing an image in MRI

An MRI image is a collection of pixels. The intensity of each pixel in the image is directly related to the intensity of the local MR signal which in turn is dependent on the intrinsic parameters of the tissue i.e. SD and relaxation times, T_1 and T_2 (and T_2*). The MR signal is always propotional to the SD while the contribution of the relaxation times to the final pixel value depends on the *pulse sequence* used which in turn is a function of the parameters such as the repetition time (TR), the echo time (TE) (for spin echo pulse sequence), and the flip angle (α). To have sufficient data to construct an image, the pulse sequences are repeated many times. The most basic pulse sequences used in MRI are: gradient echo (GRE) pulse sequence, spin echo (SE) pulse sequence and inversion recovery (IR) pulse sequence.

1.3.1 Pulse sequences [3]

GRE pulse sequence

This is the most simple pulse sequence used in imaging. The FID signal is measured by adjusting the TR and α parameters. The measured signal is directly proportional to SD because it determines the magnitude of magnetization M_0. When TR much longer than T_1 is used, the longitudinal magnetization is fully recovered and the sequence is described as SD weighted. However, the magnitude of longitudinal magnetization flipped to the transverse plane is dependent on α; therefore the obtained image is density weighted and proportional to sin α. With TR shorter than T_1, the signal is dependent on TR, T_1 and α. With $\alpha = 90°$ and $TR<T_1$, the degree of recovered longitudinal magnetization depends on T_1 value of tissue and thus the image is T_1 weighted and proportional to SD. With smaller flip angles the magnitude of transverse magnetization decreases and thus the image becomes mainly SD weighted at $TR<<T_1$.

SE pulse sequence

The prime use of SE pulse sequence is to eliminate the signal loss in the image caused due to T_2* effects. A combination of 90°-180° pulse sequences is used. At first 90° pulse flips the longitudinal magnetization to transverse plane. Initially different parts of the sample start to precess in phase and then eventually start to dephase due to inhomogeneity. After the time TE (echo time), a refocusing pulse of 180° is applied. This rotates the magnetization vector at each point of the sample by 180° but with the phase difference acquired between 90° and 180° pulse (TE/2) locked in. All vectors then start to precess in phase again and thus generate an echo. In SE pulse sequence the adjustable parameters are TE and TR. At $TE<<T_2$ the signal is not sensitive to T_2, as the refocusing pulse would be applied when a sufficient phase difference between different magnetization vectors is not achieved. At $TE>>T_2$, the vectors undergo substantial loss in phase coherence, leaving very little measurable signal. At TE ~ TR, the signal is sensitive to T_2 and the image obtained is T_2 weighted.

IR pulse sequence

This pulse sequence is used to enhance the T_1 weighting of the signal. Initially 180° RF pulse is applied which inverts the longitudinal magnetization along the –z direction. Immediately after the RF pulse the magnetization starts to grow back to equilibrium. At the delay time TI (inversion time), a 90° pulse is applied. This flips the recovered longitudinal magnetization (during the time TI) to the transverse plane, which is then measured. At TI ~ T1, the measured signal is sensitive to T1 and the obtained image is T1 weighted.

1.3.2 Magnetic field gradients

The main task in constructing an image in MRI is to localize the MR signals to their spatial locations. While the magnitude of the signal is dependent on the SD, T_1, T_2 and the pulse sequence used, the spatial information is obtained by the application of three functional gradients: *slice selection*, *frequency encoding* and *phase encoding* in three spatial directions (Figure 2).

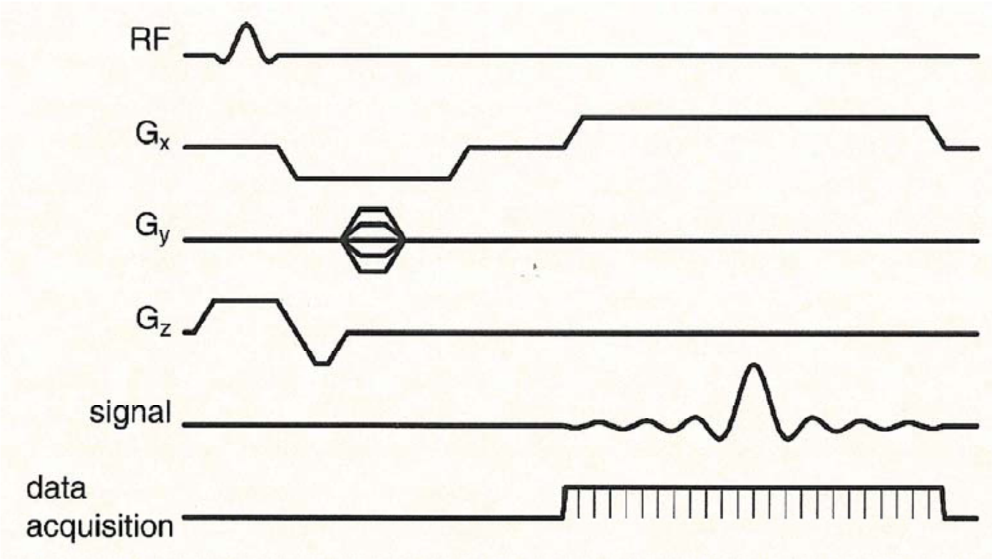

Figure 2: A basic pulse sequence timing diagram for image acquisition is shown. The RF pulses excite a signal and the spatial information is extracted by slice selection gradient along z, frequency encoding gradient along x and phase encoding gradients along y (The figure is taken from ref [3])

Slice selection

The selection of the slice is done by applying the gradient varying linearly along the z-axis. The RF pulse applied contains only a narrow band centered at the larmor frequency (ν_0). Thus only a narrow spatial band in the body is under the condition of resonance and is affected the most in flipping the M_0 to the transverse plane. The position of the slice can be selected by changing the centre frequency ν_0 of the RF pulse. The thickness of the slice can be varied by varying the ratio of frequency width of the RF pulse to the strength of magnetic field gradient. The *slice selection* thus allows the transverse magnetization to be predominately generated in the slice of interest.

Frequency encoding and Phase encoding

The *slice selection* localizes the signal along the z-axis; the rest of the localization within the slice is done in x-y plane by frequency encoding and phase encoding gradients. The frequency encoding gradient (also called read out gradient) is applied at the same time when the data acquisition (``read´´) is done while orthogonally applied phase encoding gradients encodes the second dimension in the image plane. The application of these two gradients and the final construction of the image are explained by the concept of k-space. The k-space is the spatial Fourier transform (FT) of the image and is what actually measured in MRI. The image is obtained by performing the FT of k-space matrix.

For frequency encoding, a gradient pulse along the x-axis is applied after the RF pulse. The gradient results in a large dispersion in the phase angles of the precessing nuclei. This dispersion keeps on increasing while the gradient is on and stops to grow once it is switched off. At this, the application of another gradient in the opposite direction diminishes the acquired phase dispersion and produces a strong signal at the centre of data acquisition window, called as gradient echo. The net signal measured over time is the spatial FT of the different frequencies distributed along the x-axis in the object. This signal however contains the sum of signals arising from different y positions at a single x-position. The phase encoding is therefore required to localize the signal to different y positions. A single gradient pulse is applied along the y-axis. The amplitude of the gradient is incremented each time the pulse sequence is repeated and the data sample is measured for each MR signal generated. The net measured signal $S(t)$ over time (t) is 2D FT of the image in 2D k-space (k_x, k_y). With each pulse sequence, one line in k_x with fixed k_y is measured and each phase encoding step moves the k-space sampling to a new line at a new k_y value. With these data points the filling of the *k*-space is done, from which the image is reconstructed by applying 2D FT.

1.4 Contrast in MR images

The contrast in an MRI image depends on the inherent properties of tissues responsible for MR signal generation i.e. SD, T_1 and T_2 (and T_2*). The watery tissues such as cerebrospinal fluid have high proton density as compared to more structured tissues such as white matter. The CSF in the SD weighted images therefore appears brighter. A remarkable soft tissue contrast can be obtained by exploiting the sensitivity of relaxation times to the pulse sequences. This flexibility in controlling the final contrast in the image is one of the great advantages of MRI from its clinical application point of view where the visualization of subtle anatomical differences between the healthy and diseased tissue is required. This diagnostic ability of MRI can be further enhanced by the addition of exogeneous agents called contrast agents (CAs). The recent advancement in CAs has allowed scientists to not only diagnose the small anatomical alteration in the tissue in the pathological state but also to monitor the physiological and molecular changes. The various types of contrast agents, their mechanism of action and their applications would be discussed in the following chapters.

CHAPTER 2

2. MRI and Contrast agents

2.1 Introduction

The main source of signal in MRI is water protons which are abundant in the human body. The contrast between different tissues is achieved by their difference in MRI parameters and the pulse sequences used. However, in some areas of the body the contrast is not sufficient especially if the small differences between normal and pathological tissues are needed to be diagnosed. In such cases, the addition of an exogenous agent enhancing the contrast between tissues greatly improves the diagnostic capabilities of MRI in disease specificity and pathological processes. Such agents are called contrast agents. Principally, the contrast agents alter the T_1 and/or T_2 relaxation times of the water protons and are thereby known as T_1 and T_2 agents respectively.

On the basis of magnetic properties, contrast agents can be broadly classified as:

1) The paramagnetic agents. These agents affect mainly T_1 properties of the water protons
2) The superparamagnetic agents. These agents are known to affect mainly T_2

Recently a new class of contrast agents has been developed known as Chemical Exchange Saturation Transfer (CEST) agents. The mechanisms of action of all of these agents and the underlying theories of their mechanism of action will be discussed in detail in this chapter.

2.2. Contrast agents in action: Mechanism and Theory

2.2.1 Paramagnetic agents

The paramagnetism is the property exhibited by the system containing of one or more unpaired electron pairs. As the magnetic moment of an unpaired electron pair is 700 times of a proton, a strong interaction takes place between the unpaired electron spin with the nuclear spin of the water protons in an aqueous solution [4]. The interaction between paramagnetic system and water protons is of 'dipolar coupling' type. The term dipolar means a close interaction between each individual magnetic particle and the water molecules, which falls off rapidly with distance. This interaction arises via three mechanisms: *the diamagnetic, the contact,* and *the pseudocontact* mechanisms [5]. The diamagnetic shifts are usually small and originate from effects such as conformational effects, inductive effects, and direct field effects. The contact contribution results from through bond transmission of unpaired spin density of paramagnetic metal ion to the other nuclei of interest (e.g. water proton) and the pseudocontact shift is the result of through space dipolar interaction between the same [5].

A paramagnetic system could be an organic free radical (e.g. nitroxide radical) or a lanthanide/transition metal ion with unpaired electrons in the valence shell (e.g. Mn^{2+}, Gd^{3+}, etc.). To explain the theory of paramagnetic relaxation enhancement (PRE), we will consider the relevance only to Gd(III) based complexes which are most widely used and studied in MRI contrast agent chemistry.

Gd^{3+} is a lanthanide metal ion with seven unpaired electrons in its f orbital. It has fully quenched orbital angular momentum and S = 7/2 spin state. For any aqua paramagnetic metal ion, the observed relaxation rate is the sum of diamagnetic and paramagnetic relaxation rates:

$$\frac{1}{T_{i,obs}} = \frac{1}{T_{i,d}} + \frac{1}{T_{i,p}} \qquad \text{eq(2.1)}$$

where *i* = 1, 2 corresponds to longitudinal and transverse relaxation mechanism respectively. The paramagnetic term ($1/T_{i,p}$) varies linearly with concentration of the paramagnetic species, [Gd^{3+}]:

$$\frac{1}{T_{i,obs}} = \frac{1}{T_{i,d}} + r_i[Gd^{3+}] \qquad \text{eq(2.2)}$$

The term commonly used to describe the proton relaxation rate enhancement by a paramagnetic substance is relaxivity, r_i (units, $mM^{-1}s^{-1}$). The straight line plot obtained by observed relaxation rate versus the concentration of [Gd^{3+}] gives the slope as the relaxivity of the agent and the intercept as the diamagnetic contribution ($1/T_{i,d}$) to the observed relaxation rate [6].

The relaxation rate enhancement is the result of hyperfine interaction between a nuclear spin and an electron spin. This hyperfine interaction can be divided into two components: 1) the dipole-dipole interaction between the nuclear magnetic moment and the electron outside the nucleus 2) the scalar interaction between the nuclear moment and the electron spin density at the nucleus itself, also called as Fermi contact interaction [7]. The time fluctuation of the hyperfine interaction of the electron spin and the nuclear spin is described by two types of motion: intramolecular rotational motion and intermolecular translational motion. The contribution of the intramolecular rotational motion is generally considered as inner sphere contribution to the overall observed relaxation. The inner sphere contribution is determined by (1) the rotational correlation time of the complex τ_R, (2) the water residence time τ_M in the first coordination shell, and (3) the electron spin relaxation. The equation describing this effect was developed by Solomen and Bloembergen [8, 9]. The intermolecular translational motion is generally considered as outer sphere contribution and is modulated by translational diffusion which is influenced by the electronic relaxation. Equation for outer sphere relaxation was developed by Freed and Ayant [10-13]

$$r_i = r_i^{IS} + r_i^{OS} \qquad \text{eq(2.3)}$$

The longitudinal and transverse inner sphere relaxation rates are given by:

$$\left(\frac{1}{T_1}\right) = \frac{cq}{55.5}\left(\frac{1}{T_{1m}+\tau_m}\right) = P_m \frac{1}{T_{1m}+\tau_m} \qquad \text{eq(2.4)}$$

$$\left(\frac{1}{T_2}\right)^{IS} = \frac{P_m}{T_m}\left[\frac{T_{2m}^{-2}+\tau_m^{-1}T_{2m}^{-1}+\Delta\omega_m^2}{\left(\tau_m^{-1}+T_{2m}^{-1}\right)^2+\Delta\omega_m^2}\right] \qquad \text{eq(2.5)}$$

The influence of the electronic spin relaxation on the relaxivity comes from electron spin Hamiltonian. In a system with electron spin $S \geq 1$ (e.g. for Gd^{3+}), the Hamiltonian $\hbar H(t)$ is the sum of Zeeman term $\hbar H_o = g_s \mu_B B_o S_z = \hbar \omega_o S_z$ and a time fluctuating perturbing Hamiltonian $\hbar H_1^L(t)$ which is also known as zero field splitting (ZFS) Hamiltonian. This time perturbing part can be divided in to static (S) and transient (T) part. The static part is modulated by Brownian rotation of the complex with the rotational correlation time τ_2 while the transient part is fluctuated because of the vibrations and distortions of the complex with the vibrational correlation time τ_v [14]. The Zeeman Hamiltonian varies linearly with magnetic field B_o while zero field splitting Hamiltonian is field independent.

The equation explaining PRE was first formulated by Solomen and Bloembergen which was then combined with electron spin relaxation equation [15] to the final equation referred to as SBM equation. The SBM theory was based on certain assumptions [6], the validation of which under various conditions has been studied extensively in the recent reviews by Lothar Helm [7] and Pascal Fries [14].

2.2.2 Superparamagnetic agents

As the name indicates, these agents exhibit strong paramagnetism when placed in an external magnetic field. Superparamagnetic agents (SPA) have much larger magnetic moment relative to the paramagnetic agents. The superparamagnetism is observed at the particle size of nm or smaller. At this size scale the formation of Bloch wall between the two magnetic domains (aligned and antialigned) in the particle becomes theromodynamically unstable leading to the formation of a single domain particle. Because of the single domain nature, the entire particle aligns with the magnetic field and therefore exhibit high magnetic susceptibility. The inhomogeneous distribution of such superparamagnetic agents *in vivo* gives rise to local field gradients which increases the rate of loss of phase coherence of the different proton spins. (Figure 3) [16]. The susceptibility-induced relaxation rate enhancement of SPA agents is much stronger than the paramagnetic agents where the relaxation is of close range and dipolar coupling type.

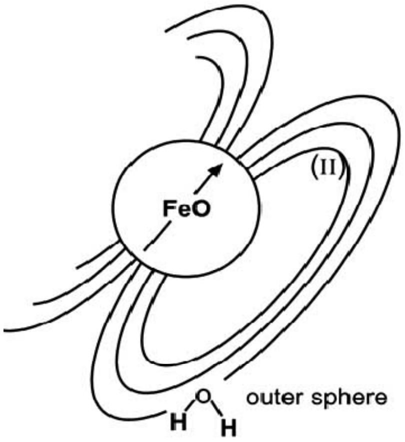

Figure 3: The protons in the outer sphere of T_2 agents loses their phase coherence rapidly

The most commonly used SPM contrast agents are iron oxide based nanoparticles composed of magnetite (Fe_3O_4) or maghemite (γ-Fe_2O_3) with a typical core diameter of 4 to 50 nm [17]. Depending on the size, crystalline structure, coating and higher order magnetization, these nanoparticles are also known as superparamagnetic iron oxide nanoparticles (SPIO), ultrasmall superparamagnetic iron oxide particles (USPIO), very small superparamagnetic iron oxide particles (VSOP), monocrystalline iron oxide particles (MION) and cross linked iron oxide (CLIO) [18].

The T_2 relaxation effect of these agents is explained by bulk-susceptibility effect which is the reformulation of the ‘outer sphere relaxation’ theory. To account for the effects of ‘magnetic saturation’ at higher magnetic fields (>0.05 T) on the particles possessing high magnetic moment, additional terms were introduced leading to the following equation [19].

$$R_2 = \frac{1}{T_2} = \left(\frac{32\pi}{405}\right) \gamma_I^2 \mu^2 \frac{N_A}{1000} \left(\frac{[M]}{rD}\right) \{6.5 j_2(\omega_s) + 1.5 j_1(\omega_I) + 2 j_1(0)\} \qquad \text{eq(2.6)}$$

$$j_n(\omega, \tau, \tau_{Sn}) = R_e \left(\frac{1 + {}^1/_4 \left(i\omega\tau + {}^\tau/_{\tau_{Sn}}\right)^{1/2}}{1 + \left(i\omega\tau + {}^\tau/_{\tau_{Sn}}\right)^{1/2} + {}^4/_9 \left(i\omega\tau + {}^\tau/_{\tau_{Sn}}\right) + {}^1/_9 \left(i\omega\tau + {}^\tau/_{\tau_{Sn}}\right)^{3/2}} \right)^2 \qquad \text{eq(2.7)}$$

Where, γ_I is the gyromagnetic ratio of protons in water, M is the molarity of magnetic nanoparticle, r is its radius, N_A is the Avagadro’s number, μ is the magnetic moment of the nanoparticle, ωs and ωI are the larmor angular frequencies of the nanoparticle electric moment and water proton magnetic moment, respectively, the functions $j_n(\omega, \tau)$ are spectral density functions in which R_e is the real part of the expression that follow in parenthesis, τ ($\tau = r^2/D$) is the time scale of fluctuations in the particle-water proton magnetic dipole interaction arising from the relative diffusion motion (*D*) of a particle with respect to water molecules, and τ_{S1} and τ_{S2} are the lifetimes of the longitudinal and transverse components of μ. The equation was further improved by Bulte and Brooks [20] to account for the elevated ‘plateau’ showed by MION particles at low field. The theory explaining the relaxation rate enhancement by iron-oxide nanoparticles compartmentalized in to the cells was later explained by Brian K. Rutt and is refrred as ‘static dephasing regime theory’ [21].

These iron-oxide nanoparticles have recently become very popular for their wide range of application to the biosystem. Many research groups have reported a vast number of applications of these particles once they are surface coated with biocompatible materials (e.g. dextran, carbodextran etc.). These coatings can be further functionalized to recognize desired targets through antigen-antibody [22, 23], nucleic acid hybridization [24, 25] and gene expression [26, 27].

2.2.3 CEST agents

CEST is based on the principle of Saturation Transfer (ST) or Magnetization Transfer (MT).

In the presence of a magnetic field the distribution of spins according to the Boltzmann equation (i.e. the number of spins aligned exceeds the number against it) gives some bulk magnetization to the system. If a RF pulse of suitable frequency is applied, the number of spins from low energy level gets promoted to higher energy and when this RF pulse is applied for enough long, saturation can be achieved. Under saturation conditions the population of the two states becomes equal and the net magnetization reduces to zero. As the MRI signal depends on the flipping of this magnetization to transverse plane, under the condition of saturation a loss of MRI signal will be observed (similar to a T_2 agent). If the saturation is done selectively to one set of protons, it is transferred to neighboring spins by chemical exchange (magnetization transfer). For such magnetization transfer to be observed, this rate of exchange (k_{ex}) must not be greater than the difference in frequency between two sets of neighboring protons (Δω) [28].

$$\Delta\omega \geq K_{ex} \qquad \text{eq(2.8)}$$

Small molecules in biological system such as sugars, proteins etc. have large pools of exchangeable protons and therefore can act as CEST agent. In the presence of an exogeneous paramagnetic CEST (PARACEST) agent, a large MT is observed. This enhancement of CEST effect is due to: 1) increased chemical shift difference, 2) enhanced chemical exchange.

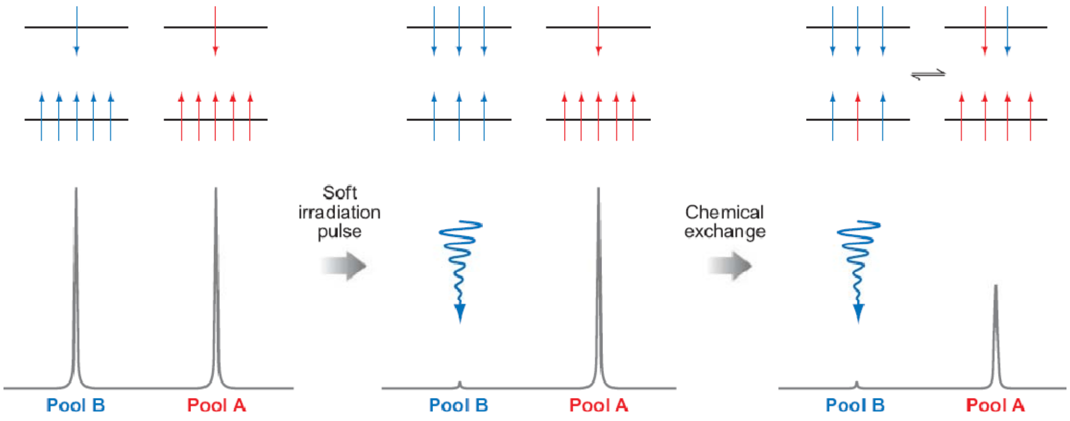

Figure 4: Two pools of protons undergoing chemical exchange after saturation. (Reprinted with permission from Annual Reviews of Biomed Eng. 10:391–411©2008 by Annual Reviews www.annualreviews.org) [29])

2.3. Contrast agents and their applications

On the basis of applications, contrast agents can be broadly classified as:

(a) Compartmental probes

(b) Targeted probes

(c) Smart probes

(d) CEST and PARACEST agents

2.3.1 Compartmental probes: These probes are the first generation of CAs and are currently in clinical use. The degree and localization of these CAs depends on the vascular permeability of the tissues and hence a better contrast in the image is obtained when the vascular (e.g. tumour) or cellular (e.g. scar) integrity in the imaged organ is challenged. The clinically used CAs have the molecular weight around 600 Da and relaxivities between 4-5 $mM^{-1}s^{-1}$ at 20 MHz and 310 K [30]. On the basis of structure these CAs can be divided into two types: acyclic and cyclic. DTPA is the common skeleton for acyclic CAs and DOTA is for cyclic (Figure 5). These CAs have proven to be a great success (Figure 6). Most of them are distributed in intravascular and interstitial spaces and are excreted via kidneys except hepatobiliary agents. Hepatobiliary agents such as MultiHance^{TM} have affinity towards human serum albumin (HSA). They are taken up by hepatobiliary cells and are excreted via both biliary and kidney sytems [30].

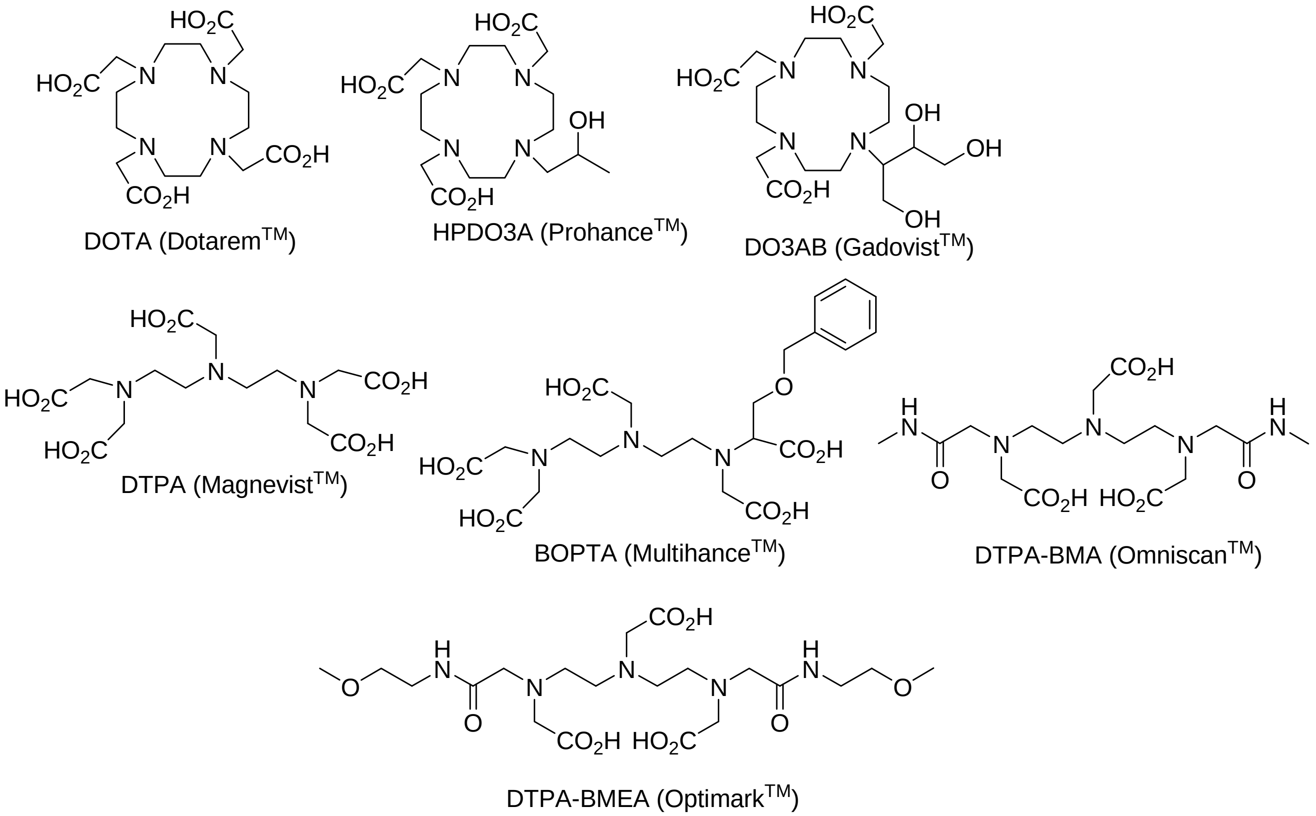
DOTA (Dotarem^{TM})

HPDO3A (Prohance^{TM})

DO3AB (Gadovist^{TM})

DTPA (Magnevist^{TM})

BOPTA (Multihance^{TM})

DTPA-BMA (Omniscan^{TM})

DTPA-BMEA (Optimark^{TM})

Figure 5: The ligand structure of various clinically approved acyclic and cyclic CAs is shown. They are used *in vivo* in Gd(III) chelated form.

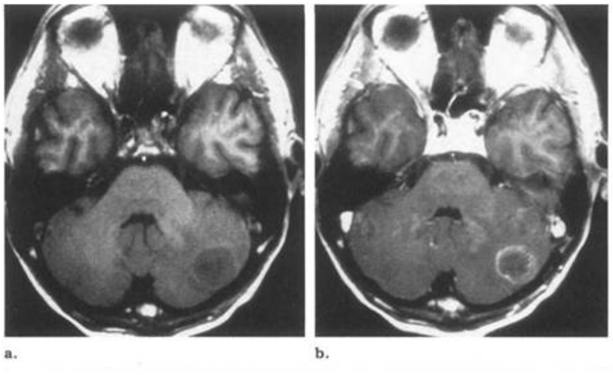

Figure 6: (a) A precontrast spin echo image (b) post contrast spin echo image after the administration of Gd-DTPA [31]. The discrimination of lesion from normal tissue is greatly enhanced after the administration of CA. (The figure is taken from the ref [31])

2.3.2 Targeted Probes:

Despite of giving high contrast images, the conventional contrast agents clinically in practice are not efficient to provide the contrast enhancement derived from specific molecular targets. Two approaches have been used to achieve the specific targeting of CAs, namely passive and active targeting. In *passive* targeting the internalization of CAs is achieved by targeting macrophages which originate in the bone marrow, circulate and localize into various organs. Uptake of the agents into phagocytic cells occurs via Fc or C3b receptors and is more efficient than the pinocytosis mechanism taking place in the non-phagocytic cells. Such techniques are mainly used for labeling macrophage rich tissues such as spleen, lymph node and bone marrow. Dextran coated USPIO [32] and nanoparticles of Gd-loaded chitosan [33] have been used for such passive targeting. In active targeting, ligand directed site specific CAs are used. Some examples of targeting ligands are:

(a) Monoclonal Antibody (mAb):- Pegylated paramagnetic liposomes with monoclonal antibody (anti E-selectin) was used to target human umbilical vein endothelial cells [34].

(b) Antibody fragment (Fab):- High-affinity anti-human E-selectin (CD62E) $F(ab')_2$ fragments conjugated to CLIO have been used for MR imaging in human endothelial cell culture [35].

(c) (recombinant) Protein:- Annexin A5 and synaptotagmin conjugated to SPIO or multiple Gd-DTPA (Figure 7) can be used to target phosphatidylserine on apoptotic cells [36].

(d) Peptidomimetics:- paramagnetic nanoparticles conjugated to anti-$\alpha_v\beta_3$-antibody was used to detect and characterize early angiogenesis induced by minute solid tumors [37].

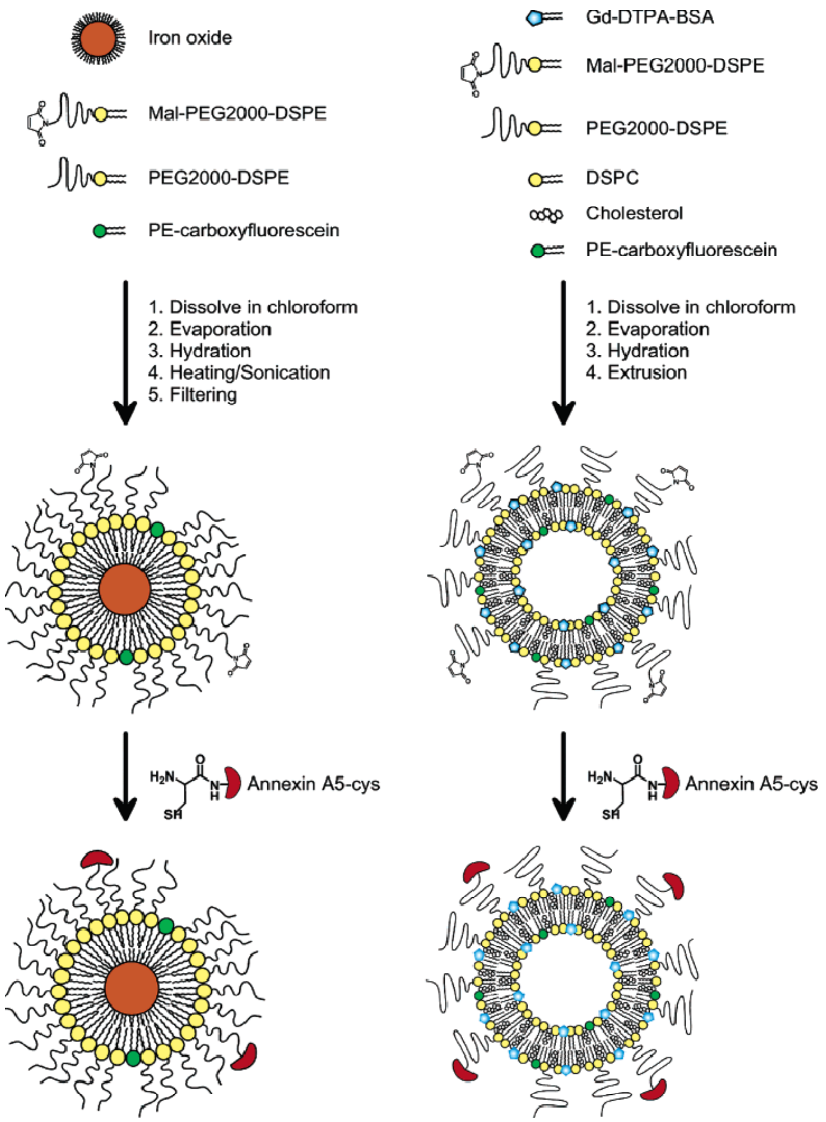

Figure 7: The design and synthesis of the constructs used to target apoptotic cells. (The figure is taken from ref [37])

2.3.3 Smart Probes

Smart probes are characterized by their controlled activation leading to the relaxivity (r_1 and/or r_2) increase. The activation here refers to the switch from 'off' state (low relaxivity) to 'on' state (high relaxivity) triggered by some biological event, for example change in pH, Ca^{2+}, pO_2 or change in any metabolite concentration. Such factors are able to modulate the parameter(s) determing the relaxivity (IS and/or OS) of the CA, thus causing the described switch. The modulation of the parameters affecting IS contribution to the relaxivity is relatively easy to control as compared to the OS contribution. The various parameters determining the IS relaxivity are depicted in Figure 8.

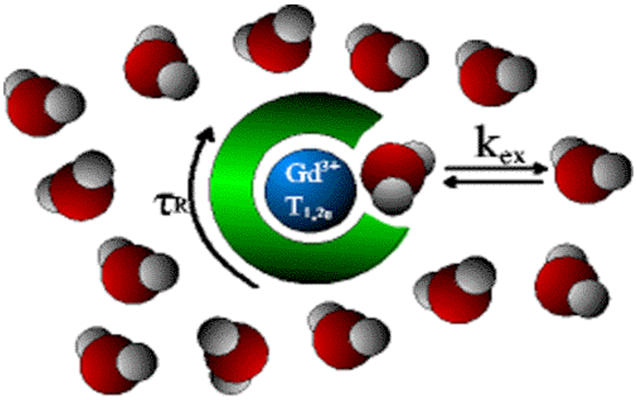

Figure 8: The various parameters influencing the relaxivity of a low molecular weight Gd-chelate.

The greatest control has been achieved by modulating the number of inner sphere water molecules (q) in presence and in absence of a biological factor. As these water molecules are directly linked to the paramagnetic centre, a decrease or an increase in their number is directly translated to the respective changes in the relaxivity. Another parameter that can be control is rotational correlation time (τ_R). The correlation time has the contribution from rotation (τ_R), electronic relaxation ($T_{i,e}$ where $i = 1,2$) and chemical exchange (τ_m). At the magnetic field of 1.5 T (64MHz proton frequency) the rotational diffusion dominates the correlation time. For low molecular weight complexes, a decrease in tumbling rate increases the relaxation rate. However at higher fields (above ~ 200MHz) the relaxivity decreases with increase of rotational correlation time. At low fields the increase in relaxivity with increase in τ_R can be offset if τ_m is not optimized. The examples of the smart probes utilizing the dependence of these parameters to the observed relaxivity are discussed below.

(a) Enzyme activated

Monitoring enzyme activity by modulating *q* parameter was demonstrated by Meade and coworkers [38, 39]. The structural design of the agent was such that the ninth coordination site of the Gd^{3+} in Ca was blocked by a β-galactose moiety. On exposure to the enzyme β-galactosidase, the cleavage of this moiety took place, allowing access of a water molecule for filling the coordination sites of Gd^{3+} (Figure 9). This increase in hydration number, lead to a relaxivity (r_1) increase of 25% [38] which was improved to 200% [39] with the slight modification in the structure.

Another example of enzyme sensitive CAs exploiting the modulation of τ_R was shown by McMurray and coworkers [40]. Activation of the CA was done by the human carboxypeptidase B, thrombin-activatable fibrinolysis inhibitor (TAFI). The enzyme action removed the shielding moiety and exposed the high human serum albumin (HSA) affinity part of the molecule (Figure 10). The binding of CA to a big macromolecule like HSA decreased the tumbling rate (τ_R) resulting in 100% r_1 enhancement.

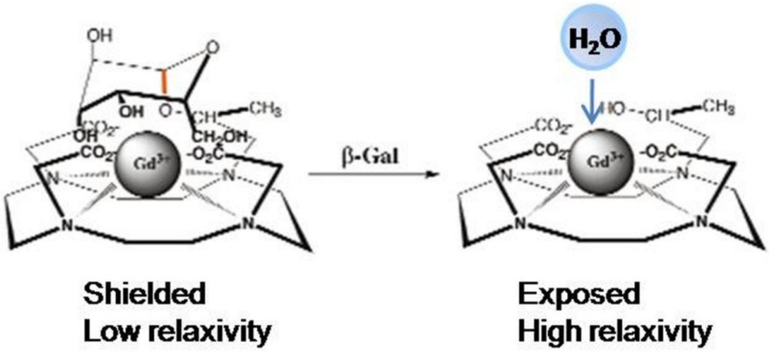

Figure 9: An enzyme selective CA (EgadMe [39]) switched on by change in hydration number of the complex.

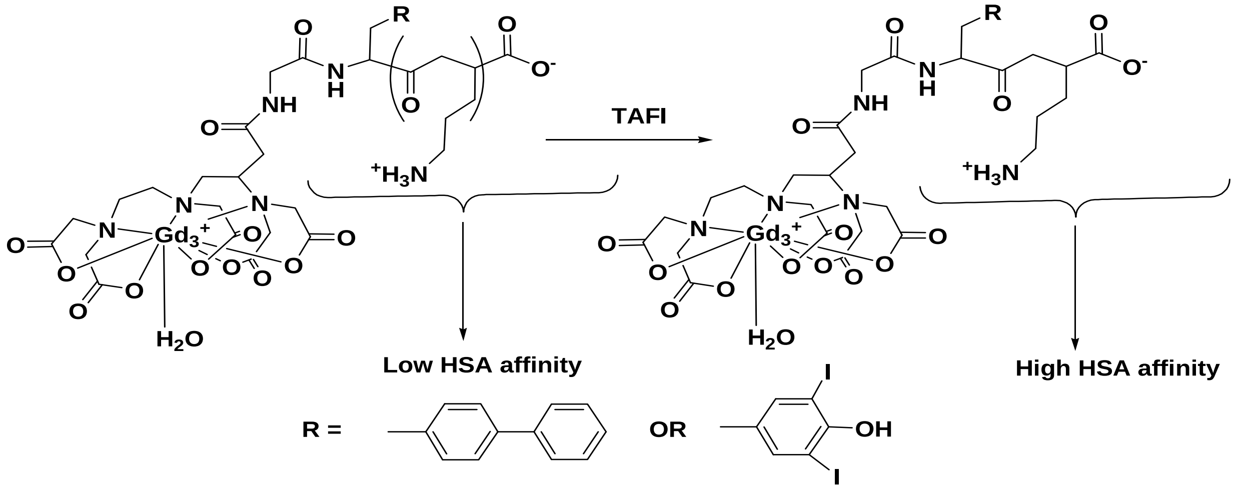

Figure 10: An enzyme sensitive CA exploiting the change in τ_R on HSA binding is shown [41]

An enzyme selective PARACEST agent was reported by Tóth and coworkers [42]. The approach demonstrated could be used to target a wide variety of enzymes (Figure 11)

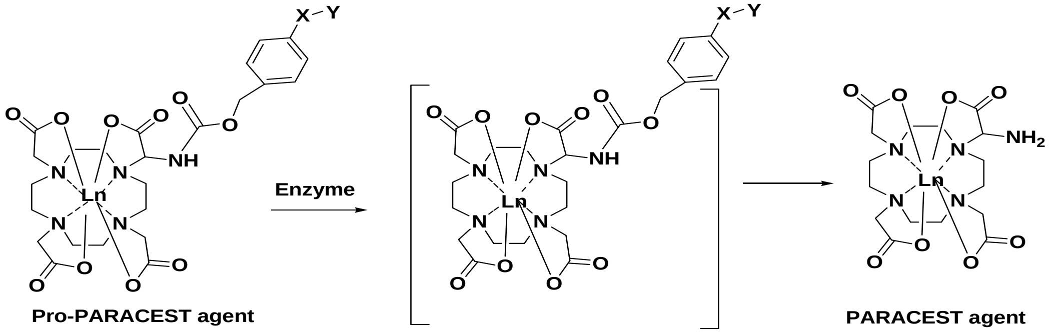

Pro-paracest agent
Ln = Yb, X-Y:
β-o-galactopyranoside[Yb-(DOTA-αBz-β-gal)]
targeted enzyme:
β-galactosidase, esterase,
lipase, sulfatase peptidase,
Reductase

X-Y:
β-o-galactopyranoside,
peptide, ester, amide Sulfate, nitro,

PARACEST agent
Ln = Yb, X-Y :
[Yb-(DOTA-NH_2)]$^-$
-

Figure 11: A self-immolative approach to target wide variety of enzymes [42]

(b) pH activated

An example of pH sensitive CA utilizing the effect of change in water (proton) exchange rate (τ_M) on relaxivity was shown by Sherry and coworkers [43]. The agent Gd-DOTA-4AmP had four phosphonate moieties at the tetraamide derivative of DOTA. The phosphonate groups act in concert as acids and bases, catalyzing the prototropic exchange (increase in τ_M) resulting in an enhanced relaxivity over a pH range that is useful for biological pH imaging (Figure 12).

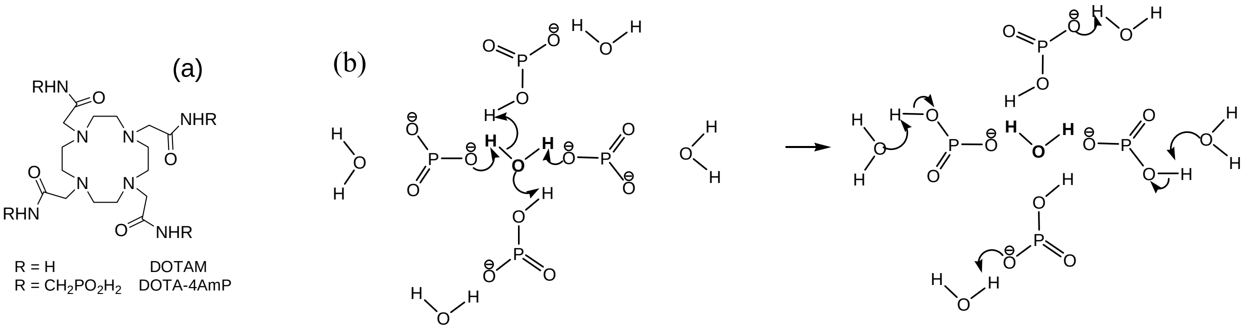

Figure 12: (a) Structure of the ligand (b) Schematic representation viewed down the Gd-OH$_2$ axes, phosphonates transfer protons between the coordinated water and the bulk [43].

The agent with some modification was later coupled to PAMAM dendrimers, to slow down τ_R, increase relaxivity and improve the pH responsive characteristics of the complex [44]. The modulation of hydration state with pH was investigeted by Parker and coworkers [45-49] where pH dependent displacement of water was observed with reversible binding of endogeneous anions (e.g. HCO_3^-) (Figure 13)

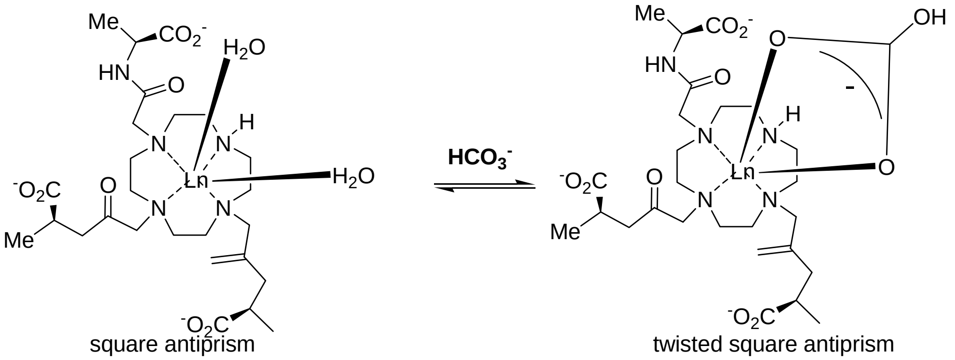

Figure 13: pH dependent reversible binding of HCO_3^- leading to equilibrium between q = 2 species and q = 0 species [45].

Another approach of change in relaxivity induced by pH and dictated by rotational correlation time was used by Aime and coworkers [50] and by Hovland and coworkers [51]. On the similar mechanism Merbach and coworkers reported the pH sensitivity of PAMAM dendrimeric CAs [52]. Beside the macrocycle based CAs, Tóth and coworkers reported high relaxivity pH responsive agents based on gadofullerenes [53] and gadonanotubes [54]. The high relaxivity and sensitivity of these agents to pH prove their potential for *in vivo* MRI.

(c) Metal ion activated

Metal ions play an important role in biological system. Many trace metal ions such as Zn^{2+}, Fe^{3+}, Cu^{2+}, Mn^{2+}, Co^{2+} are required as cofactors for many essential cellular enzyme.

The very first report of an agent sensitive to a metal ion was by Meade and coworkers [55]. The T_1 agent was designed to be sensitive to Ca^{2+}. Two DO3A units were linked to a Ca^{2+} selective chelator, BAPTA. A 75% r_1 enhancement was observed upon Ca^{2+} addition. The enhancement was proved to be due to the change in hydration number parameter [56, 57].

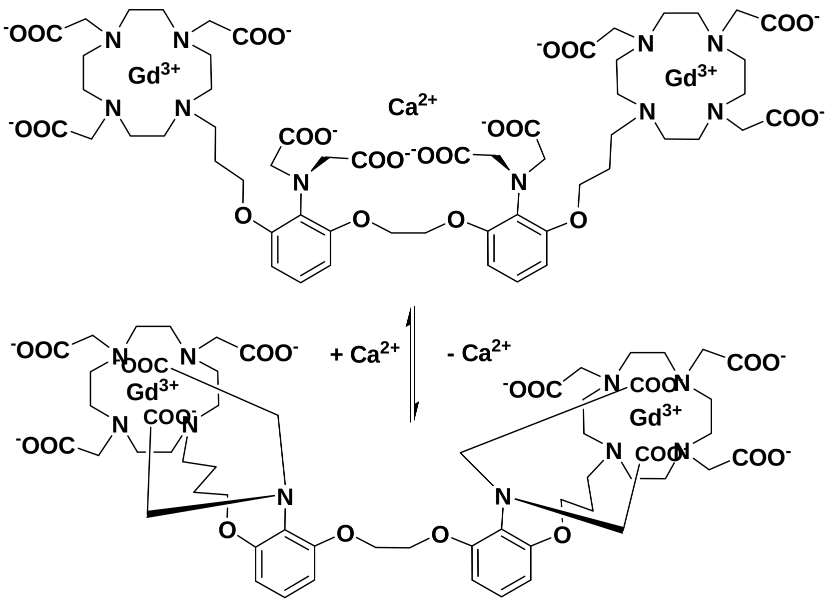

Figure 14: Gd-DOPTA sensitive to Ca^{2+}.

Another approach to target Ca^{2+} was shown by Jasanoff and coworkers [58]. A T_2 agent was developed using a SPIO particle conjugated to calmodulin, a Ca^{2+} sensor. A fivefold change in T_2 relaxivity was observed with aggregation driven by Ca^{2+}. SPIO agents could be used in low concentration because of their high relaxivity but they respond slowly to Ca^{2+} changes [59]

Recently, Zn^{2+} ion has also gained an attention since its possible role in synaptic transmission was revealed. A DTPA-bisamide containing pyridyl groups was reported to be sensitive to $Zn^{2+}$by Nagano and coworkers [60]. On the addition of Zn^{2+}, the agent binds in 1:1 fashion and the accessibility to water is reduced leading to the decrease in relaxivity by ~ 33%. However with further addition of Zn^{2+}, the agent binds two Zn^{2+} ion (1:2 ratio) restoring the relaxivity back to the initial value. A porphyrin based dual sensor was reported for Zn^{2+} sensing for MRI and optical imaging by Lippard and coworkers [61]. The Mn(III) loaded prophyrin ligand system described can be used for Zn^{2+} sensing by MRI while the metal free form serves as the fluorescent Zn^{2+} sensor. Meade and coworkers have also reported a potential Zn^{2+}sensor [62].

The Zn^{2+} binding of the agent is accompanied by 114% increase in the relaxivity with coordination of one water molecule in the inner sphere.

2.3.4 CEST and PARACEST agents

The endogeneous agents carrying some exchangeable components with the solvent protons can act as CEST agent. For example, glycogen contains exchangeable –OH protons which resonances at ~ 1 ppm downfield to the water protons. This difference in the chemical shift has been used to presaturate it and used as a CEST antenna. Due to metabolic process of breakdown of glycogen into glucose, a decrease of CEST affect in the liver was observed [63]. Amide protons of the intracellular proteins and peptides have also been used for their pH dependent chemical exchange [64]. To increase the signal to noise ratio the difference in the chemical shift of the targeted pool of the proton and the protons in the visicinity to it are to be increased. For this purpose, PARACEST (paramagnetic –CEST) agents have been used. The EuDOTA-(glycine ethyl ester)$_4$ was used as the first PARACEST agent. With this PARACEST agent, the chemical shift difference of +50 ppm was observed as compared to +5 ppm in case of any endogeneous CEST agent [65]. A large chemical shift difference between the targeted pool of protons to the background is important because it increases the signal to noise ratio. Aime and coworkers have reported a concentration independent pH sensitive PARACEST agent [66]. Two sets of complexes were used (Yb-DOTAM-gly and Eu-DOTAM-gly). Both complexes differ in their shift differences between two sets of exchangeable protons (coordinated water molecule and amide protons). The CEST effect of Eu(III) loaded complex was independent of pH while pH dependence of exchange of amide protons in Yb(III) complex was exploited

Sherry and coworkers have reported a glucose sensitive PARACEST agent. The water proton exchange was decreased on glucose binding of the agent, thereby switching on the CEST effect from the metal bound water [67, 68].

CHAPTER 3

3. MRI in brain research

3.1 Introduction

MRI had played an important role in understanding the structure and function of the brain. After the first report of MRI as a clinical imaging tool in 1971 by Raymond Damadian [69], the pace of understanding brain at morphological, cellular, neurophysiological and molecular level has been quite rapid.

A conventional MRI scan of the brain provides images with excellent tissue differentiation, giving the structural and vascular information. Recently, MRI has become an important tool to study the functional activation of the brain and is commonly referred as functional MRI (fMRI). Before the emergence of fMRI in 1990s [70-73], the activation-based neuroimaging studies of the brain involved the use of nuclear imaging techniques e.g. positron emission tomography (PET) [74, 75]. However as compared to PET, fMRI provides a better spatial resolution with no potential hazards associated with radioactive tracers required in nuclear imaging. This safety and the noninvasive nature of fMRI are significantly important for its application in clinics as well as in basic research. Furthermore, the high spatial and temporal resolution obtained in fMRI permits the delineation of the spatial extent of an activated area with the precise matching of the anatomical structures.

The physiological basis of probing regional brain activation by these techniques lies in the fact that the brain activation is associated with changes in vascular and metabolic responses. The changes in the physiological parameters linked to these responses are thus used as the indicator for the underlying function of the brain. The blood oxygenation level dependent (BOLD) contrast method used in fMRI for example, measures the magnetic field inhomogeneity (susceptibility effects) caused by the change in the ratio of deoxygenated to oxygenated blood following neuronal activation [76]. The neurometabolic and neurovascular coupling underlying the BOLD fMRI signal is based on the cascade of events that follows neuronal activation.

3.2 BOLD fMRI: an indirect method of mapping functional activity in the brain

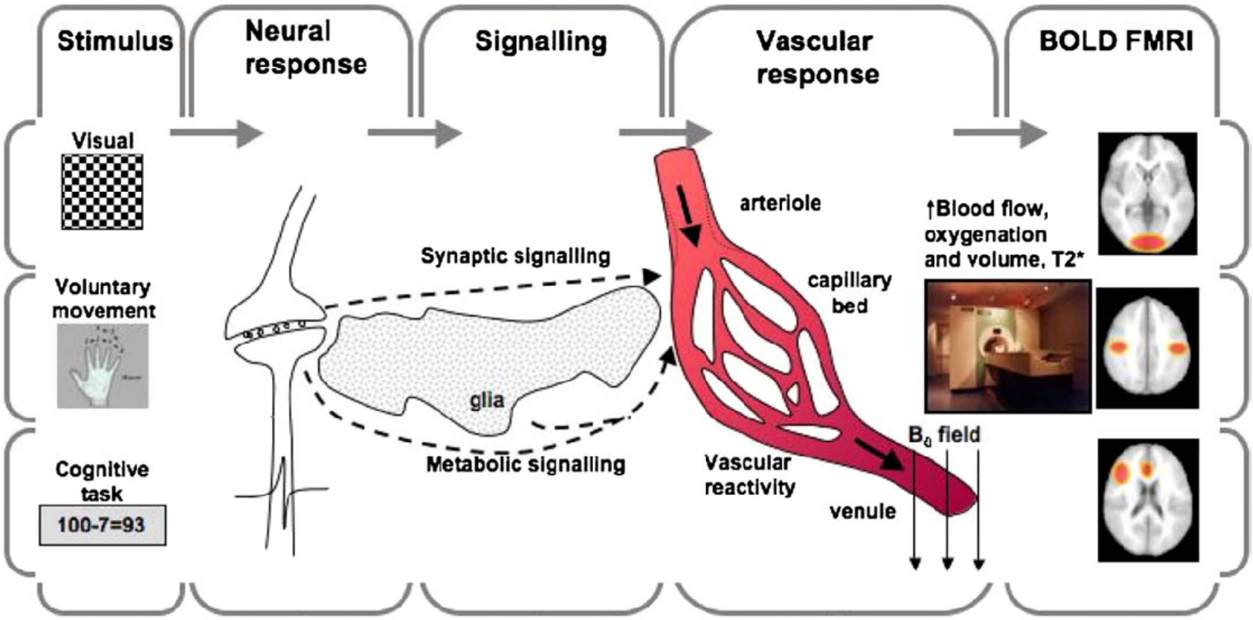

Figure 15: The BOLD signal due to increased blood flow is generated in response to enhanced neural activity (neurovascular coupling) mediated by the signaling events in astrocytes. Reproduced from ref [77] with the permission from authors.

The BOLD contrast is the most widely used method in fMRI for studying functional activity of the brain [77-83]. The physiological basis of the BOLD signal is believed to be increased vascular response coupled to neuronal activity through astrocyte signaling events [77, 83], as outlined in the Figure 15. The increase in neural activity results in an increased requirement of nutrients and oxygen supply [84, 85]. This energy requirement of the neurons is believed to be closely associated with the energy metabolism of the astrocytes [86]. The specific neuron-astrocyte interactions leads to the astrocytes induced vasodilation of the arteriols encasing the population of activated neurons. A wide variety of molecular mediators are involved in coupling this increased vascular activity to neuronal activation, such as K^+, H^+, cyclooxegenase products, adenosine etc. These mediators act on the smooth muscles of arteriols resulting in dilation or constriction [87-90]. Because of this neurovascular and neurometabolic coupling, there is a localized substantial increase in cerebral blood flow (CBF) and cerebral blood volume (CBV) and a moderate increase in cerebral metabolic rate of oxygen ($CMRO_2$) in the bloodvessels [91]. This eventually results in the changing ratio of oxy- and deoxy- haemoglobin (Hb) in a volume unit (voxel). Due to the difference in the magnetic properties of deoxyHb and oxyHb, a magnetic field inhomogeneity is found within and around blood vessels, the magnitude of which increases with the amount of deoxyHb present. In deoxyHb, Fe(II) is present in high spin state which gives the paramagnetic property to it while in oxyHb it switches to the low spin state and is thus diamagnetic. The presence of deoxyHb alters the magnetic field susceptibility and results in a rapid loss of intravoxel spin coherence (T_2* weighted signal loss) which is measured as BOLD signal [77]. Beside this microscopically inhomogeneous field (hemodynamic factors), the final BOLD signal also depends on vessel architecture (capillaries, arterioles, orientation etc.) [91]. The BOLD fMRI is therefore considered as an indirect method of mapping functional activation in the brain.

3.3 A more direct method to map functional activity in the brain: Aim of the project-1

In order to understand the brain function completely, not only the precise spatial extent of brain activation is required but the precise temporal information of the neural events is also important. The BOLD fMRI however do not measure the neural activity directly but rely on hemodynamic parameters such as CBF, CBV and $CMRO_2$ [81, 82, 91]. This causes a time lag between the actual neural event and the measurement of the signal [92] and therefore the accurate co-localization of the measured signal to the underlying neurophysiological activity becomes difficult. A more direct and accurate method of mapping the functional activation of the brain would be to measure the changes in parameters directly linked to the neural events such as membrane potential, pH, ions flux (Ca^{2+}, Na^{+}, K^{+}, Cl^{-} etc.), and neurotransmitters flux [93].

Amongst the various ions flux believed to be tightly linked with neuronal activity, the changes in the Ca^{2+} have been studied extensively by optical imaging *in vitro*, in neuronal cultures, as well as *in vivo*, in the brain of animal models. A wide variety of fluorescent indicators, originally developed by Roger Y. Tsien are available to investigate the role played by Ca^{2+} in normal and pathological conditions [94, 95]. Much of the advancement has been made in this field with the fluorescent dyes [96-98] and recently with the development of two-photon microscopy high resolution functional imaging in the living animals has also been achieved [99-103]. However even with high temporal resolution obtainable with optical imaging and the better depth penetration achieved with two photon microscopy, these techniques still suffers from the photobleaching side products of fluoresecent dyes, light scattering problems, inability to record from deeper brain structures and the limitation with whole brain coverage.

In order to have a nonhemodynamic method of mapping brain activation with no depth penetration limit and possibility to record with whole brain coverage, we **aimed at the development of MR detectable functional probes having an ability to sense the Ca^{2+} modulation and translate it in the form of dynamic MR contrast**. Such functional markers are also known as smart contrast agents (SCAs). The development of SCAs would be discussed in section B.

3.4 Studying structural organization in the brain: Aim of the project-2

In order to understand the functional activity in the brain, a detailed knowledge of anatomical connections between different brain regions would be extremely important. Various brain regions especially motor areas work in a networked manner to perform any movement related task. Along these lines, the fibre tracts which allow the signal transmission directly from one region to the other can be traced. Overlaying the information obtained from functional activity study to structural connectivity study would help us to understand the relationship between structure and function of the brain. With this we formulated the project-2 aimed at **developing markers which can reveal the anatomical connectivity in the brain noninvasively by MRI.** The currently available method to study the same and the development of the markers under the project-2 will be discussed in section C.

Section B

Project -1

Development of Magnetic Resonance Guided Functional Markers

CHAPTER 4

4. Development of Ca^{2+} sensitive SCAs

4.1. Introduction

4.1.1 Neuronal regulation of Ca^{2+}

Ca^{2+} plays an important role in regulation of several neuronal processes. Earlier studies done with ion selective micropipettes showed that the synaptic activity induces a depletion in extracellular Ca^{2+} ($[Ca^{2+}]_o$) [104-107] which was also proved later with a fluorescent probe [108, 109]. The computational studies done using a compartmental model on the dynamics of $[Ca^{2+}]_o$ in the extracellular space have shown that the flux of Ca^{2+} through channels can cause a large fluctuation in its concentration [110-114]. The activity dependent large fluctuation in $[Ca^{2+}]_o$ can affect the neuron excitability and synaptic transmission, it thus have a potential in regulating a wide variety of cellular processes. However, the impact of the $[Ca^{2+}]_o$ depletion depends on the spatial and temporal aspects of synaptic activity [115].

To generate the Ca^{2+} signal both external and internal sources of Ca^{2+} are used. The flux of Ca^{2+} from extracellular space to intracellular can take place by multiple channels: voltage operated Ca^{2+} channels (VOCs), receptor operated Ca^{2+} channels (e.g. NMDA) and channels which are sensitive to diverse number of external stimuli such as store operated Ca^{2+} channels (SOCs), transient receptor protein (TRP) ion channels, etc. [116]. The internal source of Ca^{2+} is mainly located on endoplasmic reticulum (ER) (sarcoplasmic reticulum in muscle). The Ca^{2+} release from ER is triggered by mainly two kind of receptors, inositol-1,4,5-triphosphate gated receptor ($InsP_3R$) and rynodine receptor (RyR). $InsP_3R$ is regulated by a number of messengers, such as inositol-1,4,5-triphosphate ($InsP_3$), cyclic ADP ripose, nicotinic acid adenine dinucleotide phosphate (NAADP) and sphingosine-1-phosphate. $InsP_3$ is generated by phospholipase (PLC) which is activated by: G protein coupled receptors, tyrosine kinase coupled receptors and also by an increase in [Ca^{2+}]. Beside these, various pumps and exchangers e.g. Na^{+}/Ca^{2+} exchanger, mitochondrial uniporter etc. help removing the cytoplasmic Ca^{2+} and maintaining the homeostasis [117] .

Thus the internalized Ca^{2+} has many targets and is therefore able to do cross talk with other signaling pathways [116]. The downstream effects of the Ca^{2+} signaling depend on its spatial as well as temporal organization which depends on the geometric relationship between Ca^{2+} channels and sensors. A discrete cluster of channels produces Ca^{2+}microdomains or nanodomains. The little difference in the distance of these localized domains from the sensors (20 nm for microdomains and 200 nm for nanodomains) and the diffusion restriction results in a 10 fold difference in the magnitude and 1000 fold difference in the speed of Ca^{2+} signal generated by these two domains. [118]. These Ca^{2+} signals are referred as blip/quark, puff/spark depending on their magnitude and speed [116]. For example, VOCs generate the rapid Ca^{2+} fluxes (responsible for fast muscle contraction) while TRPs operate over large time scale at low conductance of Ca^{2+} (important for smooth muscle contraction and cell proliferation). Versatality in Ca^{2+} signaling is also due to different cell types uses different isoforms of the same receptor e.g. parallel/pukerniji cell synapses uses mGluc1and PLCβ4 to generate Ca^{2+} transients while hippocampal neurons takes the pathway of mGluR5 and PLCβ1 to generate Ca^{2+} oscillations [116, 117].

4.2 Targeting the extracellular Ca^{2+}-Specific aim of the project-1

The role of Ca^{2+} in controlling various cellular processes has been investigated in detail by optical imaging using Ca^{2+} sensitive fluorescent dyes. However, the depth penetration limit of optical imaging techniques coupled with the effects of photobleaching side products of the fluorescent probes have created a need of alternate methods of reporting the Ca^{2+} dynamics. MRI on the other hand, does not suffer from such limitation. This noninvasive imaging modality provides the high quality images of soft tissues without the use of any ionizing radiations. Furthermore, the parameters determining the MRI image (T_1/T_2/SD) can be weighted differently with a variety of pulse sequences available. This unique flexibility in MRI provides a wide variety of information which cannot be obtained with other imaging modalities.

The first report of a potential MRI agent sensitive to Ca^{2+} came in 1999 by Meade and coworkers [55]. The MRI agent, Gd-DOPTA described in that report used BAPTA as calcium chelator coupled to two Gd-DO3A units. The agent showed a maximum of ~ 75% r_1 enhancement on Ca^{2+} addition and later reports proved that the r_1 enhancement was due to the change in hydration number of the complex [56]. The agent was designed to be microinjected inside the cell; however there were no reports about *in vivo* testing of the agent.

Considering our interest of reporting the functional activity in the brain by targeting Ca^{2+}, a direct reporter of neuronal activity, MRI agents sensitive to Ca^{2+} were planned to be synthesized. Unlike designing the agent for microinjections in the cells [55], we proceeded with designing agents for targeting extracellular Ca^{2+}. The concentration of Ca^{2+} outside the cell is 1-2 mM while it is 50-100 nM inside the cells [110]. The agent consisting of a strong chelator, BAPTA (K_d = 0.1-0.4 μM), most likely would saturate when the Ca^{2+} concentration reaches even 1 μM. Low affinity chelators are proved to be better reporters of the Ca^{2+} modulations and do not contribute much to Ca^{2+} buffering as does their high affinity counterparts [119]. With this we specified our aim of targeting Ca^{2+} to **'developing MRI probes for sensing extracellular Ca^{2+} dynamics using a low affinity Ca^{2+} binding construct'**.

CHAPTER 5

5. Design, synthesis and characterization of bismacrocyclic SCAs sensitive to $\mathbf{Ca^{2+}}$

5.1 Design of $\mathbf{Ln_2L^1}$ and $\mathbf{Ln_2L^2}$*:* To design a low affinity Ca^{2+} binding construct of the CA, we planned to do structural modifications on BAPTA, a high affinity Ca^{2+} selective chelator. One BAPTA molecule, with its four units of aminoacetate in conjugation with two ether oxygens coordinates to Ca^{2+} in a selective manner. As amides are weakly coordinating in comparison to carboxylates, we planned to modify two of the carboxylate units of BAPTA to two amide units. The final structures would have two carboxylates (strongly coordinating) and two amide units (weakly coordinating) to coordinate with Ca^{2+}. Two bismacrocyclic CAs were designed based on this modification ($\mathbf{Ln_2L^1}$ and $\mathbf{Ln_2L^2}$). $\mathbf{L^1}$ and $\mathbf{L^2}$ derivatives would differ from each other in the linker connecting the Ca^{2+} chelator to the Gd-DO3A units with $\mathbf{L^2}$ having a longer and flexible linker.

5.2 Results and Discussion

Scheme 1

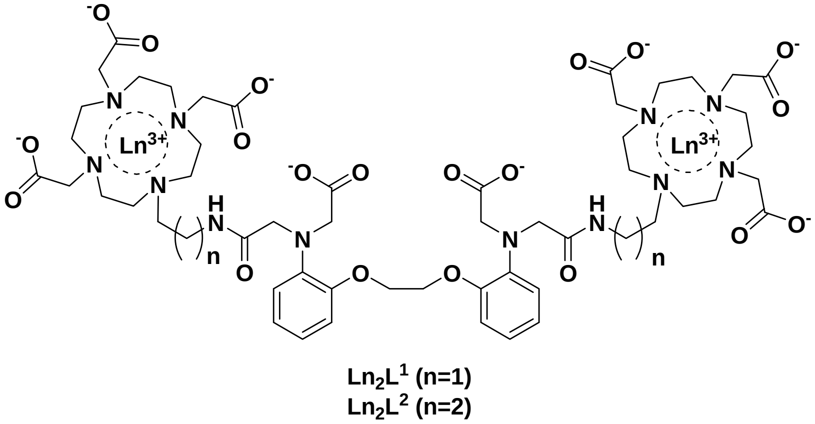

5.2.1 Synthesis of Ln_2L^1 and Ln_2L^2

Synthesis of the ligand **Ln_2L^1**, was first attempted according to the Scheme 2. *o*-nitro phenol was alkylated with dibromoethane to give bis-nitro compound **1,** which was subjected to hydrogenation with Pd-C catalyst under 1 atm H_2 pressure to give amine **2.** The reductive amination was carried out on this aromatic diamine **2** with benzaldehyde to obtain **3**. The further alkylation on **3** was done with *tert*-butylbromoacetate with proton sponge as base to obtain diester **4**. Subsequently, *tert*-butylesters in **4** were hydrolyzed using neat TFA to give the aromatic precursor **5** in quantitative yields. This was used for coupling reactions with macrocyclic precursors.

The macrocyclic precursors **10** (and **11**) was synthesized in three steps. Bromoethylamine (and bromopropylamine) was protected as carbamate in presence of carbobenzyloxy chloride to give **6** (and **7**). This was used to do alkylation of tris-*tert*-Bu-DO3A to give **8** (and **9**). The hydrogenation of **8** (and **9**) was carried out in a Parr apparatus with Pd-C catalyst under 1 atm H_2 pressure to give the primary amine **10** (and **11**).

The macrocyclic building block **10** was coupled to the aromatic precursor **5** via amide bond formation to give bismacrocycle **12** using EDC/NMM/HOBt as the coupling reagents**.** However, removal of the benzyl groups on **12** under various hydrogenation conditions was not successful. The hydrolysis of **12** in TFA yielded a new ligand **13** (Scheme 3) which could be loaded with Gd^{3+}, to have a hydrophobic bismacrocyclic contrast agent owing to the presence of in total 4 hydrophobic aromatic rings. This contrast agent could then be used to target albumin kind of protein in blood plasma to have a blood pool contrast agent. The potential of this ligand however, was not studied further.

The problem of removal of benzyl groups from **12** might be because of the steric hinderance imposed by the two macrocyclic moieties. To circumvent this problem we planned to remove them before the introduction of macrocyclic part (Scheme 4). Compound **3** was used as the initial substrate to do the further alkylation with methyl bromoacetate to give **14.** At this stage the removal of benzyl groups in **14** was successfully carried out under 1 atm H_2 pressure and Pd-C catalyst in a Parr apparatus to give secondary amine **15** in quantitative yields. To have an orthogonal protecting group situation, **15** was then alkylated with *tert*-butylbromoacetate with proton sponge as base to give **16.** When **16** was subjected to methyl ester group hydrolysis under basic conditions, both esters (*tert*-butyl and methyl-) were found to be hydrolyzed in the obtained product. This can be explained on the basis of neighbouring group participation by the carboxylate formed under basic conditions, leading to the removal of tert-butyloxy anion. The anhydride formed in situ was then cleaved in presence of water in the reaction mixture to give BAPTA (Scheme 5)

As the selective cleavage of methyl esters was not successful, we hydrolyzed the *tert*-butylesters in **16** with TFA to obtain diacid **17** in quantitative yields. This was then coupled to macrocyclic precursor **10** by amide bond formation to give **18** (40%). The global deprotection in **18** was performed followed by RP-HPLC purification (Method A) to obtain the final ligand **L**$^{\mathbf{1}}$ in 25% yield.

Scheme 2

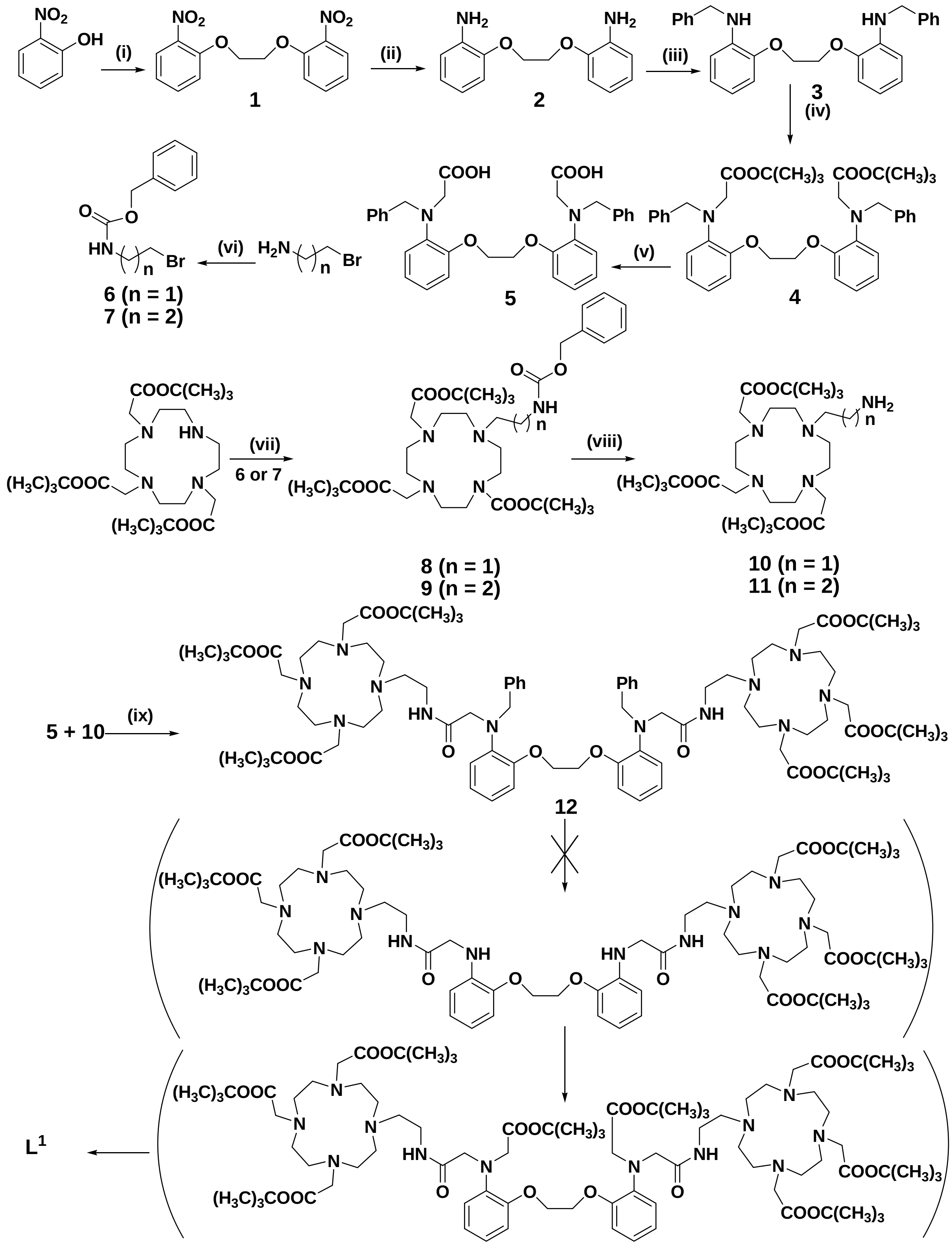
(i)
(ii)
(iii)
(iv)
(v)
(vi)
(vii)
6 or 7
(viii)
(ix)
1
2
3
4
5
6 (n = 1)
7 (n = 2)
8 (n = 1)
9 (n = 2)
10 (n = 1)
11 (n = 2)
5 + 10
12
L1

Reagents and conditions: *(i)* $BrCH_2CH_2Br/K_2CO_3/DMF$; 87% *(ii)* $Pd\text{-}C/H_2/MeOH$; 95% *(iii)* $PhCHO/Na(OAc)_3BH/DCE$; 73% *(iv)* *tert*-butyl bromoacetate/$K_2CO_3/KI/MeCN$; 87% *(v)* TFA/CH_2Cl_2; 98% *(vi)* $CBzCl/KOH/dioxane/H_2O$; 75% *(vii)* **6** or **7**/$K_2CO_3/KI/MeCN$; 73% *(viii)* $Pd\text{-}C/H_2/MeOH$; 65-70% *(ix)* NMM/HOBt/EDC/DMF; 55%

Scheme 3

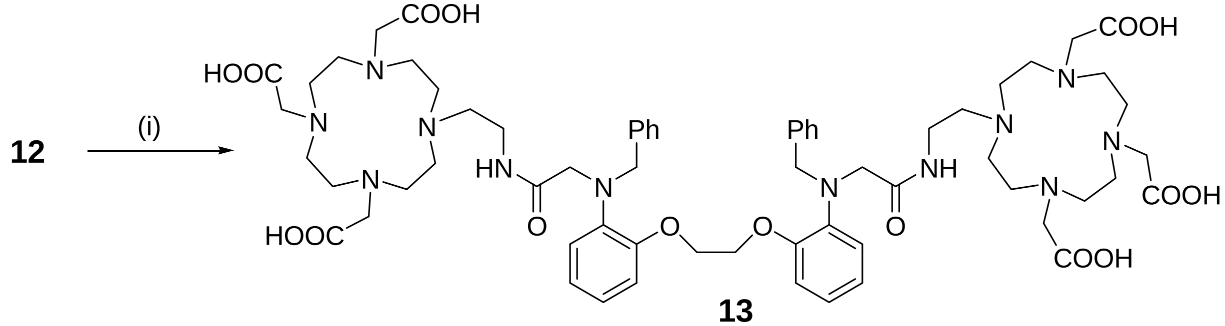

13

Reagents and conditions: *(i)* $TFA/H_2O/TRIPS$ (99:0.5:0.5), 32%

Scheme 4

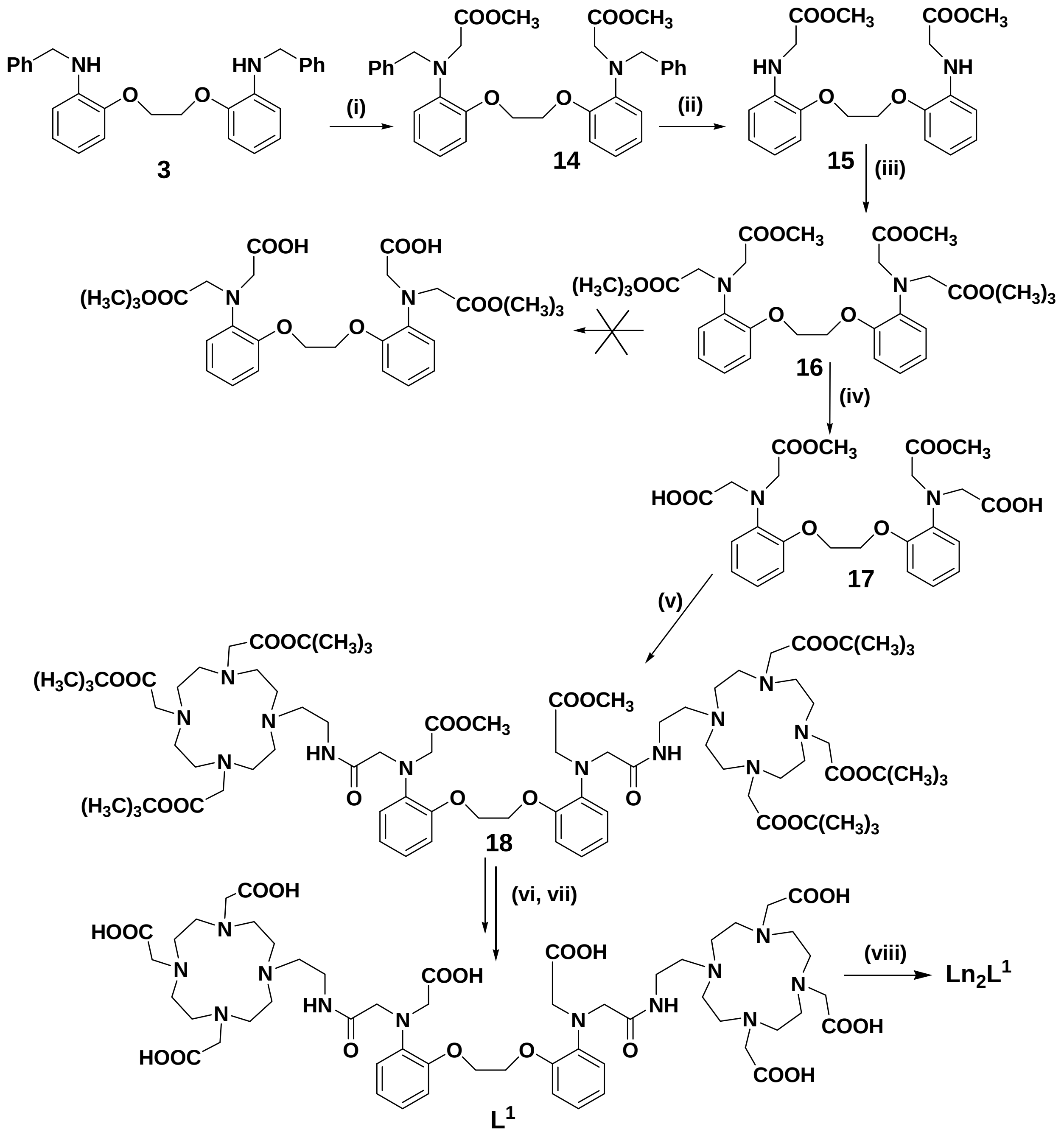

Reagents and conditions: *(i)* **3**/methylbromoacetate/K_2CO_3/KI/MeCN; 70% *(ii)* H_2/Pd-C/MeOH; 95% *(iii)* *tert*-butylbromoacetate/KI/proton sponge/MeCN; 52% *(iv)* TFA/CH_2Cl_2; 95% *(v)* **10**/NMM/HOBt/EDC/DMF; 25% *(vi)* LiOH, THF/MeOH/H_2O (3:2:2) *(vii)* TFA/H_2O/TRIPS (99:0.5:0.5); 25% *(viii)* $LnCl_3$ $6H_2O$

Scheme 5

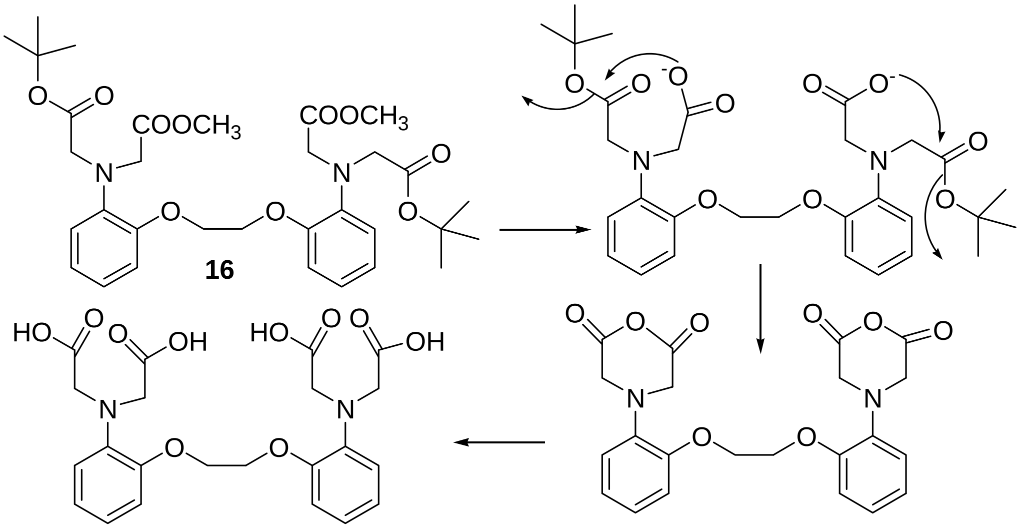

Another approach used for synthesizing the desired ligands was by synthesizing BAPTA bisanhydride and then forming amide bonds with the macrocyclic precursors by the opening of anhydride bonds (Scheme 6). BAPTA bisanhydride was synthesized according to the reported procedure [120]. The bisanhydride was reacted with the macrocyclic primary amine **10** (and **11**) under basic conditions with triethylamine in anhydrous solvent (NMP). The reaction was carried out in an inert atmosphere and at room temperature. An excess of amine (3 equiv) was used to avoid the formation of monomacroyclic byproducts. The crude product obtained was purified by RP-HPLC to obtain **20** (and **21**) in 55% (and 40%) yield, followed by global deprotection with TFA to obtain the final ligands $\mathbf{L^1}$ (and $\mathbf{L^2}$) in 60% (and 40%) yield. This scheme simplified the overall synthesis to only 6 steps with satisfactory yields. The final loading of the ligands were done with addition of $LnCl_3{\cdot}6H_2O$ (Ln^{3+} = Eu^{3+} or Gd^{3+}) solution. A general procedure was used for the loading of all bismacrocyclic ligands with Ln^{3+}. The complexes were prepared by mixing a slight excess (5%) of the ligand solution with the $LnCl_3$ solution of known concentration. The reaction was carried out in milliQ water and at 50 °C. pH was maintained at 7 with the addition of KOH solution (1 M) and monitored for 4 h. The absence of free Gd^{3+} was checked by Xylenol orange test. The water was evaporated and the obtained solid was used as such for further experiments.

Scheme 6

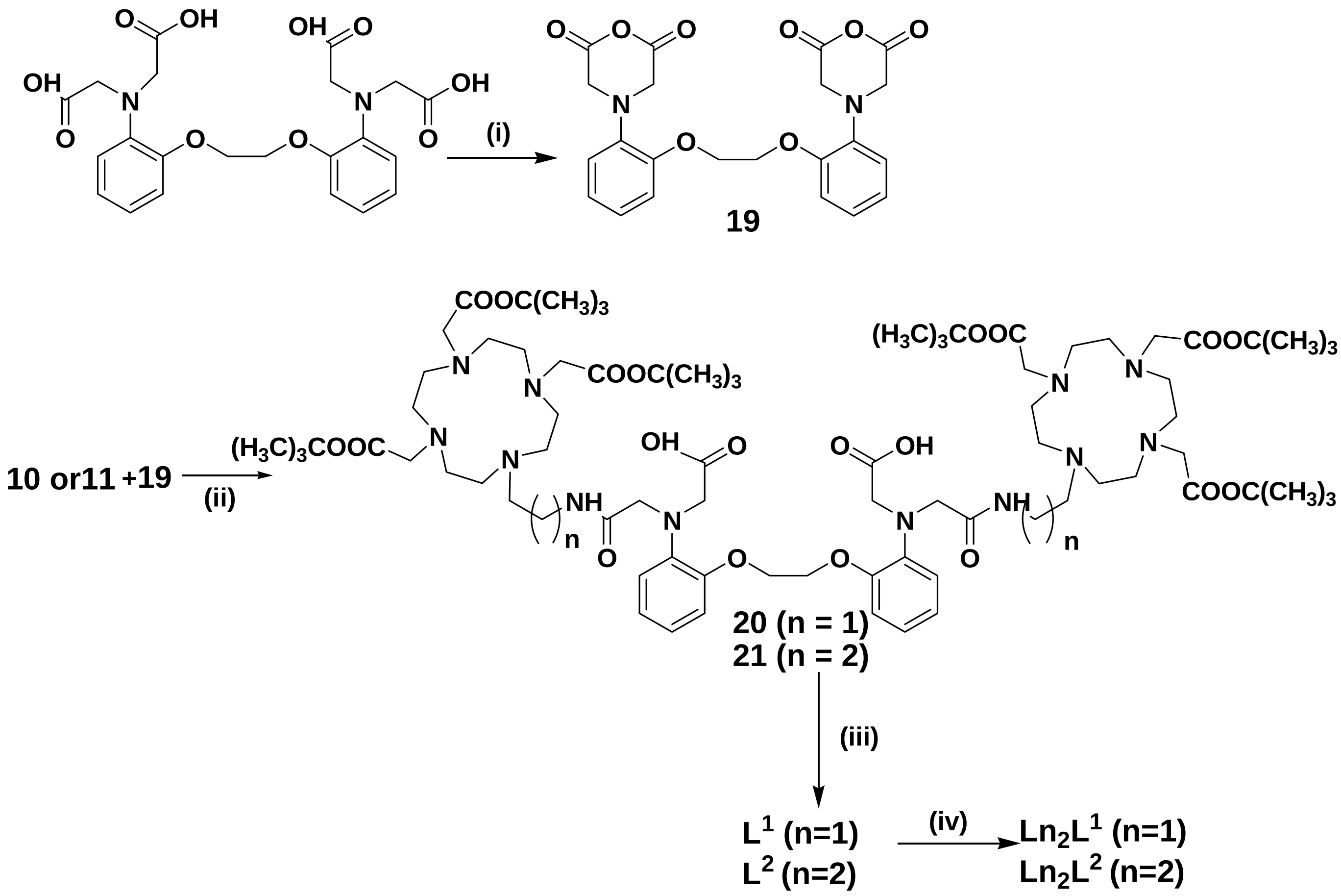

Reagents and conditions: *(i)* Ac_2O/Py; 75% *(ii)* Et_3N/NMP; 55% (**20**), 40% (**21**) *(iii)* TFA/CH_2Cl_2; 60% ($\mathbf{L^1}$), 40% ($\mathbf{L^2}$) *(iv)* $LnCl_3{\cdot}6H_2O$

5.2.2 Physicochemical characterization

To investigate the Ca^{2+} dependent relaxivity response of the synthesized CAs, we performed the relaxometric titrations of the CA solutions in buffer. The titrations were performed at 11.75 T and physiological pH 7.3. A solution of $CaCl_2$ of known concentration was added stepwise to the complex solution and the longitudinal proton relaxation time T_1 was measured after each Ca^{2+}

addition. The relaxometric Mg^{2+} titration was also performed similarly to investigate the Ca^{2+} selective properties of the agents. In order to ascertain the parameter affecting the relaxivity of the agents in the presence and absence of Ca^{2+}, **Ln_2L^1** was chosen as the representative example and a number of experiments were performed on it. A high resolution UV-Vis spectrum of $^5D_0 \leftarrow {}^7F_0$ transitions in the region 577-581 nm was obtained for **Eu_2L^1** to investigate the hydration equilibrium between two coordination states (8 and 9) of Eu (III) in the agent. Luminescence Lifetime measurement was performed on **Eu_2L^1** in order to determine the hydration number of the complex in the presence and absence of Ca^{2+}. The hydration number (q) was calculated according to equation 4.1 [121]

$$q = A'(\Delta k_{H_2O} - \Delta k_{D_2O})_{corr} \qquad \text{eq(5.1)}$$

where A' is 1.2 ms and the correction factor for the contribution of the second sphere is - 0.25 ms^{-1}. The other parameters affecting relaxivity (e.g. water exchange rate, rotational correlation time etc.) were determined by simultaneous fitting of the data obtained by ^1H NMRD and ^{17}O NMR measurements.

(a) Relaxometric Ca^{2+} titrations of ***Gd_2L^1*** *and* ***Gd_2L^2***

The titration curves are represented as the variation of the relaxivity of the Gd^{3+} complex solution vs. the Ca^{2+} concentration (Figure 16). The maximum relaxivity increase upon Ca^{2+} addition was 15% for **Gd_2L^1** and 10% for **Gd_2L^2**. The saturation of both curves occurs at relatively high Ca^{2+} concentrations (~ 20 equiv of Ca^{2+} for **Gd_2L^1** and ~ 5 equiv of Ca^{2+} for **Gd_2L^2**). The titration curves were fitted to obtain the apparent association constants, which are $\log K = 1.9 \pm 0.2$ and $\log K = 2.7 \pm 0.2$ for **Gd_2L^1** and **Gd_2L^2**, respectively. Similarly to previously investigated, BAPTA-type complexes [55, 122], 1:1 binding stoichiometry has been assumed. These association constants are to be compared with the conditional stability constant, $\log K_{cond}$ =

6.9 of $CaBAPTA^{2-}$ at pH 7.0, calculated by taking into account the protonation constants of $BAPTA^{4-}$ [122].

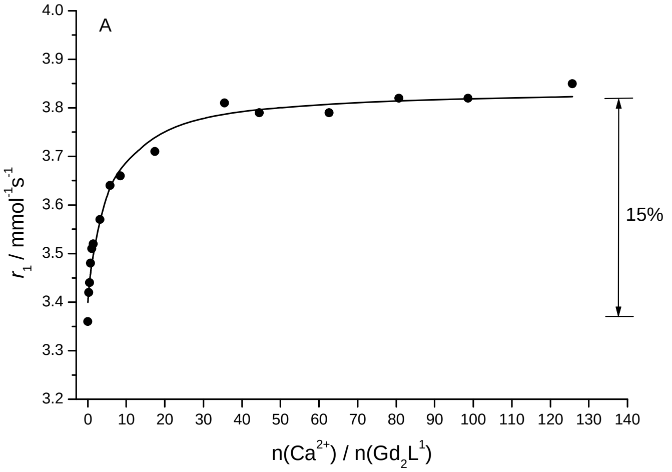

Figure 16: Relaxometric Ca^{2+} titration curves of $\mathbf{Gd_2L^1}$ performed at 25°C and 11.75 T.

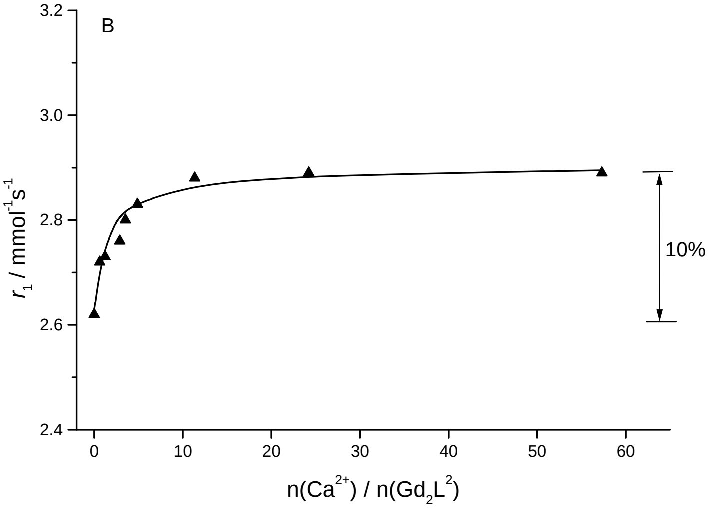

Figure 17: Relaxometric Ca^{2+} titration curves of $\mathbf{Gd_2L^2}$ performed at 25°C and 11.75 T

The constants obtained for our systems are 3-4 orders of magnitude lower. This difference can be rationalized by the fact that even on Ca^{2+} binding; the amide groups of the ligand remain coordinated to the lanthanide as indicated by proton relaxivity and luminescence data on the

Gd^{3+} and Eu^{3+} complexes, respectively. Therefore in comparison to $CaBAPTA^{2-}$, there are 2 carboxylate donors fewer coordinating to the Ca^{2+} ion, which is responsible for the considerably reduced stability. It is interesting to note that the stability of the **Gd_2L^2-Ca** complex is somewhat higher than that of **Gd_2L^1-Ca**. This is likely related to the higher flexibility of the Ca^{2+} binding site in **Gd_2L^2-Ca** where the propylene linker between the macrocycle and the Ca^{2+} binding site induces fewer steric constraints, hence ensuring a better "over-wrapping" of the cation by the chelator. We have to note that for GdDOPTA-Ca, possessing an integral $BAPTA^{4-}$ unit for Ca^{2+} binding, Li et al reported a much higher apparent association constant, $K = 1.0 \times 10^6$ M [55].

(b) Relaxometric Mg^{2+} titration of ***Gd_2L^1***

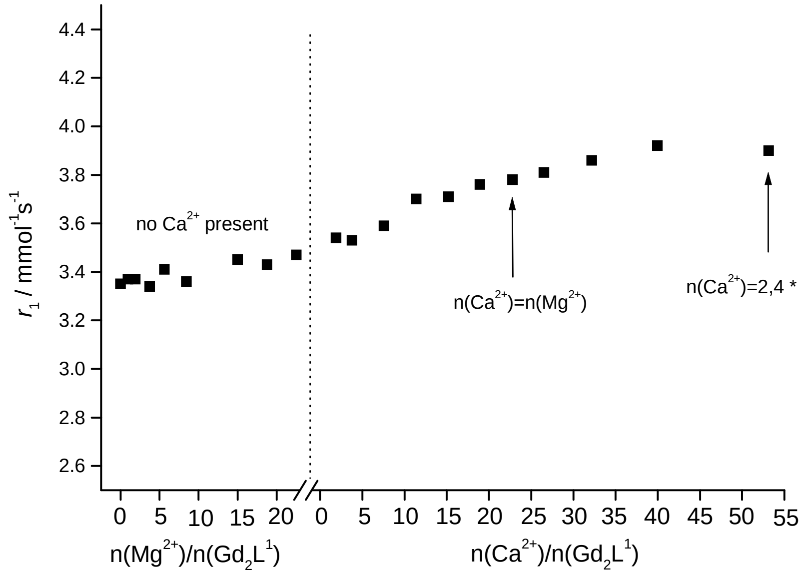

Figure 18: Relaxometric titration curve of **Gd_2L^1** with Mg^{2+} followed by addition of Ca^{2+} (25°C, 11.75 T).

The relaxivity remains approximately constant upon addition of Mg^{2+}, then it increases upon Ca^{2+} addition even in the presence of a large amount of Mg^{2+} (Figure 18). The relaxivity increase after Ca^{2+} addition (16%) was similar to that observed in the Ca^{2+} titration without the presence of Mg^{2+}. The insensitivity of $\mathbf{Gd_2L^1}$ towards Mg^{2+} is due to the lower stability of BAPTA-derived complexes with Mg^{2+} compared to Ca^{2+}. The titration curve shows that, though the affinity of our chelator for Ca^{2+} is diminished in comparison to $BAPTA^{4-}$, the selectivity versus Mg^{2+} is conserved. The discrimination of BAPTA-type ligands towards Ca^{2+} versus Mg^{2+} is supposed to stem from the right size of the binding cavity for the larger size Ca^{2+} which is already too big for Mg^{2+} and cannot constrict further to envelop snugly this smaller cation (the association constant of $MgBAPTA^{2-}$ is $\log K = 1.8$) [122]. Spectrophotometric measurements on the Mg^{2+}-BAPTA system proved that Mg^{2+} coordination affects only one half of the ligand, in contrast to Ca^{2+} coordination where the entire ligand is involved [122].

(c) Luminescence and UV-Vis absorption studies

In order to determine the number of water molecules coordinated to the lanthanide ion before and after Ca^{2+} binding to the complex, we have performed luminescence lifetime measurements on $\mathbf{Eu_2L^1}$ in H_2O and D_2O solutions [35-37]. In the absence of Ca^{2+}, the values of luminescence lifetimes were $\tau_{H2O} = 0.328$ ms and $\tau_{D2O} = 0.408$ ms. The hydration number, $q = 0.4$, was calculated according to the equation 5.1.

The longitudinal ^{17}O and ^{1}H relaxation rates (*vida supra*) indicate that we cannot neglect the effect of second sphere water molecules. The non-integer hydration number suggests the presence of both $q = 1$ and $q = 0$ species. Upon the addition of Ca^{2+} to the Eu^{3+} complex, the hydration number determined by luminescence increases to $q \approx 0.7$ ($\tau_{H2O} = 0.422$ ms and $\tau_{D2O} = 0.661$ ms) (Figure 19). Such an increase of q can be interpreted in terms of a shift towards the monohydrated species.

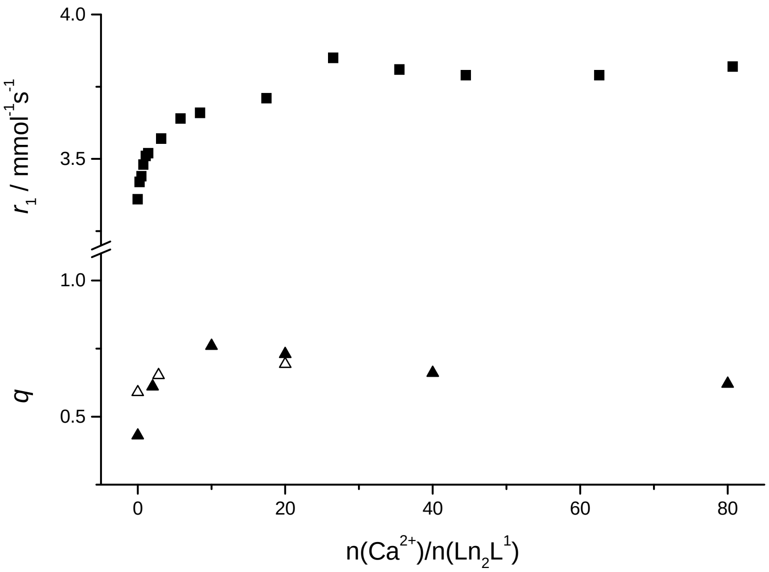

Figure 19: Dependence of the relaxivity r_1 and of the hydration number q on the Ca^{2+}/complex ratio for **Ln$_2$L^1**. Full squares correspond to the relaxivity values obtained from the relaxometric titration of **Gd$_2$L^1** (25°C, 11.75 T). Full triangles represent the hydration number obtained from luminescence lifetime studies on Eu$_2$L^1 and open triangles correspond to the molar fraction of the monohydrated species determined for **Eu$_2$L^1** by UV-Vis spectroscopy (ratio of the integrals of the absorption bands corresponding to monohydrated and nonhydrated complex; see text).

To investigate further the hydration state, variable temperature UV-Vis measurements have been performed on **Eu$_2$L^1**. In general, the presence of a hydration equilibrium of europium(III) species leads to the appearance of two absorption bands for the $^5D_0 \leftarrow {}^7F_0$ transition with peak separations of more than 0.5 nm [123, 124]. High resolution UV-Vis absorption spectra of a Eu$_2$L^1 aqueous solution (pH 7) were recorded in the 577–581 nm region at various temperatures and Ca^{2+} concentrations. The measurements revealed two temperature-invariant absorption bands, which could be deconvoluted into two symmetrical peaks (Figure 20).

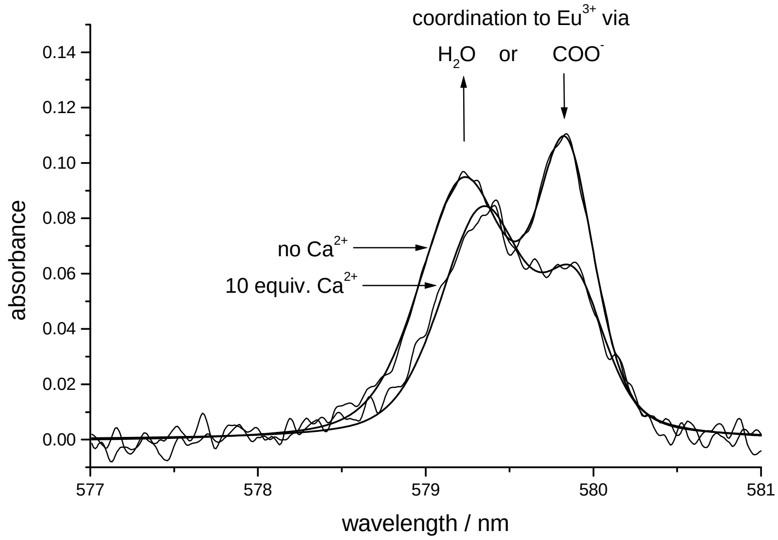

Figure 20: Experimental and fitted UV-Vis spectra (50°C, pH 7) of $\mathbf{Eu_2L^1}$ in the absence and presence of Ca^{2+}. On addition of Ca^{2+}, the relative intensity of the band at lower wavelength increases, while that of the band at higher wavelength decreases.

The separation of those peaks is about 0.5 nm and lies in the range typical of different coordination environments of Eu^{3+} [125, 126]. We assume that in the absence of Ca^{2+}, there are two nine-coordinated species present; in both species the amines and carboxylates of the macrocycle as well as the amide oxygen are coordinated to the lanthanide, and either one carboxylate from the central part or one water molecule completes the coordination sphere to CN = 9, which is the usual coordination number for this type of Ln^{3+} complexes (Figure 21).

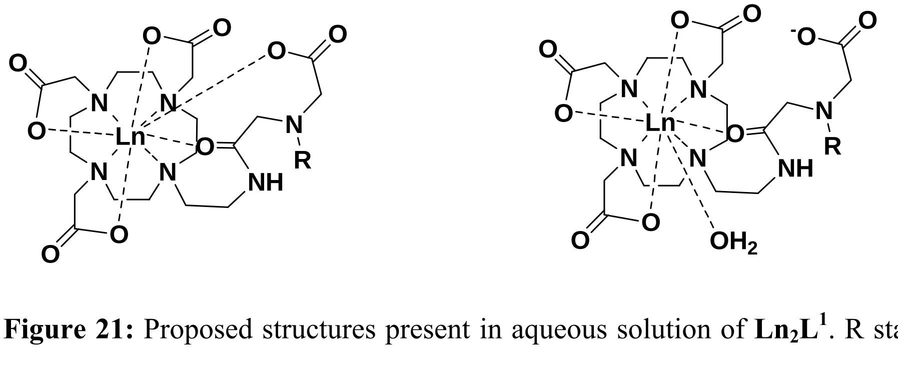

Figure 21: Proposed structures present in aqueous solution of $\mathbf{Ln_2L^1}$. R stands for the remaining part of the bismacrocyclic complex

Figure 22: IR spectrum of the ligand $\mathbf{L^1}$

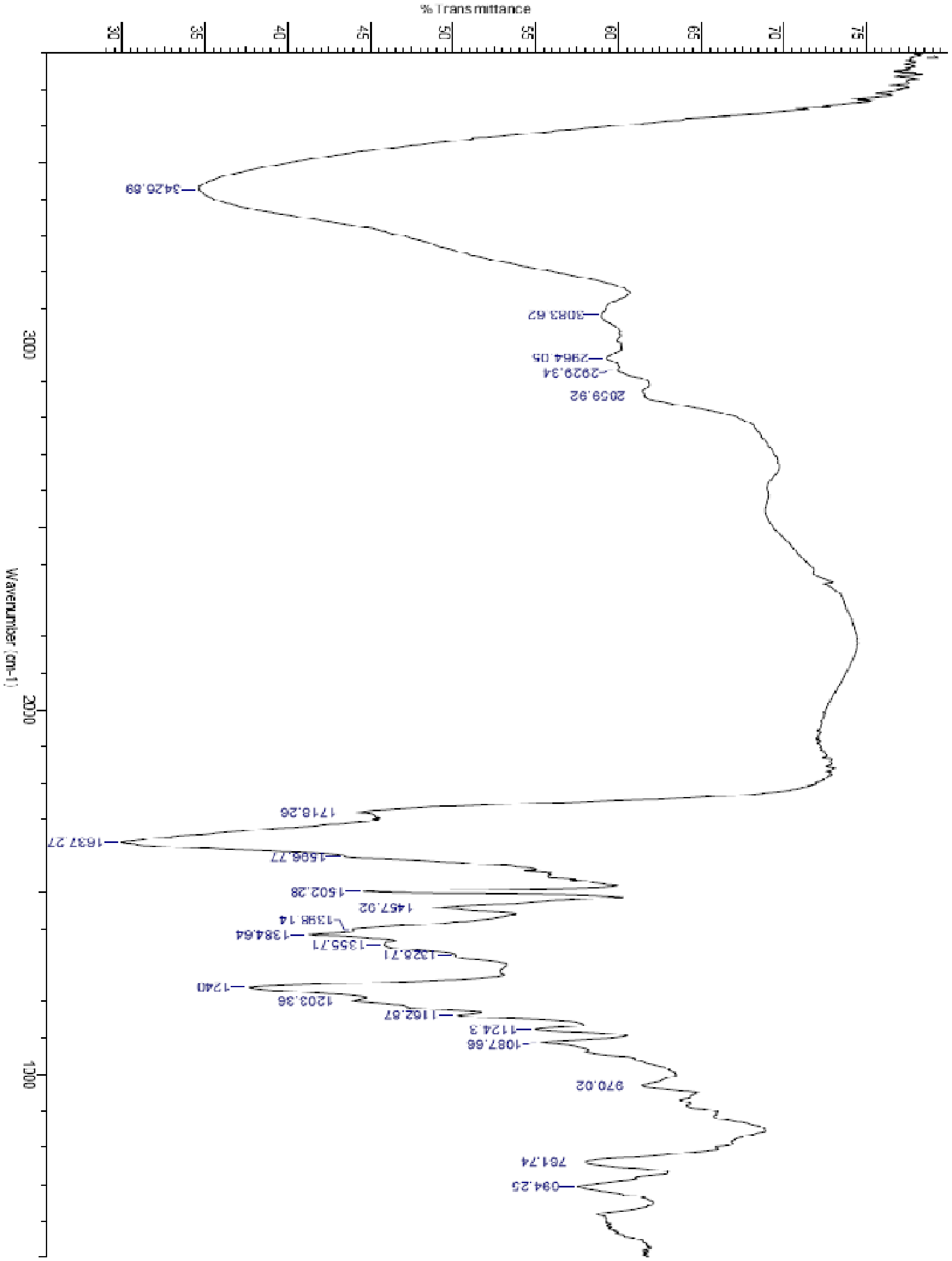

Figure 23: IR spectrum of the complex **Gd_2L^1**

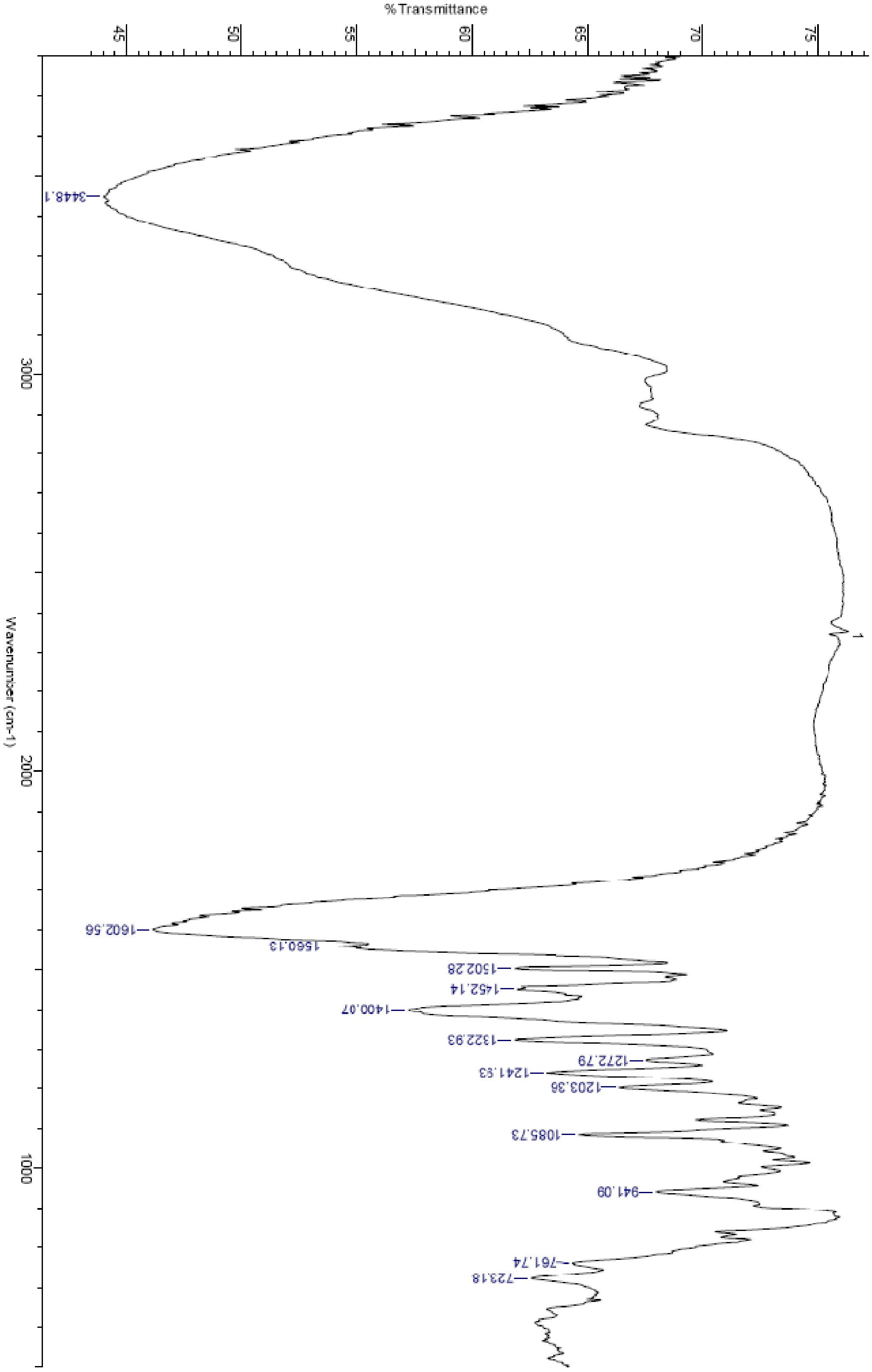

The coordination of amide oxygens is supported by IR measurements performed on the ligand $\mathbf{L^1}$ and its Gd^{3+} complex (Figure 22-23). The stretching frequencies observed in the region of 1595-1712 cm^{-1} for the ligand $\mathbf{L^1}$ had three distinguishable peaks which could be assigned to the C=O stretching frequencies corresponding to carbonyl group in carboxylates on macrocyclic units, carboxylates on aromatic units and the amides in the linker. These bands observed to merge in $\mathbf{Ln_2L^1}$ which could be explained on the basis of the coordination of these units to Ln^{3+}.

Among analogous structures, lanthanide complexes of monomeric DO3A-derivatives bearing –$(CH_2)_n$-NHCO-R (n = 2, 3) amide units have been reported in the literature [127]. With Eu^{3+} and Gd^{3+}, the n = 2 ligand forms monohydrated, while the n = 3 ligand forms non-hydrated complexes. In contrast to this, $\mathbf{Eu_2L^1}$ contains a carboxylate in the central part as a potential donor which can partially replace the water molecule in the inner coordination sphere. This leads to the presence of the two structures as proposed in Figure 38, and consequently to a reduced hydration number.

Upon Ca^{2+} addition to a $\mathbf{Eu_2L^1}$ solution, the relative intensity of the two UV-Vis absorption bands changes: the band at higher wavelengths decreases while the other band increases (Figure. 20) [128]. In parallel, the luminescence measurements indicate an increase of the hydration number. Therefore, we conclude that the band which decreases in intensity (at 579.9 nm) on Ca^{2+} addition can be attributed to the q=0 complex, while the band which increases in intensity (579.3 nm) can be attributed to the monohydrated complex. We assume that both in the presence and in the absence of Ca^{2+}, the amide oxygen remains coordinated to the lanthanide ion to preserve the overall coordination number of nine. If the amide oxygen participated also in the Ca^{2+} coordination, the concomitant increase in the hydration number and in relaxivity would be more prominent than what is experimentally observed. The Ca^{2+} binding in the central part of the complex demands the coordination of the central carboxylates, which, by leaving the coordination environment of Ln^{3+}, allow a water molecule to bind to the lanthanide ion. Therefore, the Ca^{2+} binding in the central part will favour the formation of the monohydrated complex (Figure. 21).

Upon step-wise addition of Ca^{2+}, we observe a good correlation between the relaxivity increase of the **Gd_2L^1** complex and the increase in *q* determined from the luminescence lifetime measurements on the Eu^{3+} analogue (Figure 19). In addition, we have also calculated the ratio of the integrals of the two UV-Vis absorption bands (attributed to *q*=0 and *q*=1) of **Eu_2L^1** at various Ca^{2+} concentrations. The *q* values obtained in this way overlap with those measured by luminescence. This supports our hypothesis that the complex Ln_2L^1 exists in the form of two differently hydrated species, each of an overall coordination number of nine. As it was proved by the UV-Vis studies, their ratio is temperature independent but it shifts towards the monohydrated species with increasing Ca^{2+} concentration, resulting in a relaxivity increase.

The relaxivity of the **Gd_2L^2** complex is lower than that of the **L^1** analogue which suggests that *q* is also lower. In the case of the monomeric DO3A-derivatives bearing $-(CH_2)_n$-NHCO-R amide units, with the propyl-linked (n=3) amide *q*=0 was determined for the Eu^{3+} and Gd^{3+} complexes [127]. The extra steric demand associated with the enlargement of the chelate ring incorporating the amide carbonyl group was found to be sufficient to suppress water coordination. For **Gd_2L^2**, the relaxivities suggest $q > 0$. Moreover, the relaxivity increases on Ca^{2+} addition, though to a smaller extent than for Gd_2L^1. Therefore, we assume that two differently hydrated species exist also for **Ln_2L^2** complexes, with an increased proportion of the non-hydrated species as compared to **Ln_2L^1**. The relaxivity change observed on Ca^{2+} addition indicates that the central carboxylate participates in the lanthanide coordination; on Ca^{2+} binding this carboxylate is removed off the lanthanide ion and replaced by a water molecule. The small relaxivity change shows that the participation of this carboxylate in the lanthanide coordination is limited with respect to **Gd_2L^1**. For GdDOPTA, Li et al reported a more important variation of *q* and a correspondingly greater relaxivity change on Ca^{2+} binding [55, 56]. This is likely related to the more flexible nature of the central $BAPTA^{4-}$ part of the DOPTA ligand in contrast to the BAPTA-bisamide moiety in our case, where the monoamide functionalities are integrated in the central skeleton of the ligand and have much less flexibility to change coordination from Gd^{3+} to Ca^{2+}.

(d) ^{1}H and ^{17}O relaxation studies of **Gd_2L^1**. *Evaluation of the parameters influencing proton relaxivity*

^{1}H NMRD profiles were recorded for **Gd_2L^1** with and without Ca^{2+}. In the presence of Ca^{2+}, an increase in the relaxivity was observed at all frequencies, related to an increase in the hydration number. The relaxivity at 20 MHz and 25°C in the absence and presence of Ca^{2+} is 5.74 and 6.13 $mM^{-1}s^{-1}$, respectively, slightly higher than those of currently used MRI contrast agents [6, 129].

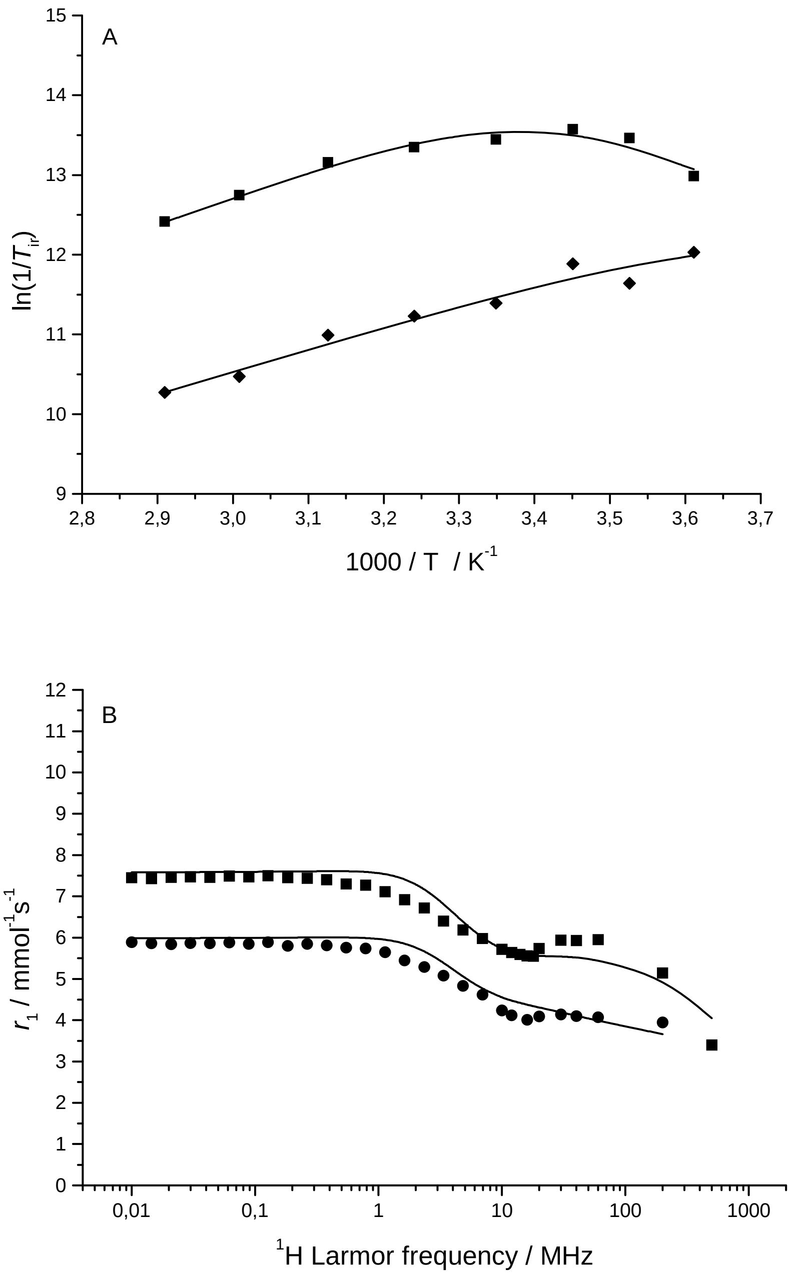

Figure 24: (a) Variable temperature ^{17}O NMR (A; ln(1/T_{1r}) diamonds, ln(1/T_{2r}) squares) and (b) ^{1}H NMRD (B; 25°C squares, 37°C circles) data of $\mathbf{Gd_2L^1}$ in the absence of Ca^{2+}

The transverse ^{17}O relaxation rates indicate a relatively slow water exchange (Figure 24), which is visible from the ln(1/T_{2r}) curve vs. inverse temperature: at low temperatures, 1/T_{2r} decreases with decreasing temperature.The reduced chemical shifts ($\Delta\omega_r$) in the absence of Ca^{2+} are smaller than it would be expected for a $q = 0.4$ complex. Such small chemical shifts have been previously observed in systems with a significant second-sphere contribution [130]. Therefore, the chemical shifts were not included in the final fitting. For the Ca^{2+}-free system, the transverse and longitudinal ^{17}O relaxation rates and the ^{1}H NMRD data were analysed simultaneously (Figure 24) on the basis of the Solomon–Bloembergen–Morgan approach, extended by a second-sphere contribution [130, 131]. The presence of free carboxylates in the complex induces a second-sphere contribution that affects both ^{1}H and ^{17}O longitudinal relaxation. In fact, by fitting the ^{17}O $1/T_1$ values without 2nd sphere contribution, inconceivably high rotational correlation times were obtained. The inner sphere hydration number q was fixed to 0.4, the value found by luminescence measurements on $\mathbf{Eu_2L^1}$. Since Eu^{3+} and Gd^{3+} have similar ionic radii, we expect a similar hydration mode for $\mathbf{Gd_2L^1}$. To describe the second-sphere contribution, one water molecule per Gd^{3+} ($q^{2nd} = 1$) was considered during the fitting. The distance between Gd^{3+} ion and the second-sphere water proton and oxygen was fixed to $r_{Gd\text{-}H}{}^{2nd} = 3.5$ Å and $r_{Gd\text{-}O}{}^{2nd} = 4.1$ Å, respectively, the enthalpy of activation to $\Delta H^{\#2nd} = 35$ kJ·mol^{-1}, and the second-sphere water residence time to $\tau_m{}^{2nd} = 50$ ps [45, 46]. Other parameters have been also fixed during the fitting in order to put some constraints. They are as follows: the hyperfine coupling constant, $A/\hbar = -3.8$ MHz; the distance between Gd^{3+} and the oxygen and proton of the first-sphere water molecule, $r_{GdO} = 2.5$ Å and $r_{GdH} = 3.1$ Å, respectively. The distance of the closest approach of outer-sphere water molecules to Gd^{3+}, a, was fixed to 3.6 Å. The quadrupolar coupling constant ($\chi(1+\eta^2/3)^{1/2}$) was set to 7.58 MHz, the value of pure water. The activation energy E_V had to be fixed to 1 kJ·mol^{-1}, otherwise the fit converged to negative values. In the fitting procedure, we used a model which considers different rotational correlation times for Gd–O and Gd–H rotating vectors

(τ_{RO}^{298} and τ_{RH}^{298}, respectively) [48]. For geometrical reasons, their ratio ($\tau_{RH}^{298}/\tau_{RO}^{298}$) has to lie between 0.65 and 1. The most important parameters obtained from the best simultaneous least-square fit to the experimental data are listed in Table 1. The complete fitting results are described in Table A1 in appendix 3.

Table 1: Kinetic and structural parameters obtained from the fit of ^{17}O NMR and NMRD data for the Gd_2L^1 complex in the absence and in the presence of Ca^{2+}, compared with those of GdDOTA. Parameters in italics were fixed during the fitting.

Parameter	**Gd_2L^1** **^{17}O NMR + NMRD**	**Gd_2L^1 + Ca^{2+}** **^{17}O NMR**	**GdDOTA** **^{17}O NMR + NMRD^a**
k_{ex}^{298} / 10^6 s^{-1}	2.4±0.2	7.5±1.6	4.1
$\Delta H^{\ddagger}$ / kJ·mol^{-1}	43.6±3.3	*43.6*	49.8
$\Delta S^{\ddagger}$ / J mol^{-1}K^{-1}	+23.5	+33.0	-
τ_{rO}^{298}/ ps	350±50	1150±250	77
E_r / kJ·mol^{-1}	24±1	21±6	16.1
τ_V^{298}/ ps	20.6±2.7	0.13±0.02	11
Δ^2 / 10^{20} s^{-2}	0.46±0.10	0.50±0.05	0.16
q	*0.4*	*0.7*	*1*
q^{2ns}	*1*	*1*	-
r_1^{298} / mM^{-1}s^{-1} 20 MHz	5.74	6.13	4.74

^{a} ref. [132]

The water exchange of Gd_2L^1 is slightly slower than that found for GdDOTA [132]. It is interesting to note that for the monohydrated Gd^{3+} complex of the DO3A ligand bearing an N-linked CH_2CH_2NHCO-pyridyl pendant arm, much faster water exchange has been reported (k_{ex}^{298} = 1.1×10^8 s^{-1}) [127]. This fast water exchange has been explained by the steric destabilization of the Ln-water binding interaction by the presence of the bulky substituent. Such a destabilization effect is expected to be less important in $\mathbf{Gd_2L^1}$ since the amide carbonyl is linked to a flexible -CH_2-N- moiety in contrast to the direct attachment to a pyridyl group in the previous case. This limited steric constraint around the water binding site will then be translated by a more sluggish water exchange as observed for $\mathbf{Gd_2L^1}$. The more than one order of magnitude difference in the water exchange rate between $\mathbf{Gd_2L^1}$ and the Gd^{3+} complex of the DO3A-CH_2CH_2NHCO-pyridyl ligand is a good example of the importance of the steric compression around the water binding site. Steric compression is indeed the main factor to determine the rate of exchange in a dissociative water exchange mechanism, characteristic of nine-coordinate complexes [133]. The dissociative activation mode for Gd_2L^1 is indicated by the positive value of the activation entropy.

The higher τ_r value of Gd_2L^1 as compared to GdDOTA is rationalized by the higher molecular weight and rigidity of the molecule. In spite of the slow rotational motion and the presence of a second hydration sphere in the bismacrocyclic system, the relaxivities are only slightly higher than those of GdDOTA, due to the low hydration number of $\mathbf{Gd_2L^1}$ ($q = 0.4$).

The simultaneous fit of the ^1H and ^{17}O relaxation rates also supplies parameters that describe the electron spin relaxation of the Gd^{3+} complexes, such as τ_v, the correlation time for the modulation of the zero field splitting (ZFS), its activation energy, E_v, and the mean zero field splitting energy, Δ^2. The values obtained for $\mathbf{Gd_2L^1}$ are in the usual range for similar complexes [132].

The ^1H NMRD and ^{17}O NMR data of the $\mathbf{Gd_2L^1}$ system containing Ca^{2+} could not be fitted simultaneously because the conditions for ^{17}O NMR and ^1H NMRD samples differed significantly in the ionic strength and viscosity, but also in the Ca^{2+}/Gd^{3+} ratio of the samples.

Only the ^{17}O ln(1/T_{1r}) and ln(1/T_{2r}) data were analyzed, while the relaxivities are given in the Table A2 and Table A3 in appendix 3.

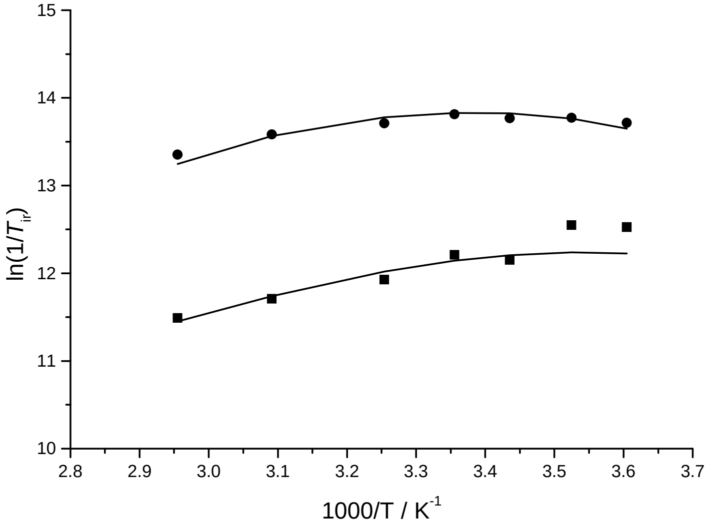

Figure 25: Variable temperature, reduced longitudinal (squares) and transverse (diamonds) ^{17}O relaxation rates for **Gd$_2$L^1**, in the presence of 1M Ca^{2+}.

The ^{17}O relaxation rates were interpreted by using the same set of equations as for the system without Ca^{2+} (Figure 25). Analogously, the same parameters were fixed in the fit (except for the hydration number, q=0.7, obtained from luminescence studies). The best fitting was obtained with parameters listed in Table 1 and Table A4 (in appendix 3). On Ca^{2+} addition, the most flagrant change is observed for the rotational correlation time as obtained from the ^{17}O longitudinal relaxation rates (τ_R = 350 vs. 1150 ps without and with Ca^{2+}, respectively). We attribute this significant increase mainly to the high ionic strength and viscosity of the ^{17}O NMR sample containing 1M CaCl$_2$, though some rigidification of the molecule on Ca^{2+} is also expected. As for the water exchange rate, it triples on Ca^{2+} binding (k_{ex}^{298} = 2.4×10^6 vs. 7.5×10^6 s^{-1}). The decreasing negative charge of the Ca^{2+} bound **Gd$_2$L^1**-Ca complex would be rather expected to diminish the exchange rate in a dissociatively activated process. Among other factors that can compensate this effect, the increased steric demand of the central part after Ca^{2+} binding can lead to a steric destabilization of the Ln-water binding interaction. Overall, the relaxivity increase upon Ca^{2+} addition is mainly related to an increase in the hydration number.

5.3 Design of $\mathbf{Ln_2L^3}$ and $\mathbf{Ln_2L^4}$: An attempt of improvement over $\mathbf{Ln_2L^1}$ and $\mathbf{Ln_2L^2}$

To improve the Ca^{2+} dependent relaxivity response obtained with $\mathbf{Ln_2L^{1\text{-}2}}$, we planned to perform the structural modifications so as to decrease the distance between the Ca^{2+} chelating moiety and the paramagnetic centre. This might ensure better interaction between the two and thereby expected to give improved response. This could be achieved by decreasing the length and steric constraints in the linker or by increasing the length of the flipping arm which is supposed to flip between paramagnetic centre and the Ca^{2+} coordination centre. $\mathbf{Ln_2L^3}$ was designed to contained aromatic aminopropionate units instead of the regular aminoacetate units and $\mathbf{Ln_2L^4}$ contained a simple alkyl linker instead of a long amide containing linker.

Scheme 7:

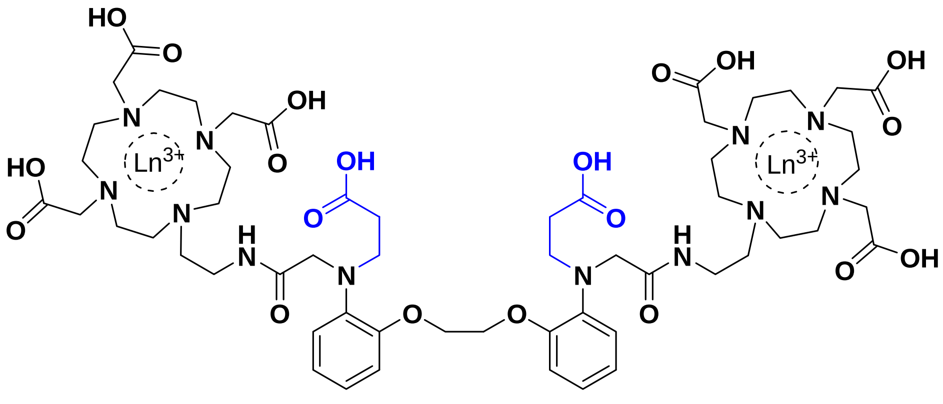

$\mathbf{Ln_2L^3}$

Scheme 8:

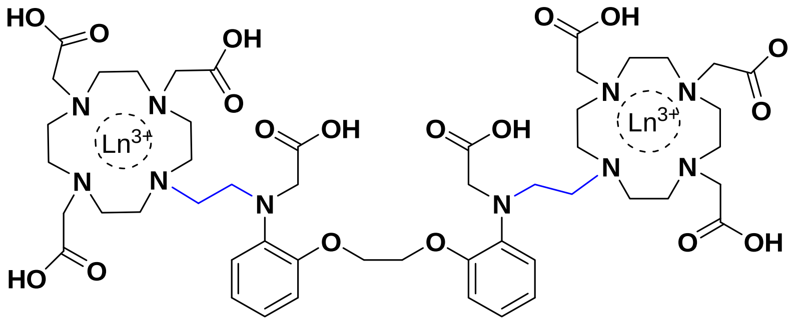

Ln_2L^4

5.4 Results and Discussion

5.4.1 Synthesis of Gd_2L^3

Synthesis of this ligand was carried out as outlined in Scheme 9. The primary aromatic amines in **2** were alkylated with methyl bromopropionate to secondary aromatic amines as in **22** (65%). The further alkylation at **22** with *tert*-butyl bromoacetate gave **23** (68%). Hydrolysis of *tert* butyl esters in **23** was carried out in neat TFA to obtain diacid **24** in quantitative yields. This was coupled to macrocyclic precursor **10** via amide bonds to the bismacrocyclic product, **25** (30% yield). The global deprotection of all the esters in **25** was done to obtain the final ligand **L^3** in 48% yield.

Scheme 9

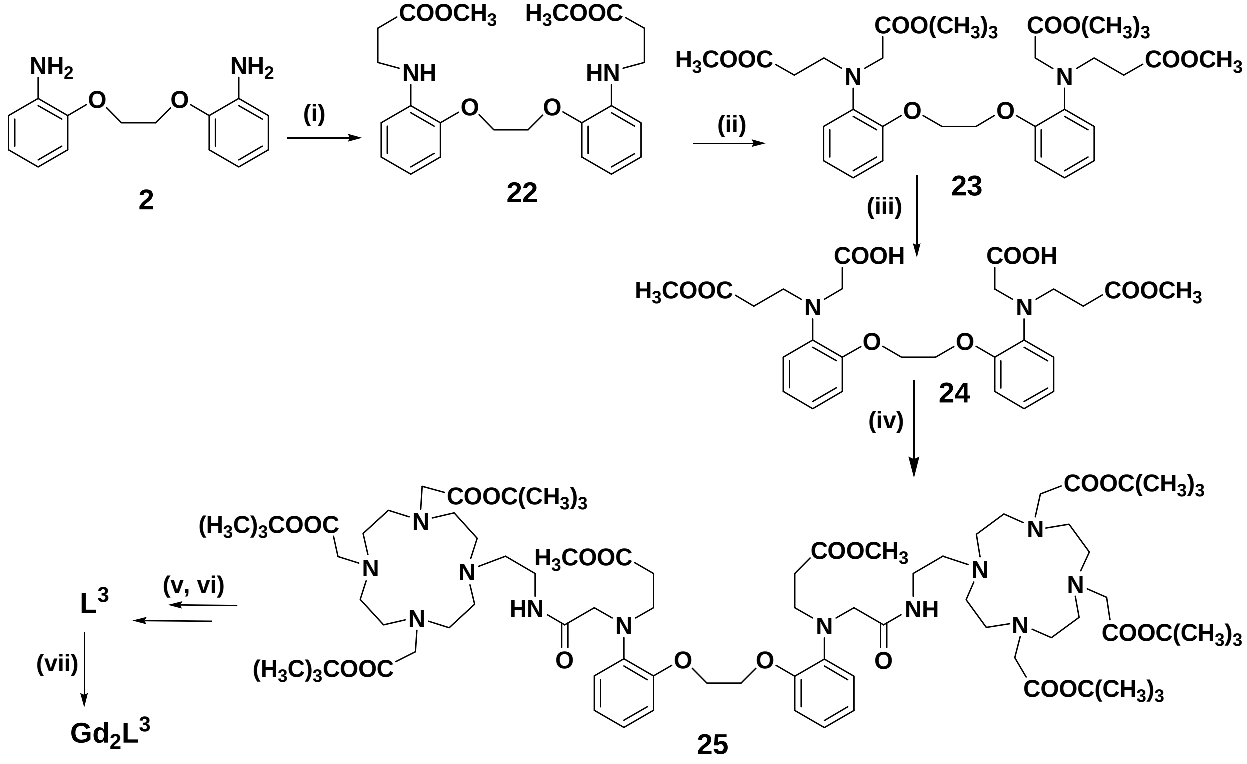

Reagents and conditions: *(i)* **2**/methylbromopropionate/proton sponge/KI/MeCN; 65% *(ii) tert*-butyl bromoacetate/K_2CO_3/KI/MeCN; 68% *(iii)* TFA/CH_2Cl_2; 98% *(iv)* **10**/NMM/HOBt/EDC/DMF; 30% *(v)* LiOH/THF:MeOH:H_2O (3:2:2) *(vi)* TFA/CH_2Cl_2; 48% *(vii)* $GdCl_3$ $6H_2O$

5.4.2 Physicochemical characterization of Gd_2L^3

(a) Relaxometric Ca^{2+} titrations of $\mathbf{Gd_2L^3}$

The Ca^{2+} dependent relaxivity response of the agent was checked at 9.4 T and physiological pH 7.3. The titrations and the measurement of T_1 were performed similar to as described in Section 5.2.2.

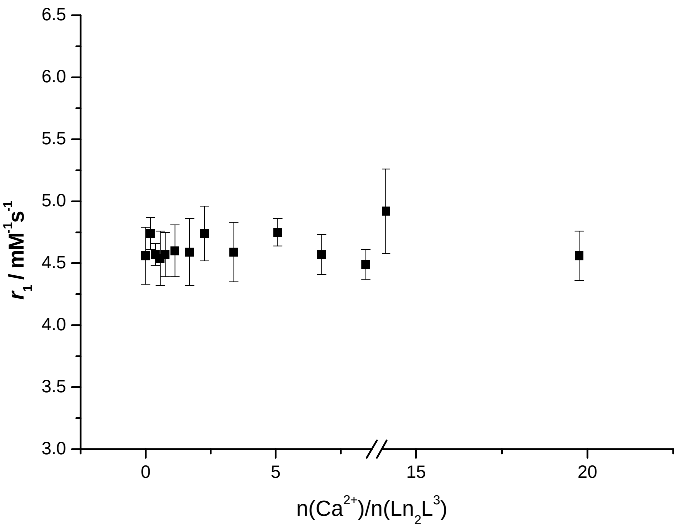

Figure 26: Relaxometric Ca^{2+} titration curves of **Gd_2L^3** performed at 25°C and 9.4 T

The relaxivity for this derivative was observed to be a bit higher than the previous two molecules. However the Ca^{2+} relaxometric titration performed on **Gd_2L^3** showed that the agent possesses no sensitivity to Ca^{2+} (Figure 26). This behavior showed that the aminopropionate units, as in the **Gd_2L^3**, do not get activated with the addition of Ca^{2+}.

5.4.3 Synthesis of Gd_2L^4

The synthetic scheme for this ligand was performed as shown in Scheme 10. The aromatic diamine **2** was reacted with bromoacetyl bromide to give **26.** The macrocyclic precursor, *tris*-Boc-DO3A (**27**), was synthesized by addition of Boc-anhydride to cyclen in presence of triethylamine. The bromoacetamide derivative **26** was used as an alkylating agent to do further alkylation of **27** to obtain the bismcrocyclic product, **28** with some amount of unreacted **27**. As the r_f value of **27** and **28** were very close, it was difficult to get pure **28**. To purify it, the mixture of **27** and **28** was subjected to further alkylation by Boc-anhydride to convert tris-Boc-DO3A to tetra-Boc-DO3A. The desired product (**28**) was purified in 35% yield by normal phase column chromatography.

Because an extra step was required to get the pure intermediate **28**, the second route was followed as shown in Scheme 11. Instead of acylating the diamine **2** with bromoacetylbromide, the 2° amine in the macrocyclic precursor **27** was amidated with bromoacetic acid to give **29** in 90% yield. This was used to do the alkylation of the diamine **2** to obtain the product **30** in 58% yield. The Boc groups were removed in CH_2Cl_2/TFA to get the crude product **31,** which was purified by RP-HPLC to obtain the pure product in 45% yield. The amide bond reduction was performed on **31** in BH_3/THF. The product **32** was formed with some unknown side products as was confirmed by ESI-MS. The crude product obtained was subjected to further alkylation with methylbromoacetate. The purification on silica column gave only traces of the product. The obtained crude product **32** was subjected to global deprotection and final purification with RP-HPLC using method B to obtain the $\mathbf{L^4}$ in 10% yield.

The synthesis of this ligand by this scheme turned out to be very cumbersome. Given the complexity of the synthesis of bismacrocyclic derivatives, no further reaction scheme was tried for this derivative.

Scheme 10:

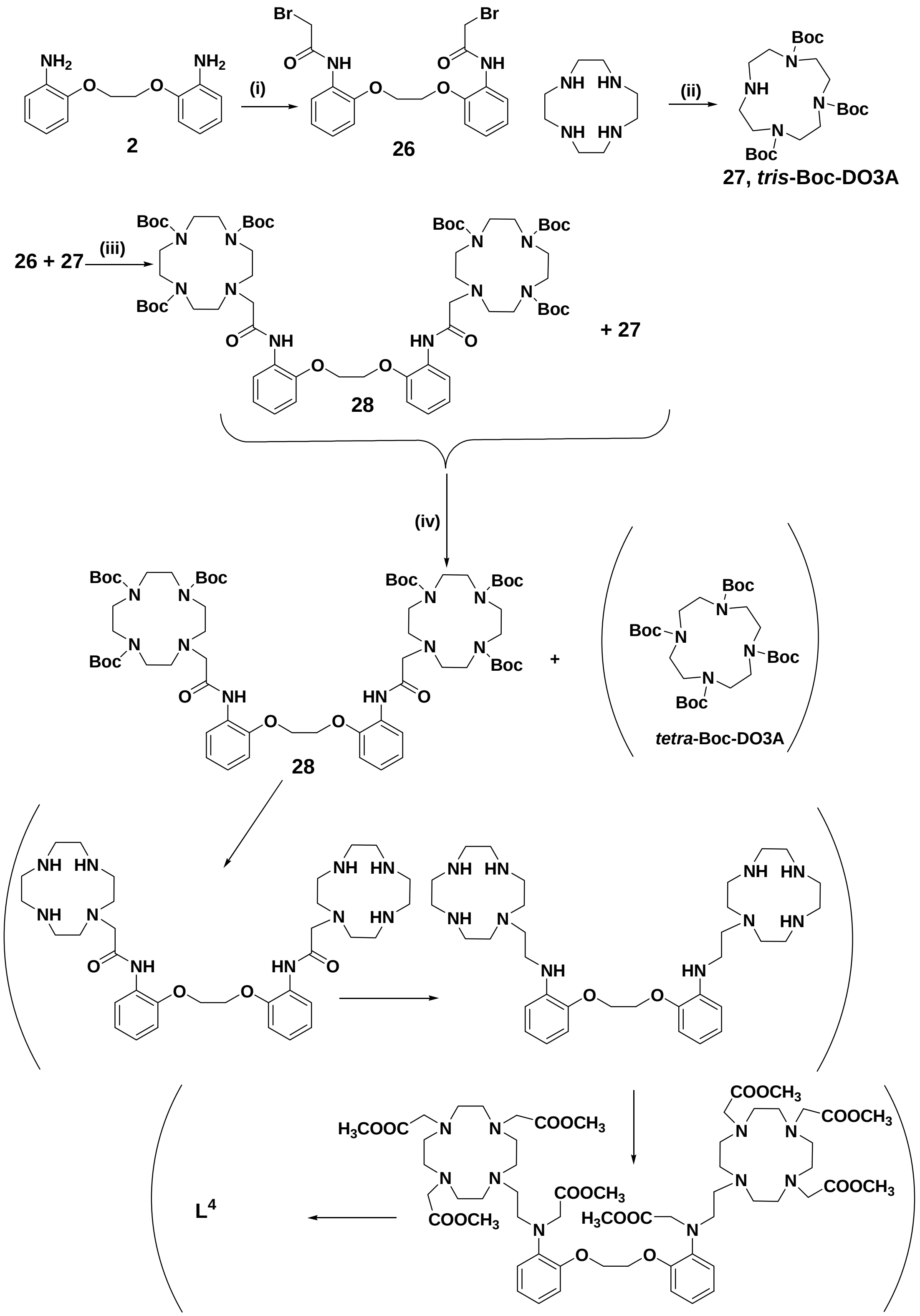
NH$_2$
O
NH$_2$
2
(i)
Br
O
NH
26
NH
HN
(ii)
Boc
N
Boc
27, *tris*-Boc-DO3A
26 + 27
(iii)
28
+ 27
(iv)
28
+
tetra-Boc-DO3A
COOCH$_3$
H$_3$COOC
L^4

Reagents and conditions: *(i)* **2**/ $BrCH_2COBr/Na_2CO_3/MeCN$/; 56% *(ii)* Boc-anhydride/$Et_3N/CHCl_3$; 50% *(iii)* Na_2CO_3/KI/DMF *(iv)* Et_3N/Boc-anhydride; 35%

Scheme 11

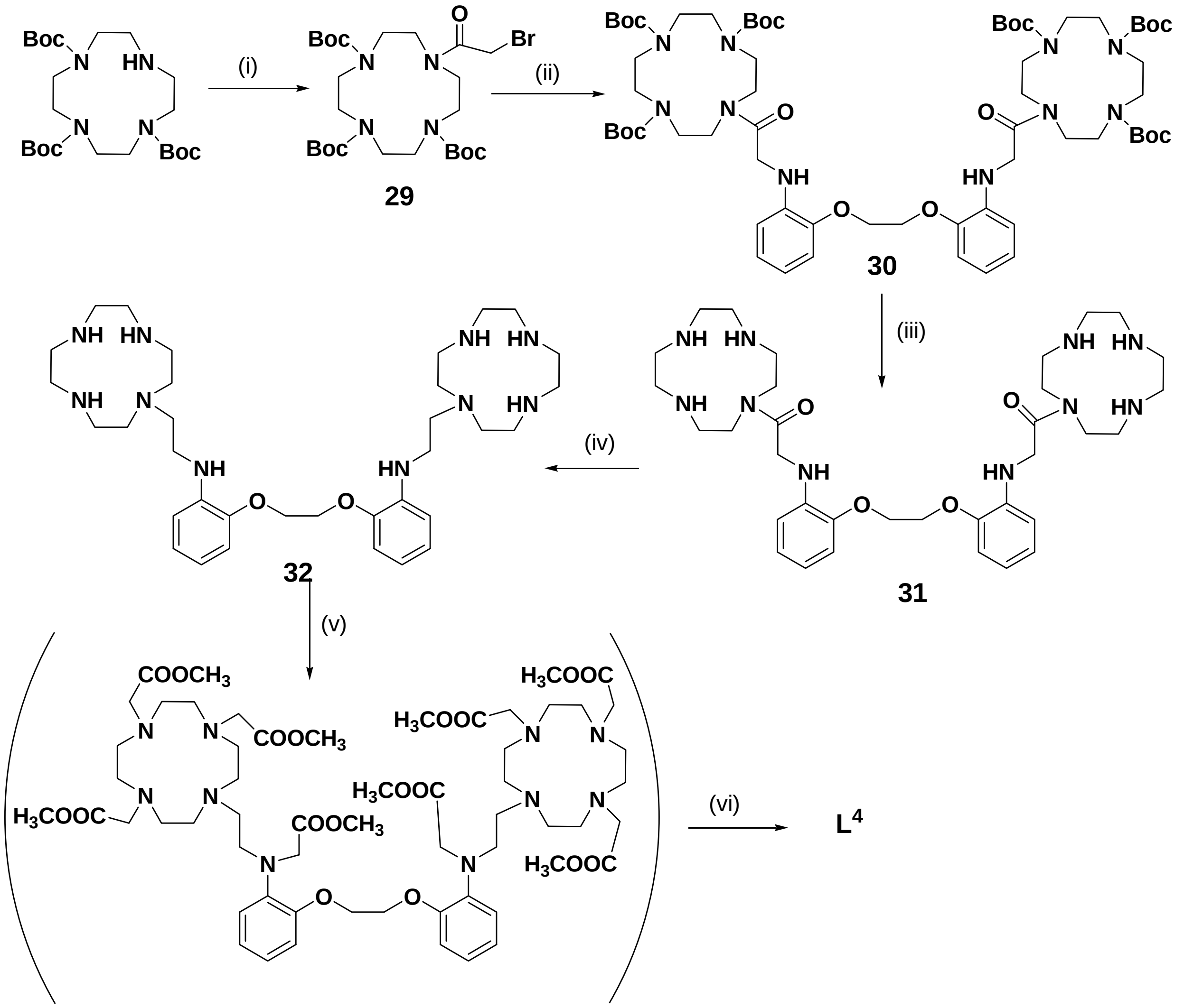

Reagents and conditions: (i) $BrCH_2COOH/DCC/CH_2Cl_2$; 91% (ii) **2**/Na_2CO_3/MeCN; 58% (iii) TFA/CH_2Cl_2; quant (iv) BH_3/THF; 24% (v) methylbromoacetate/NaH/DMF (vi) NaOH/H_2O; 10%

5.5 Conclusions

With the objective of Ca^{2+} sensing by MRI in the extracellular space, four novel modified-BAPTA based bismacrocyclic ligands were synthesized. Two of them had BAPTA-bisamide as the Ca^{2+} chelating moiety. Their Gd^{3+} complexes exhibited relaxivities comparable to that of currently used monomeric MRI contrast agents, in accordance with their larger size and low hydration number (q<1). Upon Ca^{2+} addition, the relaxivities of $\mathbf{Gd_2L^1}$ and $\mathbf{Gd_2L^2}$ increased by 15% and 10%. The changes obtained with $\mathbf{Gd_2L^1}$ and $\mathbf{Gd_2L^2}$ are likely insufficient for *in vivo* MRI detection. Gd_2L^1 was found to be practically insensitive towards Mg^{2+}. The apparent association constants for the Ca^{2+} interaction of $\mathbf{Gd_2L^1}$ and $\mathbf{Gd_2L^2}$, was obtained from the relaxometric titration curves. They were several orders of magnitude lower for these complexes than those determined for $BAPTA^{4-}$ itself or other tetracarboxylate $BAPTA^{4-}$ analogues. The hydration number of $\mathbf{Eu_2L^1}$ was determined from luminescence lifetime measurements in the absence (q=0.4) and presence of Ca^{2+} (q=0.7). UV-Vis measurements confirmed the presence of two coordination environments that we attributed to a monohydrated and a non-hydrated state (Figure 36). Upon the coordination of Ca^{2+} in the central part of the ligand, the molecule undergoes a conformational change and an acetate arm, originally coordinated to the Ln^{3+} ion, comes to bind to Ca^{2+} and leaves space for the coordination of a water molecule to the lanthanide, which shifts the hydration state towards the more hydrated species. Doing changes at the Ca^{2+} chelating acetate arm to propionate arms resulted in no sensitivity toward Ca^{2+}.

Also, it has been observed that the synthesis of the bismacrocycles is time consuming and because of their complex structure, performing the modifications to it according to the need is not so easy.

In the quest of having agents with better sensitivity to Ca^{2+} and easily modifiable structural design, monomacrocyclic SCAs were planned to be synthesized as the next step.

CHAPTER 6

6. Design, synthesis and characterization of monomacrocyclic SCAs sensitive to Ca^{2+}

6.1 General design: As it was outlined in the Section 4.1.2 that low affinity chelators are most likely to prove efficient to be active in extracellular Ca^{2+} concentration range. Considering that, we chose APTRA (*o*-aminophenol-N,N,O-triacetate) as the Ca^{2+} chelating unit. Besides being a low affinity chelator, incorporating the simple structure of APTRA would simplify the synthesis of the whole CA and also, the modification in the structure according to the requirement would be comparatively easier. The initial approach consisted of following sequences of steps:

1) At first, APTRA at its free *ortho* position would be coupled to a Gd-DO3A unit. A simple alkyl ether linker was chosen, similar to one used in Gd-DOPTA [55].

2) If the enough sensitivity would not be achieved with the above construct, the linker would be modified. The modification would consist of increasing/decreasing the linkers' length, replacement of ether linkage to simple alkyl linker or introduction of some more rigid/flexible linker.

3) With an optimized linker selected from above, the Ca^{2+} selective and Mg^{2+} rejection property of the APTRA could be improved. The appropriate structural changes on the Ca^{2+} binding part of the molecule would be done.

6.2 General physicochemical characterization for monomacrocyclic complexes

The Ca^{2+} dependent relaxivity response of the agents was checked at 9.4 T and physiological pH 7.4. The relaxometric titrations were performed in buffer, Mg^{2+} containing buffer, Zn^{2+}

containing buffer, artificial cerebrospinal fluid (ACSF) and artificial extracellular matrix (AECM). A solution of $CaCl_2$ of known concentration was added stepwise to the complex solution and the longitudinal proton relaxation time T_1 was measured after each Ca^{2+} addition. The exact concentration of CAs was determined by ICP-OES. Luminescence Lifetime measurement was performed to determine the hydration state of the complex in the presence and absence of Ca^{2+} and was carried out similar to as described in the Section 4.1.2. The dissociation constant of the agent to Ca^{2+} was determined by paramagnetic relaxation enhancement method. The relaxometric titration curve was fitted according to the equation 6.1

$$\mathrm{r_{obs}} = \left(\mathrm{r_f} \cdot [\mathrm{CA}]_t + (\mathrm{r_b} - \mathrm{r_f}) \cdot \left(\frac{\mathrm{n} \cdot [\mathrm{CA}]_t + [Ca^{2+}] + \mathrm{K_d} - \sqrt{(\mathrm{n}[\mathrm{CA}]_t + [Ca^{2+}]_t + \mathrm{K_d})^2 - 4 \cdot \mathrm{n} \cdot [\mathrm{CA}]_t \cdot [\mathrm{Ca}^{2+}]}}{2\mathrm{n}} \right) \right) \Big/ [\mathrm{CA}]_t \qquad \text{eq(6.1)}$$

Where, K_d is equilibrium dissociation constant, r_f is the relaxivity of unbound or free CA, r_b is the relaxivity of the Ca-CA complex or bound CA and n is the number of Ca^{2+} binding sites on CA. The fitting was done using K_d, r_f, r_b, and n as variable parameters.

6.3 Design of Ln-L^5

According to the construct described under the point 1 above, the structure of the first agent of this monomacrocyclic series was following:

Scheme 12:

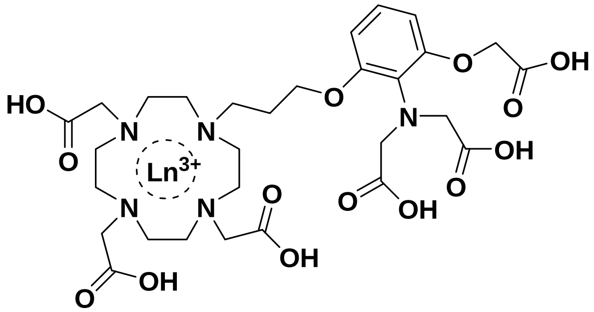

Ln-L^5

6.4 Results and Discussion

6.4.1 Synthesis of Ln-L^5

The synthesis of the ligand **L^5** was successfully done according to the Scheme 13. The synthesis started with inexpensive 2-nitroresorcinol which was monobenzylated using benzyl bromide giving **33**. Alkylation of phenol **33** was done with dibromopropane to yield the alkyl bromide **34**. This was then used for alkylation of tris-*tert*-Bu-DO3A to give the macrocycle **35**. Thereafter, the NO_2 group was reduced with simultaneous removal of the benzyl group by hydrogenation using Pd-C catalyst in a Parr apparatus to obtain **36**. The tris-*tert*-butylester in **36** was then hydrolysed with neat TFA to give triacid **37**. As the alkylation of aniline **37** with *tert*-butylbromoacetate or with methylbromoacetate was not successful yielding a mixture of two products which were difficult to separate, **L^5** was finally obtained in moderate yield by alkylation of **37** with bromoacetic acid and NaOH. The ligand **L^5** was purified by RP-HPLC using method C and loaded with Ln^{3+} (Gd^{3+} or Eu^{3+}) using $LnCl_3{\cdot}6H_2O$ in water at neutral pH. The final concentration of Gd^{3+} was determined by ICP-OES. Obtained complexes once formed were stable, however very slow hydrolysis of one acetate arm was observed similar to a previously reported molecule [134].

Scheme 13

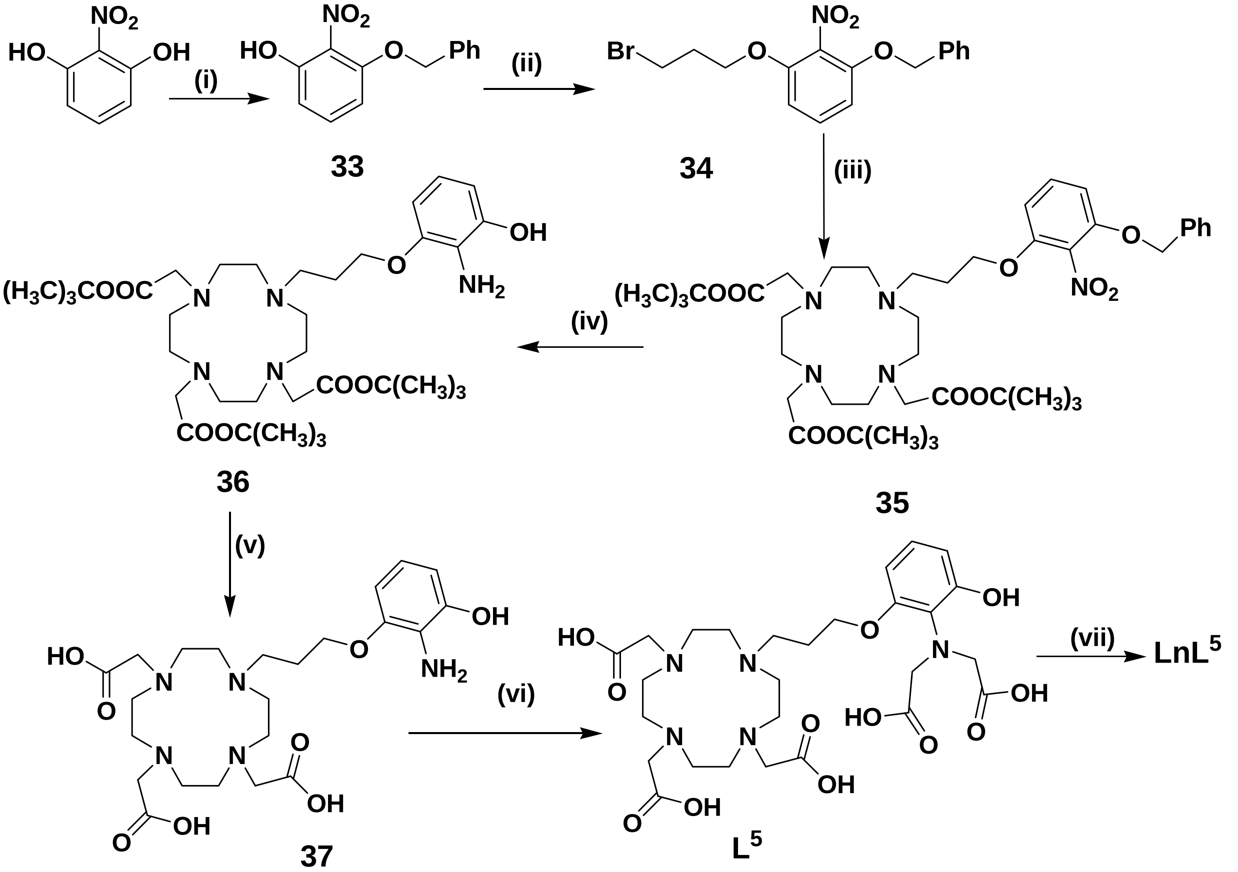

Reagents and conditions: *(i)* BnBr/K_2CO_3/MeCN; 85% *(ii)* $BrCH_2CH_2Br$/K_2CO_3/DMF; 88% *(iii)* tris-*tert*-Bu-DO3A/ K_2CO_3/DMF; 66% *(iv)* H_2/Pd-C; 85% *(v)* TFA (neat); 68% *(vi)* $BrCH_2COOH$/NaOH/H_2O; 55% *(vii)* $LnCl_3 \cdot 6H_2O$.

6.4.2 Physicochemical characterization

(a) Relaxometric Ca^{2+} titration in buffer

In the absence of Ca^{2+} the relaxivity observed was 3.5 $mM^{-1}s^{-1}$ which increased by 97% with stepwise addition of Ca^{2+} to 6.9 $mM^{-1}s^{-1}$. The r_1 enhancement was maximal at 1 equiv of Ca^{2+} and leveled off with the further Ca^{2+} addition. The observed ~100% r_1 increase, demonstrates the high sensitivity of the agent to Ca^{2+}. To check the reversibility of the agent, EDTA was added to the fully saturated solution (with 3.5 equiv. Ca^{2+}) of CA. The addition of EDTA restored the increased relaxivity to the initial value, proving the reversible binding of the agent to the Ca^{2+} (Figure 27). A strong chelator such as EDTA chelates away the Ca^{2+} bound to the low affinity chelator system e.g. **Gd-L^5**. The reversibility is an important requirement for such agents from *in vivo* perspectives, as the strong chelation of the agent to the Ca^{2+} in the brain might interfere with normal cellular processes and thus could be toxic.

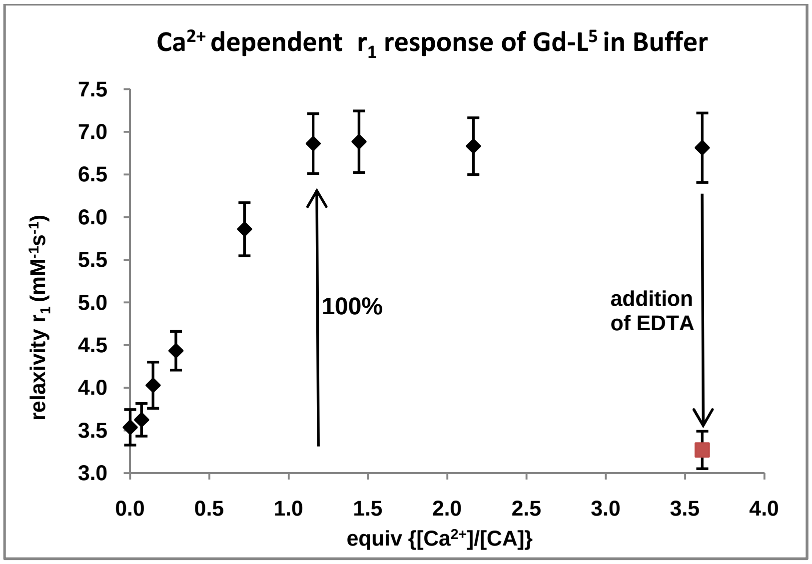

Figure 27: The Ca^{2+} dependent relaxivity response of **Gd-L^5** in KMOPS buffer. The black *diamonds* correspond to the stepwise increase in the r_1 upon Ca^{2+} addition while the red *square* correspond to the relaxivity obtained with the addition of EDTA after addition of 3.5 equiv of Ca^{2+}

(b) Relaxometric Ca^{2+} titration in Mg^{2+} containing buffer

The selectivity of the agent to Ca^{2+} in presence of other metal ions, which can compete for the Ca^{2+} binding site in the agent *in vivo* was also investigated. The concentration of major anions and cations in the extracellular space of the brain is given in Table 2 [135]:

Table 2: Ion concentrations in Millimoles

Ions	CSF	
	Human	Rat
Na^+	147	152
K^+	2.9	3.4
Ca, Total	1.14	1.1
Ca^{2+}, free	1.0	1.0
Mg, total	1.15	1.3
Mg^{2+}, free	0.7	0.88
H^+	0.000047	0.00005
pH	7.3	7.3
Cl^-	119	
HCO_3^-	23.3	28

The other metal cation that can act as the competitor for Ca^{2+} binding site in the agent is Mg^{2+}. As shown in the Table 2, the concentration of the Mg^{2+} ($[Mg^{2+}]_o$) in total is almost the same as the Ca^{2+} (~ 1.1 mM). However almost 40% of the $[Mg^{2+}]_o$ is in the bound form [136]. At resting state the cerebro spinal fluid (CSF) within the brain has 0.7 mM of Mg^{2+} as compared to 1 mM of Ca^{2+} [135]. (CSF is the fluid that occupies the subarachnoid space and ventricular system around and inside the brain. The extracellular space of the brain freely communicates with the CSF compartment and therefore the compositions of the two fluids are similar) [135, 137]. Thus we checked the selectivity of Gd-L^5 by measuring its relaxivity response toward Ca^{2+} in a Mg^{2+} containing buffer

When the CA was dissolved in a buffer containing more than half an equiv of Mg^{2+} (0.62 equiv), the relaxivity observed was 4.4 $mM^{-1}s^{-1}$ which is only 25% higher than the relaxivity of CA in Mg^{2+} free buffer, whereas the increase in relaxivity was ~ 60% with the same amount of Ca^{2+} added. When Ca^{2+} was added to the above Mg^{2+} containing buffer, still 70% relaxivity enhancement was observed (Figure 28).

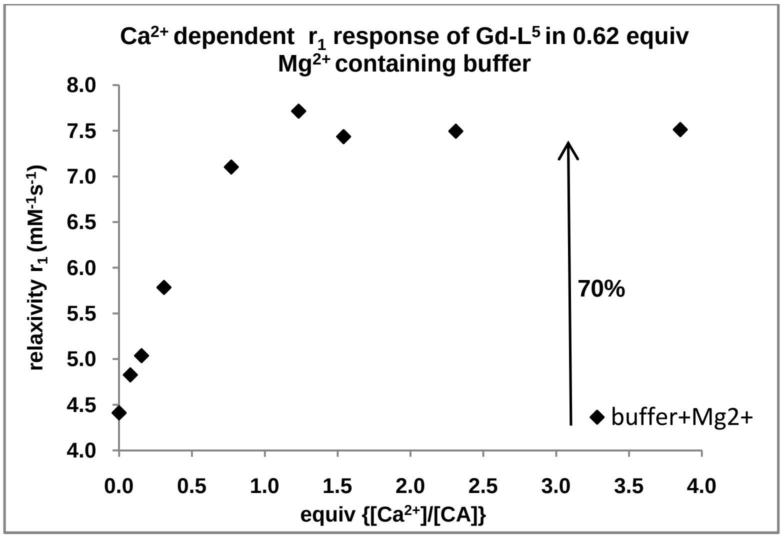

Figure 28: The Ca^{2+} dependent relaxivity response of **Gd-L^5** in 0.62 equiv. of Mg^{2+} containing buffer.

The agent was found to be sensitive and selective to Ca^{2+} even in presence of a very high concentration of Mg^{2+}. The r$_1$ enhancement with the addition of Ca^{2+} to the CA solution in the buffer containing 1.3 equiv. of Mg^{2+}, was found to be 45% (Figure 29).

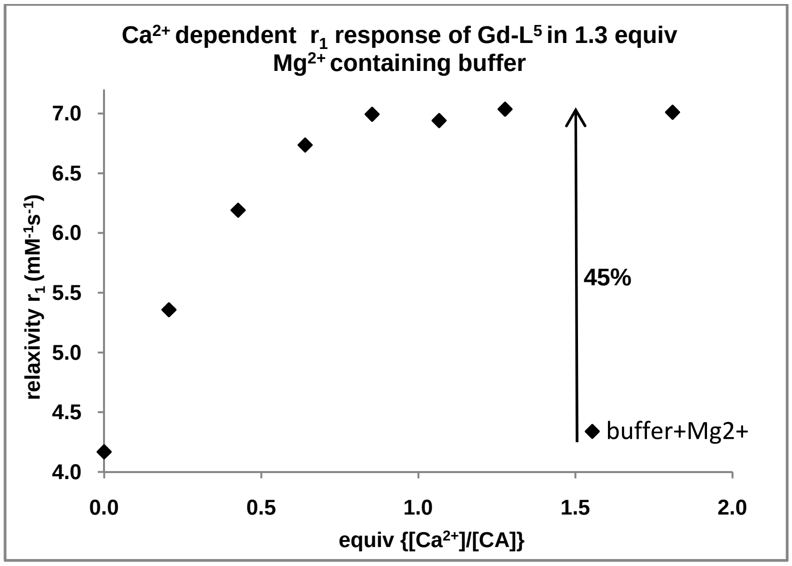

Figure 29: The Ca^{2+} dependent relaxivity response of **Gd-L^5** in 1.3 equiv. of Mg^{2+} containing buffer

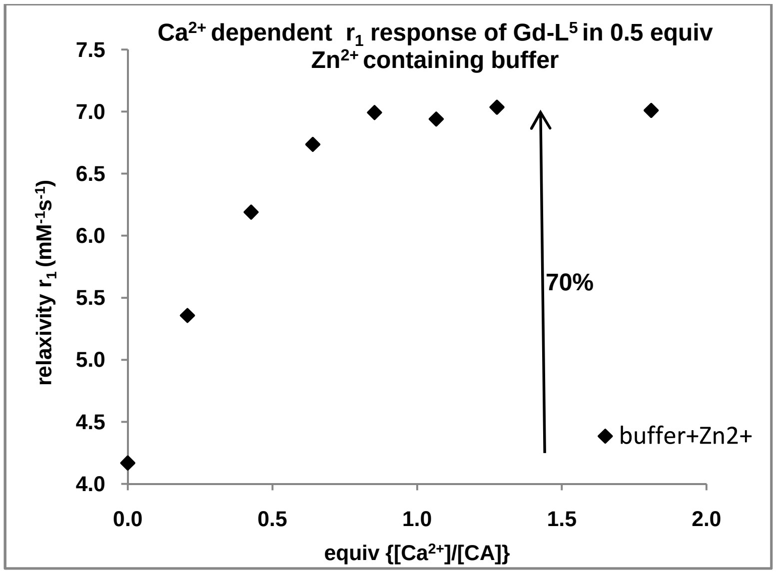

Figure 30: The Ca^{2+} dependent relaxivity response of **Gd-L^5** in 0.5 equiv. of Zn^{2+} containing buffer

(c) Relaxometric Ca^{2+} titration in Zn^{2+} containing buffer

The Ca^{2+} selectivity of the agent was also checked in the Zn^{2+} containing buffer, as a similar ligand has been investigated to show Zn^{2+} binding effect [138]. The Ca^{2+} titration was performed with Zn^{2+} containing (0.5 equiv) buffer. The initial relaxivity observed was 4.2 $mM^{-1}s^{-1}$, which is 17% higher than the relaxivity observed in Zn^{2+} free buffer, whereas the relaxivity enhancement was ~49% with same amount of Ca^{2+} added. Further addition of Ca^{2+} to Zn^{2+} containing buffer solution of CA resulted in 70% relaxivity enhancement (Figure 30). This shows the selectivity of CA for Ca^{2+} over Zn^{2+} as well. As the concentration of Zn^{2+} in the extracellular space of the brain is much lower as compared to Ca^{2+} and Mg^{2+} [139], the observed weak Zn^{2+} binding to the CA should not interfere with its response to a large Ca^{2+} modulation observed during synaptic transmission.

(d) Relaxometric Ca^{2+} titration in artificial cerebro spinal fluid (ACSF)

We further checked the relaxivity response in Ca^{2+} free artificial cerebro spinal fluid (ACSF) at 37 °C. The ACSF used contained all the major ions present in the CSF of the brain e.g. NaCl, KCl, $MgCl_2$, $NaHCO_3$. The preparation of ACSF solution is described in the experimental part (Section D). The relaxivity enhancement in the ACSF solution prepared was observed to be 37% (Figure 31). This signifies both the selectivity and sensitivity of the agent in a physiological environment toward Ca^{2+}.

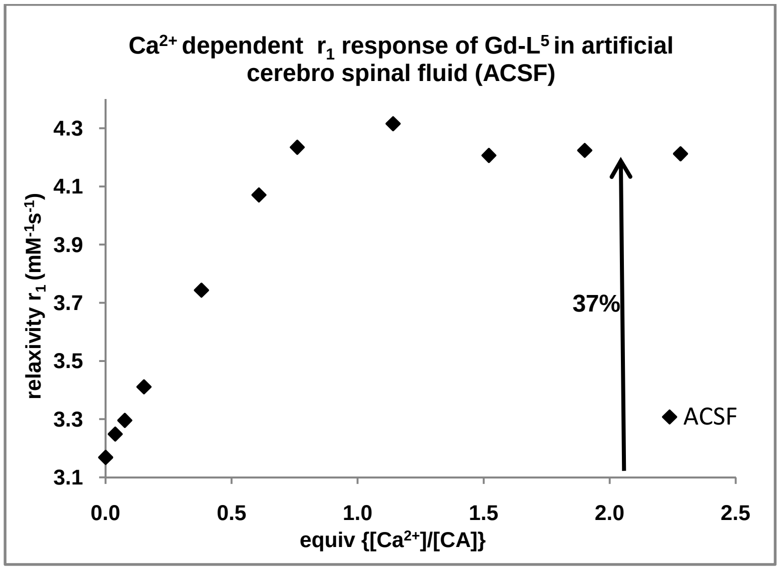

Figure 31: The Ca^{2+} dependent relaxivity response of **Gd-L^5** in ACSF.

(e) Relaxometric Ca^{2+} titration in artificial extracellular matrix (AECM)

To further explore the efficacy of CA, we performed the relaxivity measurement in the artificial extracellular matrix (AECM). ECM is a lattice of proteins, polysaccharides and various compounds attached to the plasma membrane. ECM materials are mostly present in intercellular spaces between neurons and glia [140]. The AECM was freshly prepared by mixing D-MEM : F-12 : N-2 in 50:50:1 proportion. D-MEM is well suited for supporting the growth of a broad spectrum of mammalian cell lines. F-12 Nutrient Mixture was originally formulated for single cell plating of near-diploid Chinese Hamster Ovary (CHO) cells [141]. N-2 supplement is a chemically defined, 100X concentrate of Bottenstein's N-2 formulation. This supplement is recommended for the growth and expression of neuroblastomas and for the survival and expression of post-mitotic neurons in primary cultures [142]. The exact compositions are listed in Table A5 in Appendix 2.

The maximum changes observed were 27% at 27 °C and 25% at 37 °C. The drop in relaxivity in biological media is likely due to anion binding to Gd in presence of Ca^{2+}. Anion binding will also block water access and this problem is well studied and described for the DO3A class of complexes [62, 143]. However these changes could be sufficient to report dynamics of Ca^{2+} in the brain (Figure 32)

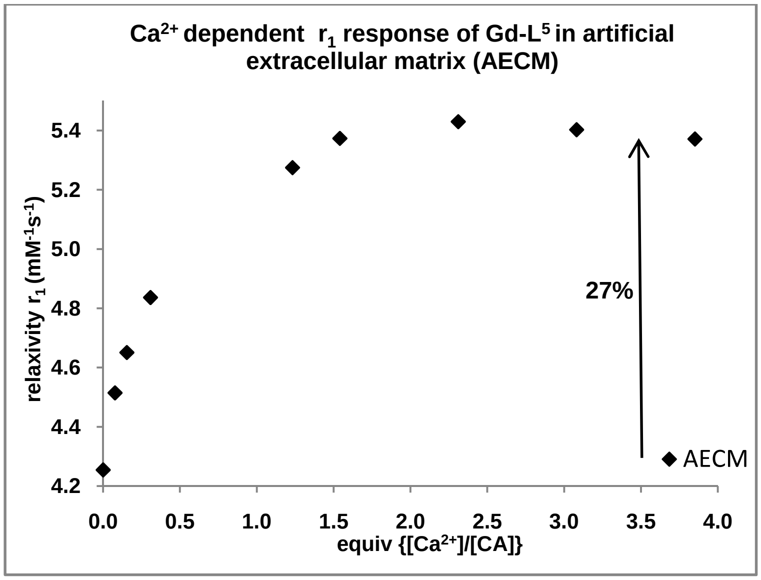

Figure 32: The Ca^{2+} dependent relaxivity response of **Gd-L^5** in AECM.

(f) Ca^{2+} dissociation constant

The dissociation constant (K_d) was determined using the paramagnetic relaxation enhancement (PRE) method. The relaxivity enhancement plot of CA vs [Ca^{2+}] was fitted to the equation described in eq(6.1). The K_d was found to be ~ 11 μM. The fitted curve is shown in the Figure 33.

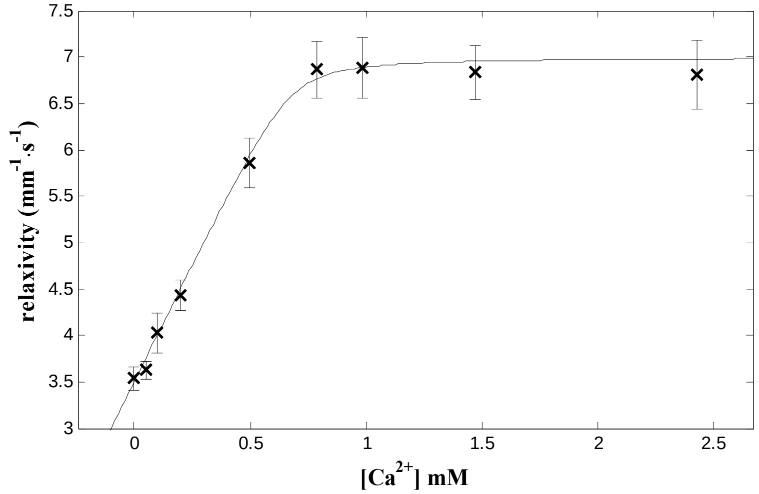

Figure 33: The fitting of the Ca^{2+} titration curve.

(g) Luminescence lifetime measurements

In order to elucidate the main parameter responsible for relaxivity enhancement, we have performed luminescence lifetime measurements on Eu^{3+} loaded ligand (**Eu-L^5**) in H_2O and D_2O solutions (Table 3). The hydration number, *q* was calculated according to the eq(5.1) In the absence of Ca^{2+}, *q* was observed to be 0.17 while in the presence of Ca^{2+}, it increases to 0.88 (Scheme 14). This proves that the relaxivity enhancement of **Gd-L^5** in the presence of Ca^{2+} is largely determined by the changes in hydration number of the complex [62, 134].

Table 3:

	τ_{H_2O}**(ms)**	τ_{D_2O}**(ms)**	**q**
Without Ca^{2+}	0.328	0.377	0.17
With Ca^{2+}	0.410	0.684	0.88

Scheme 14

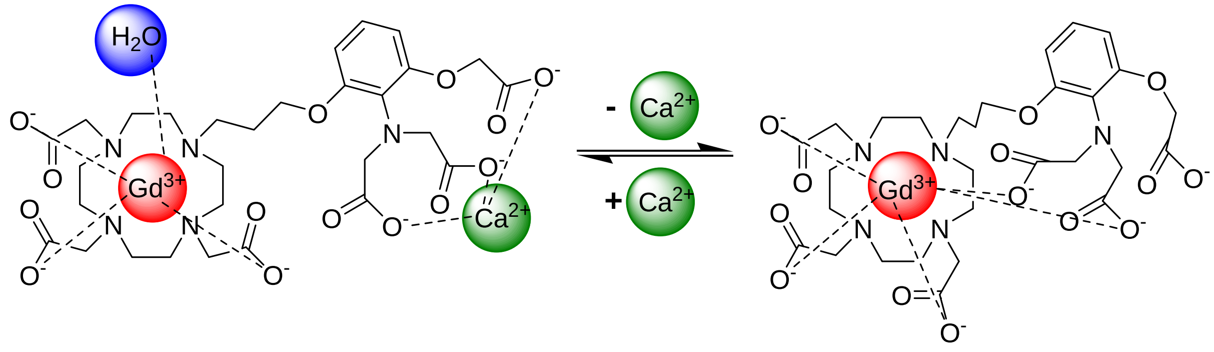

Gd-L^5

(h) Stability of Ln-L^5

The side product obtained while loading the Ln^{3+} to the solution of **L^5** was investigated by ESI-MS. The mixture of the products were separated by sephadex LH-20 column and analyzed. The *m/z* of the side product formed while loading Gd^{3+} and Eu^{3+} was 781.2 and 796.1 respectively, in the negative mode. The *m/z* of the side products corresponds to the respective molecules with loss of one acetate arm (803.2 for $[C_{37}H_{27}GdN_5O_{12} + Na - H]^-$ and 798.1 for $[C_{37}H_{27}EuN_5O_{12} + Na - H]^-$) as shown in the mass spectrum in the Figure 34-37.

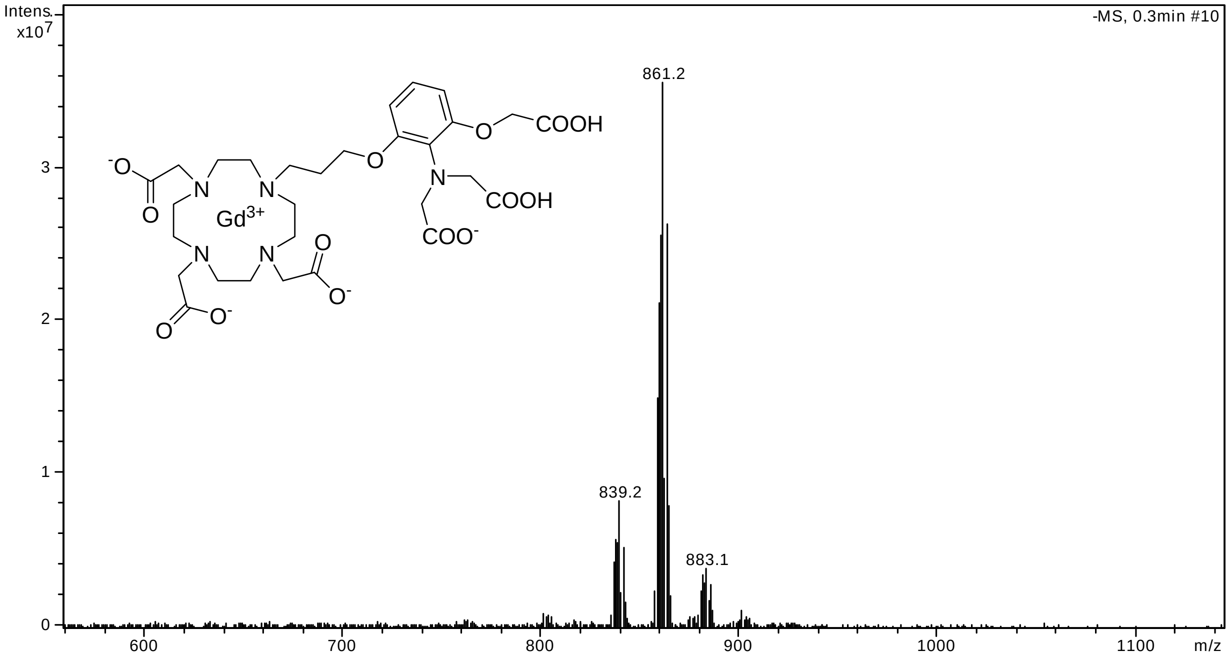

Figure 34: ESI-MS spectra of **Gd-L^5.**

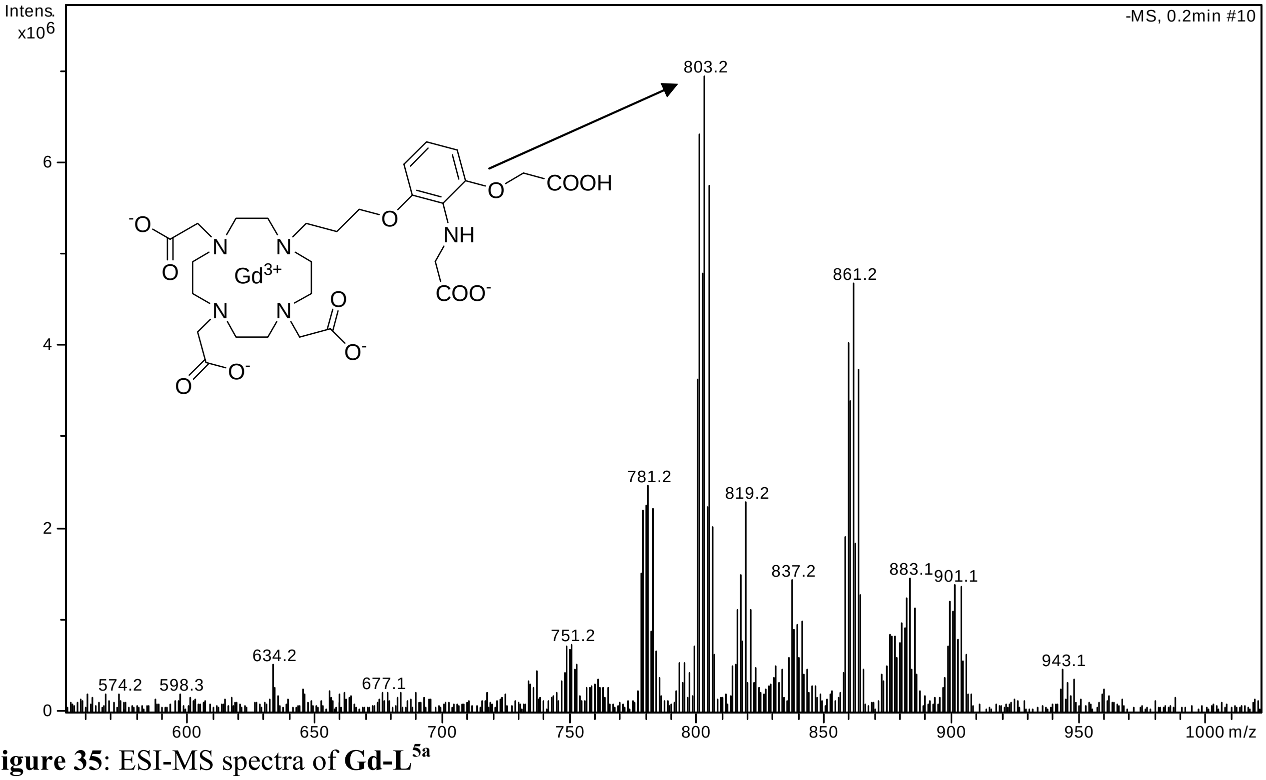

Figure 35: ESI-MS spectra of **Gd-L^{5a}**

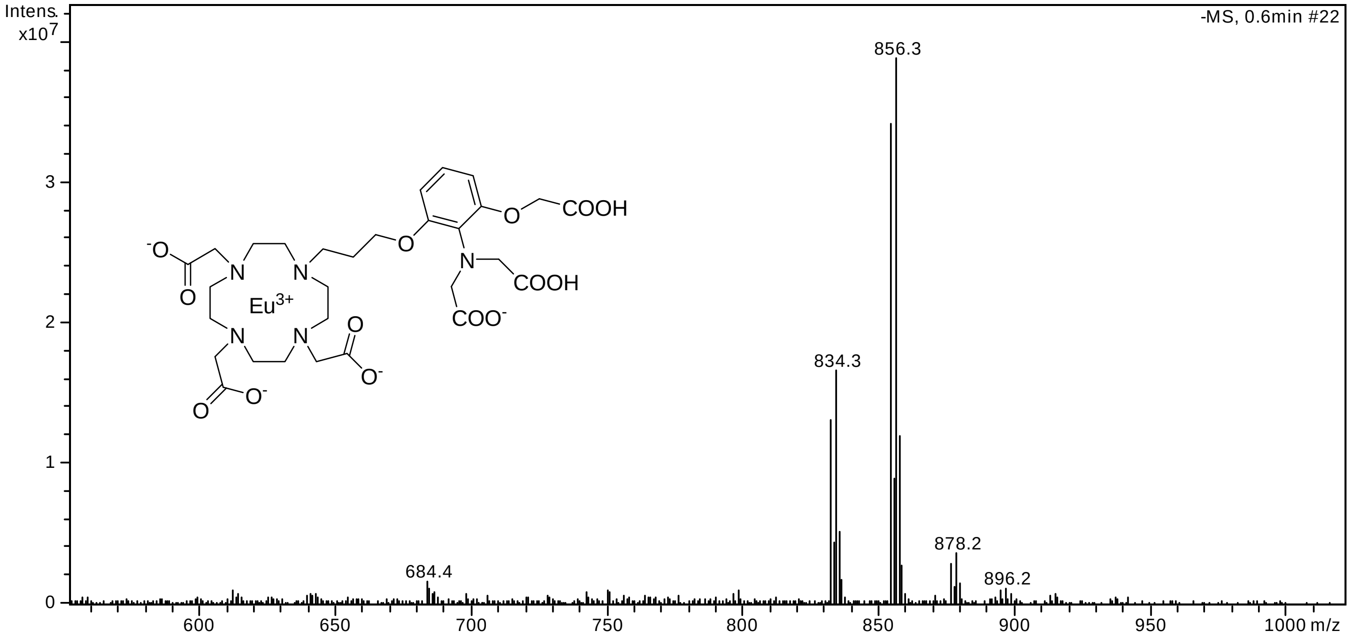

Figure 36: ESI-MS spectra of **Eu-L^5.**

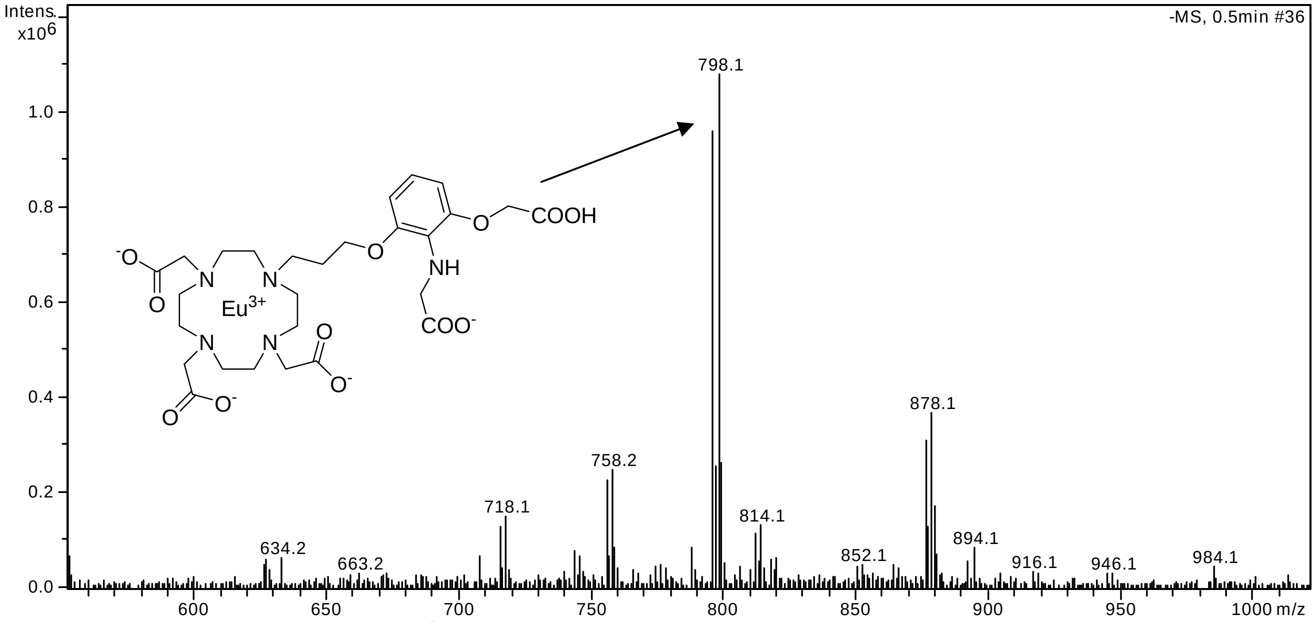

Figure 37: ESI-MS spectra of **Eu-L^{5a}.**

One of the possible mechanisms for the instability of the acetate arm is shown in Scheme 15. When the Ln^{3+} is added to the aqueous solution of the ligand solution, the oxygen in the linker between DO3A unit and APTRA unit, in conjugation with the APTRA's aminoacetate groups coordinates with Ln^{3+} and keep it maintained till the Ln^{3+} slips in to the macrocyclic cage. This facilitated caging of Ln^{3+} induces the electronic rearrangement as shown in the scheme 15 leading to the loss of an acetate arm. As the coordination of oxygen in the linker and the aminoacetate units weakens when the Ln^{3+} slips in to the cage, the rate of the hydrolysis of the acetate arm also slows down. However, on the basis of *m/z* values it cannot be ascertained that during the rearrangement, amino acetate arm is lost or the phenolic acetate.

Recently Chang and coworkers [134] had reported similar hydrolysis in their system. The structure of CA studied was very similar to **Ln-L^5** but without phenolic acetate groups. Similar hydrolysis observed for these two systems showed that in **Ln-L^5** also, the aminoacetate unit is lost during electronic rearrangement and the not the phenolic one.

Scheme 15:

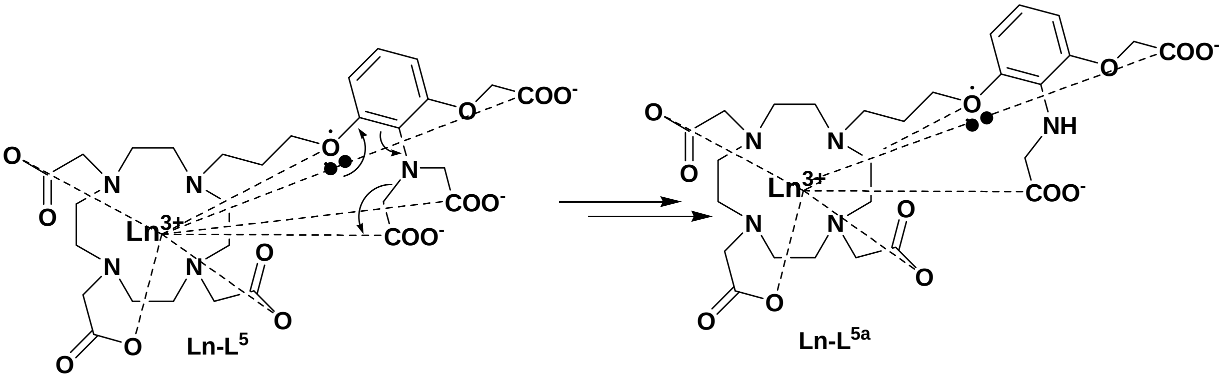

6.5 Conclusions:

The results obtained with the studies done with **Ln-L^5**, showed that the agent has an optimum distance and flexibility between the Ca^{2+} chelating moiety and the paramagnetic centre, leading to an excellent sensitivity to Ca^{2+}. It was also proven that the parameters influencing the r_1

enhancement are largely determined by the hydration number. The maximum number of water molecules interacting with Gd^{3+} in the presence of Ca^{2+} was found to be 1, leading to a 100% r_1 enhancement.

Further improvement on this agent was aimed at:

- Stability toward slow hydrolysis of acetate arm
- Increased Ca^{2+} dependent r_1 response in the physiological media or increased selectivity to Ca^{2+}.

7. Design, synthesis, and characterization of Ln-L^6: In an attempt of improvement over Ln-L^5

7.1 Design of Ln-L^6: To avoid the instability of the acetate arm, we planned to eliminate the oxygen from the linker. The use of a one carbon linker without oxygen was proposed, leading to the following construct (**Ln-L^6**).

Scheme 16

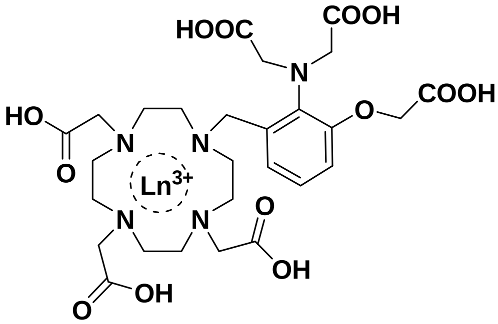

Ln-L^6

7.2 Results and Discussion

7.2.1 Synthesis of Ln-L^6

The synthesis started with the hydrolysis of the methyl ether in 3-methoxy-2-nitrobenzaldehyde and subsequent alkylation with benzyl bromide in one step to give **38**. The reduction of the aldehyde group in **38** was carried out with sodium borohydride to give alcohol **39**. The alcohol group in **39** was brominated to obtain **40**. This was used to alkylate tris-*tert*-Bu-DO3A to give **41**. The reduction of the nitro group and removal of the benzyl group was simultaneously carried out on **41** to obtain **42**. This was subjected to ester hydrolysis with neat TFA to give **43**. The alkylation of **43** was done with bromoacetic acid to give the final ligand **L^6** as solid followed by loading with $LnCl_3{\cdot}6H_2O$ to give **Ln-L^6** (Scheme 17).

Scheme 17

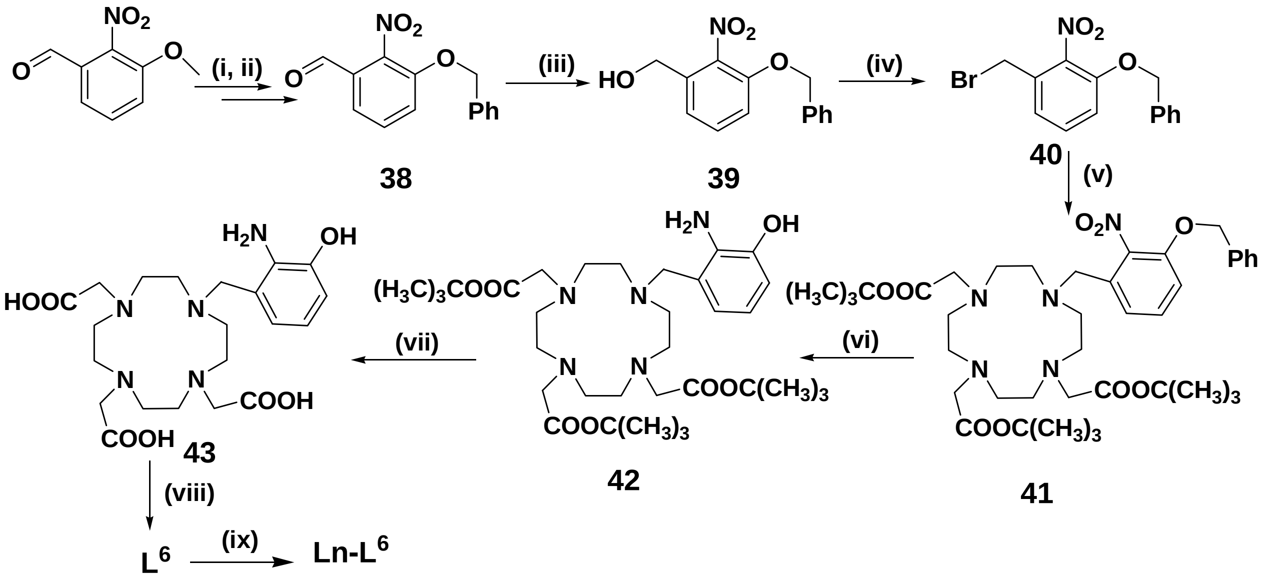

Reagents and conditions: *(i)* BBr_3/CH_2Cl_2 *(ii)* $BnBr/K_2CO_3/MeCN$; 85% *(iii)* $NaBH_4/MeOH$; 90% *(iv)* $CBr_4/PPh_3/CH_2Cl_2$; 77% *(v)* tris-*tert*-Bu-DO3A/K_2CO_3/DMF; 40% *(vi)* H_2/Pd-C/MeOH; 89% *(vii)* TFA/CH_2Cl_2; 36% *(viii)* $BrCH_2COOH/NaOH/H_2O$; 44% *(ix)* $LnCl_3$ $6H_2O$

7.2.2 Physicochemical characterization

(a) Stability

The agent was found to be stable with respect to the hydrolysis of the acetate arm. This supports the hypothesis that the electronic rearrangement is mediated through the oxygen in the linker.

(b) Relaxometric Ca^{2+} titration in buffer

The relaxivity measured in the absence of Ca^{2+} was 5.9 $mM^{-1}s^{-1}$, which decreased minimally by 13% with the addition of 3 equiv of Ca^{2} (Figure 38). Such a behavior could be explained on the basis of close interaction between the acetate arms of the Ca^{2+} chelator to the paramagnetic centre due to the short one-carbon linker. Because of the strong interaction, the acetate arm does not flip back to chelate Ca^{2+} and thus the access to the water molecules remained blocked even in the presence of Ca^{2+}.

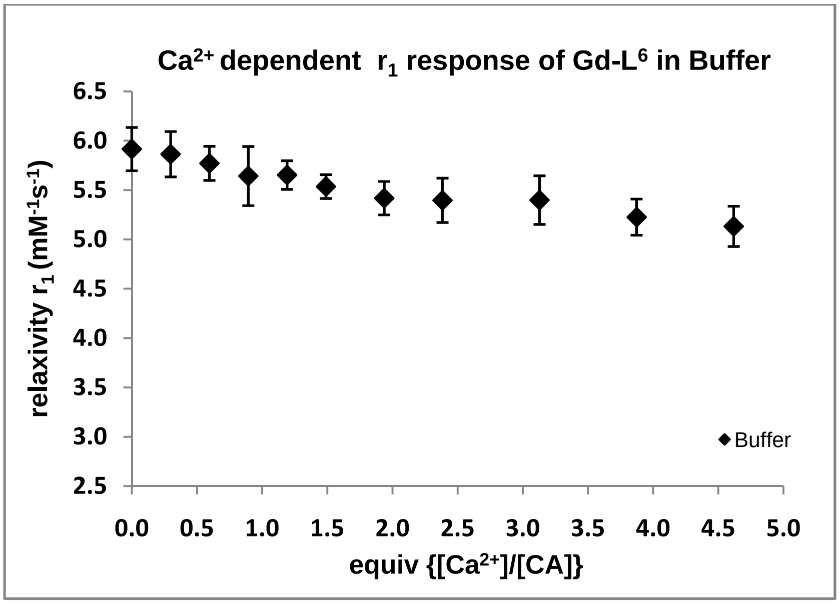

Figure 38: The Ca^{2+} dependent relaxivity response of **Gd-L^6** in KMOPS buffer.

7.3 Conclusions

- The length and the flexibility of the linker play an important role in deciding the sensitivity of the agent towards Ca^{2+}.This was found to be optimal with **Gd-L^5.**
- The presence of oxygen in the linker does influence the stability of the agent toward hydrolysis of the acetate arm. This was proved with the observed stability of **Gd-L^6.**
- The designing of the next derivative should incorporate the characteristics of both the synthesized agents, **Gd-L^5** and **Gd-L^6.**

8. Design, synthesis, and characterization of Ln-L^7: In an attempt of improvement over Ln-L^6

8.1 Design of Ln-L^7: As it was concluded in the Section 7.3, we planned to choose the linker similar to the one in **Gd-L^5** but with some minor modification to maintain the optimum flexibility observed in **Ln-L^5** and the stable system as in **Ln-L^6**. The simplest modification would be to introduce one more carbon atom in between the oxygen and the aromatic ring; this should lead to a '*break in the communication*' between the oxygen and the acetate arm. The structure of the agent in such a design would be the following:

Scheme 18:

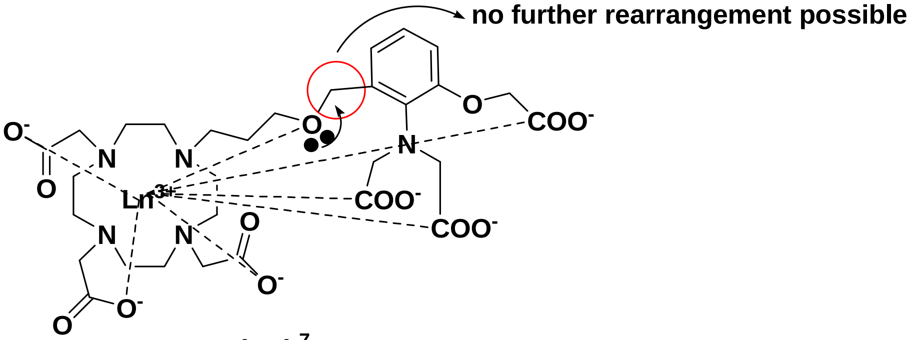

Ln-L^7

8.2 Results and Discussions

8.2.1 Synthesis of Ln-L^7

Synthesis of the agent was started with the intermediate synthesized for the synthesis of **L^6**. Compound **39** was alkylated with bromopropanol using sodium hydride as base to give **44**. The alcohol group in **44** was brominated to obtain **45**. This was used as an alkylating agent to alkylate, tris-*tert*-Bu-DO3A to give **46**. This was subjected to nitro group reduction and benzyl group removal in an one step hydrogenation to yield **47**. The ester hydrolysis was then carried out on **47** to obtain **48**. The alkylation on **45**, with bromoacetic acid and sodium hydroxide as base gave the final ligand **L**^{7} which was finally loaded with $LnCl_3$ to obtain **Ln-L**^{7} (Scheme 19).

Scheme 19

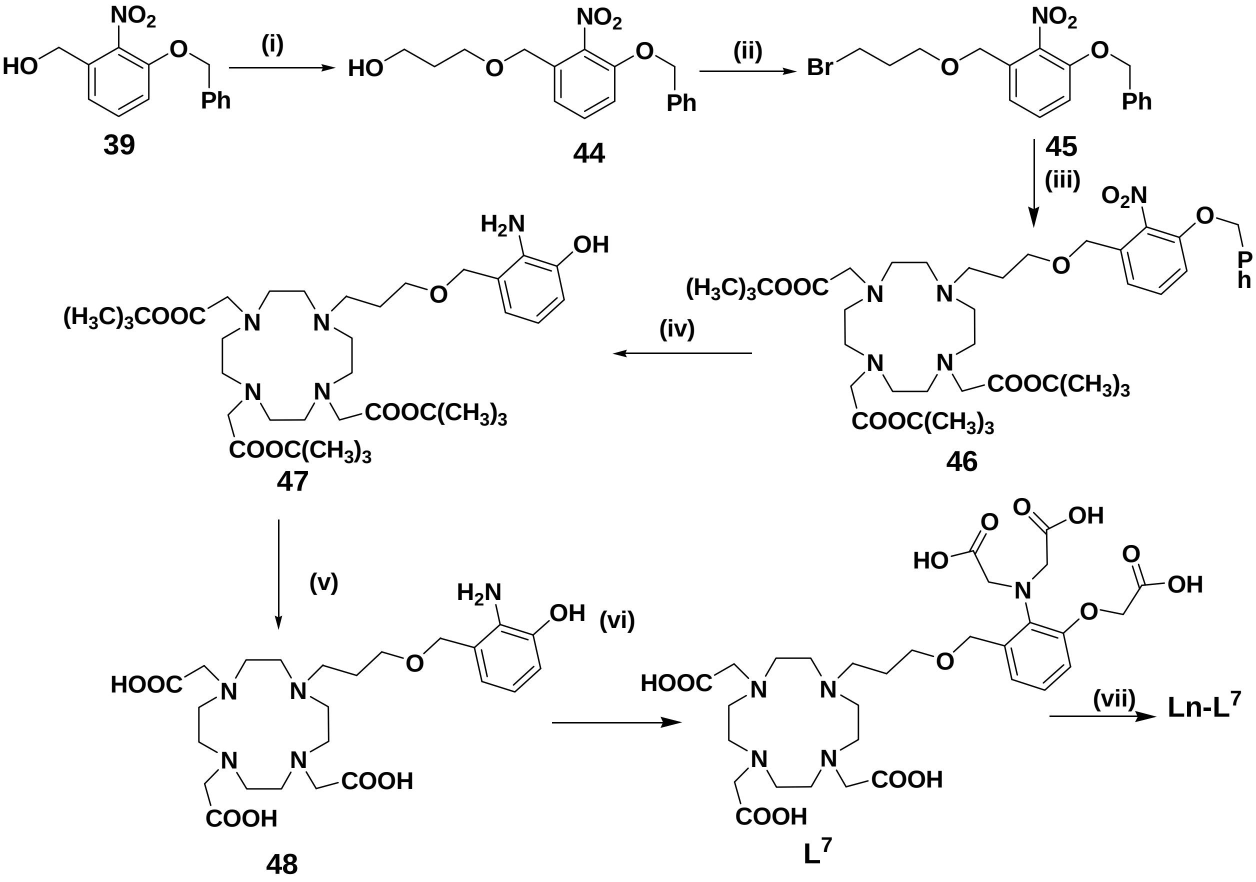

Reagents and conditions: (i) $Br(CH_2)_3OH$/NaH/THF; 83% (ii) $CBr_4/PPh_3/CH_2Cl_2$; 82% *(v)* tris-*tert*-Bu-DO3A/K_2CO_3/DMF; 50% *(vi)* H_2/Pd-C/MeOH; 90% *(vii)* TFA/CH_2Cl_2; 53% *(viii)* $BrCH_2COOH/NaOH/H_2O$; 44% *(ix)* $LnCl_3$ $6H_2O$

8.2.2 Physicochemical characterization

(a) Stability

Ln-L^7 was also found to be stable toward hydrolysis of the acetate arm. This finding further supported the drawn hypothesis (Scheme 15) of oxygen induced electronic rearrangement.

(b) Relaxometric Ca^{2+} titration in buffer

The relaxivity in the absence of Ca^{2+} was found to be 2.7 $mM^{-1}s^{-1}$ as compared to 3.6 $mM^{-1}s^{-1}$ for **Gd-L^5**. As the hydration number of **Gd-L^5** in the absence of Ca^{2+} is nearly zero, a lower relaxivity observed for **Gd-L^7** might be due to the difference in the other parameters affecting relaxivity. It is interesting to note that a small difference in the linker connecting the paramagnetic moiety and the Ca^{2+} chelating moiety, can affect the arrangement of these two moieties in aqueous media. The different conformation of the two complexes in the Ca^{2+} free aqueous media would affect the relaxivity parameters differently.

With the addition of Ca^{2+} the relaxivity increased by 157% to 7.0 $mM^{-1}s^{-1}$ which is ~ 60% higher than for **Gd-L^5**. As the final relaxivity observed in both cases are the same, it can be concluded that in the Ca^{2+} saturation conditions, both complexes shared a similar conformation. The saturation however was observed at 2 equiv for **Gd-L^7** and 1 equiv for **Gd-L^5**.

The Ca^{2+} dependent change in the relaxivity for **Gd-L^7** were found to be almost linear as compared to the steep rise as in the case of **Gd-L^5**. Considering the changes in Ca^{2+} concentration during normal brain activity i.e. 0.8-1.2 mM, the changes in r_1 for this range was found to be 30%. The increase for each 0.4 equiv (corresponding to the net change from 0.8-1.2 mM) Ca^{2+} addition was found to be constant (30%) over the broader range of 1 equiv. Such a trend could be an advantage from the *in vivo* perspectives, as the CA would respond to Ca^{2+} dynamics for a broader range of concentration ratio (CA:Ca^{2+}) (Figure 39).

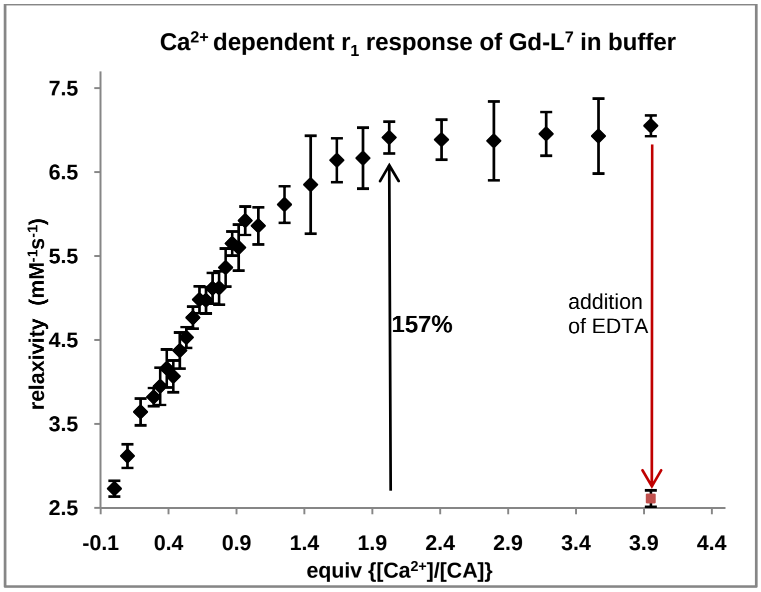

Figure 39: The Ca^{2+} dependent relaxivity response of **Gd-L^7** in KMOPS buffer. The black *diamonds* correspond to the stepwise increase in the r_1 upon Ca^{2+} addition while the red *square* correspond to the relaxivity obtained with the addition of EDTA. The concentration of CA was varied from 1.03 mM to 0.963 mM by the addition of Ca^{2+} solutions.

The evaluation of the exact parameter affecting the relaxivity change with Ca^{2+} can only be determined with detailed physicochemical characterization as previously done with **Ln$_2$L^1** and **Ln$_2$L^2**.

(c) Relaxometric Ca^{2+} titration in Mg^{2+} containing buffer

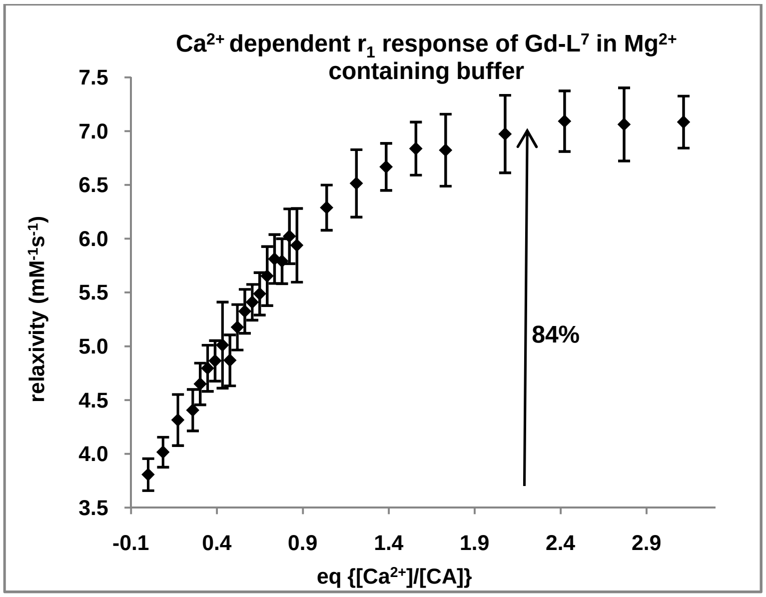

Figure 40: The Ca^{2+} dependent relaxivity response of **Gd-L^7** in Mg^{2+} containing buffer. The concentration of CA was varied from 1.15 mM to 1.08 mM by the addition of Ca^{2+} solutions.

The r_1 response of the agent was checked in the buffer containing 0.52 equiv of Mg^{2+}. The initial relaxivity of the agent was 3.8 $mM^{-1}s^{-1}$ which increased by 84% to 7.0 $mM^{-1}s^{-1}$. The saturation was observed at approx. 2 equiv of Ca^{2+} as in the buffer (Figure 40).

(d) Relaxometric Ca^{2+} titration in ACSF

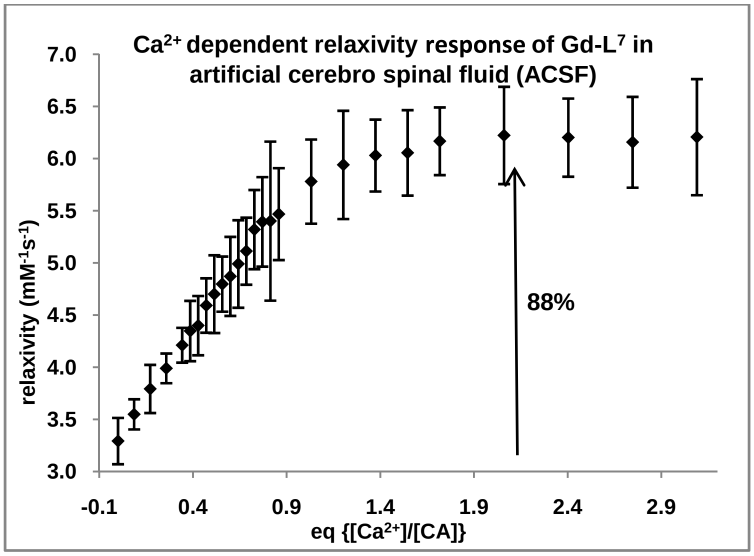

Figure 41: The Ca^{2+} dependent relaxivity response of **Gd-L^7** in ACSF. The concentration of CA was varied from 3.48 mM to 3.30 mM by the addition of Ca^{2+} solutions.

The agent showed a better response in ACSF as well. In the absence of Ca^{2+}, relaxivity was 3.3 $mM^{-1}s^{-1}$. With the addition of Ca^{2+}, r_1 enhancement of 88% was observed. The observed maximum r_1 was 6.2 $mM^{-1}s^{-1}$ at 2 equiv of $Ca^{2+.}$

(e) Relaxometric Ca^{2+} titration in AECM

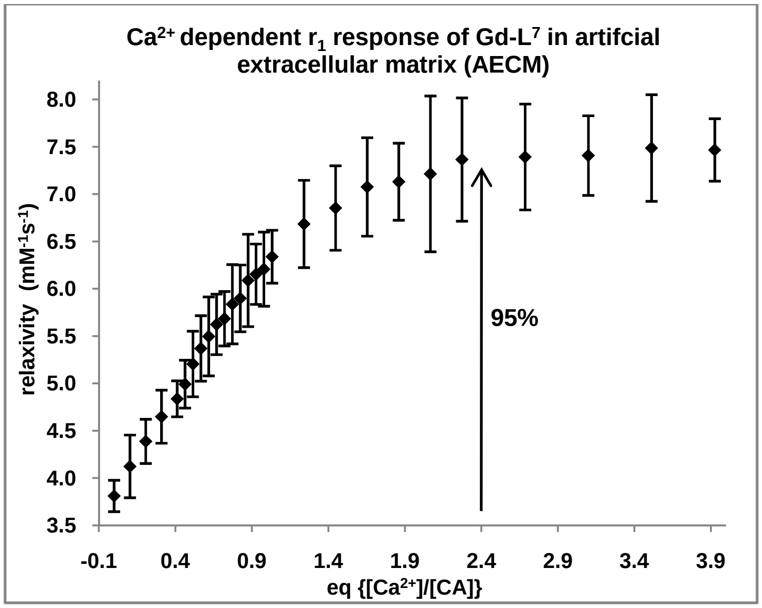

Figure 42: The Ca^{2+} dependent relaxivity response of **Gd-L^7** in AECM. The concentration of CA was varied from 2.90 mM to 2.73 mM with the addition of Ca^{2+} solutions.

In AECM, ~100% r_1 enhancement was observed with the addition of Ca^{2+}. The saturation in the r_1 increase with stepwise increase of Ca^{2+} was observed at ~ 2 equiv (Figure 42)

8.3 Conclusions

- As predicted by the hypothesis proposed for the instability of **Ln-L^5**, **Ln-L^7** was found to be stable toward hydrolysis.

- The agent showed an enhanced r_1 response of 157% to Ca^{2+} in buffer. The excellent sensitivity of the agent in the buffer was much better transferred to the physiological relevant media (~90-100%) (Figure 43). Considering the high sensitivity and the stability observed with the **Ln-L**^{7}, the ideal structural design for such a small molecular weight Ca^{2+} sensitive contrast agent is established.

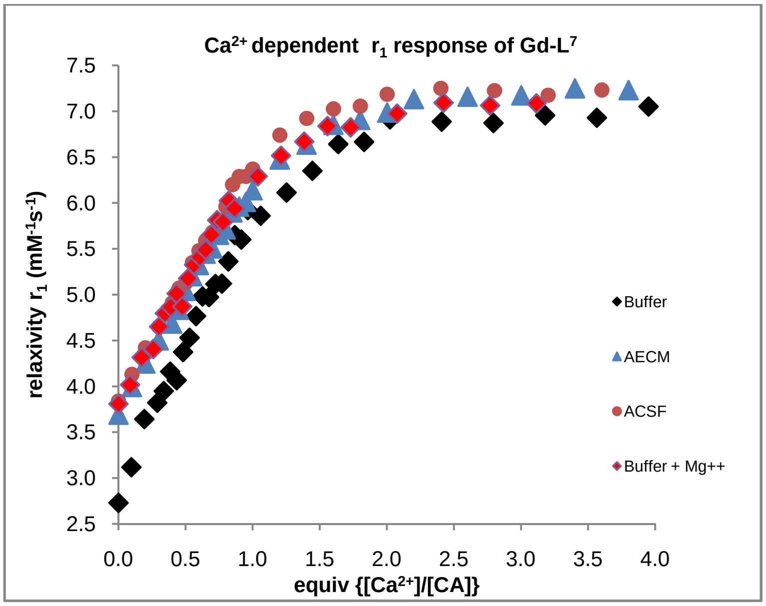

Figure 43: Ca^{2+} dependent relaxivity response of **Gd-L**^{7} in all media is collectively shown.

- The place of improvement on **Gd-L**^{7} could be aimed at further improving the transformation of the changes from buffer to physiological media.
- The simple synthetic procedure required to synthesize these derivatives makes the designing of its structural analogues and the synthesis of the same comparatively easy. Different analogues differing in their binding affinity to Ca^{2+} can therefore be synthesized.

9. Design, synthesis, and characterization of Ln-L^8 and Ln-L^9: In an attempt of improvement over Ln-L^7

9.1 Design of Ln-L^8: Considering the r_1 changes observed for the **Ln-L^7** in the Mg^{2+} free buffer, in the Mg^{2+} containing buffer, ACSF and AECM, the further improvement can be aimed at modifying the Ca^{2+} chelating part of the agent to have a chelating system with a range of Ca^{2+} binding affinities and with a better rejection to Mg^{2+}. A report published by Roger W. Tsien and coworkers discussed the modification of APTRA chelator to make it much more Ca^{2+} selective [144]. As reported, the best results were obtained by converting the acetate group on the phenolic oxygen to a morpholino amide group. A similar modification was planned next on **Ln-L^7** resulting in **Ln-L^8** as in Scheme 20.

Alternatively the phenolic acetate arm could be extended with the introduction of ether linker similar to in BAPTA (Scheme 21).

Scheme 20:

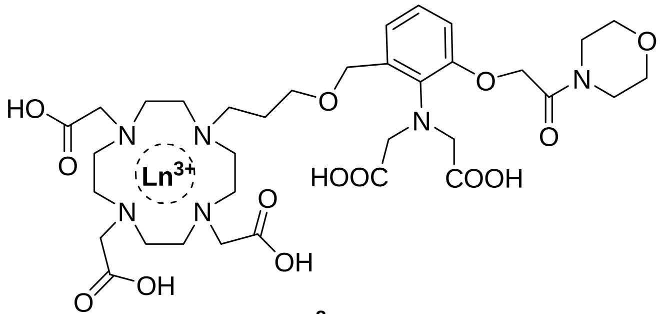

Ln-L^8

Scheme 21:

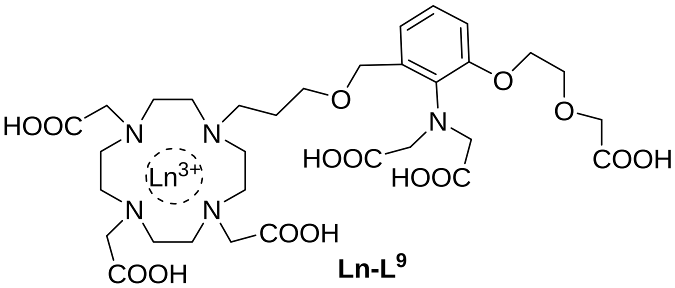

9.2 Results and Discussion

9.2.1 Synthesis of Ln-L^8

Synthesis of **L^8** was first attempted according to the Scheme 22. However an undesirable hydrolysis of the MEM group was observed while alkylating the benzyl alcohol in **50** with bromopropanol/NaH/THF. Scheme 23 was then formulated starting with the compound **46**. The idea was to use the established scheme 15 and introduce the morpholino amide group at the phenolic oxygen followed by two more additional steps to the final ligand (Scheme 23). However, it was not possible to control the hydrogenation reaction to deprotect the benzyl protecting group in **46** keeping $–NO_2$ group intact, as $–NO_2$ group reduces much faster than the benzyl group. The deprotection of the benzyl group was then carried out under acidic conditions with simultaneous hydrolysis of *tert*-butyl esters to give **51**. The morpholino precursor **(52)** was synthesized from bromoacetyl bromide and morpholine under dry ice conditions. Unfortunately, the alkylation of **51** at the phenolic oxygen with **52** could not be achieved, probably due to the insolubility of the substrate **51** in the polar aprotic solvents (e.g. THF, DMF). The reaction was also tried with *tetra*-butyl ammonium iodide as phase transfer catalyst (between CH_2Cl_2:H_2O layers) but the desired product was not obtained. As an alternative Scheme 24 was then designed in order to achieve the deprotection of benzyl group without the hydrolysis of ester groups and thus have better soluble substrates. This was done by using the macrocyclic precursor **53** with the acid stable ethyl ester groups. The alkylation of **53** with **45** was done in DMF and K_2CO_3 as base to obtain **54**. The deprotection of benzyl group in **54** was performed under acidic conditions to get nitro phenol **55**. The alkylation of the phenolic oxygen was then successfully carried out with **52** using NaH as the base to obtain the desired product, **56**. The $–NO_2$ group in **56** was then reduced to $–NH_2$ under H_2 (1 atm) in a Parr apparatus using Pd-C catalyst to obtain aniline **57**. The alkylation at the aromatic amine in **57** under basic conditions with simultaneous hydrolysis of ethyl ester groups was then planned as the last step to the final ligand (Scheme 24). However, under basic conditions the hydrolysis of the ethyl ester groups at the macrocyclic unit occurred with concomitant transamidation at the aromatic unit resulting in lactam **58** and the final desired ligand could not be obtained. The formation of **58** was confirmed by ESI-MS and the ^1H, ^{13}C NMR. To avoid the transmidation, Scheme 25 was then used in which the amino acetate units were introduced before the coupling of the aromatic unit to the macrocyclic moiety.

Scheme 22

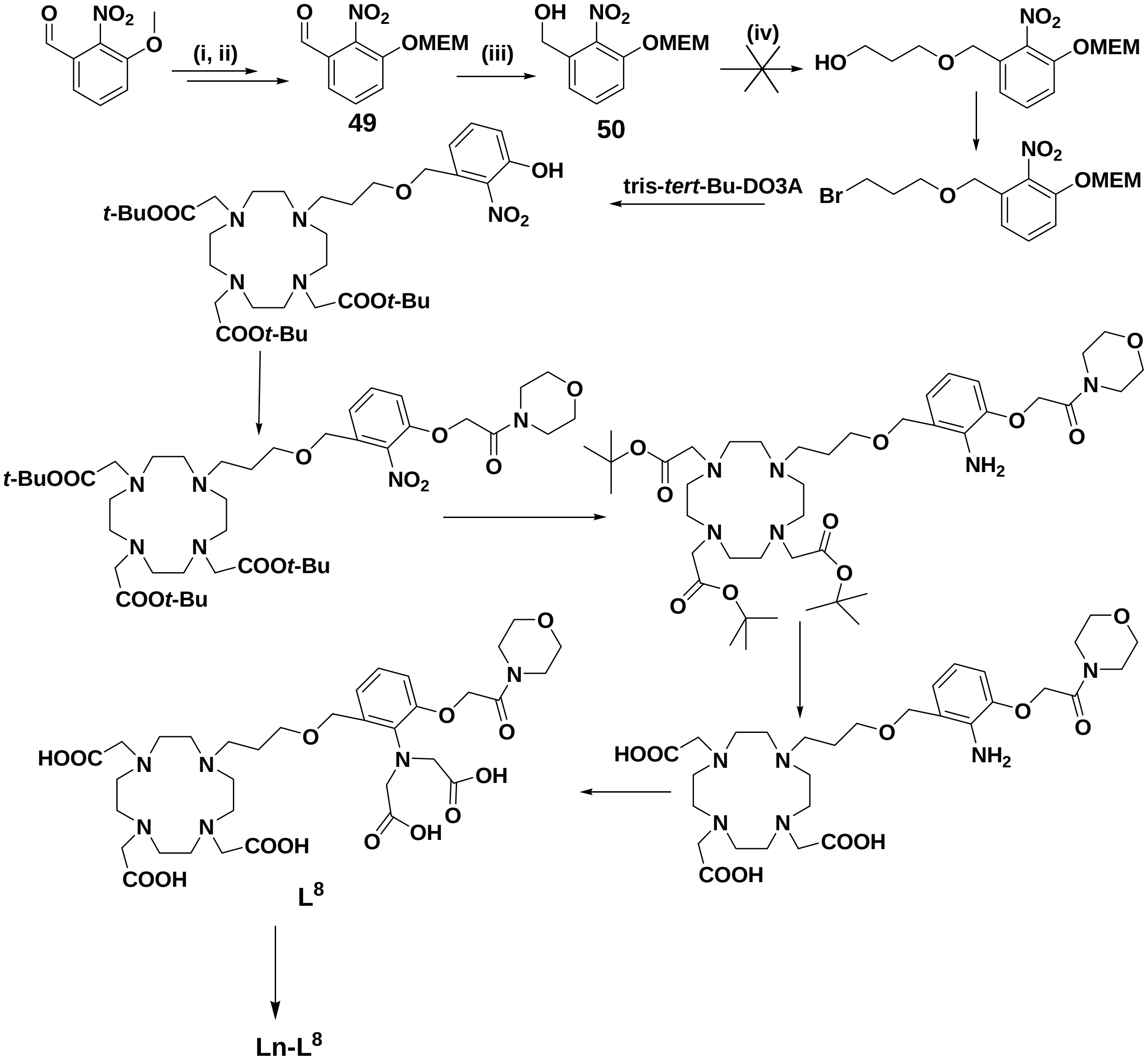

Reagents and conditions: *(i)* BBr_3/CH_2Cl_2 *(ii)* MEM-Cl/DIEA/CH_2Cl_2; 98% *(iii)* $NaBH_4$/MeOH; 79%

(iv) $Br(CH_2)_3OH$/NaH/THF

Scheme 23

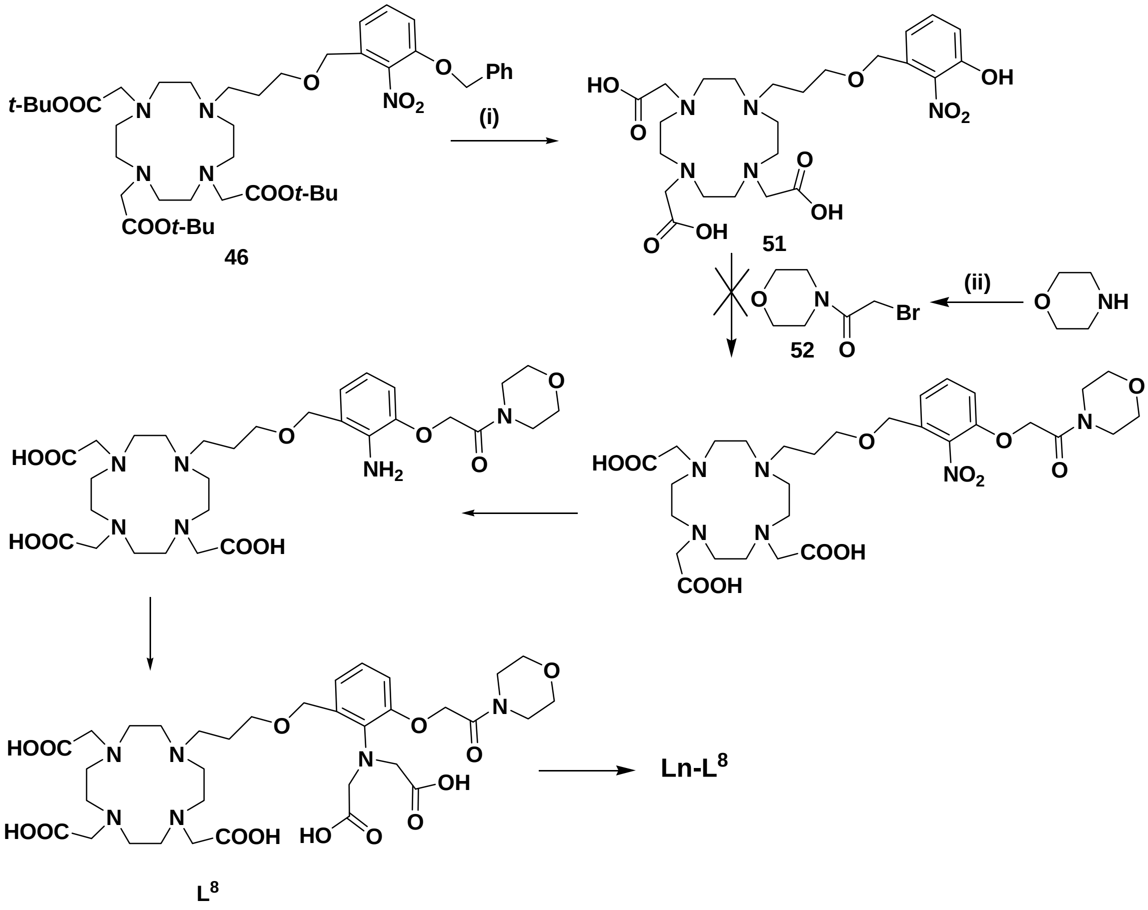

Reagents and conditions: *(i)* TFA/CH_2Cl_2; quant *(ii)* $BrCH_2COBr/Et_3N$/diethyl ether; 48%

Scheme 24

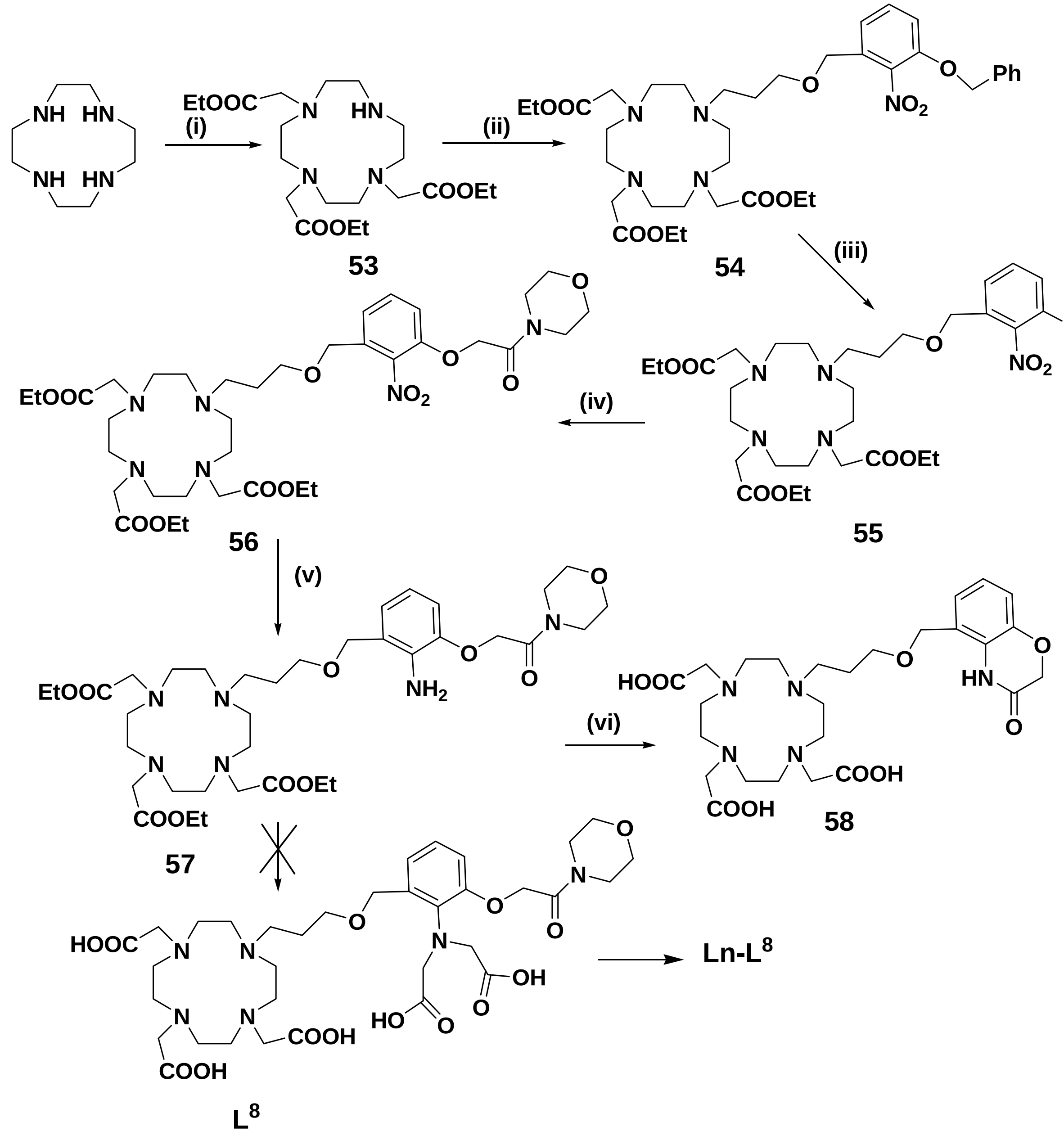

Reagents and conditions: *(i)* ethyl bromoacetate/$NaHCO_3$/$CHCl_3$; 35% *(ii)* **52**/K_2CO_3/DMF; 52% *(iii)* TFA/CH_2Cl_2; 54% *(iv)* **52**/K_2CO_3/DMF; 50% *(v)* ammonium formate/H_2/Pd-C/ MeOH; 89% *(vi)* KOH/EtOH; 50%

Scheme 25:

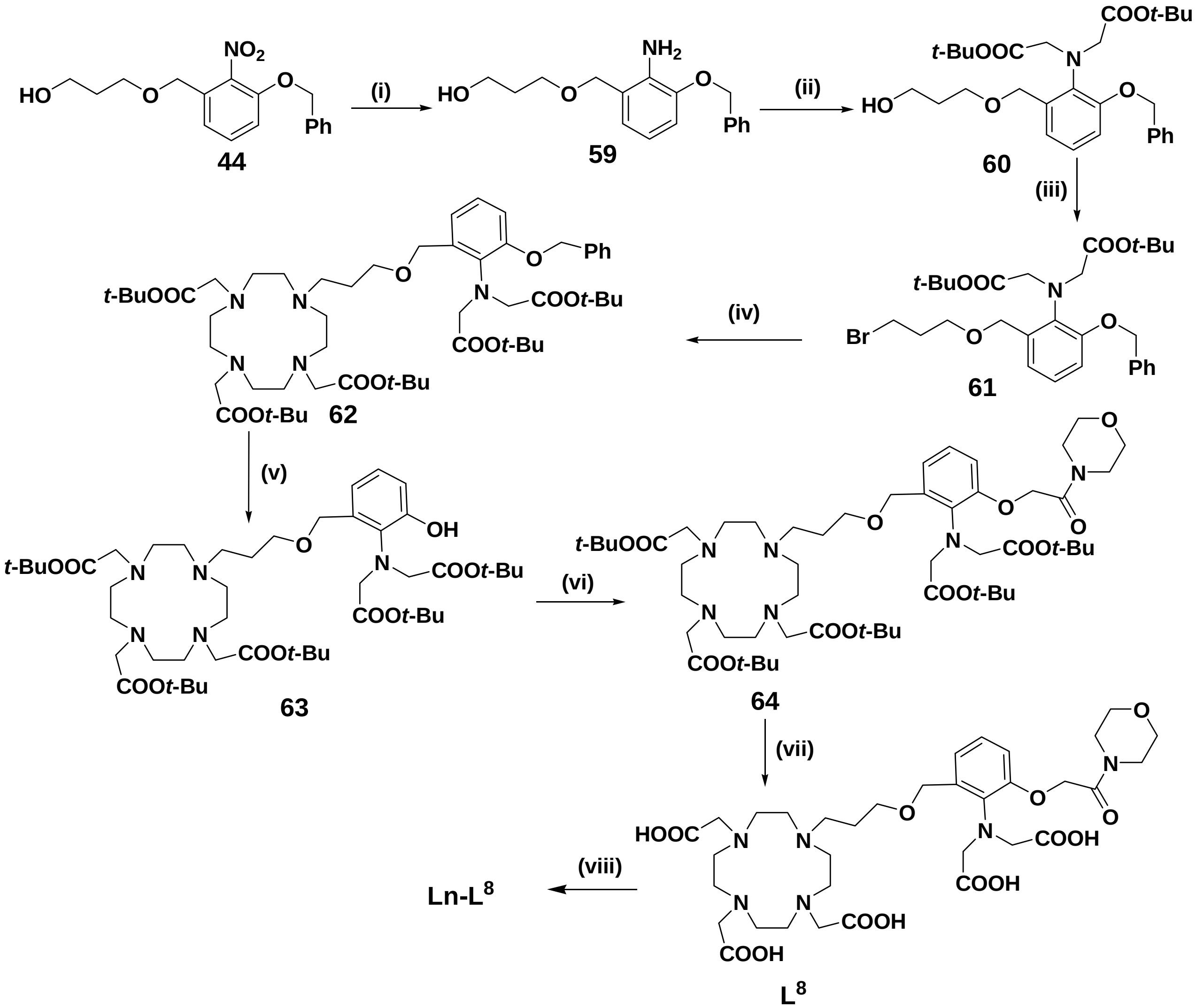

Reagents and conditions: *(i)* iron/acetic acid; 79% *(ii) tert*-butyl bromoacetate/proton sponge/KI/MeCN; 54% *(iii)* $CBr_4/PPh_3/CH_2Cl_2$; 88% *(iv)* tris-*tert*-Bu-DO3A/K_2CO_3/DMF; 55% *(v)* $H_2/Pd(OH)_2$/EtOH; 95% *(vi)* **52**/NaH/THF; 62% *(vii)* CH_2Cl_2/TFA; 65% *(viii)* $LnCl_3$ $6H_2O$

Compound **44** synthesized according to Scheme 19 was used as the starting substrate to obtain **59**. The aromatic 1° amine was refluxed with *tert*-butyl bromoacetate in presence of proton sponge in MeCN conditions for five days to obtain alkylated amine **60**. The 1° alcohol group in **60** was brominated with CBr_4/PPh_3 to **61**. Tris-*tert*-Bu-DO3A was then alkylated with bromide

61 to obtain the macrocyclic **62**. The benzyl group deprotection was then carried out on **62** using $Pd(OH)_2$/EtOH under H_2 (3 atm) for five hours. The phenol **63** obtained was then finally alkylated with **52** using NaH/THF to yield **64**. The hydrolysis of the *tert*-butylester groups in **64** with TFA yielded the ligand $\mathbf{L^8}$, which was purified by RP-HPLC using method C.

9.2.2 Physicochemical characterization

(a) Stability

No side products were formed during loading of Gd^{3+} to the solution of $\mathbf{L^8}$ and the desired complex $\mathbf{Gd\text{-}L^8}$ was obtained in quantitative yields. The $\mathbf{Gd\text{-}L^8}$ was thus found to be very stable toward hydrolysis of the acetate arm.

(b) Relaxometric Ca^{2+} titration in buffer

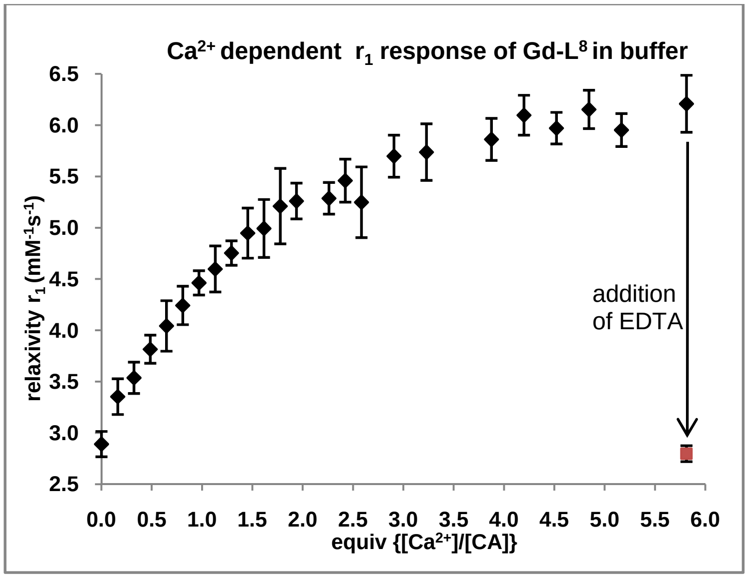

Figure 44: The Ca^{2+} dependent relaxivity response of $\mathbf{Gd\text{-}L^8}$ in KMOPS buffer. The concentration of CA was varied from 1.23 mM to 1.15 mM by the addition of Ca^{2+} solutions. The black *diamonds* corresponds to the stepwise increase in the r_1 by the Ca^{2+} addition while the red *square* corresponds to the relaxivity obtained by the addition of EDTA

The initial relaxivity observed was 2.9 mM^{-1}s^{-1} which is a bit higher than what was observed for **Gd-L^{7}** (2.5 mM^{-1}s^{-1}). The increase in r_1 with stepwise addition of Ca^{2+} was also observed. The response however was found to be different than the previous monomacrocyclic complexes. A comparatively slow increase of relaxivity was observed upon addition of Ca^{2+}. The maximum relaxivity of 6.0 mM^{-1}s^{-1} was attained at ~ 3 equiv of Ca^{2+}, which is a ~100% enhancement The trend of Ca^{2+} titration curve (Figure 44) shows that the complex has different stoichiometry and probably the different Ca^{2+} binding affinity as compared to **Gd-L^{5}** and **Gd-L^{7}**. The slow and decreased response could be because of the morpholino arm being comparatively rigid to flip away from paramagnetic centre to Ca^{2+}.

(c) Relaxometric Ca^{2+} titration in Mg^{2+} containing buffer

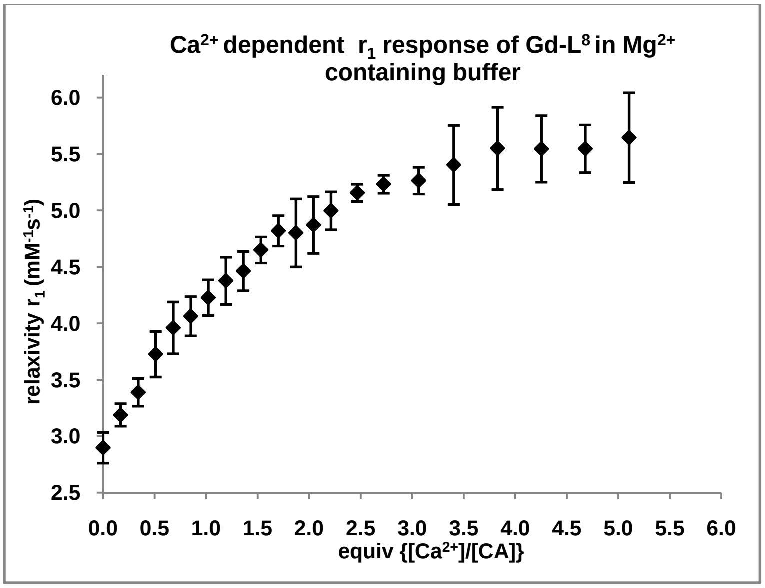

Figure 45: The Ca^{2+} dependent relaxivity response of **Gd-L^{8}** in Mg^{2+} containing buffer. The concentration of CA was varied from 1.17 mM to 1.12 mM with the addition of Ca^{2+} solutions.

The initial relaxivity for **Gd-L^{8}** in Mg^{2+} containing (0.44 equiv) buffer was 2.9 mM^{-1}s^{-1} which is the same as the initial relaxivity observed in buffer. This shows that the added equiv of Mg^{2+} in the buffer has no effect on the relaxivity of **Gd-L^{8}**. In other words, the agent is insensitive till 0.4

equiv of Mg^{2+}. The agent however showed 31% relaxivity enhancement with ~ 0.4 equiv of Ca^{2} (Figure 45). With the further addition of Ca^{2+} to the Mg^{2+} containing CA solution, the relaxivity increased to 5.3 $mM^{-1}s^{-1}$ (78%) at 3 equiv and to 5.5 $mM^{-1}s^{-1}$ (85%) at 4 equiv. This shows that the **Gd-L^{8}** has much better Mg^{2+} rejection/Ca^{2+} selectivity as compared to the agents studied before.

(d) Relaxometric Ca^{2+} titration in ACSF

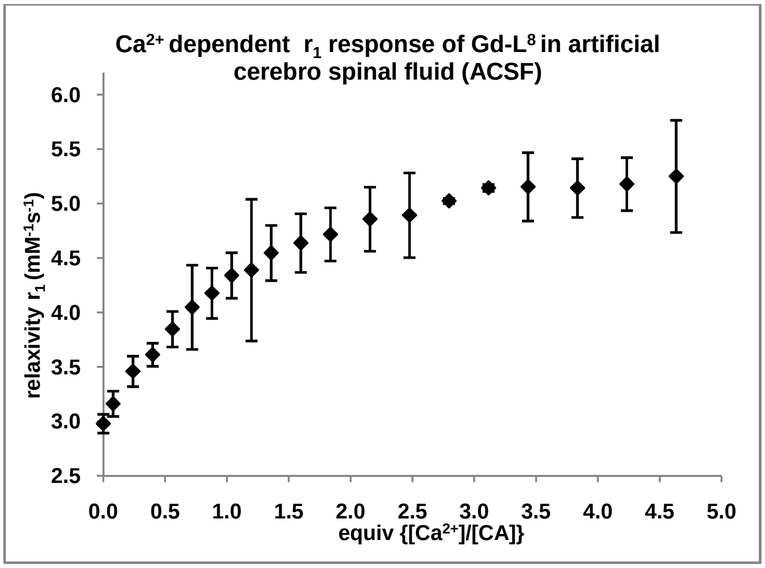

Figure 46: The Ca^{2+} dependent relaxivity response of **Gd-L^{8}** in ACSF. The concentration of CA was varied from 3.7 mM to 3.6 mM by the addition of Ca^{2+} solutions.

The initial relaxivity in ACSF was observed to be almost the same as was found in Mg^{2+} free buffer and 0.4 equiv Mg^{2+} containing buffer. It is important to note that the ACSF solution used for the titration also contains HCO_3^-; no change in the initial relaxivity of the agent in ACSF compared to the buffer shows the inertness of the agent toward bicarbonate anions also. The maximum of 72% r_1 enhancement was observed with saturation at 3 equiv of Ca^{2+} (Figure 46).

(e) Relaxometric Ca^{2+} titration in AECM

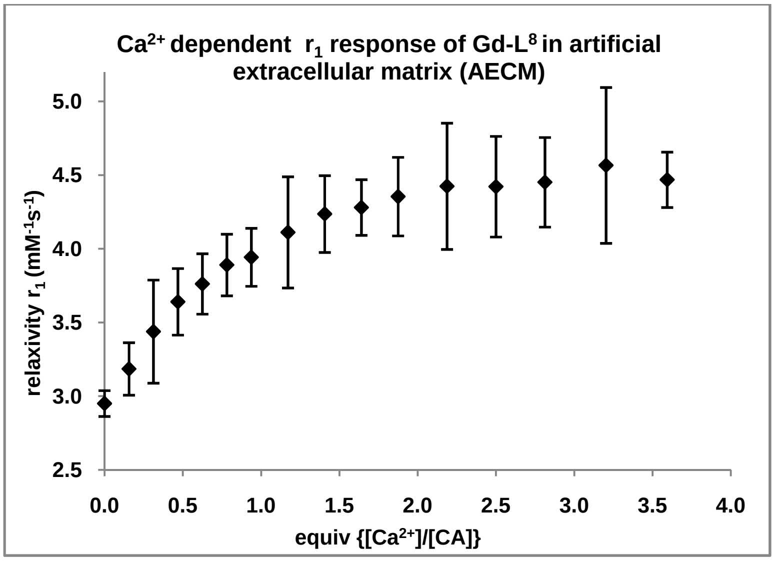

Figure 47: The Ca^{2+} dependent relaxivity response of **Gd-L^8** in ACSF. The concentration of CA was varied from 3.8 mM to 3.7 mM with the addition of Ca^{2+} solutions.

A very similar response was also observed in AECM. The overall enhancement of 50% was observed (Figure 47)

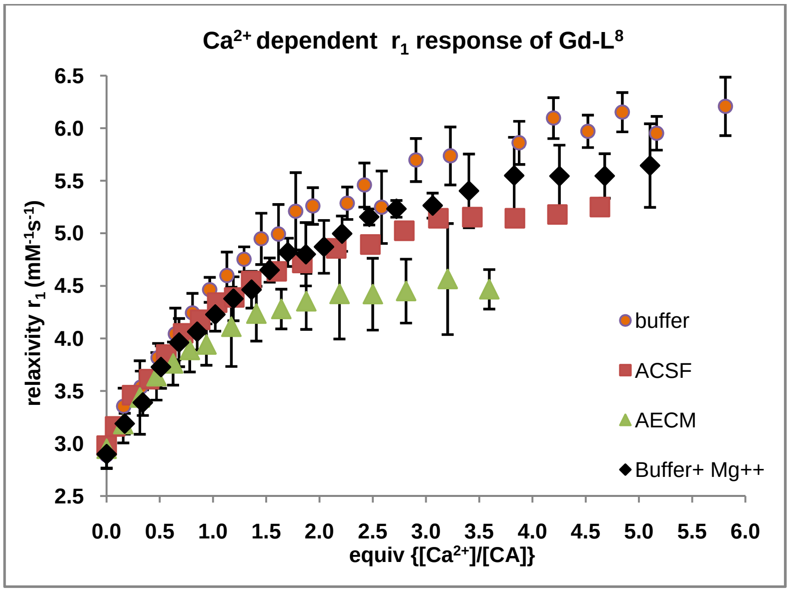

Figure 48: The Ca^{2+} titration curve for **Gd-L^8** tested in all media is collectively shown.

The comparison of the Ca^{2+} dependent relaxivity response of **Gd-L^8** is shown in Figure 65. The initial relaxivity of the agent in buffer, Mg^{2+} containing buffer, ACSF and AECM is observed to be the same. Furthermore the response of the agent till 1 equiv of the Ca^{2+} is also almost the same from simple buffer solution to the complex physiological relevant medium. The Ca^{2+} selective property is thereby improved with **Gd-L^8**.

9.3 Synthesis of Ln-L^9

The synthesis of **Ln-L^9** was done according to Scheme 26. Compound **65** was prepared by Rh(II) catalyzed *O*-alkylation of bromoethanol with ethyldiazoacetate [145]. This was used to do alkylation of **58** to obtain **66**. However the addition of water to quench the reaction basified the medium, due to which the ethylester group in the product formed **66** got partially hydrolyzed. The purification of the product **63** and its acid counterpart was difficult resulting in the loss of yield. The mixture of products obtained after the reaction was then treated with HBr/AcOH under cooling conditions for 4 h resulting in the formation of the final ligand **L^9** which was purified by RP-HPLC using method C. The loading of the ligand was finally done with $LnCl_3$ $6H_2O$ solution.

Scheme 26:

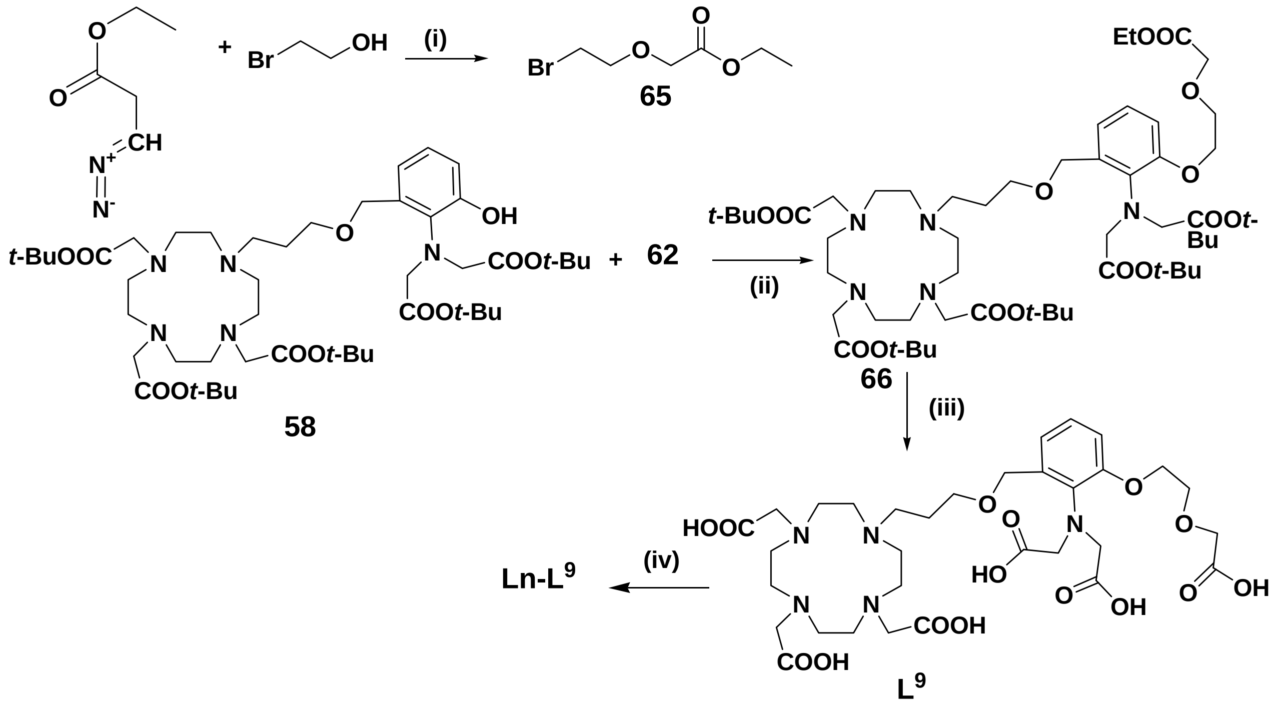

Reagents and conditions: *(i)* $Rh_2(OAc)_4/CH_2Cl_2$; 75% *(ii)* NaH/THF *(iii)* HBr/AcOH; 25% *(iv)* $LnCl_3$ $6H_2O$

9.4 Initial results:

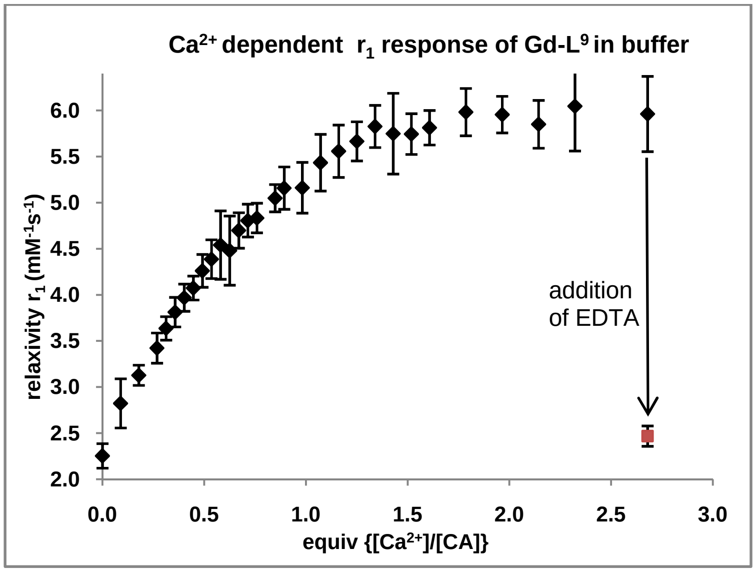

Figure 49: The Ca^{2+} dependent relaxivity response of **Gd-L^9** in KMOPS buffer. The concentration of CA was varied from 1.12 mM to 0.99 mM with the addition of Ca^{2+} solutions. The black *diamonds* points

corresponds to the stepwise increase in the r_1 by the Ca^{2+} addition while the red *square* correspond to the relaxivity obtained by the addition of EDTA

The preliminary Ca^{2+} dependent relaxivity analysis of **Gd-L**^{9} in buffer showed 168% r_1 enhancement with the Ca^{2+} addition. The saturation observed at ~ 2 equiv was 5.9 $mM^{-1}s^{-1}$. The Ca^{2+} relaxivity curve (Figure 49) was found to be similar to **Gd-L**^{7}, showing that unlike **Gd-L**^{8} the flipping of chelating arms in **Gd-L**^{9} at the aromatic units are enough flexible. This agent similar to other analogues synthesized, found to be coordinating reversibly with Ca^{2+}, as observed by restoration of relaxivity on addition of EDTA. The Ca^{2+} selectivity study of the agent in the Mg^{2+} containing buffer and other physiological media is under progress.

9.5 Comparative analysis and Conclusions (Chapter 6)

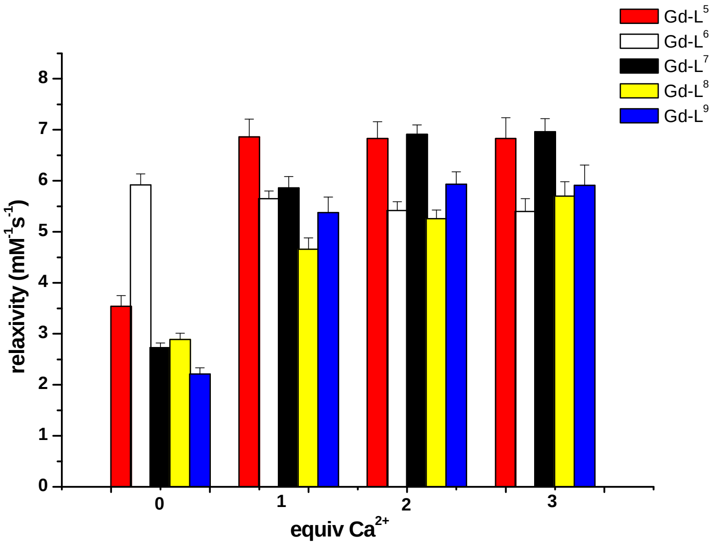

Figure 50: A histogram showing the Ca^{2+} dependent relaxivity response of **Gd-L**$^{5\text{-}9}$ in buffer

In total 9 potential Ca^{2+} sensitive SCAs have been synthesized. Compared to the synthesis of bismacrocycles, the monocyclic CAs were relatively easy to synthesize. The structural modification was also found to be easy to plan and execute. A series of five monomacrocyclic

Ca^{2+} sensitive SCAs (**Ln-L$^{5-9}$**) were synthesized. The first agent of the series **Ln-L^{5}** showed good sensitivity (100%) and selectivity to Ca^{2+}. It was also shown that the change in relaxivity was because of the change in the hydration number of the complex from 0 in absence of Ca^{2+} to 1 in the presence of Ca^{2+} [146]. The instability observed in case of **Ln-L^{5}** urged us to investigate in detail and propose some antidotes. This lead to the synthesis of the stable complex, **Ln-L^{6}**. The stability observed in the case of **Ln-L^{6}** proved the hypothesis proposed for instability of **Ln-L^{5}**. The structural changes incorporated in **Ln-L^{5}** to synthesize **Ln-L^{6}**, however made the system nonresponsive to Ca^{2+}. We then incorporated minor modifications in the structure of **Ln-L^{5}**, to not disturb the Ca^{2+} responsive property of the system but at the same time eliminate the cause of instability. **Ln-L^{7}** was designed by introduction of small structural modification to **Ln-L^{5}**. The complex, **Ln-L^{7}** was found to be not only stable but also showed an enhanced relaxivity response to Ca^{2+} in buffer (157%) as well as in physiological media (90-95%). Taking the stable system of **Ln-L^{7}** as the lead compound we carried out some modifications in the Ca^{2+} chelating part of the structure. Two types of modifications were done: 1) introduction of the morpholino amide moiety at the phenolic oxygen and 2) extension of the phenolic acetate arm with the introduction of the ether linker. The first modification leads to the synthesis of **Ln-L^{8}**. This system was found to be much more selective to Ca^{2+} as compared to others. The increase in relaxivity with the Ca^{2+} (100%) was however at a slower rate, saturating at 3 equiv as compared to 1 equiv in **Ln-L^{5}** and 2 equiv in **Ln-L^{7}**. This could be because of the morpholino arm being not so flexible to flip from paramagnetic centre to Ca^{2+}. The second described modification lead to the synthesis of **Ln-L^{9}.** The initial Ca^{2+} dependent relaxometric titration curve showed that the Ca^{2+} responsive property of the agent is even better than **Ln-L^{7}** (168%), also signifying the flexibility of the chelating arms. The observed stoichiometry of 2 was also similar to **Ln-L^{7}**. The Ca^{2+} selectivity study of this agent however is under progress. The Ca^{2+} dependent relaxivity response of all the agents synthesized in this series is shown in the Figure 50. A detailed physicochemical characterization of these agents is required to assess the parameters mainly affecting the relaxivity change with the Ca^{2+}.

Section C

Project -2

Part A

Development of Magnetic Resonance Guided Anatomical Markers

CHAPTER 7

10. Development of Biocytin based Anatomical Markers

10.1 Introduction

It is believed that the cognitive ability of the human brain involves the synchronous activity of the different regions of the cerebral cortex [93]. For a detailed understanding of the brain function it is important to understand the organization of the neuronal circuit connecting different regions. To chart the anatomical connections between various components of neural network, the neuronal tract tracing technique has been proved to be very useful. The history of neural tracing date back to 19th century when Golgi and Cajal through their pioneer work demonstrated the network of neurons by silver impregnation of individual neurons. Another milestone in the neuroanatomy research came up with the discovery of the plant enzyme horse radish peroxidase (HRP) [147, 148]. The HRP is readily taken up by axons and transported to cell somata (retrograde axonal transport) which allowed tracing neural networks till long distances. A large number of markers have been developed since then, based on their mode of transport i.e. anterograde or retrograde. The anterograde transport involves uptake via cell somata and/or its dendrites and transport to cell synaptic terminal along the axonal microtubular system. In the retrograde transport, the tracer is taken up by axons by endocytosis and is transported back to the cell body [149]. Biotinylated dextran amine, neurobiotin, biocytin, plant lectins and bacterial toxins etc are some of the examples of neural tracer widely used in neuroanatomy research employing neurohistochemical techniques [149].

Another approach of studying the neuronal connectivity is manganese enhanced MRI (MEMRI) [150-153]. Two properties of Mn^{2+} makes it an important neuronal tracer. First is that Mn^{2+} is a paramagnetic metal ion which makes it a potential contrast agent and second is, the transport of Mn^{2+} along neuronal pathway is in anterograde mode. The tracing of neuronal projections is thereby achieved with a plus of contrast enhancement in MRI [154]. The potential of Mn^{2+} to give detailed cytoarchitecture of the brain has also been studied. [155, 156]. The major drawback of Mn^{2+} is its cytotoxicity. Mn^{2+} acts as the biological analogue of Ca^{2+} due to which it can internalize in to the excitable cells via the transport mechanism of Ca^{2+}. It can thus accumulate in the activated brain regions following the neuronal activation. As it is known that the chronic exposure to Mn^{2+} leads to the neurological disorders, use of Mn^{2+} as a tracer for *in vivo* studies could be challenged.

In light of these considerations we aimed at the development of the nontoxic, efficient and multimodal neuronal tracer that can allow the investigation of neuronal networks by tract tracing using MRI and the postmortem microscopic investigations in the same experimental animal.

10.2 Design of the agents

For the designing of desired agents we chose biocytin as the model compound. Biocytin is a naturally occurring conjugate of biotin (Vitamin H) and lysine and acts as the intermediary in biotin metabolism. Biocytin is a well known neuronal tract tracer and has been used extensively to visualize neuronal morphologies and axonal projections by both light and electron microscopic methods. Due to the high affinity of biotin for avidin, the tract tracing of biocytin can be easily visualized by using avidin conjugated with fluorochrome (e.g. Lucifer yellow) or chromogenic enzymes (e.g. Horse radish peroxidase, HRP) [157, 158]. HRP produces permanent and opaque images after reaction with a chromogenic substrate (e.g. diaminobenzidine) and thus can be visualized by light and electron microscopic method [158].

Structurally, biocytin consist of D-biotin and L-lysine connected via an amide bond. This amide bond is susceptible to cleavage by biotinidase enzyme. Biotinidase is the enzyme mainly responsible for recycling of the vitamin biotin by cleaving biocytin and biotinyl peptides [159-161]. Biotinidase plays an important role in the brain function [162, 163]. A deficiency in the biotinidase enzyme has been linked to several neurological disorders [164-166]. The action of biotinidase may thus be responsible for short half life of the neural tracer biocytin *in vivo.* The designing of the agents were therefore done keeping the susceptibility of cleavage by biotinidase in to the account. To have neural tracers with enhanced stability, the amide linkage connecting biotin and lysine was modified. Wilbur and coworkers [167-170] have reported several such modifications which make a biotin containing construct stable to the biotinidase. This involves modification of the amide linkage by either introduction of a substituent α to the amide bond or the substitution directly at the amidic –NH. Similar strategy has been used by Paganelli and coworkers where they reduced the biotinamide bond to simple amine and thus achieved the biotinidase stability [171]. The stability of the system was also tested *in vivo* in humans by nuclear imaging [172].

For *in vivo* stability we introduced a carboxylic unit in α position to the amide bond and for MR detection, Gd-loaded macrocyclic building block was also introduced. A novel DO3A macrocyclic precursor was synthesized bearing an amine group for conjugation to biotin and α carboxyl unit for the enzyme stabilization (Scheme 27). The α carboxyl unit would be utilized to link to lysine, leaving an amide substituent α to the biotin amide bond.

Scheme 27

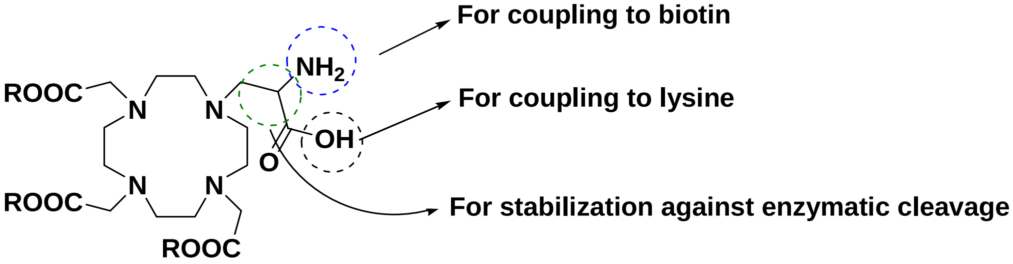

The final structure of the CA according to the above explained construct would be the following:

Scheme 28

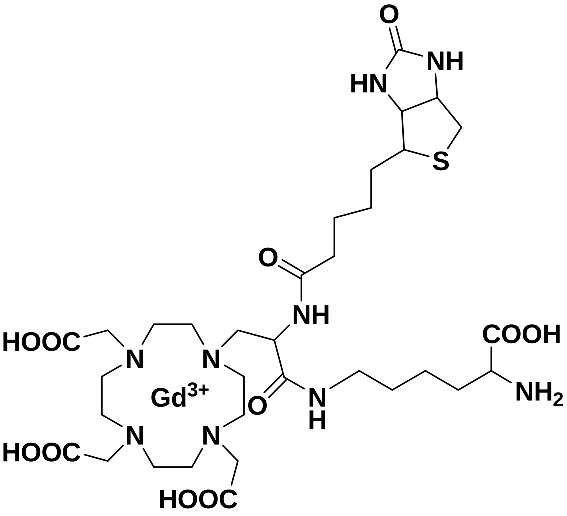

Gd-L^{11}

The potential of this agent as the neural tracer would be tested by MRI and postmortem microscopic techniques. However to understand the effect of such a linkage between biotin and lysine, the molecule without the macrocyclic unit but bearing the same linkage type was synthesized (Scheme 29). The purpose of synthesizing this derivative was to check the stability of this agent under *in vivo* conditions as compared to the conventional biocytin.

Scheme 29

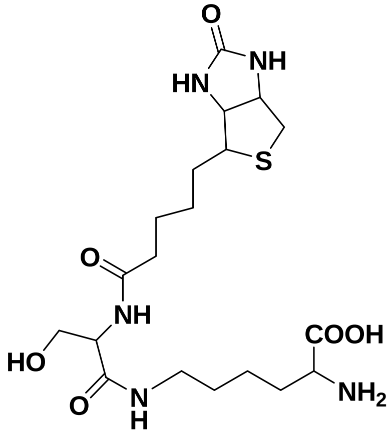

L^{10}

10.3 Results and discussion

10.3.1 Synthesis of the CAs

Synthesis of **L^{10}** was carried out according to the Scheme 30. The primary alcoholic group in L-serine methyl ester was protected with TBDMS group to give **67**. The hydrolysis of methylester in **67** was carried out with LiOH as base to obtain acid **68**. The lysine precursor was synthesized from Boc-Lys-(Z)-OH by first esterifying the acid group with DCC/MeOH to get **69** and then removing the Cbz protecting group to get amine **70** [145]. The amine **70** was coupled to the acid **68** via amide bond using EDC/HOBt/NMM as the coupling reagents to obtain the product **71**. The TBDMS group in **71** was then removed with TBAF to get the alcohol **72**. The primary alcohol group was then reprotected with *iso*-butyl chloroformate to give **73**. The CBz group in **73** was removed using Pd-C as the catalyst and 3 atm H_2 pressure in a Parr apparatus to obtain the amine **74**. The acid group in the biotin was then coupled to the amine **74** via amide bond to give **75**. The methylester in **75** was then hydrolysed under basic conditions followed by TFA treatment to remove Boc group and the *iso*-butyl carbonate group to give the final product **L^{10}**.

The deprotection of TBDMS group in **71** and then reprotection by *iso*-Butyl chloroformate to get **73** was carried out because removal of TBDMS at the last stage with TBAF gives the product with some impurities from TBAF reagent. The impurities and the final product both being soluble in water, the purification of the product was difficult. To avoid the extra protection and deprotection step, we started with protection of the alcohol group on L-serine methyl ester with *iso*-butyl chloroformate. However, in the next step the hydrolysis of methyl ester with LiOH removed the *iso*-butyl carbonate group because of its instability to the acid formed after hydrolysis of ester in the molecule. The synthesis was finally performed successfully according to the Scheme 30.

Scheme 30

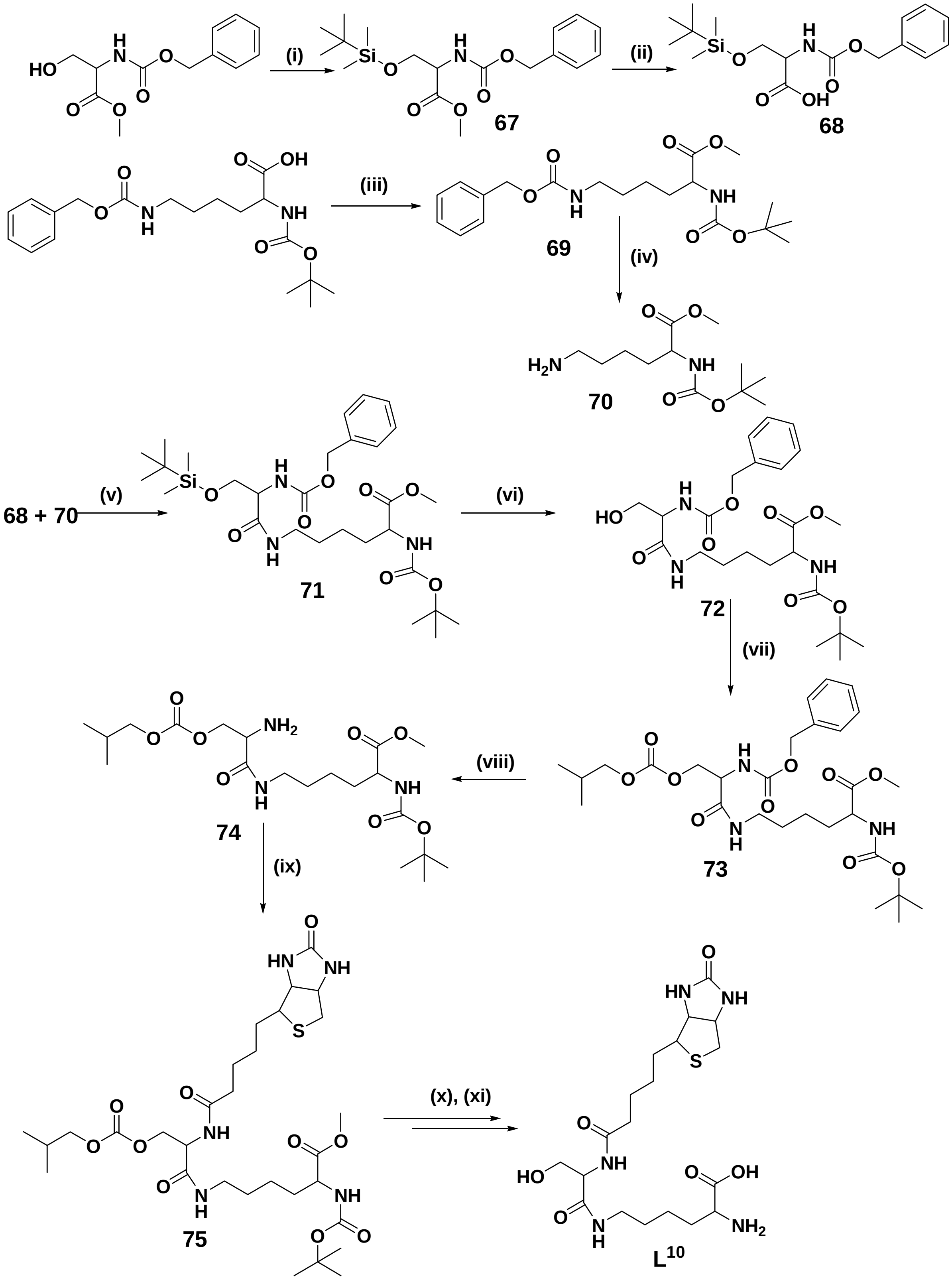

Reagents and conditions: *(i)* TBDMS-Cl/imidazole/DMF; 92% *(ii)* LiOH/THF:MeOH:H_2O (3:2:2) *(iii)* MeOH/DCC/CH_2Cl_2; 95% *(iv)* H_2/Pd-C/MeOH; quant. *(v)* EDC/NMM/HOBt/DMF; 40% *(vi)* TBAF/THF; 80% *(vii)* *i*-Bu-chloroformate/Pyridine/CH_2Cl_2; 60% *(viii)* H_2/Pd-C/MeOH; quant *(ix)* HATU/DIPEA/DMF *(x)* LiOH/MeOH:THF:H_2O (3:2:2) *(xi)* TFA/CH_2Cl_2; 25%

For the synthesis of **Gd-L^{11}**, Scheme 31 was formulated. N-carbobenzyloxy-L-serine methyl ester was brominated with CBr_4 and PPh_3 to **76**. The bromination reaction was run for not more than 30 min else the brominated product undergoes elimination yielding the allyl analogue of the product. The crude product obtained after extraction with water was immediately flash chromatographed to obtain the product. The alkylation reaction of **76** with macrocyclic was first carried out with trsi-*tert*-Bu-DO3A under basic conditions with no product formation. The alkylation was thus performed on cyclen without added base yielding the monosubstituted product **77**. The formation of product was confirmed by ESI-MS, however due to high polarity of the product and reactant no purification was performed to separate the product **77** from excess of cyclen. The crude product obtained was subjected to further alkylation by *tert*-butyl bromoacetate. The purification was then performed to get the product **78** with small amount of tetra-*tert*-Bu-DOTA. The methylester group in **78** was hydrolyzed with LiOH to obtain the product **79**. The execution of the rest part of the scheme to get the final ligand **Gd-L^{11}** is under progress.

Scheme 31

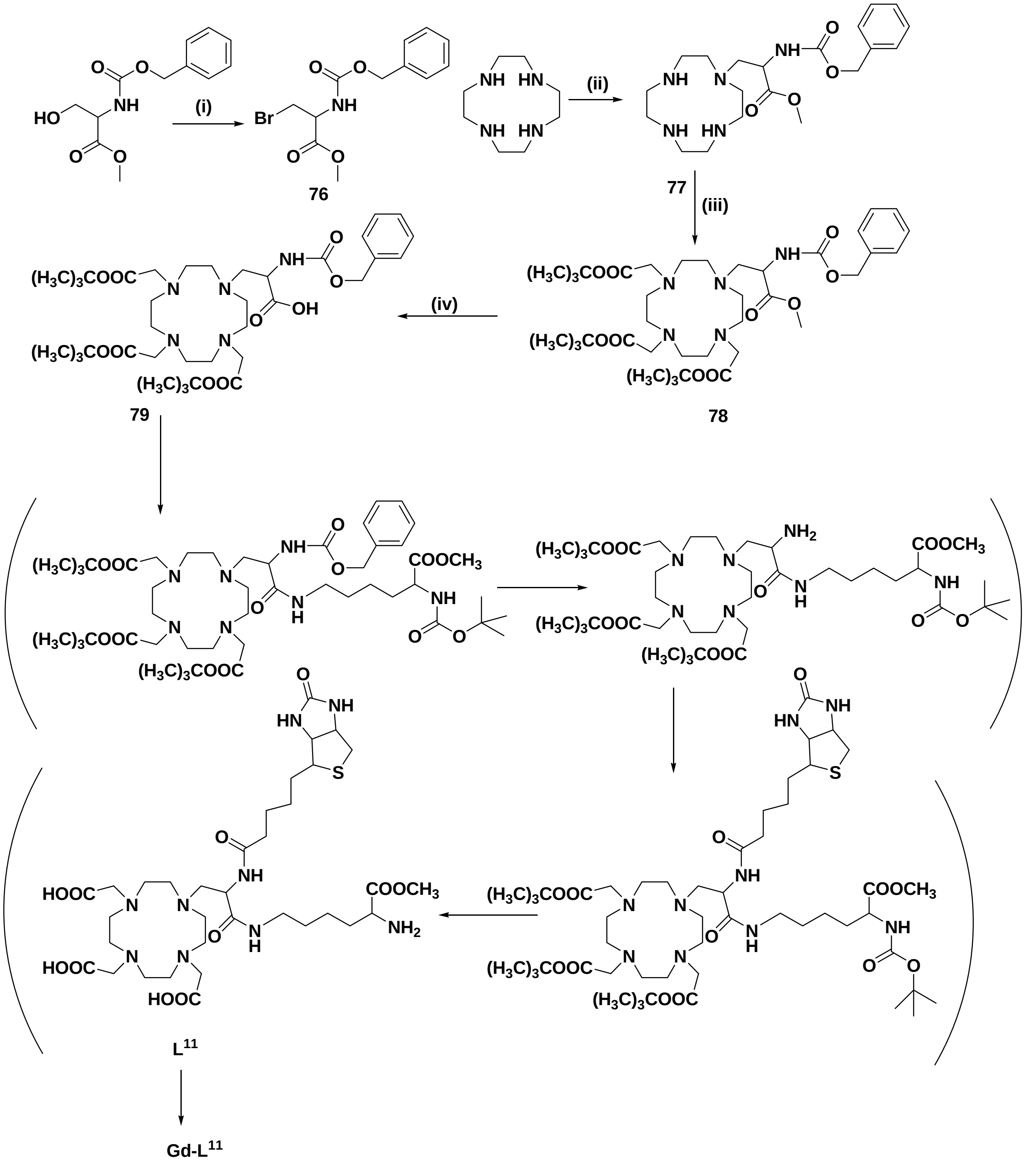

Reagents and conditions: *(i)* NBS/PPh_3/DMF; 84% *(ii)* **76**/Toluene *(iii)* tert-butyl bromoacetate/Na_2CO_3/MeCN; 72% *(iv)* LiOH/THF:MeOH:H_2O (3:2:2)

10.3.2 Investigations of L^{10} as the neural tracer

In order to investigate the uptake and transport ability of the tracer and thereby its comparison with normal biocytin, a series of experiments were carried out. *In vivo* injections of the commercially available biocytin and the synthesized $\mathbf{L^{10}}$ derivative in the rat brain were performed. Iontophoretic injections were done bilaterally to the primary mortor cortex (right and left hemisphere) of rats. Perfusions were then carried out after the survival time of 24 h and 96 h. The uptake and transport of the tracer in the neurons was examined by histochemical treatment of the brain slices (The details of injections, perfusion and histochemical procedures are given in the Section D).

The tracer $\mathbf{L^{10}}$ showed an efficient neuronal uptake and transport as well. The histochemically processed brain slices are shown in Figures 51-54. Figure 51 shows the neuronal uptake of the tracers after 24 h of injection. The region shown is the injection site. On the left is the synthesized tracer $\mathbf{L^{10}}$ while on right is the conventional biocytin.

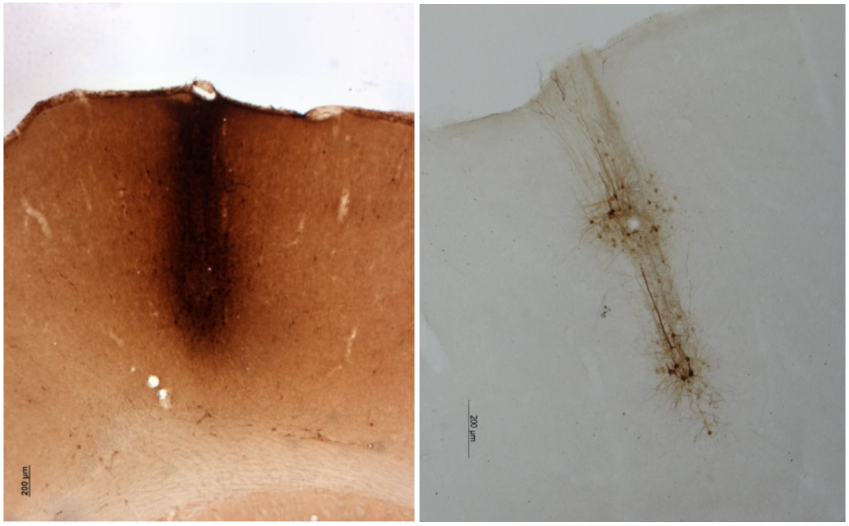

(a) **(b)**

Figure 51: Injection site after 24 h survival time (a) $\mathbf{L^{10}}$ (b) Biocytin

The figure showed that the amount of **L**^{10} retained in the injection site is higher than the biocytin. The instability of biocytin to the endogeneous biotinidase enzyme activity degrades it rapidly, while the high retention of **L**^{10} indicates that it is resistant to the cleavage action of the enzyme. The stability of the synthesized derivative **L**^{10} is also clearly visible in the Figure 52 where the injection site after 96 h of survival time is shown. The biocytin was almost completely washed out (Figure 52b) while staining from **L**^{10} was clearly visible (Figure 52a).

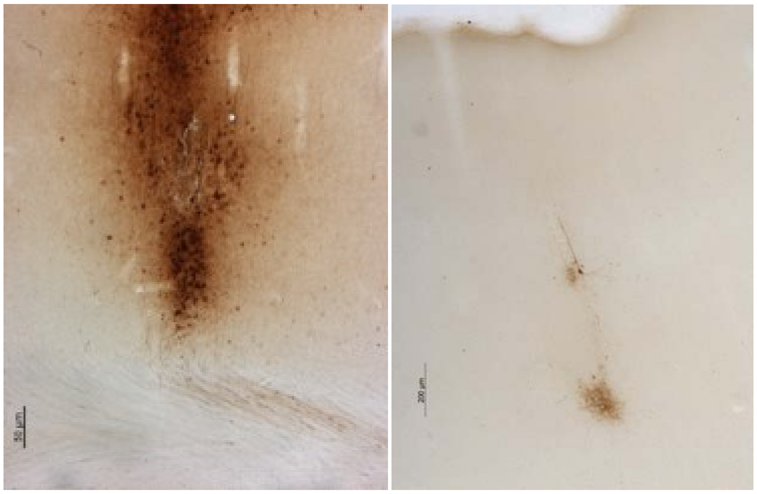

(a) **(b)**

Figure 52: Injection site after 96 h survival time (a) **L**^{10} (b) Biocytin

Beside the high stability, the tracer **L**^{10} also showed an efficient transport, most probably via both modes: retrograde and anterograde. Figure 53a showed the patch of stained cells and fibres located 4 mm latero-posteriorly to the injection site while the Figure 53b showed the stained axonal bundles running through the striatum.

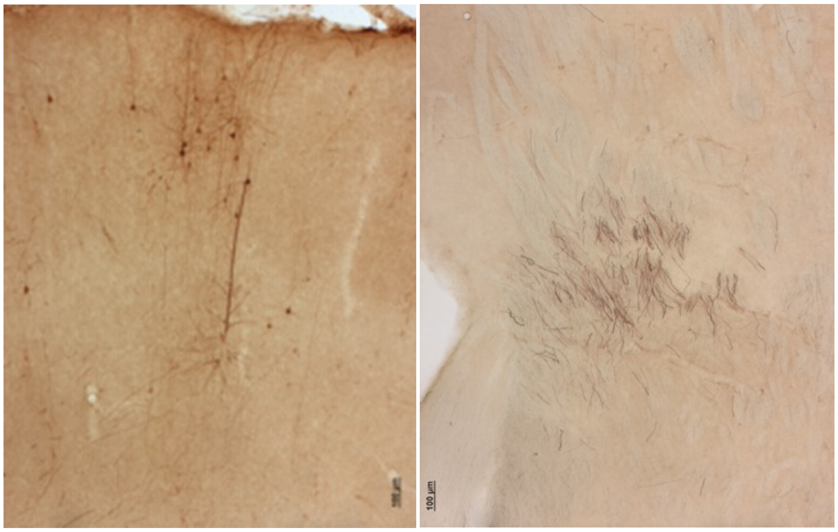

(a) **(b)**

Figure 53: (a) Stained cells and fibres at 4 mm from injection site (b) Axonal bundles running through striatum

Axonal ramification and some cell bodies in the thalamus were also got traced by the tracer $\mathbf{L}^{10}$ (Figure 54a). Figure 54b showed that the fibres in gray matter of the contralateral hemisphere got traced as well.

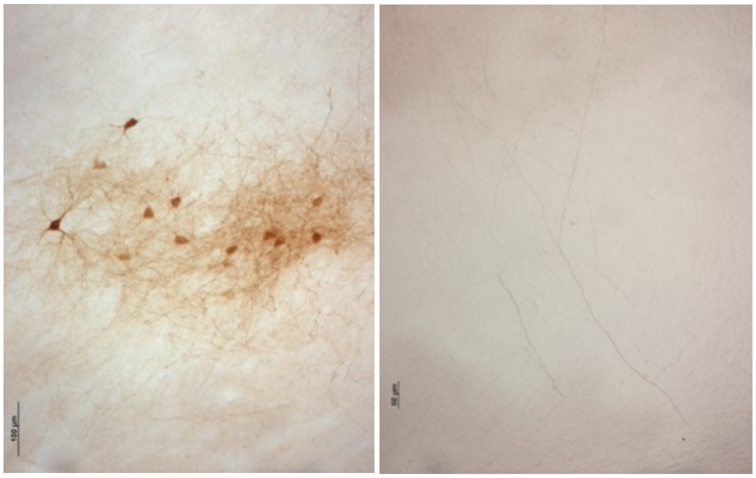

Figure 54: (a) Axonal ramification (b) Fibres in gray matter of contralateral hemishere

10.4 Conclusions

With our interest of tracing the neuronal networks in the brain with MRI and postmortem microscopic techniques in the same experimental animal, we proposed **Gd-L^{11}** as the potential agent. The agent was designed to be MR detectable and at the same time be able to transported anterogradely and/or retrogradely in the neurons. The structure of **Gd-L^{11}** would allow us to assess its uptake and transport ability by commonly used histochemical procedures. The linking of biotin and lysine moieties in **Gd-L^{11}** was done in a way to be resistant to cleavage by the action of biotinidase enzyme present in the brain. The complete synthesis of the **Gd-L^{11}** is under progress, we meanwhile investigated the effect of the linkage connecting biotin and lysine in **Gd-L^{11}** inducing the stability of the whole construct against biotinidase. For this purpose **L^{10}**.was proposed consisting of the similar linkage but without the macrocyclic unit. The *in vivo* experiments performed on the synthesized derivative (**L^{10}**) of biocytin proved that it is indeed a more stable derivative. The cells at the injection site were found to be retained with **L^{10}** even after 4 days of injection while biocytin appeared to be nearly washed out. The staining of the cells was also obtained in the thalamus, striatum, and the gray matter of the contralateral hemisphere, which demonstrated that it is efficiently transported along the neurons.

The structural modification done on biocytin to obtain **L^{10}** is the similar in **Gd-L^{11}** therefore **Gd-L^{11}** is also expected to show similar behavior. The neuronal tract tracing by such a MR detectable tracer would help us to understand in detail the neuronal networks in the brain.

The synthesis of **Gd-L^{11}** and the assessment of its tracing abilities by MRI followed by histochemical examinations is under progress.

Section C

Project -2

Part B

Development of Magnetic Resonance Guided Targeted Markers

CHAPTER 8

11. Development of Biotin based Targeted Markers

11.1 Introduction

The macrocyclic precursor **78** synthesized to obtain the neural tracer **Gd-L^{11}** was explored for its other possible applications [173]. This precursor consists of a carboxylic acid as the methyl ester and a primary amine protected as carbamate. These groups can be deprotected selectively and coupled to two different agents yielding bifunctional CA. The agents could be any functional organic molecule having an ability to seek and target some biological factor. The target can be any receptor such as folate receptor or vascular endothelial growth factor receptors (which are overexpressing in the tumors) or any enzyme such as β-galactocidase (which is used as marker gene for gene expression). The presence of a Gd loaded moiety would also allow the visualization of these molecular targets by MR.

The visualization of molecular targets by MR however can be limited by the low sensitivity of this imaging modality and the other biological constraints such as less accessibility and lower number of receptors. This limitation can be overcome either by using the CA having high relaxivity or by allowing high payload of the CA per target molecule or by using mAb to selectively accumulate CA to the target. To increase relaxivity, a larger complex such as dendrimer particles and liposomes with multiple sites for CA coupling are used. The huge size (300-350 nm) of such constructs however restricts their delivery and diffusion in tissue. The direct coupling of a low molecular weight CA to mAb is also not advantageous because only a limited number of functional groups are usually available for coupling to monolclonal antibody (mAb).

The multistep targeting using biotin/avidin amplification strategy has been proved to be very efficient. This technique was introduced more than a decade ago and has been used widely in nuclear medicine. The approach is primarily based on the very high affinity of biotin to the tetrameric avidin ($K_a \sim 1x10^{15}$ M^{-1}) [174] while the selectivity to the target is achieved by using mAb. In a typical multi step targeting approach, a biotinylated mAb is used as the first injectale followed by introduction of avidin. The radioloabeled biotin is injected at the last stage. The multistep approach allows washing out of unspecifically bound mAb before the radioactive probe is injected, thereby minimizing the exposure of radioactivity to normal organs. The use of similar system for MRI was reported by Bhujwalla and coworkers (2003), where Her-2/*neu* receptors overexpressing in breast tumor were targeted. Gd-DTPA conjugated with avidin was used as the MR detectable moiety in the multistep targeting approach [175]. The contrast enhancement was observed to be rapidly decreased to baseline at the early time points. Further reports in the same year came up with demonstrating the use of nanoparticle as the MR active moiety in targeting $\alpha_v\beta_3$ integrin [176] and Her-2/*neu* receptors [177]. The large size of nanoparticles however limits the extravasations of CA in to the solid tumor interstitium. Recently Bhujwalla and coworkers reported PAMAM dendrimer based CA for targeting Her-2/*neu* receptors, however the agent did not show any binding and thus no contrast enhancement was observed [178].

11.2 Design of the contrast agents

In the light of above discussed examples from the literature, the intermediate **78** was explored for its possible applications in targeting specific receptor type, cell type or protein. Considering the low sensitivity problems of MR, we chose to exploit the amplification strategy of biotin/avidin system and conjugate **78** with biotin. The coupling of **78** with biotin would yield a low molecular weight chelator system which should not suffer with problems associated with large size of nanoparticles or PAMAM dendrimers. Furthermore, as discussed in the Section 10.2, the presence of α carboxylate substituent to the biotinamide bond would make the molecule resistant to cleavage action of biotinidase enzyme. This characteristic might ensure the longer half life of the agent and thus would not suffer with fast wash out problems. The thermodynamically more stable macrocyclic chelate (i.e. Gd-DO3A as compared to Gd-DTPA) would also be beneficial regarding their stability toward release of Gd^{3+} from the chelate *in vivo*. The final structure of the agent with biotin conjugated to the intermediate **78** would be following

Scheme 32

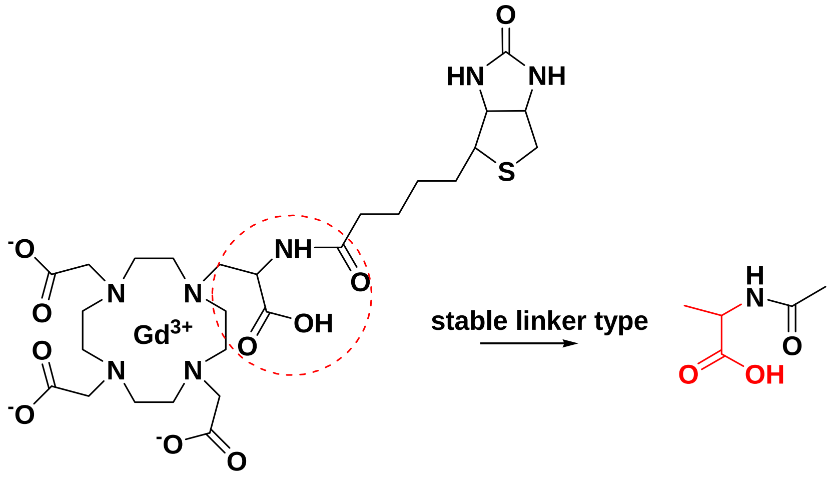

Gd-L^{12}

We also designed another derivative bearing all the discussed characteristic of **Gd-L^{12}** but differing in the flexibility of the linker connecting biotin to the macrocyclic moiety. The biotinidase stability was introduced by substituting the amidic –NH with methyl group. This modification has also been reported to be stable to biotinidase cleaving action [168]. The structure of the molecule is shown in Scheme 33.

Scheme 33

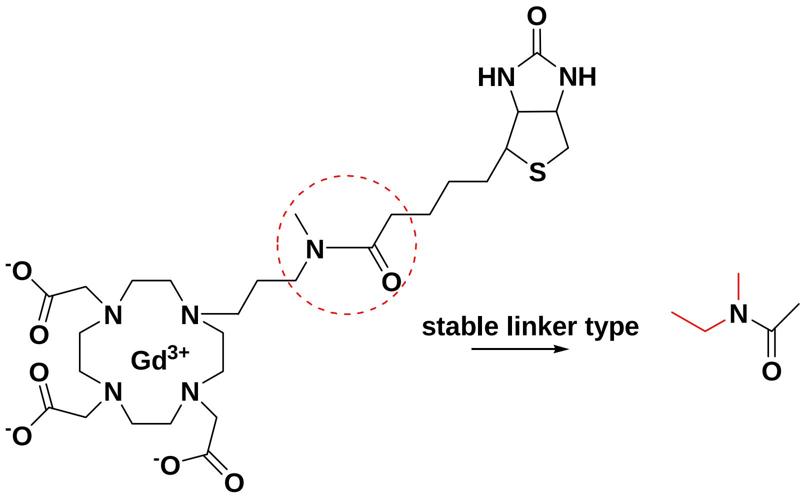

Gd-L^{13}

11.3 Results and discussion

11.3.1 Synthesis

The complex **Gd-L^{12}** was synthesized from the intermediate **79** which was subjected to Pd-C cataluzed hydrogenation to obtain **80**. The precursor **80** was then coupled to D-Biotin by EDC/HOBt supported amidation. The global deprotection of **81** and purification by RP-HPLC yielded the ligand **L^{12}** in moderate yield. This ligand was then complexed with Gd^{3+} in water, to give the final contrast agent, **Gd-L^{12}**.

The complex, **Gd-L^{13}** was synthesized in six steps (Scheme 35). The secondary amine group in N-methyl bromopropanol was protected as carbamate using carbobenzyloxy chloride to give **82**. The alcohol group in **82** was brominated to **83.** This was then used to alkylate tris-*tert*-butyl-DO3A to yield **84.** Removal of N-carbobenzyloxy group by Pd-C catalysed hydrogenation gave

85, the global deprotection of which gave **L^{13}.** The final ligand, **L^{13}** was purified by RP-HPLC and then complexed with Gd^{3+} to give the final contrast agent, **Gd-L^{13}**.

Scheme 34

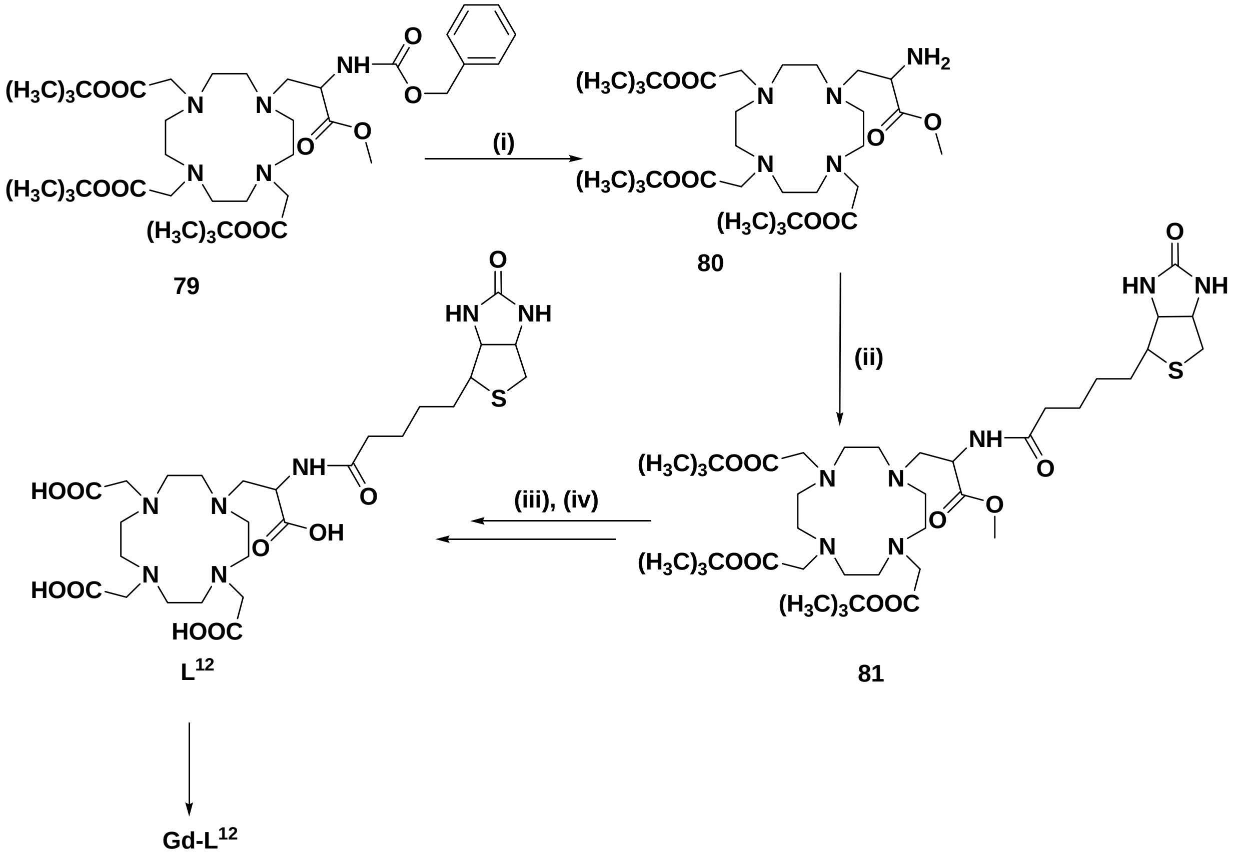

Reagents and conditions: *(i)* H_2/Pd-C/MeOH; 85% *(ii)* Biotin/EDC/HOBt/NMM/DMF *(iii)* LiOH/MeOH:THF:H_2O (3:2:2) *(iv)* TFA/CH_2Cl_2; 40% *(v)* $GdCl_3{\cdot}6H_2O$

Scheme 35

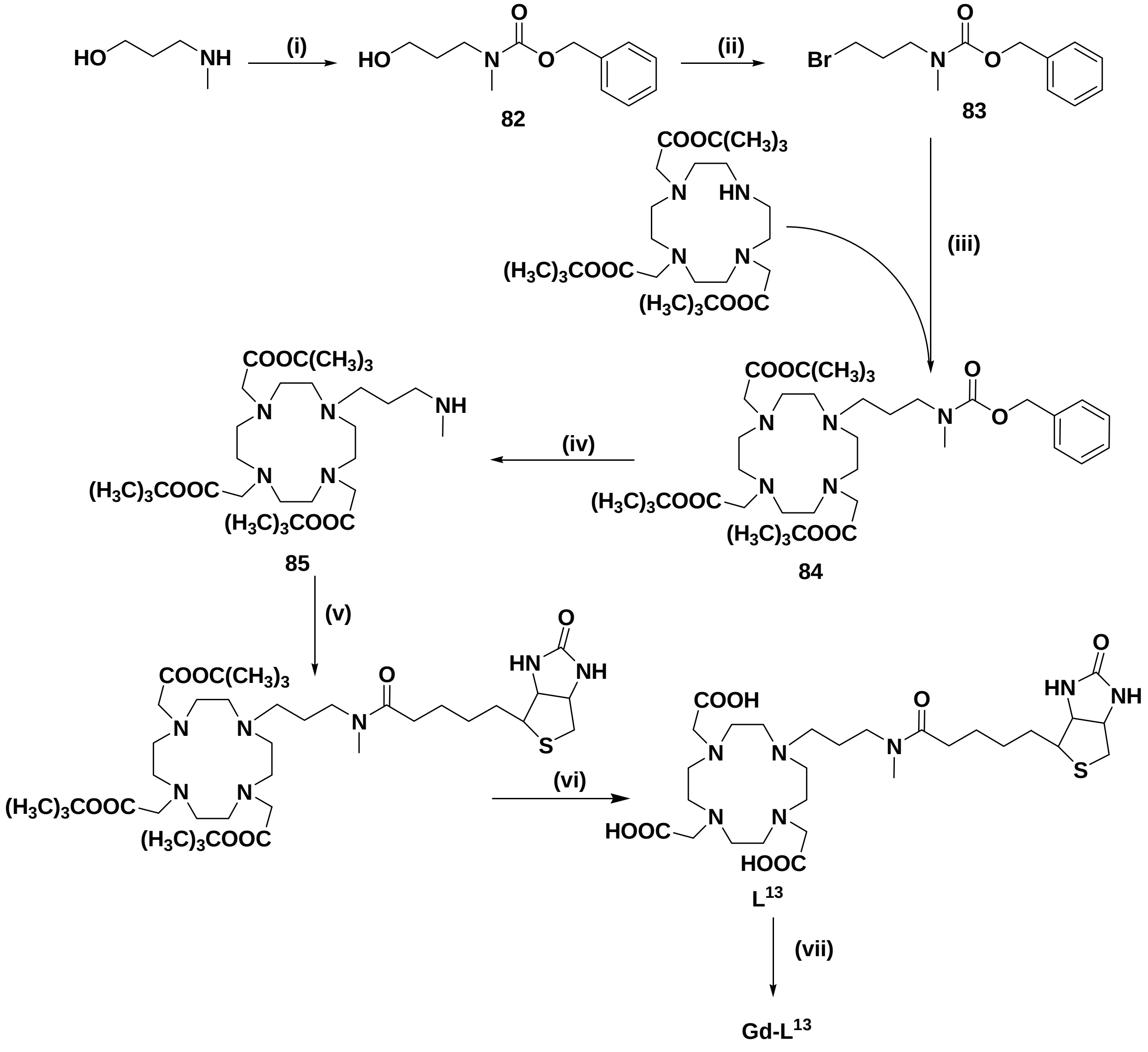

Reagents and conditions: *(i)* CBz-Cl/KOH/dioxane:H_2O; 82% *(ii)* $CBr_4/PPh_3/CH_2Cl_2$; 80% *(iii)* K_2CO_3/MeCN; 55% *(iv)* H_2/ Pd-C/MeOH; quant. *(v)* Biotin/PyBrop/DIEA/CH_2Cl_2 *(vi)* TFA (neat); 50% *(vii)* $GdCl_3{\cdot}6H_2O$

11.3.2 *In vitro* relaxivity measurement with Avidin

The *in vitro* relaxivity measurement on **Gd-L^{12}** and **Gd-L^{13}** was performed on 16.4 T, 9 T, 7 T, 3 T, and 1.5 T animal MR scanners. The T_1/T_2 values of the CAs solutions were measured in absence and in presence of avidin and the % of increase/decrease were measured from the initial value to the value corresponding to the saturation. For comparison of different systems % was calculated considering the measured initial value and the value at the ratio of 0.3 equiv (avidin/CA).

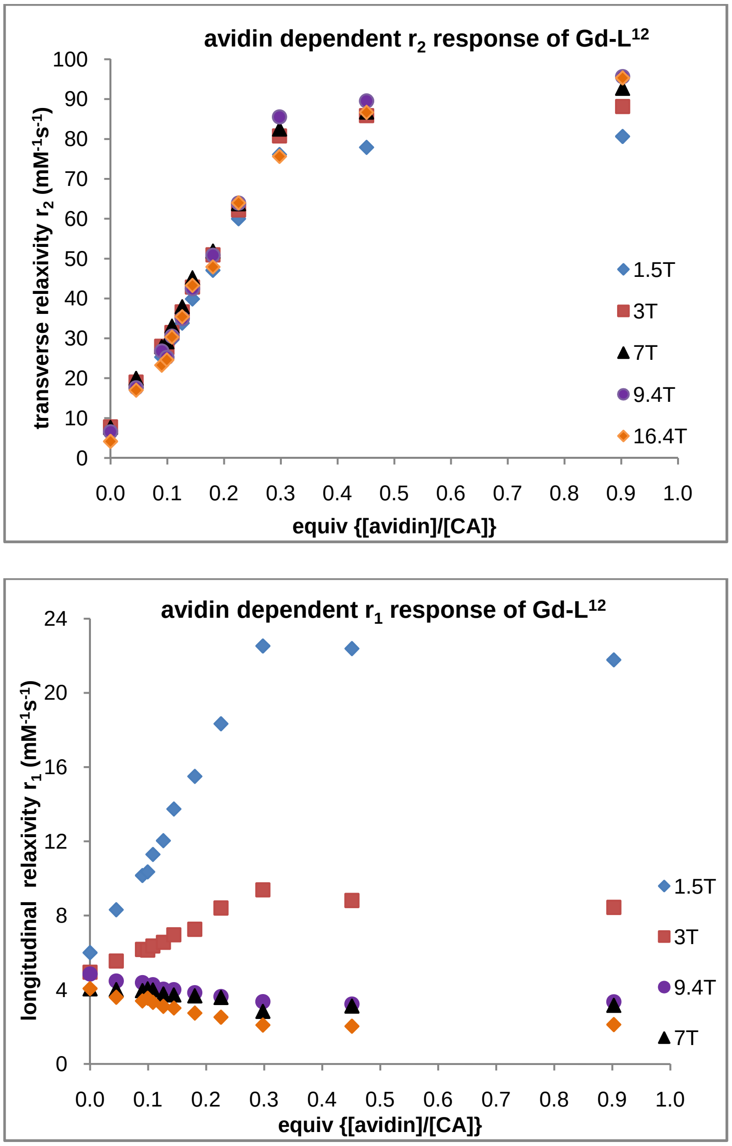

Figure 55: The changes in r_1/r_2 of **Gd-L^{12}** by the addition of avidin.

At 7 T, the longitudinal relaxivity (r_1) of **Gd-L^{12}** in absence of avidin was observed to be 4.0 mM^{-1}s^{-1}. The r_1 showed a decreasing trend with addition of avidin to the CA solution. The r_1 at the saturation state was ~ 2.8 $mM^{-1}s^{-1}$, which is a 45% decrease. The saturation was observed at the ratio 0.3 (avidin:CA), which corresponds to approximately four molecule of CA to one molecule of avidin. This is in agreement with the tetrameric nature of avidin binding to four molecules of biotin. This shows that the CA has a good fit to the binding sites without much of steric hindrance imposed. However, a decrease is in contrary to a usual increase observed for such a low molecular weight complex when they bind to a big macromolecule e.g. protein avidin. The transverse relaxivity (r_2) of **Gd-L^{12}** at 7 T in absence of avidin was 7.7 $mM^{-1}s^{-1}$. The r_2, unlike r_1 showed a usual increasing trend till ~ 82 $mM^{-1}s^{-1}$. This corresponds to a marked increase of 970%.

An increasing behaviour of r_1 with binding to a big macromolecule has been described in the literature as the receptor induced magnetisation enhancement (RIME) [179]. The binding to the macromolecules decreases the molecular rotation of the complex, resulting in an increase in r_1 through the rotational correlation time. The same is applicable to r_2 as well, however the parameters affect r_2 and r_1 differently. The effect on r_2 due to slow down of rotational correlation has been explained by Caravan and co-workers [180]. In that report different Ln^{3+}analogues of the agent were prepared and number of experiments was performed based on the properties of Ln^{3+} used. The rotational correlation and water-exchange rate was determined and the relation of these to the relaxivity enhancement was proposed. It was concluded that the increase in r_2 is mainly due to decreased rotational correlation time which alters the water exchange rate at the metal ion.

A large increase in r_2 observed for **Gd-L^{12}** at 7 T did verify this finding. However, the decrease in r_1 at the same time was not explainable. The literature reported increasing trend of r_1 was reported at low magnetic fields (0.5 T), we therefore measured the same tubes at different magnetic fields. An interesting decreasing to increasing trend was observed from high magnetic field (16.4 T) to low magnetic field (1.5 T). At 16.4 T, a decrease of 93% was observed in r_1 which reduced to 47% decrease at 9.4 T. This trend was continued at 7 T with 45% decrease.

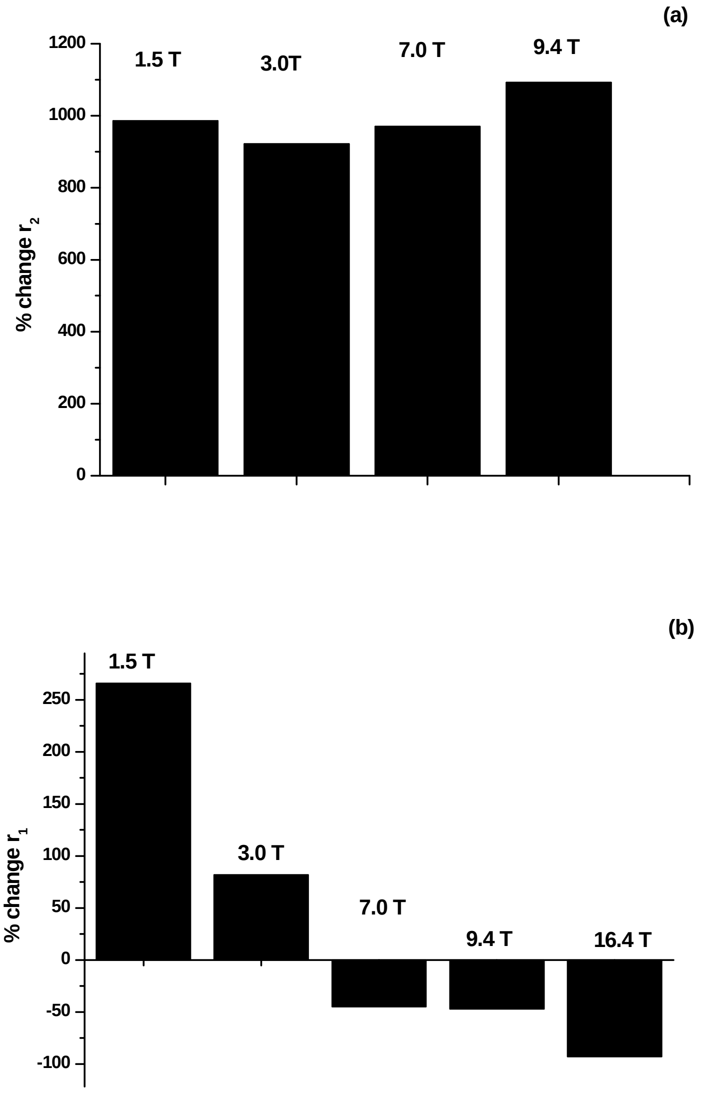

Figure 56: % change in r_1/r_2 at different magnetic field.

However lowering the magnetic field further inverted the trend, with an increase of 82% at 3T and 267% at 1.5 T (Figure 56b). The r_2 however showed an increasing trend at all magnetic fields with the % change ~ 1000% at all magnetic field. The pattern of the increase/decrease at different magnetic fields is shown in the Figure 55. Where the final value at 0.3 equiv was taken and % was calculated according to the initial value obtained. The Figure 56 shows the relaxivity response at all ratios of avidin/CA with varying magnetic fields.

At lower magnetic field of 1.5 T, r_1 and r_2 both showed an increasing trend with r_1 increasing to 266% while r_2 increasing to 980%. This behaviour could be an advantage because a single agent has the potential to act as the T_1 agent (with positive contrast) and T_2 agent (with negative contrast) at a magnetic field which is most widely used at the clinics.

The behaviour of **Gd-L**^{13} was also investigated at different magnetic fields. A similar decreasing to increasing trend was observed from higher magnetic field to lower magnetic field. The % decrease at 16.4 T was however much more than with **Gd-L**^{12}. A decrease of 343% was observed at 16.4 T which reduced to 155% at 9.4 T and 7T and a minimal decrease of 23% at 3T. Further reduction of magnetic field inverted the decreasing trend to increasing one, with 41% increase. The pattern of the increase/decrease at different magnetic fields is shown in the Figure 57.

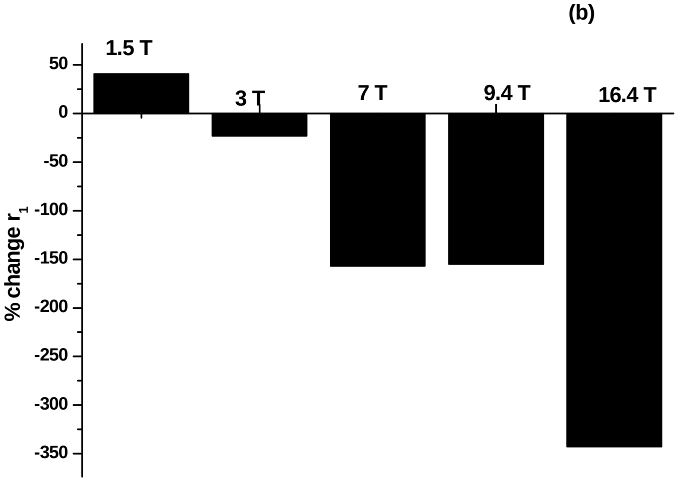

Figure 57: % change in r_1 for **Gd-L**^{13} at different magnetic fields

The response of r_2 was however could not be checked at all magnetic fields and is under progress. The measurement done at 7 T is shown in the Figure 58.

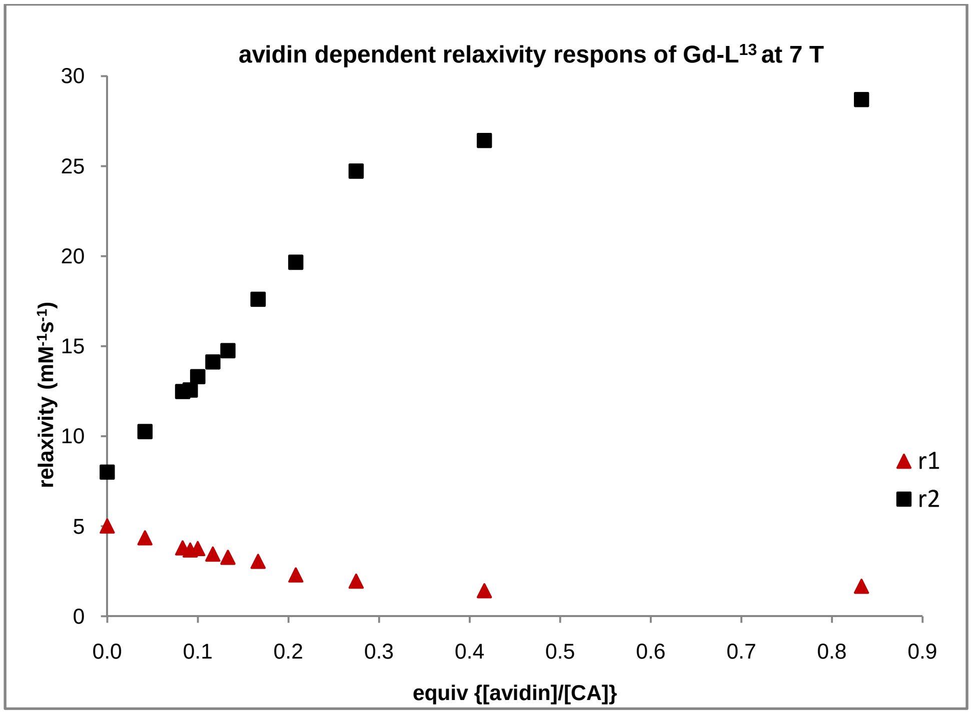

Figure 58: The change in r_1/r_2 of Gd-L^{13} by the addition of avidin

The complex **Gd-L^{13}** however does not show a huge increase in r_2 (212%) as was observed in the case of **Gd-L^{12}** (970%) at 7 T, although in both cases the saturation was observed at ~ 3 equiv of avidin/CA ratio. This shows that the stereochemical requirement of fitting of biotin molecule in the avidin pockets was met in both the cases. The low relaxivity response in the case of **Gd-L^{13}** can be explained on the basis of difference in their structures which would result in different conformation of avidin:CA complex. As was reported in the study done by Caravan and co-workers, the increase in relaxivity is due to decrease in rotational correlation time which alters the water-exchange rate. The increase in relaxivity however, could be limited if the final conformation also allows fast internal motion around the metal ion. A fast internal motion could be possible with a longer and flexible linker as in the case of **Gd-L^{13}**. The **Gd-L^{12}** on the other hand has a short linker and thus the internal motion around the metal ion would be restricted due to the closeness to avidin. Thus, it could be concluded that the stereochemical requirement of the binding of **Gd-L^{12}** and avidin is well matched resulting in the conformation of the final complex with slow rotational correlation time and optimum water exchange rate.

11.4 Conclusions

Two CAs were synthesized and characterized. The designing of CAs was done keeping their *in vivo* applicability in mind. A thermodynamically stable Gd-DO3A unit was used as the MR detectable moiety as compared to less stable Gd-DTPA. The biotinidase stable construct was designed and synthesized to avoid the problems of rapid wash out of the agents *in vivo*. Also, the low molecular weight of the complexes should not limit their extravasations into solid tumors as has been seen with nanoparticle constructs.

The two molecules synthesized showed a different relaxivity response with the addition of avidin. **Gd-L^{12}** showed a marked increase in r_2 on binding to avidin. In contrast to high magnetic field, both r_2 and r_1 at lower magnetic field of 1.5 T showed an increasing trend, with 266% increase in r_1 and 986% in r_2. An increase in both r_1 and r_2 on conjugation with avidin could be very useful as the single agent could work as T_1 and T_2 agent, showing positive contrast when the image is T_1 weighted while a negative contrast in T_2 weighted images. **Gd-L^{12}** is thus a potential agent to be used to target any biological factor (protein, receptor etc) using mAb against it and well established multistep targeting approach.

Gd-L^{13} showed an increase of 212% at 7 T as compared to 970% in the case of **Gd-L^{12}**. The less marked increase in this case could be explained on the basis of two complxes differing in the conformation of the final construct after conjugating with avidin. **Gd-L^{13}** has a long and flexible linker which allows fast internal motion around metal ion. This offset the expected increase in relaxivity with slowing down of correlation time in macromolecular conjugate. Thus, the linkers' length and the flexibility has a crucial role in determing the relaxivity of the macromolecule:CA conjugate.

CHAPTER 9

12. Summary, Conclusions, and Future Directions

The main goal of the projects for this thesis work was to develop probes which can trace the functional activity and the anatomical connectivity in the brain by MRI.

Currently, fMRI techniques are widely used to study the functional activity in the brain. However these techniques are based on hemodynamic responces to report the neural activity and therefore regarded as the indirect method of reporting brain activation. Also, because of the hemodynamic delay these methods are not able to report the temporal aspect of neural activity precisely. To have a nonhemodynamic and a direct method of reporting brain activation, Ca^{2+} was chosen as the target which is believed to be involved in early synaptic events such as vesicle fusion and chemical release in the synapse. Thus, we aimed at the development of Ca^{2+} sensitive MR detectable markers (also known as smart contrast agents) which would potentially reveal the functional activity in the brain in detail. The markers were designed to be capable of sensing the Ca^{2+} in extracellular space where its concentration is ~ 1-2 mM.

The first part of this project dealt with the synthesis and characterization of BAPTA based bismacrocyclic agents. Two units of Gd-DO3A were coupled symmetrically to BAPTA via amide bonds leaving two carboxylate and two amide units for Ca^{2+} chelation. Such modification was planned to decrease the strong affinity of BAPTA to Ca^{2+} to make it suitable for its extracellular concentration range. Two molecules, $\mathbf{Ln_2L^1}$ and $\mathbf{Ln_2L^2}$ were synthesized with this design which showed 15% and 11% relaxivity enhancement respectively. A complete physiochemical characterization was performed on these two molecules (in collaboration with

Dr. Eva Toth, CNRS, France) to assess the parameters responsible for Ca^{2+} dependent relaxivity change. Relaxometric titrations with Ca^{2+}, ^{1}H NMRD, ^{17}O NMR, UV-Vis absorption, and luminiscence lifetime measurement were performed on the complexes. It was concluded from this detailed investigation that the activity of the agents to Ca^{2+} was due to the change in the hydration number of the complex (0.4 to 0.7 in presence of Ca^{2+}) [181]. However, the sensitivity to Ca^{2+} was not enough for their *in vivo* applicability. In order to improve the sensitivity two more bismacrocyclic agents were synthesized, **Gd_2L^3** and **Gd_2L^4**. **Gd_2L^3** showed no relaxivity change with the addition of Ca^{2+} while the synthesis of **Gd_2L^4** turned out to be very cumbersome.

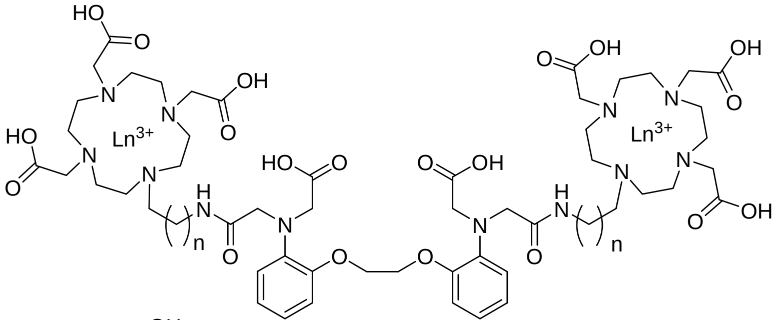

Ln_2L^1 (n=1)
Ln_2L^2 (n=2)

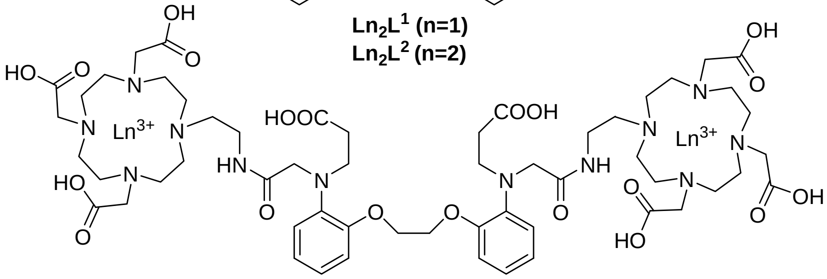

Ln_2L^3

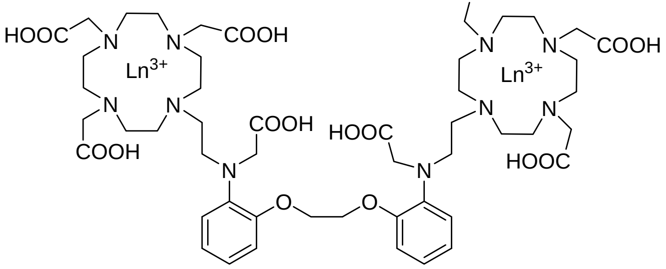

Ln_2L^4

To avoid the complex synthetic procedures, monomacrocyclic agents were designed, synthesized and characterized. APTRA was chosen as the low affinity Ca^{2+} chelator. The comparative analysis of all the agents synthesized from APTRA series was done in Section 9.5. In a nutshell, all of the agents synthesized in this series (**Ln-L$^{5\text{-}9}$**), except **Ln-L^{6}** were found to be highly sensitive to Ca^{2+} with the range of sensitivity varying from 100-168% of relaxivity enhancement. The saturation in the relaxivity, varying from 1:1 to 1:3 ($CA:Ca^{2+}$) was observed which might be due to their different binding affinities of the agents to Ca^{2+}. A good sensitivity and the selectivity of the agents toward Ca^{2+} proved their potential for *in vivo* tests. The detailed physicochemical characterization would be done to calculate their binding affinities and the parameters resulting in relaxivity enhancement in presence of Ca^{2+}.

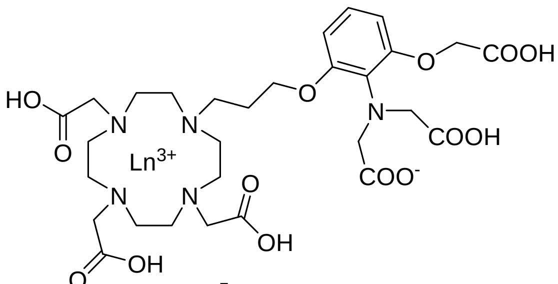

Ln-L^{5}

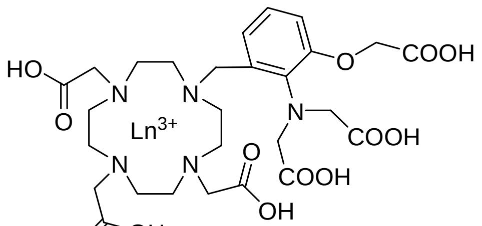

Ln-L^{6}

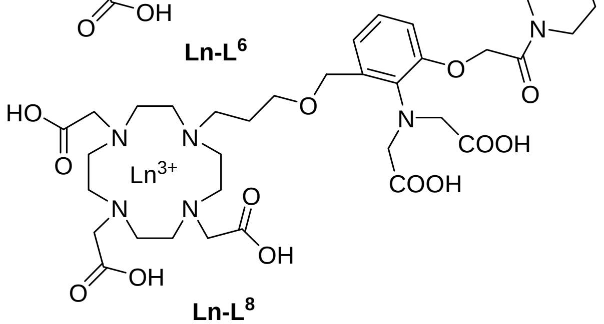

Ln-L^{8}

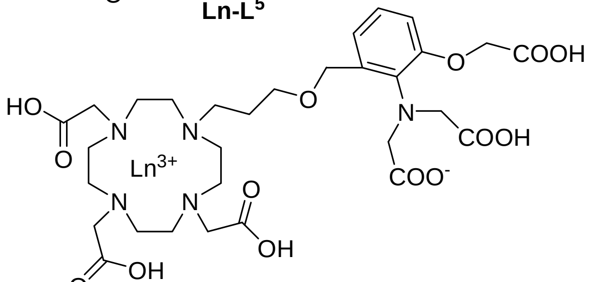

Ln-L^{7}

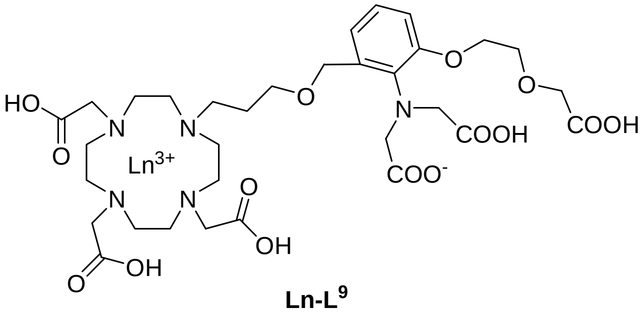

Ln-L^{9}

Under the second project anatomical markers were designed. These markers were designed on the basis of neuronal tract tracing ability of biocytin. To trace the uptake and transport of the neural tracer, we designed an agent with Gd-DO3A coupled to biocytin (**Gd-L^{11}**). The conjugation of these two units was done in a way to make the whole construct stable to the cleavage by endogenous biotinidase enzyme. Complete synthesis of this agent is under progress. We also designed and synthesized an agent with similar construct to **Gd-L^{11}** but without the macrocyclic moiety. This was done to investigate the stability of the system to biotinidase when certain structural modifications are used on the biocytin structure. **L^{10}** was synthesized and tested *in vivo* in rat brains. The neural tracing abilities of this agent were followed by histochemical procedure similar to what is applicable to biocytin. Our initial results showed that the agent is very stable *in vivo* as compared to biocytin. The cells were found to be stained with **L^{10}** at the injection site even after 4 days of survival time whereas biocytin nearly washed away. With the good cellular uptake, **L^{10}** also showed efficient transport with cells being stained at thalamus, striatum and the gray matter of the contralateral hemisphere.

Similar experiments would be performed with **Gd-L^{11}**. The presence of MR detectable moiety in **Gd-L^{11}** with the possible tract tracing ability would open up new possibilities to study the neuronal networks noninvasively with MRI.

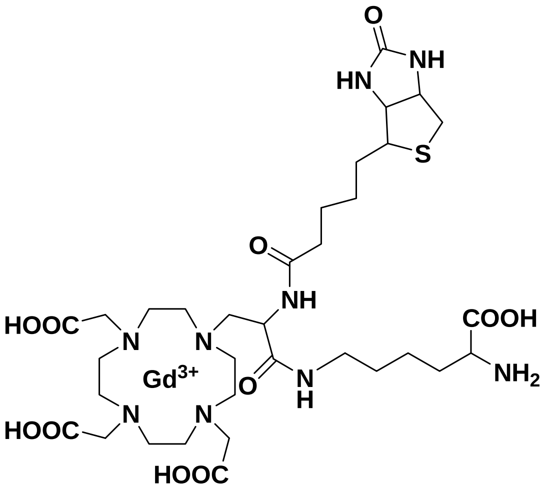

Gd-L^{11}

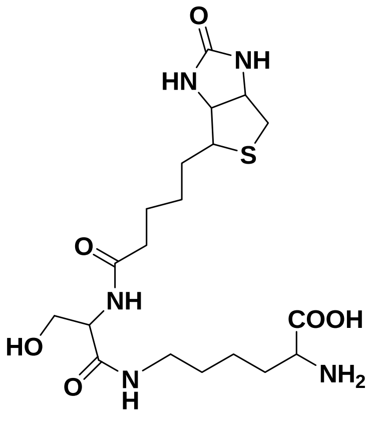

L^{10}

At last, we investigated the possible applications of one of the intermediate (**78**) synthesized for the preparation of neural tracer **Gd-L^{11}**. The coupling of biotin to the acid derivative of **78** with further deprotection steps yielded **Gd-L^{12}**. This construct had one α carboxylate unit to biotinamide bond that would make the whole construct stable to biotinidase enzyme. This agent can be used as the targeted agent using biotin/avidin amplification strategy well established in nuclear imaging. The presence of Gd^{3+} would allow the visualization of molecular targets by MR. The relaxometric titrations of **Gd-L^{12}** were performed with avidin at 1.5 T, 3 T, 7 T, 9.4 T and 16.4 T. The transverse relaxivity showed an excellent enhancement of ~ 1000% at all magnetic fields. While % change in r_1 showed the field dependence with increasing trend at low magnetic field (1.5 T) and decreasing trend at 9.4 T with inversion around 3 T. Another agent **Gd-L^{13}** was also synthesized for a comparison of results obtained with **Gd-L^{12}**. **Gd-L^{13}** was also designed takeing the stability to biotinidase into account. A 220% r_2 enhancement was observed, which is a quarter of what was obtained for **Gd-L^{12}**. The difference in the relaxivity response of these two agents was explained on the basis of length and flexibility of linkers connecting biotin to macrocyclic moiety. The longer and flexible linker in **Gd-L^{13}** allows a fast internal motion around metal ion which limits the relaxivity increase which is normally observed with conjugation to macromolecules. With these initial results, it can be concluded that **Gd-L^{12}** can be used as a potential targeting marker. A marked enhancement in r_2 observed on conjugation with avidin would be favourable for multistep targeting approach *in vivo* by MR.

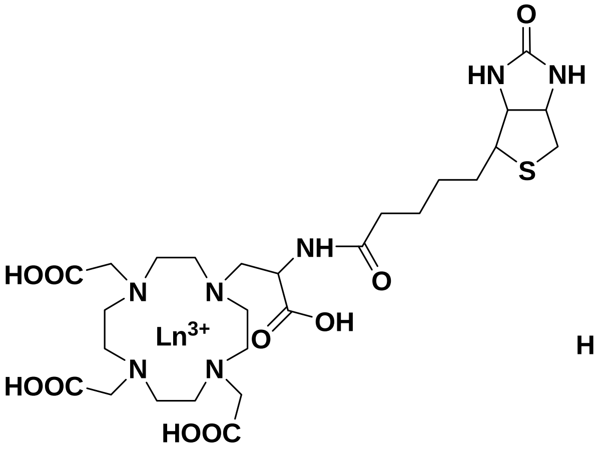

Ln-L^{12}

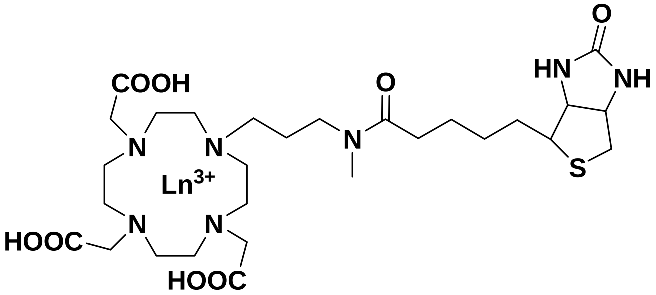

Ln-L^{13}

Section D

Materials and methods

CHAPTER 10

13. Materials and Methods

13.1 Chemicals and Working techniques

The chemicals were purchased from the companies, Acros organics, Sigma-Aldrich, Merck, Strem and VWR. All reagents were obtained of reagents grade from commercial sources and were used without further purifications. The anhydrous solvents, CH_2Cl_2, MeCN, MeOH, DMF, NMP were purchased from Sigma-Aldrich. Dulbecco's Modified Eagle Medium (D-MEM) liquid (high glucose), F-12 Nutrient Mixture (Ham), and N-2 Supplement liquid was purchased from Invitrogen. The anhydrous THF was obtained by freshly distilling it from sodium and benzophenone. Unless otherwise mentioned all reactions were carried out under nitrogen atmosphere and the flasks were dried with heat gun under vacuum. Air and water sensitive reagents were kept in inter atmosphere. The distilled water was used for the reaction work up and milliQ water was used throughout after the last deprotection steps. All glass wares were washed with mixed acid solution and rinsed with milliQ water and acetone. Compound that are not described in the experimental sections were synthesized according to the reported procedures.

13.2 Reverse Phase High Performance Liquid Chromatography (RP-HPLC)

HPLC was performed at room temperature on a Varian PrepStar Instrument, Australia, equipped with PrepStar SD-1 pump heads. UV absorbance was measured using ProStar 335 photodiode array detector at 214 nm and 254 nm. This detector is equipped with a dual-path length flow cell which enables measurement of absorbance of analytical and preparative samples without changing the flow cell. All solvents used were of HPLC grade and were bought from Merck-

VWR and used without further purifications. Reversed phase analytical HPLC was performed in a stainless steel Chromsep (length 250 mm, internal diameter 4.6 mm, outside diameter 3/8 inch and particle size 8µm) C18 column. For preparative HPLC two kind of column of different dimensions were used:

Column 1: Stainless steel Chromsep (length 250 mm, internal diameter 41.4 mm, outside diameter 2 inch and particle size 8), Agilent.

Column 2: Stainless steel Polaris (21.2*250 mm, 5µm, 100 Å), Varian.

Method A

Column 1 (flow rate 65 ml/min): 60% solvent A (water) and 40% solvent B (methanol) to 100% solvent B in 5 minutes running isocratic at 100% solvent B for 10 minutes and then to 60% solvent B in next 2 minutes.

Method B

Column 1 (flow rate 65 ml/min): 5% solvent A (water, 0.1% HCOOH) and 95% solvent B (acetonitrile, 0.1% HCOOH) to 70% solvent B in 10 minutes and then 100% in next 8 minutes running isocratic for 12 minutes after that and then to 5% in next 2 minutes.

Method C

Column 2 (flow rate 15 ml/min): 95% solvent A (H_2O, 0.1% HCOOH) and 5% solvent B (acetonitrile, 0.1% HCOOH) to 70% solvent B in 10 minutes and then to 100% in next 8 minutes running isocratic for 12 minutes after that and then back to 5% solvent B in next 2 minutes.

13.3 NMR-spectroscopy

^{1}H and ^{13}C NMR analysis of all the ligands and the intermediates were done on bruker 400MHz, 300MHz, or 250MHz spectrometer. ^{1}H NMR of Eu^{3+} loaded ligands were performed on 500MHz and 300MHz spectromter. ^{1}H and ^{13}C NMR spectra were performed in deuterated solvents and chemical shifts were assigned by comparison with the residual proton and carbon resonance of the solvents and tetramethylsilane as the internal reference (δ = 0). Data are reported as follows: chemical shift (multiplicity: s = singlet, d = doublet, t = triplet, dd = double of doublet, br., s = broad singlet, J = coupling constant (Hz), integration, peak assignment in italic form)

13.4 Mass spectrometry

ESI low resolution mass spectras (ESI-MS) were recorded on SL 1100 system (Agilent, Germany) with ion trap detection in positive and negative mode. ESI high resolution mass spectras (ESI-HRMS) were performed on a Bruker Daltonics Apex II FT-ICR-MS (Bruker, Germany). MS values were reported as ESI-MS: calculated for the related compound by found mass.

13.5 Infrared Spectroscopy

Infrared spectras were recorded with a Nicolet Impact 400 D spectrometer using neat compounds as disks with KBr and only the major bands are noted.

13.6 Chromatographic methods

Column chromatography was performed using silica gel 60 (70-230 mesh) from Merck. Analytical thin layer chromatography (TLC) was performed on aluminum sheet silica gel plates with 0.2 mm thick silica gel 60 F254 (E. Merck, Germany) using different solvent system as mobile phase. The compounds were visualized by UV254 light and the chromatographic plates were developed in Iodine chamber or aqueous solution of molybdophophorous acid. The molebdate solution as prepared by 20 g ammonium molybdate [$(NH_4)_6Mo_7O_{24}$. $4H_2O$] and 0.4 g $Ce(SO_4)_2$ $4H_2O$ were dissolved in 400 ml of 10% H_2SO_4.

13.7 Relaxometric Measurement Parameters

For in vitro relaxometric Ca^{2+} titration at 9.4 T spectrometer

The measurement of relaxation times T_1 and T_2 (longitudinal and transverse relaxation) was performed on a Bruker Avance 400 spectrometer. The T_1 measurements were done by using the system software Topspin® for data acquisition and T_1 evaluation. An inversion-recovery measurement was used with 32 logarithmic inversion time steps between 50 µs and 3 s. The inversion delay was 6 s and the power for the 90° reference pulse was adjusted for every sample individually. T_1 was calculated by fitting the intensities (I) of the spectrum proton peaks into equation 12.1.

$$I_{(t_i)} = I_0\,(1 - 2A\exp\left(-\frac{t_1}{T_1}\right)) \qquad \text{eq (12.1)}$$

Where $I_{(t_i)}$ is the measured proton peak intensity at inversion time t_i, I_0 is the proton peak intensity without inversion, T_1 is longitudinal relaxation time and factor A takes the finite inversion delay in to account. The samples were measured in 40 µl capillary tubes inserted in 5 mm NMR tubes.

For in vitro relaxometric measurement at 11.7 T spectrometer

The measurement of relaxation times T_1 and T_2 (longitudinal and transverse relaxation) was performed on a Bruker Avance 500 spectrometer. The samples were measured in 5 mm NMR tubes and were enriched with *tert*-butanol to allow for the BMS correction. The T1 was calculated by according to the equation 12.1.

For in vitro relaxometric measurement with avidin

The measurement was done at 1.5 T, 3 T 7 T, 9.4 T and 16 T. The samples were prepared in Phosphate-Buffered-Saline (PBS-Dulbleco's) at pH 7.4 and measured in Eppendorf tubes. Each tube was filled with 400µl of the sample solution. Four samples were prepared with different concentration of CA (0.4 mM, 0.6 mM, 0.8 mM, 1.0 mM) in buffer. The intercept of the plot of relaxation rate obtained for these tubes with the corresponding concentration of CA gave the diamagnetic relaxation rate ($1/T_d$). For samples containing avidin, a fixed concentration of CA was used (~ 0.3 mM) with differing in the ratio of Avidin:CA. Avidin stock solution was prepared in PBS buffer at pH 7.4.

At 7 T

At 7 T MR imaging was performed in a vertical BioSpec 7T/60-cm diameter bore magnet equipped with a BGA38-cm inner diameter gradient (Bruker Biospin, Ettlingen, Germany) using a multislice spin-echo sequence (MSME). One slice of interest was positioned axial to the tubes.

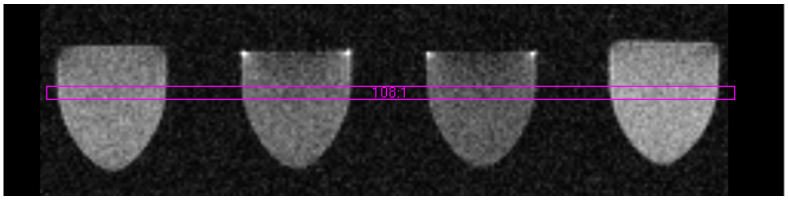

Figure 59: Positioning of axial slice

To determine T_1, saturation recovery images with varying repetition times TR were acquired. T2 was measured with a spin-echo method that acquire several echo-images after each excitation using a long repetition time TR. The experimental parameters have been:

T1: field of view 7.2x5.6cm^2; matrix 288x244; slice thickness 1mm; SW 70kHz; TE 12ms; TR 45-800ms (logarithmic interleaved time steps, 80 images); two averages

T2: field of view 7.2x5.6cm^2; matrix 288x244; slice thickness 1mm; SW 70kHz; TE 12-720ms (linear time steps, 60 echoes); TR 10000ms; ten averages

The data analysis was performed by fitting the single Voxel intensities of the acquired images to relaxivity curves resulting in parameter maps of T1, T2 and S0 (initial signal at t = 0) and the corresponding error maps σ_{T1}, σ_{T2} and σ_{S0}.

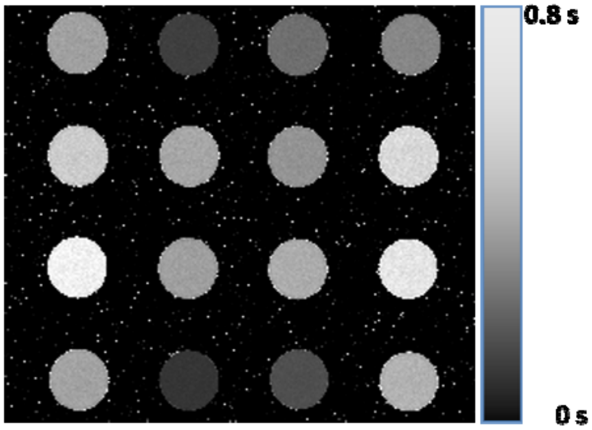

Figure 60 T1/T2 maps of the tubes at 7 T

Within these maps the single tubes have been selected manually and an iterative Gaussian fit was used to determine mean and standard deviations of the single T1 and T2 distributions.

For calculation of R_0 weighted linear regression was used and the relaxivity r [$s^{-1}mM^{-1}$] for the single Avidin concentrations finally have been calculated using equations 12.2.

$$
\begin{gathered}
\mathrm{r} = \frac{\mathrm{R} - \mathrm{R}_0}{\mathrm{c}_\mathrm{B}} \\
\Delta\mathrm{r} = \frac{1}{c_B} \cdot \sqrt{\left(\Delta R^2 + \Delta R_0^2\right)} \\
\textit{with} \\
\mathrm{R} = 1/\mathrm{T} \\
\Delta\mathrm{R} = \sqrt{\left(\frac{1}{\mathrm{T}^2}\right)^2 \cdot \Delta T^2}
\end{gathered}
\qquad \text{eq(12.2)}
$$

At 1.5 T, 3 T, 9.4 T, and 16.4 T

Relaxation time measurements at 1.5T, 3T and 9.4T were performed in human MR scanners (Siemens). Experiments at the field of 16.4T were performed in a horizontal scanner for small animals with a bore diameter of 12 cm, equipped with a Bruker console and software. On the human scanners, vendor supplied head coils were used for signal reception and, at 9.4 T, for transmit. The 16.4 T measurements were done with a volume coil with sufficient space for up to six samples; for the total set of 16 samples three separate measurements were required at 16.4 T. The samples were placed in a container filled with water to reduce susceptibility-induced field homogeneities and to enable automatic scanner adjustments. For measuring T_1, an inversion-recovery sequence was used, with an adiabatic inversion pulse followed by a turbo-spin-echo acquisition. Between 10 and 15 images were taken, with the inversion time TI between inversion and spin-echo excitation varying from 20 ms to 3000 ms in the human scanners and from 100 ms to 5000 ms at 16.4 T. With a repetition time of 10 s to 12 s, between 8 and 15 echoes were acquired per scan. For T_2, a spin-echo sequence was used with echo times varying from 19 ms to 1000 ms in about 10 steps. For the 3 T measurements, a home written sequence was used to reduce diffusion effects by minimizing the crusher gradients surrounding the refocusing pulse. A repetition time of 8 s was used in those images. The experiments in human scanners covered 256^2 voxels in a field-of-view of 110 mm in both directions; the 16.4 T sampled 192×96 voxels over a 60×30 mm^2 field of view.

Data analysis was performed by the fitting to relaxation curves with self written routines under MATLAB 7.1 R14 (The Mathworks Inc.). The series of T_1 relaxation data were fitted to the equations S = S0 (1 - exp(-TI / T1) + S(TI = 0) exp(-t / T1), where S0, S(TI = 0) and T1 were determined by the fitting routine. For T_2, the parameters S0 and T2 were fitted in the equation S = S0 exp(-t / T2). Signals from manually selected regions-of-interest, each positioned inside one of the sample tubes, were added and nonlinear least-squares fitting was performed with the Trust-Region Reflective Newton algorithm implemented in Matlab. The quality of the fit was controlled by visual inspection and by calculating the mean errors and residual. In this case, for calculation of R_0 normal linear regression was used and Equation 12.2 was used again for calculation of the single relaxivities but without doing error estimation.

13.8 *In vivo* rat experiments

In order to test the stability of the synthesized neural tracer as compared to the conventional biocytin, a series of experiments were carried out. *In vivo* injections of the commercially available biocytin and the synthesized $\mathbf{L}^{\mathbf{10}}$ derivative in the rat brain were performed. Iontophoretic injections were done to the primary cortex (right and left hemisphere) of rats. Perfusions were then carried out after the survival time of 24 h and 96 h. The uptake and transport of the tracer in the neurons was examined by histochemical treatment of the brain slices

Surgery and tracer injections

Rats were anesthetized with 1.5-2% isoflorane and positioned within a stereotaxic frame. After additional administration of local anesthetic in the surgery area a trepanation was performed over the primary motor cortex. The positioning of the injection was done according stereotaxic coordinates relative to Bregma, the sagittal suture and the surface of the brain (+1.2mm anterior, 2.5mm lateral, 1-1.2mm deep). Two kinds of injections were used, pressure injections using 0.5µl Hamilton syringes fitted with 32G (diameter~200µm) needles and iontophoretic injection using glass electrodes with 20-30 µm tip diameter. For the pressure injections a total volume of 100-300 nl was injected within a time period of 30-60 min. For the pressure injections a total volume of 100-300 nl was injected within a time period of 30-60 min. At the end of the surgery the hole in the skull was closed by replacing the bone, the skin was sutured and the animal received regular subcutaneous injections of analgesic and antibiotics for the following days.

Perfusions

24h, 48h and 96h after injections, a deep anesthesia was induced with the intraperitoneal injection of pentobarbital (Narcoren®). After cessation/disappearance of all reflexes, the chest of the animal was opened and Heparin (Liquemin®) was injected in to the heart in order to prevent coagulation of blood. A catheter was inserted in the aorta via the left ventricle, a small incision made in the right auricle and the animal perfused with PBS (phosphate buffer saline) for about 5 min and then fixated with the fixative (4% formaldehyde in PBS). After the fixation in situ for 1-3 h, the brain were removed from the skull and kept in the fixative overnight. During the next days, the brains were transferred stepwise in to 10%, 20% and 30% sucrose solution, kept in each of these solutions steps until the brain sunk to the bottom. This took altogether 96 h. The brains were then cut with a freezing microtome in to serial sections at a thickness of 70 µm.

13.9 Histochemical experiments

The following protocol was followed for the preparation of slices:

- Collect slices in PBS (0.1 M, pH 7.3)
- 1% H_2O_2 in PBS (NaCl in 0.1 M PBS) for 1 h to suppress the endogen peroxidase activity.
- Rinse with PBS
- Treatment for 1 h with Triton X-100 (0.5 % in 0.1 M PBS) (Triton cracks the membrane protein and makes avidin-peroxidase solution to enter the cells easier in the next step)
- Incubation in avidin-conjugated peroxidase (vector laboratories, 1% in PBS)
- Rinse with PBS (3 x 10 min)
- Rinse 3 x 10 min with Tris/HCl (0.15 M, pH 7.9) (Tris is made more basic than PBS, that makes the staining with DAB solution faster in the next step)

- Incubation of the slices in DAB-fast Tablet Set-solution in water (diaminobenzidine 0.5% in Tris/HCl) and H_2O_2.
- Washing with Tris/HCl (3 x 10 min)
- The slices were then mounted on slices and air dried overnight

Dehydration was performed on the mounted slices on the next day with graded ethanol (70%, 80%, 2 x 99%, 2 x 100% ethanol), 2 x terpineole and 2 x xylene. They were then covered with Eukitt or DePex.

13.10 ^{1}H NMRD and ^{17}O NMR measurement

The ^{1}H NMRD profiles were recorded at the Laboratory of Inorganic and Bioinorganic Chemistry, Ecole Polytechnique Fédérale de Lausanne, Switzerland, on Stelar Spinmaster FFC fast-field-cycling relaxometer covering magnetic fields from 2.35×10^{-4} T to 0.47 T (proton Larmor frequency range 0.01–20 MHz). The temperature was controlled by a VTC90 temperature control unit and fixed by a gas flow. At higher fields, the relaxivity was recorded using Bruker Minispecs mq30 (30 MHz), mq40 (40 MHz) and mq60 (60 MHz), on a Bruker 4.7 T (200 MHz) cryomagnet connected to a Bruker Avance-200 console and on a Bruker Avance 500 spectrometer (500 MHz). The temperature was measured by a substitution technique [27] or via a preliminary calibration using methanol and ethyleneglycol standards [28]. The longitudinal ($1/T_1$) and transverse ($1/T_2$) ^{17}O NMR relaxation rates were measured in the temperature range of 277–344 K. The data were recorded on a Bruker Avance 500 (11.75 T, 67.8 MHz) spectrometer. The temperature was calculated according to previous calibration with ethylene glycol and methanol [28]. The samples were measured in 5 mm NMR tubes and were enriched with *tert*-butanol to allow for the BMS correction [29]. The $1/T_1$-data were obtained by the inversion recovery method, while the $1/T_2$-data were measured by the Carr–Purcell–Meiboom–Gill spin-echo technique. Acidified water ($HClO_4$, pH 3.8) was used as external reference. Analyses of the ^{17}O NMR and ^{1}H NMRD experimental data were performed with the Visualiseur/Optimiseur programs running on a Matlab platform version 6.5 [30].

13.11 UV-Vis absorbance measurement

UV-Vis spectra of $^5D_0 \leftarrow ^7F_0$ transitions of were obtained on a PERKIN ELMER Lambda 19 spectrometer in the region 577–581 nm with data steps of 0.05 nm [26]. The sample concentrations were ~ 0.02 M and the temperature dependence was measured in the interval 15–50 °C in the absence and presence of Ca^{2+}. To maintain a constant temperature, thermostatisable cells with a 10 cm optical length were used.

13.12 Luminescence Lifetime measurement

The luminescence measurements were performed on a Varian eclipse spectrofluorimeter, equipped with a 450 W xenon arc lamp, a microsecond flash lamp and a red-sensitive photomultiplier (300–850 nm). The luminescence spectra were obtained after excitation at $^5L_6 \leftarrow ^7F_0$ band (394 nm).

13.13 Preparation of ACSF

A Ca^{2+} free ACSF solution was prepared by making a 100 ml standard solution of Hepes buffer (1.668 g), NaCl (0.723 g), KCl (0.0216 g), MgCl2.6H2O (0.01423g) and NaHCO3 (0.1957 g). The pH of teh finally obtained solution was adjusted at pH 7.4 by addition of solid KOH.

13.14 Preparation of AECM

Stock solution of AECM was prepared afresh by mixing 5 ml of Dulbecco's Modified Eagle Medium (D-MEM) liquid (high glucose) (Invitrogen, Catalog Number: 21068028), 5 ml of F-12 Nutrient Mixture (Ham) (Invitrogen, Catalog Number: 21765029) and 100 µl of N-2 Supplement liquid (Invitrogen, Catalog Number: 17502048). D-MEM is well suited for supporting the growth of a broad spectrum of mammalian cell lines. F-12 Nutrient Mixture was originally formulated for single cell plating of near-diploid Chinese Hamster Ovary (CHO) cells. N-2 supplement is a chemically defined, 100X concentrate of Bottenstein's N-2 formulation. This supplement is recommended for the growth and expression of neuroblastomas and for the survival and expression of post-mitotic neurons in primary cultures. The exact compositions are listed in the Table A5.in the Appendix 2.

13.15 Experimental synthetic procedure

General procedure for preparation of Ln(III) complexes for bismacrocyclic ligand

The Ln(III) complexes of bismacrocyclic ligands were prepared by mixing a slight excess of the ligand (5%) with the $LnCl_3$ solution of known concentration. The reaction mixture was kept for stirring at 50 °C and the pH was maintained at 7 with the addition of 1 M KOH solution. The absence of free Ln^{3+} was checked by xylenol orange indicator in HCl/urotropine buffer (pH 5.5). After approx 4 h, water was evaporated the solid obtained was used as such. For each Gd_2L sample, the Gd^{3+} concentration has been determined by measuring the bulk magnetic susceptibility shifts

General procedure for preparation of Ln(III) complexes of monomacrocyclic ligands

The Ln(III) complexes of monomacrocyclic ligands were prepared by adding 1.1 equiv of $LnCl_3$ solution of known concentration. The reaction was kept for stirring at 50 °C and the pH was maintained at 7 with the addition of 1 M NaOH solution. The reaction mixture was then kept for stirring at the same temperature overnight. Chelex 100 was added to the reaction mixture and the reaction was allowed to stir at RT for 1 h. The absence of free Ln^{3+} was checked by xylenol orange indicator in HCl/urotropine buffer (pH 5.5). It was then filtered and the water evaporated to obtain the complex as solid. This was purified by sephadex LH-20 column (13 * 2.5 cm for ~ 50-150 mg) with elution by pure water without application of pressure from top. The fractions collected were analyzed by ESI-MS. The desired fractions were mixed and the water was evaporated to obtain the Ln(III) complex. For each Ln-L sample the final concentrations were determined by ICP-OES.

1,2-bis(2-nitrophenoxy)ethane

(1)

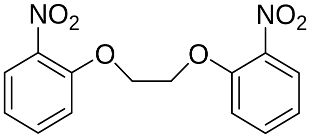

o-nitro-phenol (5.0 g, 36 mmol) and K_2CO_3 (11.0 g, 79 mmol) were taken in oven dried round bottom flask. 25 ml of DMF (dry) was added and the contents were heated at 90 °C for 1 h. The reaction mixture (RM) was cooled down under ice and dibromoethane (1.4 ml, 16.2 mmol) was added. The RM was heated at 90 °C for 3 h. It was brought to room temperature and added to crush ice. The precipitated product (**1**)was filtered, washed with water and air dried (4.7 g, 87%).

^{1}H NMR (250 MHz, DMSO-*d5*), δ ppm: 4.53 (s, 4 H), 7.10 - 7.18 (m, 2 H), 7.40 - 7.46 (m, 2 H), 7.61 - 7.70 (m, 2 H), 7.82 - 7.88 (m, 2 H).

^{13}C NMR (62 MHz, DMSO-*d5*), δ ppm: 68.4, 115.9, 121.3, 125.1, 134.6, 140.1, 151.2.

ESI-MS: calculated for $[C_{14}H_{12}N_2O_6 + K]^+$ *m/z* 343.0 found 343.1

2,2'-(ethane-1,2-diylbis(oxy))dibenzenamine

(2)

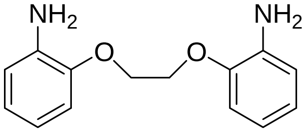

Compound **1** (3.0 g, 9.9 mmol) was dissolved in 15 ml methanol with Pd-C catalyst (10% w/w) and kept for stirring under H_2 (1 atm) in Parr apparatus till the consumption of H_2 ceases. RM was then filtered and the solvent evaporated to obtain the product (**2**) as light yellow solid (2.3 g, 95%).

^{1}H NMR (300 MHz, DMSO-*d*$_6$), δ ppm: 4.27 (s, 4 H), 6.49 - 6.57 (m, 2 H), 6.64 - 6.75 (m, 4 H), 6.83 - 6.89 (m, 2 H).

^{13}CNMR (62 MHz, DMSO-*d6*), δ ppm: 144.5, 137.3, 120.6, 115.4, 113.3, 111.8, 66.3.

ESI-MS: calculated for $[C_{14}H_{16}N_2O_2 + H]^+$ *m/z*: 245.1, found 245.0

2,2'-(ethane-1,2-diylbis(oxy))bis(N-benzylbenzenamine)

(3)

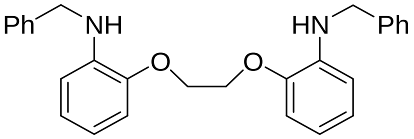

Compound **2** (2.0 g, 8.2 mmol) was dissolved in 1,2 dichloroethane (dry) under N_2. Benzaldehyde (1.6 ml, 16.4 mmol,) was added dropwise and the reaction mixture was kept for stirring for 3 h. Sodium triacetoxy borohydride (5.2 g, 24.6 mmol) was added slowly in small lots under cooling conditions. The reaction was quenched after 5 h by addition of saturated $NaHCO_3$. Ethylacetate was added and the mixture was washed with water. Organic layer was collected, dried under anhydrous Na_2SO_4 and evaporated to get yellow oil. To the oil obtained, cooled diethyl ether was added and the content was kept under ice. The precipitated product (**3**) was filtered and washed with cooled diethylether (2.5 g, 73%).

^{1}H NMR (250 MHz, $CDCl_3$), δ ppm: 4.66 (s, 4 H), 4.77 (s, 4 H), 6.89 - 7.05 (m, 4 H), 7.17 - 7.26 (m, 4 H), 7.59 - 7.70 (m, 10 H).

^{13}C NMR (62 MHz, $CDCl_3$), δ ppm: 47.7, 67.5, 110.6, 111.6, 122.1, 126.9, 127.1, 128.5, 138.7, 145.7.

ESI-MS: calculated for $[C_{28}H_{28}N_2O_2 + H]^+$ *m/z*: 425.2, found 425.3

di-tert-butyl 2,2'-(2,2'-(ethane-1,2-diylbis(oxy))bis(2,1-phenylene))bis(benzylazanediyl)diacetate

(4)

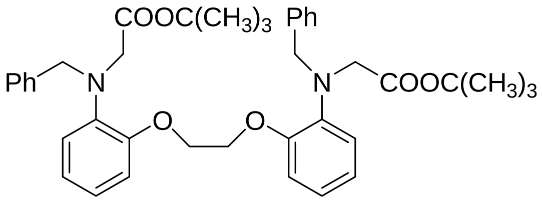

Compound **3** (1.0 g, 2.3 mmol), K_2CO_3 (1.3 g, 9.4 mmol) and KI (0.039 g, 0.23 mmol) were taken up in 25 ml MeCN (dry) and refluxed for 2 h. The RM was brought to room temperature and *tert*-butylbromoacetate (1.4 ml, 9.4 mmol) was added. The reaction mixture was refluxed overnight. It was then filtered and the solvent evaporated to obtain yellow oil. Cold diethylether was added to it and the contents were kept under ice .It was then filtered to obtain the product (**4**) as white solid (1.3 g, 87%).

^{1}H NMR (400 MHz, $CDCl_3$), δ ppm: 1.39 (s, 18 H), 3.85 (s, 4 H), 4.32 (s, 4 H), 4.51 (s, 4 H), 6.83 - 6.93 (m, 6 H), 6.97 - 7.03 (m, 2 H), 7.19 - 7.25 (m, 6 H), 7.31 - 7.37 (m, 4 H).

^{13}C NMR (100 MHz, $CDCl_3$), δ ppm: 27.7, 52.7, 55.6, 80.4, 113.7, 120.3, 121.2, 126.5, 127.9, 138.4, 138.9, 150.7, 170.3.

ESI-MS: calculated for $[C_{40}H_{80}N_2O_6 + H]^+$ *m/z*: 653.3, found 653.3

2,2'-(2,2'-(ethane-1,2-diylbis(oxy))bis(2,1-phenylene))bis(benzylazanediyl)diacetic acid (5)

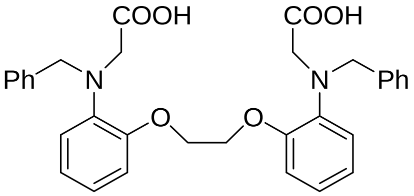

Compound **4** (1.0 g, 1.5 mmol) was dissolved in minimum CH_2Cl_2 and 30 ml of cooled TFA was added to it under cooling conditions. The reaction mixture was stirred overnight and then evaporated under vacuum. The obtained crude oil was dissolved in cold methanol and diethylether was added. The precipitated solid was filtered out to obtain the product (**5**) as white solid (0.77g, 98%).

^{1}**H NMR** (400 MHz, MeOD), δ ppm: 4.27 (s, 4 H), 4.33 (s, 4 H), 4.64 (s, 4 H), 6.99 - 7.09 (m, 4 H), 7.15 - 7.28 (m, 14 H).

^{13}**C NMR** (100 MHz, MeOD), δ ppm: 56.2, 61.4, 68.9, 115.1, 122.9, 123.1, 128.6, 129.8, 130.0, 131.4, 134.9, 135.1, 152.8, 172.1.

Compound **6, 7, 8, 10** were synthesized according to previously reported procedure [182] Analytical data was found as reported. Using analogous method, compound **11** was synthesized via **9** from the substrate **7** [183]

tert-butyl 4-(3-(benzyloxycarbonylamino)propyl)-7,10-bis(2-tert-butoxy-2-oxoethyl)-1,4,7,10-tetraazacyclododecane-1-carboxylate

(9)

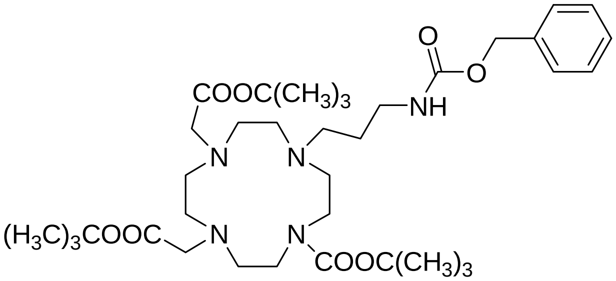

Yield: 73%; ^{1}**H NMR** (CDCl$_3$, 400MHz), δ (ppm): 6.97-6.84 (m, 5H), 4.65 (s, 2H), 2.98-2.89 (m, 2H), 2.86-2.70 (m, 5H), 2.70-2.60 (m, 3H), 2.58-2.17 (m, 7H), 2.16-1.75 (m, 9H), 1.32 (br. s, 2H), 1.06-1.03 (m, 27H).

^{13}**CNMR** (CDCl$_3$, 100MHz), δ (ppm): 25.2, 26.5, 28.2, 37.8, 38.5, 48.9, 50.3, 55.4, 64.7, 65.7, 81.0, 81.3, 126.4, 127.1, 135.6, 152.9, 155.2, 171.2, 172.2.

ESI-MS: calculated for $[C_{37}H_{63}N_5O_8 + H]^+$ *m/z*: 706.5 found: 706.5

tert-butyl 4-(3-aminopropyl)-7,10-bis(2-tert-butoxy-2-oxoethyl)-1,4,7,10-tetraazacyclododecane-1-carboxylate

(11)

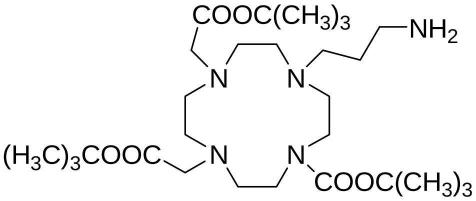

Yield: 65%; ^{1}**H NMR** (CDCl$_3$, 400MHz), δ (ppm): 8.19 (br. s, 2H), 3.42-2.99 (m, 8H), 2.85-2.20 (m, 16H), 1.61 (br.s, 2H), 1.41 (s, 27H).

^{13}**C NMR** (CDCl$_3$, 100MHz), δ (ppm): 22.9, 27.1, 27.2, 38.5, 48.9, 49.4, 50.1, 55.9, 57.2, 81.1, 169.8, 172.0.

ESI-MS: calculated for $[C_{29}H_{57}N_5O_6 + H]^+$ *m/z*: 572.4 found 572.4.

Compound 12

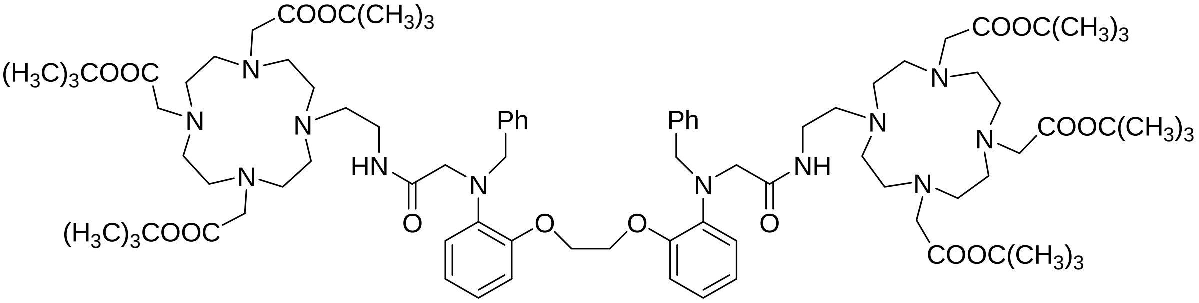

Compound **5** (0.2 g, 0.5 mmol), compound **10** (0.84 g, 1.5 mmol), NMM (0.4 ml, 1.0 mmol) and HOBt (0.27 g, 0.55 mmol) were dissolved in 7 ml of dry DMF under N_2 in an over dried round bottom flask. After an hour of stirring, EDC (0.39 g, 0.55 mmol) was added and the RM was heated at 60 °C overnight. The DMF was evaporated and the contents were redissolved in CH_2Cl_2 and extracted with water. The collected organic layer was dried under anhydrous. Na_2SO_4 and evaporated under vacuum. The crude oil obtained was purified by column chromatography using $MeOH/CH_2Cl_2$ (0.1:1) to obtain the desired product (**12**) (0.45 g, 55%).

^{1}H NMR (300 MHz, $CDCl_3$): δ ppm: 1.17 - 1.30 (m, 54 H), 2.38 - 2.61 (m, 13 H), 2.62 - 2.77 (m, 7 H), 2.83 - 3.01 (m, 16 H), 3.08 (br. s., 8 H), 3.15 - 3.32 (m, 6 H), 3.39 - 3.64 (m, 4 H), 3.99 - 4.32 (m, 6 H), 6.57 - 6.85 (m, 8 H), 6.88 - 7.09 (m, 10 H).

^{13}C NMR (62 MHz, $CDCl_3$), δ ppm: 27.9, 29.5, 47.7, 49.6, 51.5, 53.1, 55.1, 56.5, 57.6, 66.9, 81.5, 81.7, 110.7, 118.2, 123.8, 124.9, 128.0, 128.3, 128.5, 137.2, 139.8, 142.9, 169.8, 170.1, 172.3.

ESI-MS: calculated for $[C_{88}H_{138}N_{12}O_{16} + H]^+$ *m/z* 1620.0 found 1620.0

Compound **13**

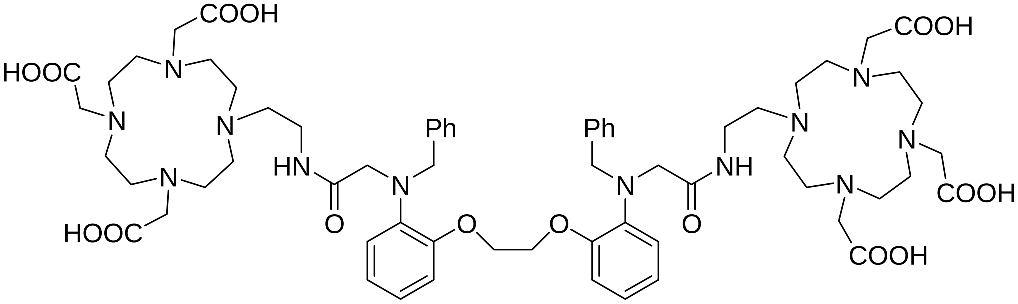

The ester groups in compound **12** (0.3 g, 0.2 mmol) were hydrolyzed using the cleavage cocktail (TFA:H_2O:TIPS, 99:0.5:0.5). After stirring overnight at rt, the reaction mixture was evaporated under vacuum and purified by RP-HPLC using the method A to obtain the product (**13**) in 32% yield.**^{1}H NMR** (400 MHz, D_2O), δ ppm: 2.25-2.6 (m, 11 H), 2.75-3.15 (m, 29 H), 3.25-3.50 (m, 16 H), 3.90 (s, 3 H), 4.30 (s, 3H), 6.65-7.10 (m, 18 H).

^{13}C NMR (100 MHz, D_2O), δ ppm: 27.9, 32.3, 40.5, 45.5, 45.6, 45.7, 46.5, 47.8, 48.5, 48.9, 51.9, 53.4, 53.8, 53.9, 56.2, 64.8, 64.9, 95.4, 110.7, 118.6, 119.2, 125.3, 126.0, 126.8, 134.2, 134.9, 149.1, 169.8.

ESI-MS calculated for $[C_{64}H_{90}N_{12}O_{16} - H]^-$ *m/z* 1281.7 found 1281.9

dimethyl 2,2'-(2,2'-(ethane-1,2-diylbis(oxy))bis(2,1-phenylene))bis(benzylazanediyl)diacetate

(14)

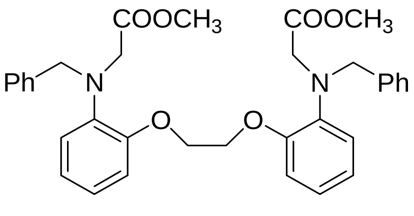

Compound **3** (2.0 g, 4.7 mmol), K_2CO_3 (2.6 g, 18.9 mmol), and KI (0.15 g, 0.94 mmol) were taken in MeCN (dry) and refluxed for 2 h. The reaction mixture was brought to room temperature and methylbromoacetate (1.8 ml, 18.9 mmol) was added. The obtained mixture was refluxed for another 24 h. The RM was cooled down and filtered. The solvent was evaporated and the obtained residue was redissolved in CH_2Cl_2 and washed with water. The organic layer collected was dried under anhydrous Na_2SO_4 and evaporated to obtain the yellow oil. The crude product was purified by column chromatography using ethylacetate/hexane (0.2:1) solvent mixture (1.8 g, 70%).**^{1}H NMR** (400 MHz, $CDCl_3$), δ ppm: 3.53 (s, 6 H) 3.99 (s, 4 H) 4.32 (s, 4 H) 4.52 (s, 4 H) 6.84 - 6.95 (m, 6 H) 6.99 - 7.06 (m, 2 H) 7.16 - 7.26 (m, 6 H) 7.30 - 7.38 (m, 4 H).

^{13}C NMR (100 MHz, $CDCl_3$), δ ppm: 51.7, 52.5, 56.5, 67.7, 113.9, 121, 121.9, 122.5, 127.4, 128.6, 128.7, 138.9, 140.3, 151.3, 172.5

dimethyl 2,2'-(2,2'-(ethane-1,2-diylbis(oxy))bis(2,1-phenylene))bis(azanediyl)diacetate

(15)

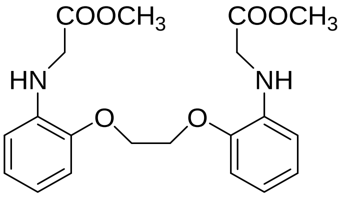

Compound **14** (1.5 g, 2.6 mmol) was dissolved in methanol with Pd-C catalyst (10%, w/w) and stirred for 5 h under H_2 atmosphere (1 atm) in a Parr apparatus. The heterogeneous reaction mixture was filtered through celite pad and the solvent evaporated to obtain the product (**15**) (0.96 g, 95%). The product obtained was used as such without further purification. ^{1}H NMR (400 MHz, $CDCl_3$), δ ppm: 3.74 (s, 6 H) 3.95 (s, 4 H) 4.41 (s, 4 H) 6.47 - 6.53 (m, 2 H) 6.68 - 6.76 (m, 2 H) 6.85 - 6.95 (m, 4 H). ^{13}C NMR (100 MHz, $CDCl_3$), δ ppm: 45.7, 52.4, 67.7, 110.5, 112.2, 117.7, 122.3, 138.1, 146.2, 172.1

2-((2-tert-butoxy-2-oxoethyl)(2-(2-(2-((2-tert-butoxy-2-oxoethyl)(2-methoxy-2-oxoethyl)amino)phenoxy)ethoxy)phenyl)amino) methyl acetate

(16)

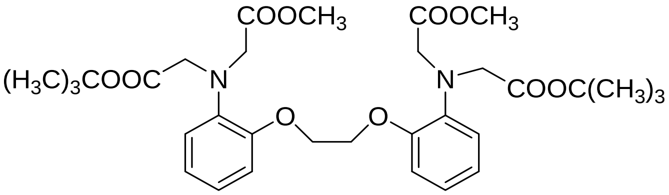

Compound **15** (1.8 g, 4.6 mmol), proton sponge (3 g, 13.8 mmol) and KI (0.15 g, 0.92 mmol) were taken in 100 ml MeCN and refluxed for 1 h. The RM was cooled down and *tert*-butylbromoacetate (2.7 ml, 18.4 mmol) was added. It was then kept for refluxing for five days. The reaction mixture was filtered and the solvent was evaporated. The residue obtained was redissolved in CH_2Cl_2 and washed with water. The organic layer collected was dried under anhydrous Na_2SO_4 and evaporated to yellow oil. This was purified by column chromatography using ethylacetate/hexane (0.15:1) solvent mixture to obtain the product (**16**) (1.4 g, 52%). **^{1}H NMR** (400 MHz, $CDCl_3$), δ ppm: 1.45 (s, 18 H) 3.48 (s, 6 H) 4.04 (s, 4 H) 4.19 (s, 4 H) 4.30 (s, 4 H) 6.81 - 6.85 (m, 2 H) 6.92 - 6.97 (m, 2 H) 7.28 - 7.34 (m, 2 H) 7.35 - 7.40 (m, 2 H).

^{13}C NMR (100 MHz, $CDCl_3$), δ ppm: 28.5, 44.8, 51.9, 53.9, 54.6, 67.5, 81.8, 113.7, 119.3, 121.9, 122.4, 125.8, 139.8, 150.7, 170.9, 172.7

2,2'-(2,2'-(ethane-1,2-diylbis(oxy))bis(2,1-phenylene))bis((2-methoxy-2-oxoethyl)azanediyl)diacetic acid

(17)

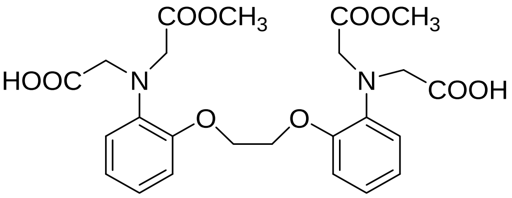

Compound **16** (1.3 g, 2.2 mmol) was dissolved in minimum amount of CH_2Cl_2 and 15 ml of TFA added to it. The RM was stirred overnight at RT. It was then evaporated under vacuum and redissolved in CH_2Cl_2 (2*10 ml) and MeOH (2*10 ml), and evaporated under vacuum till dry. The obtained product (**17**) was used as such without further purification (1.0 g, 95%). **^{1}H NMR** (400 MHz, acetone-*d₆*), δ ppm: 3.51 (s, 6 H) 4.12 (s, 4 H) 4.19 (s, 4 H) 4.33 (s, 4 H) 6.82 - 6.95 (m, 6 H) 6.98 - 7.03 (m, 2 H).

^{13}C NMR (100 MHz, $CDCl_3$), δ ppm: 42.0, 49.98, 45.01, 58.3, 104.6, 110.3, 112.2, 113.3, 130.2, 141.8, 162.7, 163.4.

Compound **18**

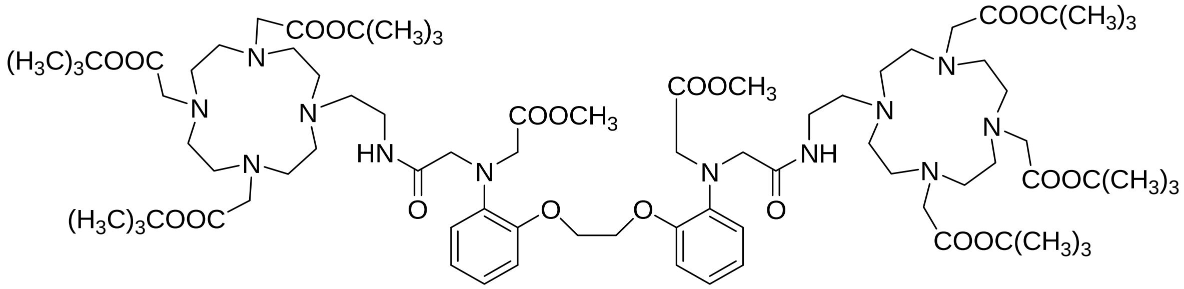

Compound **17** (1.1 g, 2.0 mmol), compound **10** (2.8 g, 5.0 mmol), NMM (1.1 ml, 10.0 mmol), and HOBt (0.75 g, 5.5 mmol) were dissolved in 8 ml DMF (dry) under N_2. The RM was stirred for 1 h and EDC (1.0 g, 5.5 mmol) was added. The contents were heated at 60 °C overnight. The DMF was evaporated under vacuum and the mixture obtained was redissolved in CH_2Cl_2 (25 ml) and extracted with water (4*25 ml). The collected organic layer was dried under anhydrous Na_2SO_4 and evaporated to yellow oil. This was purified by column chromatography using MeOH/CH_2Cl_2 (0.1:1) as the solvent mixture to obtain the product as solid (0.78 g, 25%). The compound was obtained with small amount of HOBt as the impurity which was removed in the next step by RP-HPLC. **^{1}H NMR** (400 MHz, $CDCl_3$), δ ppm: 1.33 (s, 20 H), 1.34 (s, 34 H), 2.61 (d, *J*=11.44 Hz, 16 H), 2.84 (br. s., 8 H), 3.06 - 3.16 (m, 9 H), 3.21 (s, 12 H), 3.28 (s, 4 H), 3.32 -

3.36 (m, 2 H), 3.42 - 3.44 (m, 2 H), 3.47 (s, 5 H), 3.85 (s, 4 H), 3.99 (s, 4 H), 4.15 (s, 4 H), 7.02 - 7.08 (m, 4 H), 7.36 - 7.43 (m, 2 H), 7.59 - 7.66 (m, 2 H).

^{13}C NMR (100 MHz, $CDCl_3$), δ ppm: 27.8, 32.8, 47.8, 49.6, 50.3, 51.5, 52.9, 53.3, 54.0, 54.8, 56.5, 56.6, 66.6, 81.4, 81.5, 109.2, 110.8, 118.1, 119.9, 143.2, 150.0, 169.8, 170.0, 171.6, 172.1.

ESI-MS: calculated for $[C_{80}H_{134}N_{12}O_{20}\text{-}H]^-$ *m/z* 1581.9, found 1581.7

1,2-bis{[2-{[({1-[1,4,7-tris(carboxymethyl)-1,4,7,10-tetraazacyclododecane-10-yl]eth-2-yl}amino)carbonyl]methyl}-(carboxymethyl)amino]phenoxy}ethane

(L^1)

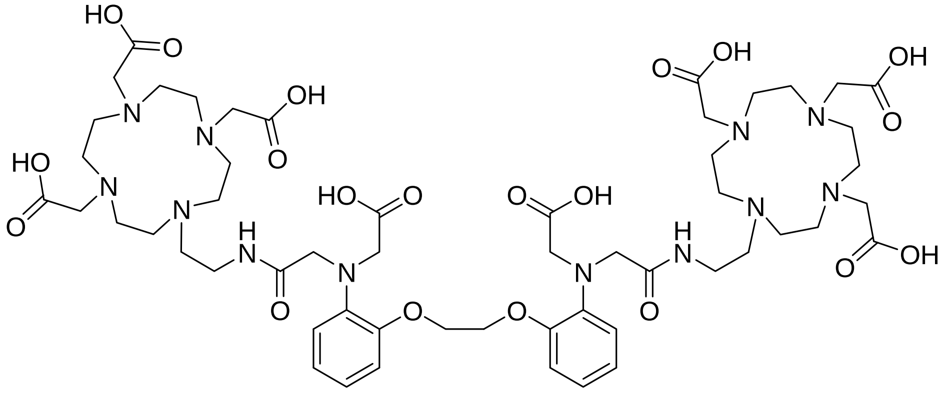

Compound 18 (0.7 g, 0.4 mmol) was dissolved in 25 ml TFA:H_2O:TIPS (99:0.5:0.5) and stirred at room temperature overnight. The solvents were evaporated under vacuum and redissolved in CH_2Cl_2 (2*10 ml) and MeOH (2*10 ml) and evaporated under vacuum till dry. The crude oil obtained was then purified by RP-HPLC using method B to obtain the final ligand (**L^1**) as white solid (0.12 g, 25%). **^{1}H NMR** ($CDCl_3$, 400MHz), δ (ppm): 7.06-6.99 (m, 4H), 6.94 (t, *J*=7.0 Hz, 2H), 6.87-6.85 (m, 2H), 4.27 (s, 4H), 3.83 (s, 4H), 3.77 (s, 4H), 3.58 (br. s, 8H), 3.45 (s, 4H), 3.28-3.12 (m, 24H), 3.02-2.97 (m, 4H), 2.82-2.75 (m, 12H).

^{13}C NMR (D_2O, 100MHz), δ (ppm): 33.5, 47.6, 49.2, 50.5, 50.6, 51.0, 55.3, 56.1, 56.7, 57.9, 67.0, 113.0, 117.4, 121.4, 122.5, 138.9, 150.1, 169.9, 170.5, 174.7, 177.6.

ESI-MS: calculated for $[C_{54}H_{82}N_{12}O_{20} - H]^-$ *m/z* 1217.6, found 1217.6

General method for preparation of 20 and 21

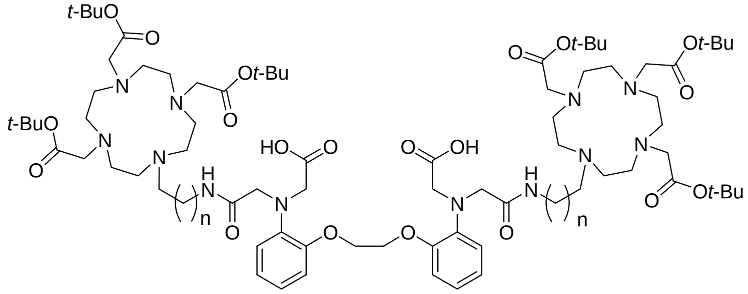

Compound **10/11** (2 mmol) was dissolved in 5 ml of dry N-methylpyrollidinone (NMP) with 50 μl of dry Et_3N and heated at 60°C for 15 min. Anhydride **19** was then added to this reaction mixture (295 mg, 0.67 mmol) in small lots under N_2. After complete addition of **19**, the solution was kept under continuous stirring at 60°C overnight. The solvent was then evaporated and the crude mixture was re-dissolved in CH_2Cl_2 and extracted with water. The collected organic layer evaporated to get yellow oil. The crude product (**20/21**) was then purified by RP-HPLC using method A to get light yellow fluffy solid.

1,2-bis{[2-{[({1-[1,4,7-tris(*tert*-butoxycarbonylmethyl)-1,4,7,10-tetraazacyclododecane-10-yl]eth-2-yl}amino)carbonyl]methyl}-(carboxymethyl)amino]phenoxy}ethane

(20)

Yield : 0.57 mg (55%).

^{1}H NMR ($CDCl_3$, 400MHz), δ (ppm): 7.01-6.98 (m, 2H), 6.92-6.89 (m, 2H), 6.77-6.74 (m, 4H), 4.56 (d, *J*=6.4 Hz, 2H, CH*H*O), 4.34 (d, *J*=15.5Hz, 2H, CH*H*CONH), 4.01 (d, *J*=17.8 Hz, 2H, CH*H*COOH), 3.91 (d, *J*=6.4 Hz, 2H, C*H*HO), 3.48 (d, *J*=17,8 Hz, 2H, CH*H*COOH), 3.36-3.21 (m, 22H), 3.08-2.80 (m, 12H), 2.78-2.69 (m, 6H), 2.76-2.56 (m, 18H), 1.47 (s, 36H), 1.43 (s, 18H).

^{13}C NMR ($CDCl_3$, 100MHz), δ (ppm): 28.1, 29.6, 32.1 (CH_2*C*H_2CONH), 47.8, 49.7, 50.3, 51.3, 53.5, 54.8, 56.5, 58.5 (*C*H_2COOH), 60.7 (N*C*H_2CONH), 66.4 (*C*H_2O), 81.5, 81.8, 112.1, 115.4, 119.5, 120.6, 139.2, 149.4, 170.1, 170.2, 175.0 (*C*ONH), 175.2 (*C*ONH).

ESI-MS: calculated for $[C_{78}H_{130}N_{12}O_{20} - H]^-$ *m/z* 1553.9, found 1554.0

1,2-bis{[3-{[({1-[1,4,7-tris(*tert*-butoxycarbonylmethyl)-1,4,7,10-tetraazacyclododecane-10-yl]prop-3-yl}amino)carbonyl]methyl}-(carboxymethyl)amino]phenoxy}ethane

(21)

Yield: 0.42 mg (40%).

^{1}H NMR ($CDCl_3$, 400MHz), δ (ppm): 7.08-7.06 (m, 2H), 6.91-6.89 (m, 2H), 6.85-6.82 (m, 4H), 4.49 (br. s, 2H), 4.31 (br. s, 4H), 4.08-3.73 (m, 8H), 3.57-3.09 (m, 20H), 3.04-2.47 (m, 32H), 2.40 (br. s, 4H), 2.01 (br. s, 2H), 1.53 (s, 18H), 1.48 (s, 36H).

^{13}C NMR ($CDCl_3$, 100MHz), δ (ppm): 175.7, 173.4, 170.9, 170.2, 150.2, 139.8, 120.3, 120.2, 115.7, 112.2, 82.2, 82.0, 66.6, 61.0, 58.7, 56.5, 55.3, 49.6, 49.1, 47.6, 35.5, 28.6, 28.4, 22.2.

ESI-MS: calculated for $[C_{80}H_{134}N_{12}O_{20}+ H]^+$ *m/z* 1584.0, found 1584.0

General method for the synthesis of L^1 and L^2. Neat triflouoroacetic acid (70 ml) was added to the previously obtained compound **20 or 21** (0.32 mmol) and the reaction was stirred at rt for 24 hrs. TFA was then evaporated, the residue dried on vacuum and purified by RP-HPLC using method B.

1,2-bis{[2-{[({1-[1,4,7-tris(carboxymethyl)-1,4,7,10-tetraazacyclododecane-10-yl]eth-2-yl}amino)carbonyl]methyl}-(carboxymethyl)amino]phenoxy}ethane

(L^1)

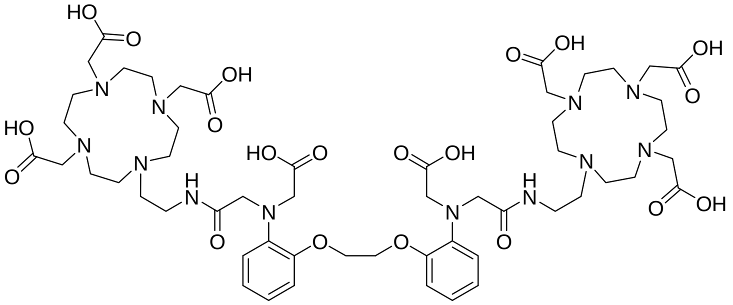

Yield: 0.22 mg (60%).

^{1}H NMR ($CDCl_3$, 400MHz), δ (ppm): 7.06-6.99 (m, 4H), 6.94 (t, *J*=7.0 Hz, 2H), 6.87-6.85 (m, 2H), 4.27 (s, 4H), 3.83 (s, 4H), 3.77 (s, 4H), 3.58 (br. s, 8H), 3.45 (s, 4H), 3.28-3.12 (m, 24H), 3.02-2.97 (m, 4H), 2.82-2.75 (m, 12H).

^{13}C NMR (D_2O, 100MHz), δ (ppm): 33.5, 47.6, 49.2, 50.5, 50.6, 51.0, 55.3, 56.1, 56.7, 57.9, 67.0, 113.0, 117.4, 121.4, 122.5, 138.9, 150.1, 169.9, 170.5, 174.7, 177.6. IR [cm^{-1}]: 3426 (vs), 2964 (m), 2929 (m), 2860 (m), 1718 (s), 1637 (vs), 1384 (s), 1355 (s), 1328 (m), 1240 (s), 1203 (s), 762 (m), 694 (m).

ESI-MS: calculated for $[C_{54}H_{82}N_{12}O_{20} - H]^-$ *m/z* 1217.6, found 1217.6

ESI-MS of **Gd_2L^1**: calculated for $[C_{54}H_{76}Gd_2N_{12}O_{20} – H + Na]^-$ *m/z* 1547.1, found 1547.6

ESI-MS of **Eu_2L^1**: calculated for $[C_{54}H_{76}Eu_2N_{12}O_{20} – H]^-$ *m/z* 1155.4, found 1155.5

1,2-bis{[3-{[({1-[1,4,7-tris(carboxymethyl)-1,4,7,10-tetraazacyclododecane-10-yl]prop-3-yl}amino)carbonyl]methyl}-(carboxymethyl)amino]phenoxy}ethane

(L^2)

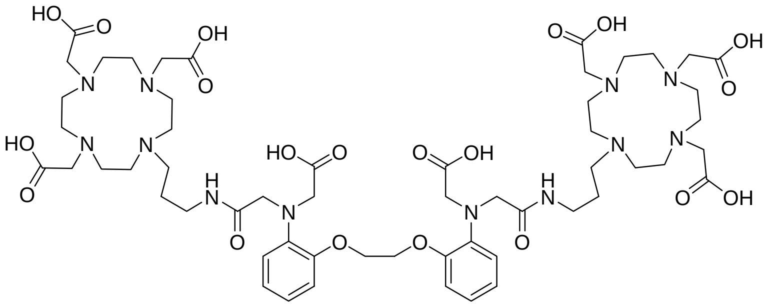

Yield: 0.13 mg from 400 mg of **11** (40%).

^{1}H NMR (D_2O, 400MHz), δ (ppm): 6.98-6.91 (m, 4H), 6.88 (t, *J*= 7.4, 2H), 6.82-6.80 (m, 2H), 4.20 (s, 4H), 3.78 (s, 4H), 3.74 (s, 4H), 3.57 (s, 4H), 3.39-3.31 (m, 8H), 3.27-3.20 (m, 8H), 3.13-2.92 (m, 20H), 2.89-2.83 (m, 8H), 2.65 (br. s, 4H), 1.61-1.53 (m, 4H).

^{13}C NMR (D_2O, 100MHz), δ (ppm): 177.7, 174.4, 149.9, 138.5, 122.3, 121.5, 117.4, 113.2, 67.1, 57.6, 56.2, 56.1, 55.4, 50.9, 50.5, 49.6, 49.2, 36.4, 22.6.

ESI-MS: calculated for $[C_{56}H_{86}N_{12}O_{20} - H]^-$ *m/z* 1245.6 found 1245.5

ESI-MS of **Gd_2L^2:** calculated for $[C_{56}H_{80}Gd_2N_{12}O_{20} + H]^+$: *m/z* 1553.1, found 1553.6

dimethyl 3,3'-(2,2'-(ethane-1,2-diylbis(oxy))bis(2,1-phenylene))bis(azanediyl)dipropanoate

(22)

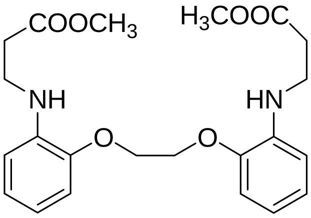

Compound **2** (3.9 g, 15.9 mmol), proton sponge (13.7 g, 63.6 mmol) and KI (0.53 g, 3.2 mmol) were taken in 30 ml MeCN and refluxed for 1 h. The RM was cooled down and methylbromopropionate (7 ml, 63.6 mmol) was added. The contents were refluxed for two days. The reaction mixture was filtered, redissolved in toluene and filtered again. The crude product obtained after evaporation was purified by column chromatography using ethylacetate/hexane (0.05:1) solvent mixture to obtain the pure product as solid (4.3 g, 65 %). **^{1}H NMR** (400 MHz, $CDCl_3$), δ ppm: 2.60 (t, 4 H), 3.45 (t, 4 H), 3.64 (s, 6H), 4.34 (s, 4H), 6.65-6.69 (m, 4 H), 6.83-6.9 (m, 4 H).

^{13}C NMR (100 MHz, $CDCl_3$), δ ppm: 34.2, 39.6, 52.1, 37.8, 110.7, 112.1, 122.5, 138.3, 146.4, 173.0.

Compound 23

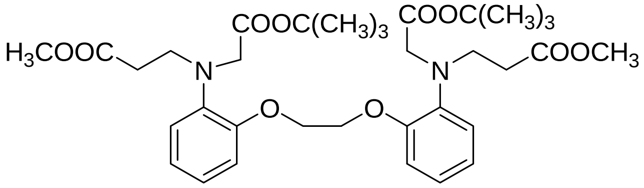

Compound **22** (3.0 g, 7.2 mmol), K_2CO_3 (4.0 g, 28.8 mmol) and KI (0.24 g, 1.4 mmol) was taken in MeCN and kept for refluxing for 1 h. The RM was cooled down and *tert*-butylbromoacetate (4.2 ml, 28.8mmol) was added. This was further refluxed for 2 days. The RM was filtered and the solvent was evaporated to obtain yellow oil. This crude oil was purified by column chromatography to obtain the pure product (**23**) as solid (3.1 g, 68%).

^{1}H NMR ($CDCl_3$, 400 MHz,), δ ppm: 1.39 (s, 18 H), 2.58 (t, 4 H), 3.58 (s, 6 H), 3.63 (t, 4 H), 3.95 (s, 4H), 4.33 (s, 4 H), 6.93-7.01 (m, 8 H).

^{13}C NMR ($CDCl_3$, 100 MHz,), δ ppm: 26.4, 31.4, 46.2, 53.5, 65.7, 79.2, 112.9, 119.5, 119.9, 120.9, 137.1, 149.8, 168.9, 171.1.

Compound 24

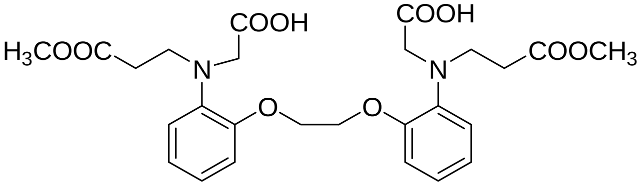

Compound **23** (1 g, 1.5 mmol) was dissolved in minimum CH_2Cl_2 and 15 ml of TFA was added. The RM was stirred overnight. TFA was evaporated and the contents were dried under vacuum. The obtained oil was redissolved in CH_2Cl_2 (2*25 ml) and MeOH (2*25ml), and evaporated under vacuum. The product obtained was obtained in quantitative yields and was used as such without further purification.

^{1}**H NMR** (400 MHz, acetone-*d6*), δ ppm: 2.40 (t, 4 H), 3.35 (s, 6 H), 3.4 (t, 4 H), 3.75 (s, 4H), 4.25 (s, 4 H), 6.65-6.95 (8 H).

^{13}**C NMR** (100 MHz, $CDCl_3$), δ ppm: 33.6, 49.5, 52.1, 56.5, 115.3, 122.5, 123.0, 124.7, 139.8, 172.9, 173.7.

ESI-MS: calculated for $[C_{26}H_{32}N_2O_{10} + H]^+$ *m/z* 531.2, found 531.2

Compound 25

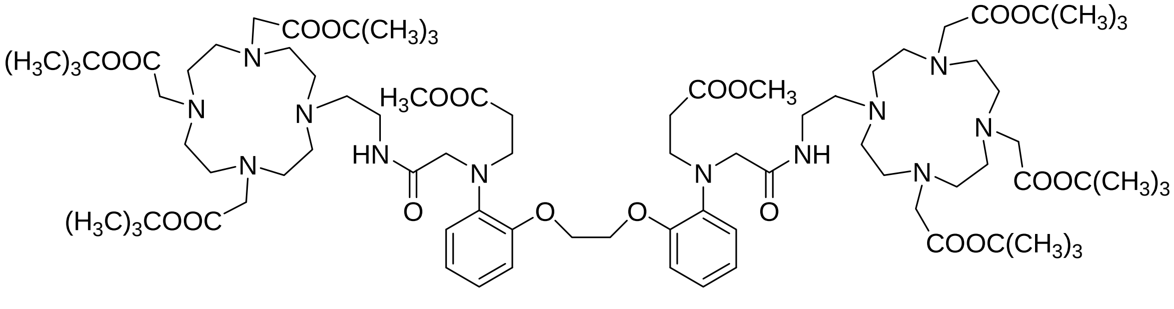

Compound **24** (0.28 g, 0.52 mmol), compound **10** (0.88 g, 1.56 mmol), NMM (0.22 ml, 2 mmol) and HOBt (0.15 g, 1.1 mmol) were dissolved in 4 ml of DMF (dry) under N_2. The reaction mixture was stirred at 60 °C. After 1 h, it was brought to room temperature and EDC (0.22 g, 1.1 mmol) was added. The contents were stirred overnight at 60 °C. DMF was evaporated and dried under vacuum. The obtained mixture was dissolved in $CHCl_3$ and extracted with water. The collected organic layer was dried under anhydrous Na_2SO_4 and evaporated under vacuum. The crude product obtained (**25**) was purified by column chromatography using $MeOH/CH_2Cl_2$ (0.1:1) as the solvent mixture to obtain the pure product as yellow solid (0.28 g, 30 %).

ESI-MS calculated for $[C_{82}H_{138}N_{12}O_{20} + 2H]^{2+}$ *m/z*: 806.0, found 806.5

Compound L^3

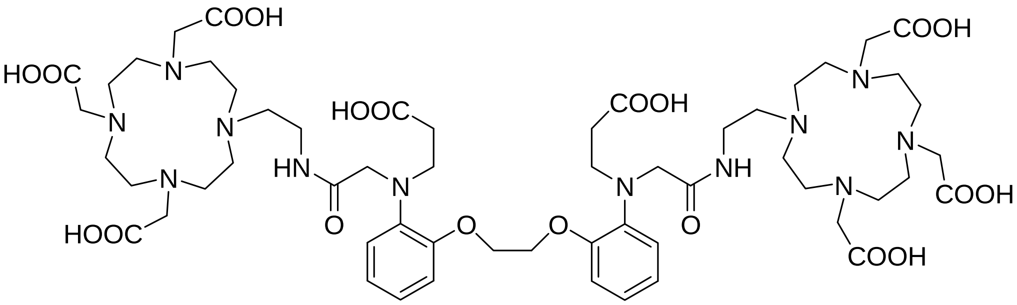

Compound **25** (0.2 g, 0.1 mmol) was dissolved in THF:MeOH:H_2O (3:2:2) and LiOH (0.06 g, 0.25 mmol) was added. The reaction mixture was stirred for 2 h. The completion of reaction was monitored by ESI-MS. The solvent was evaporated and 20 ml of TFA was added to it. The RM was stirred overnight at RT. TFA was evaporated under vacuum and the crude product obtained was purified by RP-HPLC to obtain the pure lyophilized product (**L^3**) as white solid (0.56 g, 48%).

^{1}H NMR (250 MHz, D_2O), δ ppm 2.79 - 2.92 (m, 4 H) 3.03 - 3.14 (m, 4 H) 3.14 - 3.27 (m, 8 H) 3.38 - 3.53 (m, 14 H) 3.55 - 3.70 (m, 16 H) 3.81 - 3.91 (m, 8 H) 4.06 (br. s., 8 H) 4.32 (s, 4 H) 4.81 (s, 4 H) 7.41 (t, 2 H) 7.52 (d, 2 H) 7.66 (t, 2 H).

^{13}C NMR (62 MHz, D_2O), δ ppm: 29.1, 32.7, 45.9, 46.7, 47.9, 48.6, 48.8, 51.6, 51.7, 53.7, 56.1, 65.2, 111.3, 119.5, 119.9, 125.4, 131.3, 149.8, 173.8.

ESI-MS calculated for $[C_{56}H_{86}N_{12}O_{20} + H]^+$ *m/z*: 1245.6, found 1245.7.

Gd_2L^3

ESI-MS: calculated for $[C_{56}H_{78}Gd_2N_{12}O_{20} - H]^-$ *m/z*: 1554.4, found 1554.8

N,N'-(2,2'-(ethane-1,2-diylbis(oxy))bis(2,1-phenylene))bis(2-bromoacetamide)

(26)

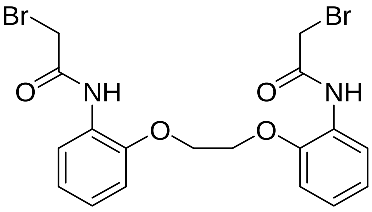

Compound **2** (1.3 g, 5.3 mmol) was taken in MeCN (30 ml) with Na_2CO_3 (1.7 g, 16 mmol) and kept under ice. Bromoacetyl bromide (1.0 ml, 11.7 mmol) was added slowly to it. After complete addition, the RM was stirred for 4 h under ice. Few drops of water were added to quench the reaction and the solvent was evaporated under vacuum. The oil obtained was dissolved in minimum amount of MeOH and then the cold diethylether was added. The precipitates were filtered out to obtain the pure product (**26**) as white solid (1.4 g, 56%).

^{1}H NMR (400 MHz, acetone-*d*$_6$), δ ppm: 2.85 (s, 4 H), 4.63 (s, 4 H), 7.16 (t, *J*=7.88 Hz, 2 H), 7.45 (d, *J*=8.39 Hz, 2 H), 7.66 (t, *J*=7.88 Hz, 2 H), 7.82 (d, *J*=7.88 Hz, 2 H).

^{13}C NMR (100 MHz, acetone-*d*$_6$), δ ppm: 30.7, 69.4, 116.5, 121.9, 125.9, 135.0, 152.5.

ESI-MS: calculated for $[C_{12}H_{18}Br_2N_2O_4 + Na]^+$ *m/z*: 508.9 found, 509.0 with isotopic distribution of - Br.

tri-tert-butyl 1,4,7,10-tetraazacyclododecane-1,4,7-tricarboxylate

(27)

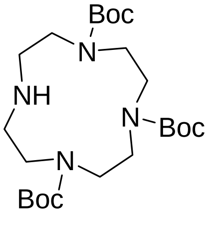

Cyclen (3 g, 17.5 mmol) was dissolved in 100 ml of $CHCl_3$ containing triethylamine (7.5 ml). Boc-anhydride (11.4 g, 52.5 mmol) dissolved in $CHCl_3$ was added slowly at 0 °C. After the complete addition the RM was stirred overnight at RT. The solvent was evaporated and the crude product was flash chromatographed with diethylether as eluent to obtain the pure product as transparent fluffy solid (4.0 g, 50%).

^{1}H NMR (300 MHz, $CDCl_3$), δ ppm: 1.36 (s, 18 H), 1.38 (s, 9 H), 2.69 - 2.82 (m, 4 H), 3.15 - 3.33 (m, 8 H), 3.55 (br. s., 4 H).

^{13}C NMR (75 MHz, $CDCl_3$), δ ppm: 28.3, 28.5, 45.2, 45.5, 49.1, 49.2, 49.4, 50.8, 53.3, 79.0, 79.2, 155.2. 155.5.

ESI-MS: calculated for $[C_{23}H_{44}N_4O_6 + H]^+$ *m/z:* 473.3333, found 473.3338

hexa-tert-butyl 10,10'-(2,2'-(2,2'-(ethane-1,2-diylbis(oxy))bis(2,1-phenylene))bis(azanediyl)bis(2-oxoethane-2,1-diyl))bis(1,4,7,10-tetraazacyclododecane-1,4,7-tricarboxylate)

(28)

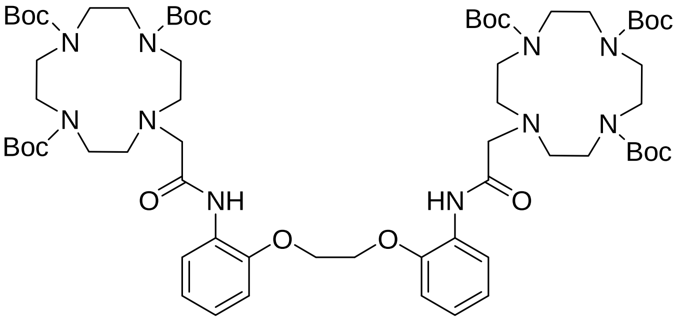

Compound **27** (3.9 g, 8.3 mmol), Na_2CO_3 (2.8 g, 20.7 mmol) and KI (0.27 g, 1.6 mmol) were dissolved in DMF (dry) and heated at 60 °C for 1 h. The RM was cooled down and compound **26** (1.6 g, 3.3 mmol) dissolved in DMF was added. The contents were heated at the same temperature overnight. It was then filtered and the solvent was evaporated under vacuum. To the oil obtained, 25 ml of CH_2Cl_2 and triethylamine (0.28ml, 2 mmol) was added. After half an hour, Boc-anhydride (0.22g, 1 mmol) was added and the reaction mixture was stirred for another 3 hrs.

The solvent was then evaporated and the obtained oil was purified by column chromatography using MeOH/CH_2Cl_2 (0.05:1) as the solvent mixture to get the product (**28**) in 40% yield.

^{1}H NMR (400 MHz, $CDCl_3$), δ ppm: 1.38 (br. s., 34 H), 1.43 (s, 24 H), 2.74 (br. s., 6 H), 3.14 - 3.53 (m, 30 H), 4.40 (s, 4 H), 6.93 (t, *J*=7.38 Hz, 4 H), 7.05 (t, *J*=7.63 Hz, 2 H), 7.78 - 8.16 (m, 2 H).

^{13}C NMR (100 MHz, $CDCl_3$), δ ppm: 28.8, 29.0, 31.3, 47.9, 48.1, 48.3, 49.7, 49.8, 50.6, 51.0, 55.8, 67.4, 79.8, 79.9, 111.9, 121.6, 121.8, 121.9, 122.8, 122.9, 125.4, 127.3, 149.5, 155.7, 156.4, 156.6, 169.6.

ESI-MS calculated for $[C_{64}H_{104}N_{10}O_{16} + H]^+$ *m/z:* 1269.7, found 1269.8.

tri-tert-butyl 10-(2-bromoacetyl)-1,4,7,10-tetraazacyclododecane-1,4,7-tricarboxylate

(29)

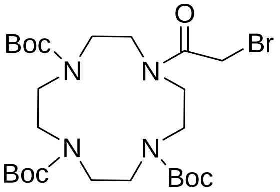

Compound **27** (1.0 g, 2.1 mmol) and bromoacetic acid (0.4 g, 2.7 mmol) were dissolved in 25 ml of CH_2Cl_2. After 15 min, DCC (0.6 g, 2.7 mmol) was added and the RM was stirred for another 6 h. It was then filtered and the solvent was evaporated to obtain the crude oil. The oil was flash chromatographed using diethylether as the eluent to obtain the pure product as the white fluffy solid (1.1 g, 91%).

^{1}H NMR (400 MHz, $CDCl_3$), δ ppm: 3.42 (s, 18 H), 3.46 (s, 9 H), 5.27 - 5.49 (m, 12 H), 5.81 (s, 4 H).

^{13}C NMR (100 MHz, $CDCl_3$), δ ppm: 25.2, 25.9, 28.7, 28.8, 34.0, 49.7, 49.9, 50.1, 50.5, 51.3, 51.9, 60.7, 80.7, 80.8, 81.0, 155.7, 157.6, 167.9.

ESI-MS: calculated for $[C_{25}H_{45}BrN_4O_7 + Na]^+$ *m/z*: 615.23638, found 615.23701.

Compound **30**

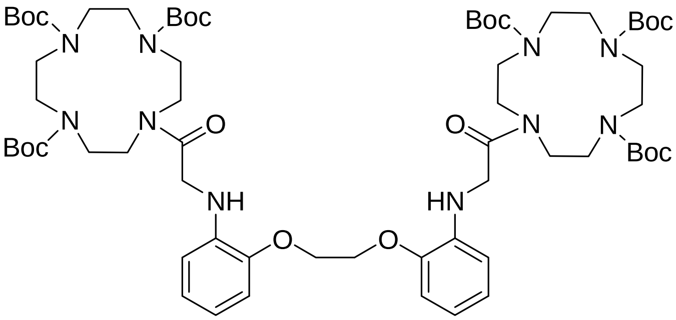

Compound **2** (0.62 g, 2.5 mmol) and Na_2CO_3 (0.66 g, 6.2 mmol) were taken up in MeCN (50 ml) and stirred for two hours. Compound **29** (3 g, 5.1 mmol) dissolved in 20 ml of MeCN was added to the reaction mixture slowly. After complete addition, the RM was stirred for 18 h at RT It was filtered, the solvent evaporated and the residue obtained was re-dissolved in CH_2Cl_2. The CH_2Cl_2 was extracted with water and washed with brine. The organic layer collected was dried under anhydrous Na_2SO_4 and evaporated to obtain the crude product. This was purified by column chromatography using $MeOH/CH_2Cl_2$ (0.05:1) as the solvent mixture to obtain the pure product (**30**) (1.8 g, 58%).

^{1}H NMR (400 MHz, $CDCl_3$), δ ppm: 1.45 (s, 36 H), 1.50 (s, 18 H), 3.24 - 3.72 (m, 32 H), 3.88 (s, 4 H), 4.42 (s, 4 H), 6.52 (d, *J*=7.38 Hz, 2 H), 6.69 (t, *J*=7.38 Hz, 2 H), 6.84 (t, *J*=7.38 Hz, 2 H), 6.90 (d, *J*=7.88 Hz, 2 H).

^{13}C NMR (100 MHz, $CDCl_3$), v ppm: 28.8, 28.9, 41.2, 45.8, 50.1, 50.4, 50.9, 51.9, 53.8, 67.3, 80.8, 80.9, 110.9, 111.9, 117.6, 122.0, 137.8, 146.5, 155.9, 157.6, 157.7.

ESI-MS calculated for $[C_{64}H_{104}N_{10}O_{16} + H]^+$ *m/z*: 1269.7,found 1269.8

2,2'-(2,2'-(ethane-1,2-diylbis(oxy))bis(2,1-phenylene))bis(azanediyl)bis(1-(1,4,7,10-tetraazacyclododecan-1-yl)ethanone)

(31)

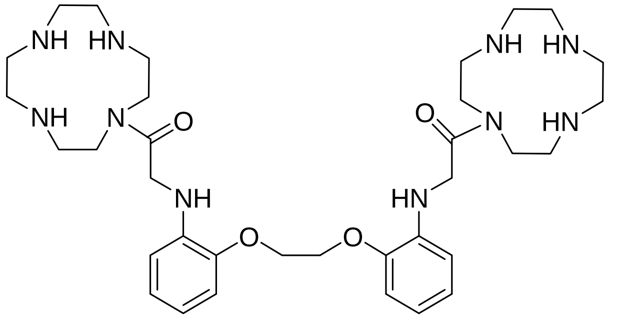

Compound **30** (1.5 g, 0.92 mmol) was dissolved in minimum amount of CH_2Cl_2 and 15 ml of TFA was added. The RM was stirred for 2 h and the solvent was evaporated under vacuum till dry. The product was obtained as TFA salt in quantitative yields and was used as such for the next reaction without further purification.

^{1}H NMR (400 MHz, D_2O), δ ppm: 2.81 - 2.91 (m, 8 H), 2.97 (s, 8 H), 3.09 - 3.18 (m, 8 H), 3.20 - 3.32 (m, 8 H), 4.26 (s, 4 H), 4.37 (s, 4 H), 6.93 (t, *J*=7.76 Hz, 2 H), 7.08 (d, *J*=8.65 Hz, 2 H).

^{13}C NMR (100 MHz, D_2O), δ ppm: 41.6, 43.0, 43.5, 44.4, 45.2, 45.5, 45.8, 46.3, 46.6, 49.5, 50.6, 50.9, 67.6, 112.2, 113.8, 115.1, 117.9, 120.9, 122.1, 123.6, 123.8, 131.5, 151.1.

ESI-MS calculated for $[C_{34}H_{56}N_{10}O_4 + H]^+$, *m/z* 669.4, found 669.5.

2,2'-(ethane-1,2-diylbis(oxy))bis(N-(2-(1,4,7,10-tetraazacyclododecan-1-yl)ethyl)benzenamine)

(32)

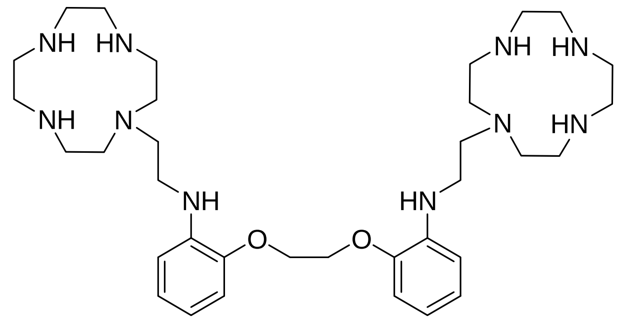

Compound **31** (0.6 g, 0.9 mmol) was taken up in oven dried round bottom flask and cooled to 0 °C under ice bath. BH_3-THF solution (1 M, 8.0 ml) was added to it under N_2 atmosphere while maintaining the temperature at 0 °C. The RM was refluxed for 1-2 h and the completion of the reaction was monitored by ESI-MS. It was then brought to room and acidified with 2 N HCl. The solvent was evaporated under vacuum. The obtained oil was basified with 2 N NaOH and extracted with ethylacetate. The organic layer collected was dried under anhydrous Na_2SO_4 and evaporated under vacuum to obtain the crude product which was purified by RP-HPLC (method A) to obtain the pure product (**32**) (0.14 g, 24%)

^{1}H NMR (400 MHz, D_2O), δ ppm: 2.67 - 2.74 (m, 12 H), 2.78 - 2.84 (m, 6 H), 2.85 - 2.89 (m, 10 H), 2.91 - 3.02 (m, 8 H), 3.17 (t, *J*=5.60 Hz, 4 H), 3.23 (s, 4 H), 4.43 (s, 4 H), 6.72 - 6.79 (m, 4 H), 6.92 (t, *J*=7.63 Hz, 1 H), 7.00 (d, *J*=7.88 Hz, 2 H).

^{13}C NMR (100 MHz, $CDCl_3$), δ ppm: 32.4, 37.8, 40.5, 40.6, 42.5, 47.2, 47.5, 49.3, 57.2, 67.2, 109.9, 112.0, 117.1, 121.3, 136.2, 145.1.

ESI-MS calculated for $[C_{34}H_{60}N_{10}O_2 + H]^+$, *m/z* 641.5, found 641.5

Compound L4

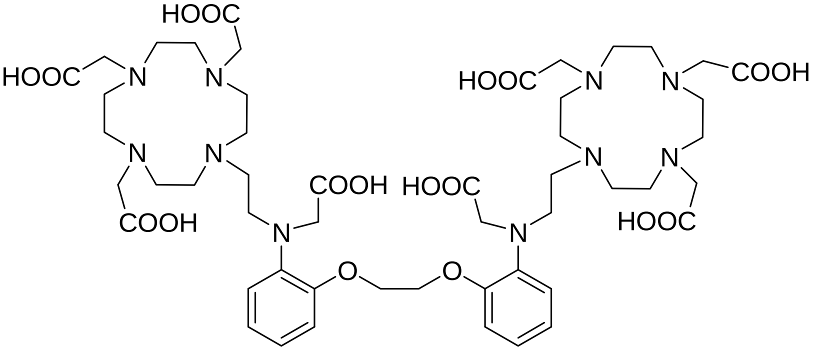

Sodium hydride (0.72 g, 1.8 mmol, 60% emulsion in oil) was taken in 4 ml of freshly distilled THF in an oven dried round bottom flask. The mixture was stirred under ice and after 5 min, compound **32** (0.12 g, 0.18 mmol) was added under N_2. After 20 minutes, methylbromoacetate (0.17 ml, 1.8 mmol) was added and the mixture was kept for stirring at the RT. The completion of reaction was monitored by ESI-MS. After two days, 2 ml of water was added to it and stirred for another 4 h to hydrolyze the methyl esters. This was then evaporated and purified by RP-HPLC to obtain the pure product (0.02 g, 10%).

^{1}H NMR (250 MHz, D_2O), δ ppm: 2.74 - 2.94 (m, 11 H), 2.95 - 3.11 (m, 13 H), 3.12 - 3.33 (m, 12 H), 3.45 (s, 4 H), 3.54 - 3.67 (m, 12 H), 4.12 (s, 4 H), 4.58 (s, 4 H), 7.15 (t, *J*=7.94, 7.32 Hz, 2 H), 7.25 (d, *J*=7.93 Hz, 2 H), 7.35 - 7.55 (m, 4 H).

ESI-MS calculated for $[C_{50}H_{76}N_{10}O_{18} + H]^+$, *m/z*: 1105.5 found 1105.5

3-(benzyloxy)-2-nitrophenol

(33)

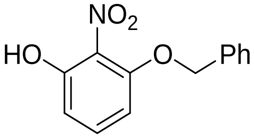

A suspension of 2-Nitroresorcinol (5.0 g, 32.2 mmol) and K_2CO_3 (0.45 g, 3.22 mmol) in dry MeCN (25 ml) was heated at 60°C under nitrogen atmosphere for 1 h. To the resulting solution, benzyl bromide (0.39 ml, 3.22 mmol) dissolved in 10 ml of MeCN (dry) was added slowly within 1 h. The mixture was heated at the same temperature overnight under N_2. It was then cooled down to RT, filtered and the solvent was evaporated. The resulting residue was purified by column chromatography using ethylacetate/hexane. Unreacted 2-nitroresorcinol was recovered in 75% yield as bright orange solid using 2% ethylacetate/hexane as eluent while the benzyl ether **33** was obtained in 0.66 g yield (85%) as bright yellow solid using 5-10% ethylacetate/hexane.

^{1}H NMR (400 MHz, $CDCl_3$, 25°C), δ ppm: 5.21 (s, 2 H), 6.61 (d, *J*=8.4 Hz, 1 H), 6.72 (d, *J*=8.4 Hz, 1 H), 7.32–7.38 (m, 2 H), 7.38–7.45 (m, 2 H), 7.47–7.52 (m, 2 H).

^{13}C NMR (100 MHz, $CDCl_3$, 25°C) δ ppm: 71.3, 105.0, 110.9, 126.8, 128.1, 128.6, 135.4, 135.5, 154.6, 155.6.

ESI-HRMS calculated for $[C_{13}H_{11}NO_4 - H]^-$ *m/z* 244.06153, found 244.06156.

1-(benzyloxy)-3-(3-bromopropoxy)-2-nitrobenzene

(34)

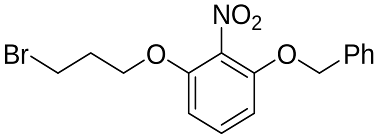

A mixture of phenol **33** (0.98 g, 4 mmol) and K_2CO_3 (1.4 g, 8.0 mmol) in dry DMF was heated to 70°C under nitrogen atmosphere for 1 h. After cooling to RT, dibromopropane (0.9 ml, 12 mmol) was added. The resulting mixture was heated to 85°C for 2 h. The RM was cooled down to room temperature and water was added to it. After extraction with chloroform, the organic layer was dried with anhydrous Na_2SO_4, filtered, and evaporated. The residue was purified by column chromatography using ethylacetate/hexane (0.07-0.1:1) to obtain the ether **34** as light yellow oil (1.20 g 88%).

^{1}H NMR (400 MHz, $CDCl_3$, 25°C), δ ppm: 2.13–2.24 (m, 2 H), 3.45 (t, *J*=6.4 Hz, 2 H), 4.10 (t, *J*=5.8 Hz, 2 H), 5.06 (s, 2 H), 6.55 (t, *J*=6.9 Hz, 2 H), 7.15–7.19 (m, 1 H), 7.19–7.25 (m, 1 H), 7.25–7.30 (m, 4 H).

^{13}C NMR (100 MHz, $CDCl_3$, 25°C), δ ppm: 29.6, 31.9, 66.7, 70.9, 105.6, 106.2, 126.9, 128.2, 128.7, 131.0, 135.5, 150.8, 150.9.

ESI-HRMS calculated for $[C_{16}H_{16}BrNO_4 + Na]^+$ *m/z* 365.01549, found 388.01569

tri-tert-butyl 2,2',2''-(10-(3-(3-(benzyloxy)-2-nitrophenoxy)propyl)-1,4,7,10-tetraazacyclododecane-1,4,7-triyl)triacetate

(35)

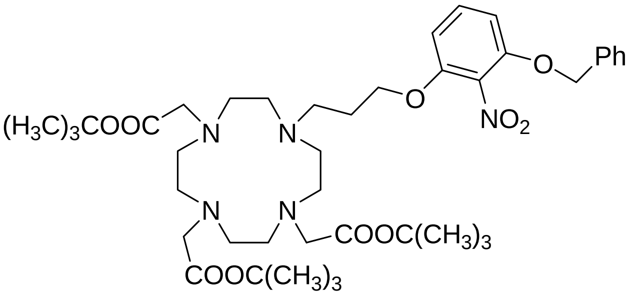

A mixture of Tris-*tert*-Bu-DO3A (1.84 g, 3.7 mmol) and K_2CO_3 (1.3 g, 9.25 mmol) in dry DMF (15 ml) was heated for 1 h under nitrogen atmosphere at 60°C. To this KI (0.083 g, 0.05 mmol) was added followed by slow addition of bromide **34** (1.75 g, 4.8 mmol) dissolved in dry DMF (5 ml). After complete addition the RM was heated overnight at the same temperature. It was then cooled down and excess of DMF was evaporated. Water was added to it and the resulting mixture was extracted with dichloromethane. The organic layer was dried with anhydrous Na_2SO_4, filtered, and evaporated to obtain yellow oil. The crude product was purified by column chromatography using $MeOH/CH_2Cl_2$ (0.02:1) to obtain product **35** as light yellow fluffy powder.(1.80 g 66%).

^{1}H NMR (250 MHz, CDCl$_3$), δ ppm: 1.72–1.88 (m, 2 H), 2.26 (s, 7 H), 2.49 (s, 4 H), 2.68 (br s, 4 H), 2.74 (s, 3 H), 2.83 (s, 2 H), 2.96 (d, *J*=6.9 Hz, 2 H), 3.05 (br s, 4 H), 3.94 (t, *J*=5.9 Hz, 2 H), 5.04 (s, 3 H), 6.57 (t, *J*=8.3 Hz, 2 H), 7.14–7.21 (m, 2 H), 7.25 (s, 4 H).

^{13}CNMR (62 MHz, CDCl$_3$, 25°C), δ ppm: 25.2, 27.8, 27.9, 50.1, 50.2, 50.7, 52.8, 55.8, 56.6, 68.1, 71.0, 82.6, 82.9, 106.0, 106.4, 127.1, 128.2, 128.6, 131.5, 135.7, 150.7, 151.0, 172.6, 173.6.

ESI-HRMS calculated for $[C_{42}H_{65}N_5O_{10} + H]^+$ *m/z* 800.48042, found 800.48049.

di-tert-butyl 2,2'-(7-(3-(2-amino-3-hydroxyphenoxy)propyl)-10-(pivaloyloxymethyl)-1,4,7,10-tetraazacyclododecane-1,4-diyl)diacetate

(36)

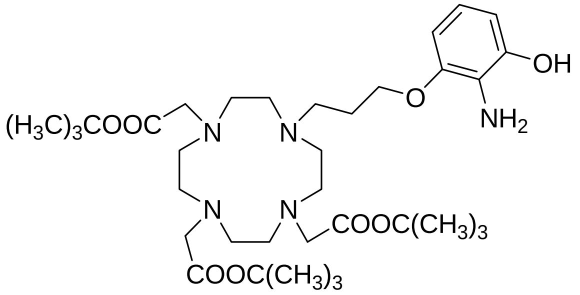

A solution of nitro compound **35** (1.5 g, 1.87 mmol) in methanol (10 ml) was hydrogenated under 2 atm of hydrogen over Pd-C (10%, 0.15 mg) for 4 h in a Parr apparatus Thereafter, the mixture was filtered and the filtrate was concentrated in vacuo. The crude product (**36**) was used as such for the next reaction without further purification (1.0 g 85%).

^{1}H NMR (400 MHz, CDCl$_3$, 25°C), δ ppm: 1.45 (s, 9 H), 1.46 (s, 18 H), 1.82 (s, 2 H), 2.50 (br. s., 7 H), 2.76 (s, 4 H), 2.83 (s, 4 H), 3.00 (br. s., 3 H), 3.05 (s, 3 H), 3.17 (s, 8 H), 4.21 (br. s., 2 H), 6.91 (d, *J*=8.1 Hz, 1 H), 6.97 (d, *J*=8.1 Hz, 1 H), 7.37 (t, *J*=8.4 Hz, 1 H).

^{13}C NMR (100 MHz, CDCl$_3$), δ ppm: 26.4, 27.8, 27.9, 0.4, 51.4, 52.7, 55.7, 56.5, 66.9, 82.5, 82.8, 103.8, 109.5, 117.3, 124.3, 145.3, 147.0, 172.6, 173.6.

ESI-HRMS calculated for $[C_{35}H_{65}N_5O_8 + H]^+$ *m/z*: 680.45201, found 680.45891.

2,2',2''-(10-(3-(2-amino-3-hydroxyphenoxy)propyl)-1,4,7,10-tetraazacyclododecane-1,4,7-triyl)triacetic acid

(37)

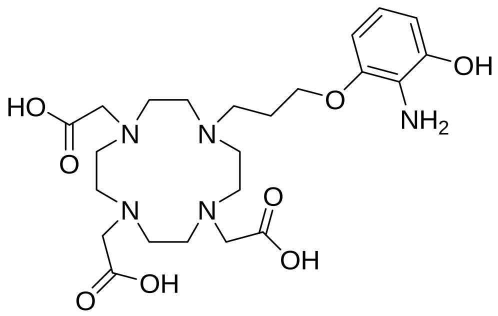

The triester **36** (0.5 g, 0.7 mmol) was hydrolyzed in neat TFA (50 ml) for 24 h at room temperature. The TFA was then evaporated and the residue was dried on vacuum. The residue was then dissolved in water, pH was adjusted to 7 with 1 N NaOH and the solution was purified by RP-HPLC using methanol as solvent B in method C. (0.25 g, 68%).

^{1}H NMR (400 MHz, D_2O), δ ppm: 1.96 (br s, 2 H), 2.91–3.25 (m, 20 H), 3.42–3.65 (m, 6 H), 4.00 (t, *J*=5.3 Hz, 2 H), 6.48–6.57 (m, 2 H), 7.06–7.16 (m, 1 H).

^{13}CNMR (100 MHz, D_2O), δ ppm: 49.2, 50.0, 50.7, 54.6, 55.9, 66.6, 104.4, 107.4, 108.9, 130.2, 150.9, 152.9, 167.5.

ESI-HRMS calculated for $[C_{23}H_{37}N_5O_8 + H]^+$ *m/z*: 512.27149, found 512.27093.

2,2',2''-(10-(3-(2-(bis(carboxymethyl)amino)-3-(carboxymethoxy)benzyloxy)propyl)-1,4,7,10-tetraazacyclododecane-1,4,7-triyl)triacetic acid

(L^5)

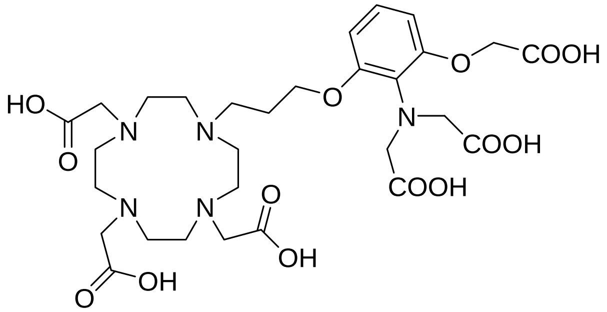

A solution of aniline **37** (0.1 g, 0.2 mmol) in water (8.0 ml) was taken in a three neck round bottom flask equipped with a pH meter and a water condenser. The pH was adjusted to 10 using solid NaOH followed by addition of bromoacetic acid (0.22 g, 1.6 mmol). The reaction mixture was heated to 90°C. The pH was maintained at 10 by occasional addition of solid NaOH. After the pH remained constant, the reaction mixture was heated for additional 2 h at pH 11. The reaction mixture was then cooled down to room temperature and pH was adjusted to 7 with 1 n HCl. The water was evaporated under vacuum. The ligand was finally purified by RP-HPLC using method C (0.07 g 55%).

^{1}H NMR (400 MHz, D_2O): δ ppm: 1.90 (br s, 2 H), 2.60–2.85 (m, 8 H), 3.01 (br s, 8 H), 3.13 (s, 4 H), 3.21 (br. s., 1 H), 3.25 (br. s., 1 H), 3.45 (s, 2 H), 3.77 (br. s., 2 H), 3.81 (s, 4 H), 4.33 (s, 2 H), 6.22 (d, *J*=8.7 Hz, 1 H), 6.32 (d, *J*=8.39 Hz, 1 H), 6.81–6.91 (m, 1 H).

^{13}C NMR (100 MHz, D_2O): δ ppm: 21.3, 46.9, 47.0, 48.2, 49.7, 50.1, 50.9, 54.5, 57.5, 64.5, 64.8, 104.6, 104.8, 118.2, 128.9, 150.7, 150.8, 168.5, 170.4, 171.7, 172.6.

ESI-HRMS calculated for $[C_{29}H_{43}N_5O_{14} + H]^+$ *m/z* 686.28793, found 686.28920.

ESI-MS of **Gd-L^5:** calculated for $[C_{39}H_{38}GdN_5O_{14} - H]^-$ *m/z* 837.2, found 837.2 $[M - H]^-$, 861.1 $[M – H + Na]^-$ with isotopic distribution for Gd^{3+}

ESI-MS of **Eu-L^5:** calculated for $[C_{39}H_{40}EuN_5O_{14} - H]^-$ *m/z* 834.2, found 834.3 with appropriate isotopic distribution for Eu^{3+}.

3-(benzyloxy)-2-nitrobenzaldehyde

(38)

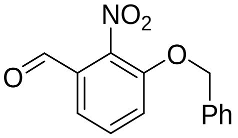

To a solution of 3-methoxy 2-nitro benzaldehyde (2.5 g, 13.8 mmol) in 70 ml CH_2Cl_2 under dry ice, borontribromide (3 ml, 30.3 mmol) was added dropwise. After the complete addition, the RM was stirred at the same temperature for 30 min. MeOH was added slowly to quinch the reaction. The RM was removed from cooling bath and evaporated under vacuum. The crude product obtained was mixed with K_2CO_3 (4.7g, 34.5 mmol) and 60 ml MeCN, and heated at 60 °C for 1 h. The contents were then removed from heating and benzyl bromide (2.5 ml, 20.7 mmol) was added. This was heated again at 60 °C for another 2 h. The RM was filtered, washed with CH_2Cl_2 and evaporated under vacuum. The yellow oil obtained was chromatographed and purified in ethylacetate/hexane (0.2:1) solvent mixture to obtain the product as light yellow solid (3g, 85%).

^{1}H NMR (400 MHz, $CDCl_3$), δ ppm: 4.99 (s, 2 H), 7.09 - 7.18 (m, 6 H), 7.24 (d, *J*=7.63 Hz, 1 H), 7.34 (t, *J*=8.01 Hz, 1 H), 9.69 (s, 1 H).

^{13}C NMR (100 MHz, $CDCl_3$), δ ppm: 70.9, 119.7, 122.5, 126.6, 127.5, 128.0, 128.3, 131.2, 134.4, 139.6, 149.5.

ESI-MS calculated for $[C_{14}H_{11}NO_4 + CH_3OH + Na]^+$ *m/z*: 312.08424, found 312.08420

(3-(benzyloxy)-2-nitrophenyl)methanol

(39)

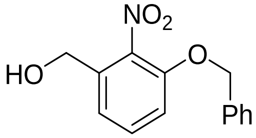

Compound **38** (2 g, 7.8 mmol) was dissolved in minimum amount of CH_2Cl_2 (dry) and 30 ml of MeOH (dry). This was kept under ice and sodium borohydride (98 mg, 2.6 mmol) was added slowly. After complete addition, the RM was stirred at RT for 2 h. The reaction was quenched with the addition of saturated. $NaHCO_3$ solution dropwise. This was evaporated and re-dissolved in CH_2Cl_2 and washed with water. The organic layer was collected and dried under anhydrous. Na_2SO_4 and evaporated under vacuum. The crude mixture obtained was flash chromatographed in CH_2Cl_2 to obtain the desired product as light yellow solid (1.9 g, 90%).

^{1}H NMR (400 MHz, $CDCl_3$), δ ppm: 4.45 (s, 2 H), 4.99 (s, 2 H), 6.84 (d, *J*=8.39 Hz, 1 H), 6.93 (d, *J*=7.88 Hz, 1 H), 7.12 - 7.27 (m, 6 H).

^{13}C NMR (100 MHz, $CDCl_3$), δ ppm: 60.4, 70.6, 113.2, 120.2, 126.6, 127.8, 128.2, 131.7, 133.9, 135.1, 139.9, 149.5.

ESI-MS calculated for $[C_{14}H_{13}NO_4 + K]^+$ *m/z*: 298.04762, found 298.04770

1-(benzyloxy)-3-(bromomethyl)-2-nitrobenzene

(40)

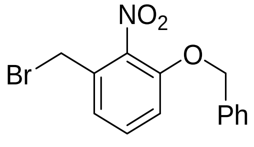

To a solution of **39** (1.8 g, 6.9 mmol) in CH_2Cl_2 (dry) under ice, PPh_3 (3.6 g, 13.8 mmol) was added. Carbon tetrabromide (4.8g, 14.5 mmol) was then added in small lots to it. The reaction mixture was stirred for an hour at room temperature. After an hour, it was evaporated and the crude oil obtained was purified by column chromatography using ethylacetate/hexane (0.1:1) solvent mixture to obtain the product as yellow oil (1.7 g, 77%).

^{1}H NMR (400 MHz, $CDCl_3$), δ ppm: 4.20 (s, 2 H), 4.89 (s, 2 H), 6.80 (t, 2 H), 7.05 - 7.19 (m, 6 H).

^{13}C NMR (100 MHz, $CDCl_3$), δ ppm: 26.4, 71.2, 114.6, 122.8, 127.1, 128.4, 128.8, 130.8, 131.6, 135.4, 141.1, 150.2.

ESI-MS calculated for $[C_{14}H_{12}BrNO_3 + Na]^+$ *m/z* 343.98928, found 343.98911

tri-tert-butyl 2,2',2''-(10-(3-(benzyloxy)-2-nitrobenzyl)-1,4,7,10-tetraazacyclododecane-1,4,7-triyl)triacetate

(41)

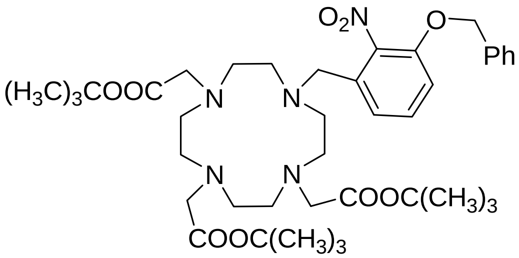

To a solution of tris-*tert*-Bu-DO3A (4 g, 7.8 mmol) in DMF (dry), K_2CO_3 (2.7 g, 19.4 mmol) was added and the resulting mixture was heated for 1 h at 60 °C. Compound **40** (3.2 g, 10.1 mmol) was dissolved in 5 ml of DMF (dry) and added slowly to the RM. The resulting mixture was heated at the same temperature overnight. It was then filtered, the solvent evaporated and the contents re-dissolved in CH_2Cl_2. The organic layer after washing with water was collected, dried under anhydrous Na_2SO_4 and evaporated to yellow oil. This was purified by column chromatography in $MeOH/CH_2Cl_2$ (0.02-0.05:1) to obtain light yellow oil (2.3 g, 40 %).

^{1}H NMR (300 MHz, $CDCl_3$), δ ppm: 1.31 - 1.46 (m, 27 H), 2.02 - 2.44 (m, 2 H), 2.56 (br. s., 4 H), 2.64 - 2.95 (m, 10 H), 3.00 (br. s., 2 H), 3.25 (s, 4 H), 3.49 (br. s., 2 H), 5.05 - 5.17 (m, 2 H), 6.82 - 7.07 (m, 1 H), 7.11 - 7.38 (m, 7 H).

^{13}C NMR (75 MHz, $CDCl_3$), δ ppm: 27.7, 27.9, 28.07, 28.12, 50.2, 51.9, 52.3, 53.8, 55.7, 55.8, 56.04, 56.14, 70.9, 82.3, 82.8, 112.8, 113.3, 122.2, 122.6, 126.90, 126.98, 128.0, 128.2, 128.5, 128.6, 135.2, 135.6, 141.7, 143.3, 149.5, 149.6, 172.6, 173.4.

ESI-MS calculated for $[C_{40}H_{61}N_5O_9 + 2H]^{2+}$ *m/z*: 378.73074, found 378.73094.

tri-tert-butyl 2,2',2''-(10-(2-amino-3-hydroxybenzyl)-1,4,7,10-tetraazacyclododecane-1,4,7-triyl)triacetate

(42)

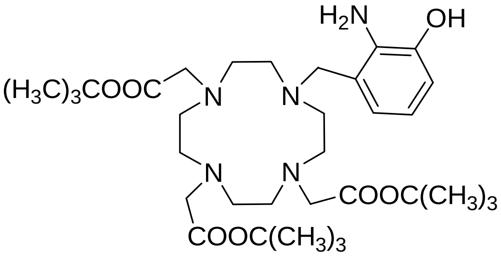

Compound **41** (2 g, 2.6 mmol) was dissolved in MeOH and Pd-C (10%, w/w) catalyst was added. The heterogenous mixture was stirred for 6 h under H_2 atmosphere (3 atm) in a Parr apparatus. The RM was filtered and the solvent was evaporated to get yellow oil. This was used for the next reaction without further purification. (1.7 g, 89%).

^{1}H NMR (300 MHz, $CDCl_3$), δ ppm: 1.37 (s, 5 H), 1.40 - 1.46 (m, 22 H), 2.48 - 2.63 (m, 2 H), 2.63 - 2.93 (m, 11 H), 2.93 - 3.05 (m, 2 H), 3.10 (s, 2 H), 3.21 - 3.29 (m, 2 H), 3.33 (s, 2 H), 6.40 - 6.63 (m, 2 H), 6.73 - 6.86 (m, 1 H).

^{13}C NMR (75 MHz, D_2O), δ ppm : 28.3, 28.4, 48.9, 49.2, 52.1, 52.4, 55.9, 58.9, 82.5, 83.1, 115.9, 119.5, 123.9, 124.2, 133.7, 146.3, 172.8, 173.0.

ESI-MS: calculated for $[C_{33}H_{57}N_5O_7 + H]^+$ *m/z* 363.43308, found 636.43364.

2,2',2''-(10-(2-amino-3-hydroxybenzyl)-1,4,7,10-tetraazacyclododecane-1,4,7-triyl)triacetic acid

(43)

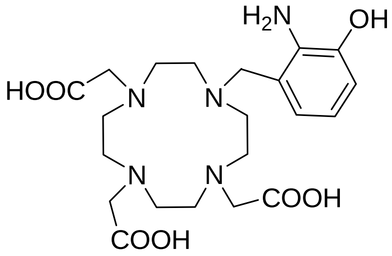

Compound **39** (1.5 g, 2.3 mmol) was dissolved in minimum amount of CH_2Cl_2 and added 20 ml TFA to it. The RM was stirred overnight and then evaporated under vacuum. The crude oil was re-dissolved in CH_2Cl_2 (2*25 ml) and MeOH (2*25 ml) and evaporated until dry. The crude oil was purified by RP-HPLC using the method C using MeOH as solvent B to obtain the desired product as solid (0.4 g, 36 %).

^{1}H NMR (300 MHz, D_2O), δ ppm: 2.53 - 2.84 (m, 5 H), 2.84 - 3.03 (m, 3 H), 3.03 - 3.19 (m, 4 H), 3.18 - 3.45 (m, 8 H), 3.45 - 4.07 (m, 4 H), 6.75 (d, 1 H), 6.82 (d, 1 H), 7.11 (dd, 1 H).

^{13}C NMR (75 MHz, D_2O), δ ppm: 47.89, 47.97, 49.8, 49.9, 51.37, 51.44, 53.1, 54.5, 55.5, 111.9, 114.8, 116.5, 117.7, 120.6, 124.7, 130.1, 150.7, 169.4, 175.4.

ESI-MS calculated for $[C_{21}H_{33}N_5O_7 + H]^-$ *m/z* 468.24527 found 468.24541.

2,2',2''-(10-(2-(bis(carboxymethyl)amino)-3-(carboxymethoxy)benzyl)-1,4,7,10-tetraazacyclododecane-1,4,7-triyl)triacetic acid

(L^6)

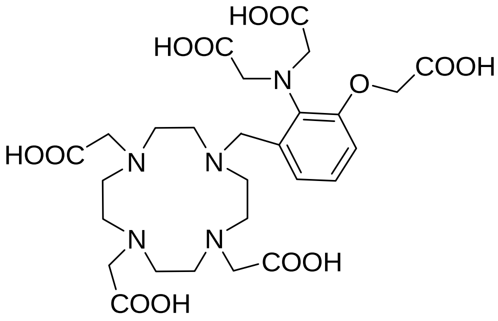

The final ligand $\mathbf{L^6}$ was synthesized from compound **43** (0.1 g, 4.3 mmol) similarly to the synthesis of $\mathbf{L^5}$ from **37**. Desired ligand ($\mathbf{L^6}$) was obtained as solid (0.06 g, 44%)

^{1}**H NMR** (250 MHz, D_2O), δ ppm: 2.97 - 3.55 (m, 22 H), 3.73 (br. s., 2 H), 3.81 - 4.03 (m, 4 H), 4.68 (s, 2 H), 6.89 (d, *J*=3.66 Hz, 1 H), 7.05 - 7.22 (m, 2 H).

^{13}**C NMR** (62 MHz, D_2O), δ ppm: 46.6, 47.2, 47.3, 47.9, 50.9, 51.9, 53.2, 52.3, 63.3, 111.8, 119.6, 126.8, 136.8, 153.7, 171.4, 174.5.

ESI-MS calculated for $[C_{27}H_{39}N_5O_{13} + H]^-$ *m/z* 642.2, found 642.3

ESI-MS of **Gd-L^6**: calculated for $[C_{27}H_{36}GdN_5O_{13} - H]^-$ 794.4, found 794.2 $[M - H]^-$, 817.2 $[M - H + Na]^-$ with appropriate isotopic distribution for Gd^{3+},

ESI-MS of **Eu-L^6** calculated for $[C_{27}H_{35}EuN_5O_{13} - H]^-$ 788.1, found 788.1 with appropriate isotopic distribution for Eu^{3+}.

3-(3-(benzyloxy)-2-nitrobenzyloxy)propan-1-ol

(44)

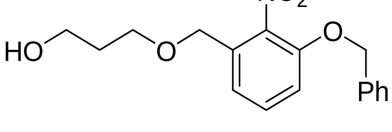

In an oven dried flask, sodium hydride (60% emulsion in oil) (0.8 g, 15.4 mmol) was dispersed in 2 ml of THF (dry) under N_2. After 10 minutes of stirring under ice, compound **39** (2.0 g, 7.7 mmol) dissolved in THF was added slowly. The RM was stirred at the same temperature for 20 minutes. Bromopropanol (1.7 ml, 19.3 mmol) was added dropwise and the mixture was kept for stirring at room temperature overnight. Excess of NaH was destroyed with the addition of water and the mixture was extracted with $CHCl_3$. The organic layer was collected and dried under anhydrous Na_2SO_4 and evaporated to get yellow oil. The crude oil obtained was purified by column chromatography using ethylacetate/hexane as the solvent mixture. The unused reactant (compound **39**) was recovered (0.5 g, 1.9 mmol) at (0.2:1) while the product was obtained at (0.3:1) as yellow solid (1.5 g, 83%).

^{1}H NMR (300 MHz, $CDCl_3$), δ ppm: 1.53 - 1.64 (m, 2 H), 3.35 (t, *J*=5.85 Hz, 2 H), 3.48 (t, *J*=5.85 Hz, 2 H), 4.29 (s, 2 H), 4.90 (s, 2 H), 6.78 (t, *J*=7.38 Hz, 2 H), 7.02 - 7.18 (m, 6 H).

^{13}C NMR (62 MHz, $CDCl_3$), δ ppm: 31.9, 60.3, 68.7, 68.9, 70.9, 113.7, 120.6, 126.8, 128.0, 128.5, 130.9, 131.7, 135.4, 140.5, 149.8.

ESI-HRMS calculated for $[C_{17}H_{19}NO_5 + Na]^+$ *m/z* 340.11554, found 340.11542

1-(benzyloxy)-3-((3-bromopropoxy)methyl)-2-nitrobenzene

(45)

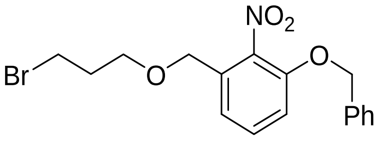

Compound **45** was synthesized from compound **44** (3.5 g, 10.9 mmol) similarly to the synthesis of compound **40** from compound **39**. The product was eluted with ethylacetate/hexane (0.2:1) solvent mixture as light yellow oil (3.6 g, 82 %).

^{1}H NMR (300 MHz, $CDCl_3$), δ ppm: 2.07 - 2.18 (m, 2 H), 3.51 (t, *J*=6.49 Hz, 1 H), 3.58 (t, *J*=5.72 Hz, 1 H), 4.56 (s, 2 H), 5.18 (s, 2 H), 7.04 (dd, *J*=10.55, 8.27 Hz, 2 H), 7.29 - 7.50 (m, 6 H).

^{13}C NMR (75 MHz, $CDCl_3$), δ ppm: 30.7, 32.9, 68.7, 69.0, 71.4, 114.1, 121.0, 127.3, 128.5, 128.9, 131.3, 132.2, 135.8, 150.3.

ESI-MS: calculated for $[C_{17}H_{18}BrNO_4 + Na]^+$ *m/z* 402.03114, found 402.03124

tri-tert-butyl 2,2',2''-(10-(3-(3-(benzyloxy)-2-nitrobenzyloxy)propyl)-1,4,7,10-tetraazacyclododecane-1,4,7-triyl)triacetate

(46)

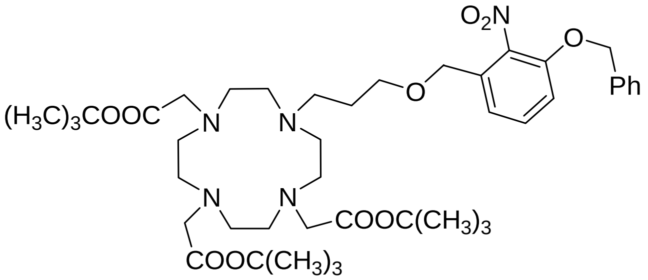

Compound **46** was synthesized from compound **45** (3.0 g, 7.9 mmol) similarly to the synthesis of compound **41** from compound **40**. The product was obtained as yellow solid (3.0 g, 50%) by eluting with $MeOH/CH_2Cl_2$ (0.05:1) solvent mixture ^{1}H NMR (300 MHz, $CDCl_3$), δ ppm: 1.41 (s, 27 H), 1.61 - 1.76 (m, 1 H), 1.91 - 2.10 (m, 1 H), 2.19 - 2.55 (m, 4 H), 2.77 (br. s., 6 H), 2.86 (s, 1 H), 2.94 (s, 1 H), 2.97 - 3.22 (m, 5 H), 3.31 (s, 3 H), 3.41 (s, 4 H), 3.54 (t, *J*=5.21 Hz, 2 H), 4.51 (d, *J*=20.85 Hz, 2 H), 5.16 (s, 2 H), 6.97 (t, *J*=7.12 Hz, 1 H), 7.05 (dd, *J*=8.39, 2.80 Hz, 1 H), 7.29 - 7.42 (m, 6 H).

^{13}C NMR (100 MHz, $CDCl_3$), δ ppm: 28.2, 28.3, 28.5, 48.2, 50.5, 50.8, 52.3, 53.3, 53.5, 55.7, 56.1, 57.2, 67.9, 69.2, 69.8, 70.0, 71.48, 71.5, 82.14, 82.8, 83.2, 114.3, 114.7, 121.0, 121.7, 127.4, 128.6, 129.0, 135.9, 141.1, 150.4, 150.5, 170.4, 170.7, 172.9.

ESI-MS: calculated for $[C_{43}H_{67}N_5O_{10}/2 + H]^+$ *m/z* 407.75167 found 407.75186

tri-tert-butyl2,2',2''-(10-(3-(2-amino-3-hydroxybenzyloxy)propyl)-1,4,7,10-tetraazacyclododecane-1,4,7-triyl)triacetate

(47)

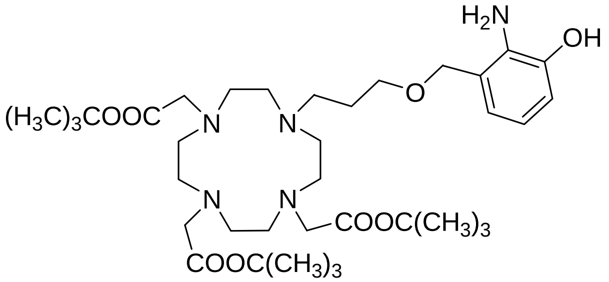

Compound **47** (2 g, 95%) was obtained from compound **46** (2.5 g, 3 mmol) similarly to the synthesis of compound **42** from compound **41**.

^{1}H NMR (300 MHz, $CDCl_3$), δ ppm: 1.38 (s, 9 H), 1.42 (s, 18 H), 1.53 - 1.67 (m, 2 H), 2.13 - 2.52 (m, 12 H), 2.53 - 2.86 (m, 6 H), 3.05 (s, 6 H), 3.37 (t, 2 H), 4.43 (s, 2 H), 6.44 - 6.55 (m, 2 H), 7.10 (s, 1 H).

^{13}C NMR (75 MHz, $CDCl_3$), δ ppm: 27.7, 27.8, 49.9, 50.1, 51.4, 55.6, 56.3, 67.9, 71.9, 82.3, 82.7, 115.6, 117.4, 120.8, 122.8, 134.5, 144.5, 172.4, 173.3.

ESI-HRMS calculated for $[C_{36}H_{63}N_5O_8 + H]^+$ *m/z* 694.47494, found 694.47654

2,2',2''-(10-(3-(2-amino-3-hydroxybenzyloxy)propyl)-1,4,7,10-tetraazacyclododecane-1,4,7-triyl)triacetic acid

(48)

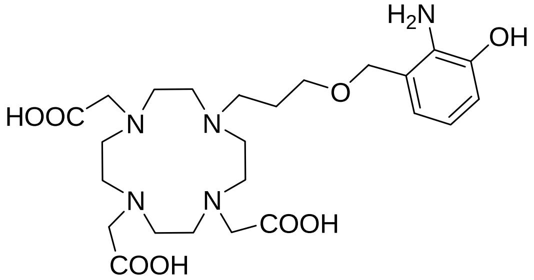

Compound **48** (0.8, 53%) was obtained from compound **47** (2 g, 2.9 mmol) similarly to the synthesis of compound **43** from compound **42**.

^{1}H NMR (250 MHz, D_2O), δ ppm: 1.82 (br. s., 2 H), 3.08 (s, 18 H), 3.28 - 3.51 (m, 6 H), 3.58 (br. s., 2 H), 4.47 (s, 2 H), 6.74 (br. s., 1 H), 6.85 (br. s., 1 H), 6.98 (br. s., 1 H).

^{13}C NMR (62 MHz, D_2O), δ ppm: 24.1, 49.4, 49.7, 50.9, 51.5, 55.1, 55.8, 67.9, 70.0, 115.2, 116.5, 118.2, 121.6, 121.9, 127.2, 130.2, 149.0, 162.7, 163.1.

ESI-MS calculated for $[C_{24}H_{39}N_4O_8 + H]^+$ *m/z* 526.28714 found 526.28604

2,2',2''-(10-(3-(2-(bis(carboxymethyl)amino)-3-(carboxymethoxy)benzyloxy)propyl)-1,4,7,10-tetraazacyclododecane-1,4,7-triyl)triacetic acid

(L^7)

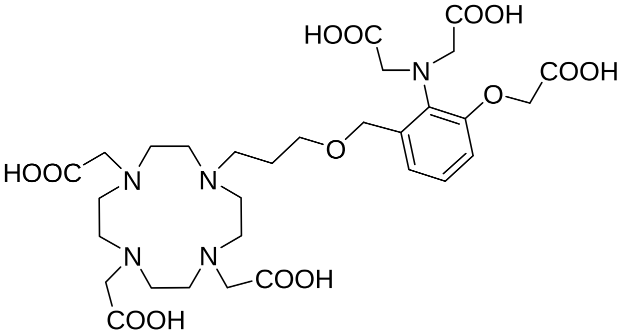

The ligand **L^7** (0.058 g, 44%) was obtained from compound **48** (0.1 g, 0.19 mmol) similarly to the synthesis of ligand **L^6** from compound **43**.

^{1}H NMR (250 MHz, D_2O), δ ppm: 1.89 (br. s., 2 H), 2.80 - 2.91 (m, 4 H), 2.91 - 3.02 (m, 4 H), 3.10 - 3.22 (m, 6 H), 3.26 (br. s., 4 H), 3.31 (br. s., 2 H), 3.36 - 3.47 (m, 2 H), 3.48 - 3.57 (m, 2 H), 3.70 (s, 2 H), 4.01 (br. s., 4 H), 4.63 (s, 2 H), 4.65 (s, 2 H), 6.81 (t, *J*=8.01 Hz, 2 H), 7.13 (t, *J*=8.01 Hz, 1 H).

^{13}C NMR (62 MHz, D_2O), δ ppm: 25.3, 50.86, 50.97, 52.2, 54.3, 55.9, 58.7, 62.0, 68.1, 70.4, 73.1, 116.3, 125.1, 132.1, 135.6, 137.3, 155.9, 172.45, 175.8, 176.7, 176.8.

ESI-MS: calculated for $[C_{30}H_{45}N_5O_{14} + H]^+$ *m/z*: 700.3, found 700.2

ESI-MS of **Gd-L^7**: calculated for $[C_{30}H_{42}GdN_5O_{14} - H]^-$ *m/z:* 852.6, found 853.2 $[M – H]^-$, 875.1 $[M – H + Na]^-$

ESI-MS of **Eu-L^7:** calculated for $[C_{30}H_{42}EuN_5O_{14} - H]^-$ *m/z*: 847.2, found 846.2 $[M – H]^-$, 870.2 $[M – H +Na]^-$ 847.2.

3-((2-methoxyethoxy)methoxy)-2-nitrobenzaldehyde

(49)

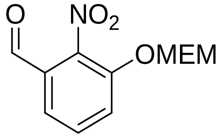

3-methoxy-2-nitro benzaldehyde (1.0 g, 5.5 mmol) was dissolved in CH_2Cl_2; and borontribromide (1.2 ml, 12.3 mmol) was added dropwise under dry ice. After the complete addition, the RM was stirred at the same temperature for 30 min. MeOH was added slowly to quench the reaction. The reaction mixture was removed from cooling bath and evaporated under vacuum. The crude product was re-dissolved in CH_2Cl_2 and DIEA (2.4 ml, 13.7 mmol) was added. Beta-methoxyethoxymethyl ether (1.2 ml, 11 mmol) was then added slowly to it. The reaction mixture was stirred for two hours. It was then evaporated and purified by column chromatography using ethylacetate/hexane (0.1:1) as the solvent mixture to obtain the pure product as oil (1.4 g, 98%).

^{1}H NMR (300 MHz, $CDCl_3$), δ ppm: 3.29 (s, 3 H), 3.48 - 3.52 (m, 2 H), 3.75 - 3.82 (m, 2 H), 5.32 (s, 2 H), 7.49 - 7.53 (m, 1 H), 7.56 - 7.60 (m, 2 H).

^{13}C NMR (75 MHz, $CDCl_3$), δ ppm: 58.7, 68.3, 71.1, 94.1, 122.1, 123.7, 127.8, 131.4, 148.5, 186.8.

ESI-MS: calculated for $[C_{11}H_{13}NO_6 + Na]^+$ *m/z* 278.1, found 278.0

(3-((2-methoxyethoxy)methoxy)-2-nitrophenyl)methanol

(50)

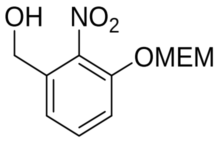

Compound **49** (1.4 g, 5.4 mmol) was dissolved in minimum amount of CH_2Cl_2 and added 25 ml of MeOH (dry) to it. This was kept under ice and sodium borohydride (0.1 g, 2.7 mmol) was added slowly in small lots. After complete addition, the RM was stirred for 1 h. 2 ml of saturated $NaHCO_3$ was added to quench the reaction. The solvent was evaporated, redissolved in CH_2Cl_2 and washed with water and brine. The organic layer collected was dried under anhydrous Na_2SO_4 and evaporated under vacuum. The oil obtained was purified by column chromatography using ethylacetate/hexane (0.1-0.2:1) as the solvent mixture (1.21 g, 79%).

^{1}H NMR (300 MHz, $CDCl_3$), δ ppm: 3.31 (s, 3 H), 3.45 - 3.55 (m, 2 H), 3.71 - 3.83 (m, 2 H), 4.59 (s, 2 H), 5.28 (s, 2 H), 7.13 (d, *J*=7.36 Hz, 1 H), 7.22 (d, *J*=7.93 Hz, 1 H), 7.30 - 7.43 (m, 1 H).

ESI-MS calculated for $[C_{11}H_{15}NO_6 + Na]^+$ *m/z*: 280.07916, found 280.07924

2,2',2''-(10-(3-(3-hydroxy-2-nitrobenzyloxy)propyl)-1,4,7,10-tetraazacyclododecane-1,4,7-triyl)triacetic acid

(51)

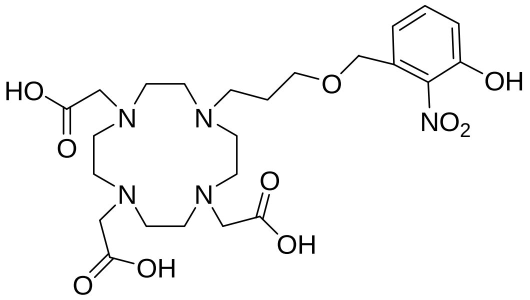

Compound **43** (1 g, 1.2 mmol) was dissolved in minimum amount of CH_2Cl_2 and 15 ml of TFA added to it. The RM was stirred overnight. TFA was evaporated under vacuum and the obtained residue was re-dissolved in CH_2Cl_2 (2*15 ml) and MeOH (2*15 ml) and evaporated to obtain the product in quantitative yields. This was used as such for the next reaction without further purification.

^{1}H NMR (300 MHz, D_2O), δ ppm: 1.63 (br. s., 2 H), 2.71 - 3.03 (m, 14 H), 3.03 - 3.16 (m, 4 H), 3.16 - 3.34 (m, 6 H), 3.53 (s, 2 H), 4.21 (s, 2 H), 6.60 (d, *J*=7.36 Hz, 1 H), 6.79 (d, *J*=7.93 Hz, 1 H), 7.07 (t, *J*=7.74 Hz, 1 H).

^{13}C NMR (100 MHz, D_2O), δ ppm: 22.8, 48.7, 49.3, 50.8, 51.2, 54.3, 55.7, 67.6, 69.0, 117.8, 120.5, 131.4, 132.5, 138.0, 149.1, 170.26, 174.1.

ESI-MS calculated for $[C_{24}H_{37}N_5O_{10} + H]^+$ *m/z*: 556.2, found 556.2

2-bromo-1-morpholinoethanone

(52)

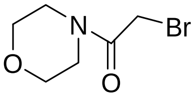

Morpholine (dry) (3.5 ml, 40 mmol) was dissolved in 70 ml diethyether (dry) with triethyamine (11.0 ml, 80 mmol). After 1 h, the RM was cooled down to 0 °C and bromoacetylbromide (5.2 ml, 60 mmol) was added dropwise. After complete addition, the RM was stirred for another 2 h at 0 °C. The salts formed were filtered out and the residue was washed with diethylether and concentrated under vacuum. The diethylether layer was collected, dried under saturated Na_2SO_4 and evaporated to brown oil. This was purified by column chromatography using ethylacetate/CH_2Cl_2 (0.2:1) as the solvent mixture to obtain the pure product (4.0 g, 48%) as oil.

^{1}H NMR (300 MHz, $CDCl_3$), δ ppm: 3.50 (t, *J*=5.10, 4.53 Hz, 2 H), 3.58 - 3.64 (m, 2 H), 3.64 - 3.75 (m, 4 H), 3.84 (s, 2 H).

^{13}C NMR (75 MHz, $CDCl_3$), δ ppm: 25.6, 42.6, 47.3, 66.5, 66.8, 165.7.

ESI-MS: calculated for $[C_6H_{10}BrNO_2 + H]^+$ *m/z*: 207.99677, found 207.99663

triethyl 2,2',2''-(1,4,7,10-tetraazacyclododecane-1,4,7-triyl)triacetate

(53)

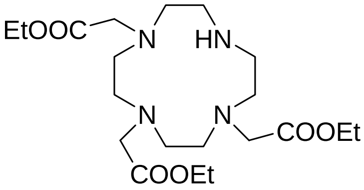

Cyclen (5.0 g, 29 mmol) was dissolved in 200 ml of $CHCl_3$ and $NaHCO_3$ (5.3 g, 63.8 mmol) was added in small lots to it with stirring. Ethyl bromoacetate (7.0 ml, 63.8 mmol) dissolved in 100 ml $CHCl_3$ was added to it dropwise at 0 °C. The reaction mixture was stirred for three days. It was then filtered, concentrated under vacuum and washed with water (5*50 ml). The organic layer collected was dried under anhydrous Na_2SO_4 and evaporated under vacuum to obtain the oily residue. This was purified by column chromatography using $MeOH/CH_2Cl_2$ (0.02-0.05:1) as the solvent mixture. The product (**53**) (4.0 g, 35 %) was eluted with approximately 25% tetra substituted derivative (1.3 g) as the side product.

^{1}H NMR (300 MHz, $CDCl_3$), δ ppm: 1.10 (t, *J*=7.18 Hz, 12 H), 2.77 (s, 15 H), 2.95 (s, 5 H), 3.25 (s, 2 H), 3.34 (s, 5 H), 3.99 (q, *J*=7.05 Hz, 8 H) (integration of protons being reported with 25% of side product).

^{13}C NMR (75 MHz, $CDCl_3$), δ ppm: 13.9, 14.09, 14.03, 47.1, 48.2, 48.9, 51.0, 51.0, 53.6, 54.9, 56.8, 60.4, 61.2, 170.2, 171.0, 176.4.

ESI-MS calculated for $[C_{20}H_{38}N_4O_6 + H]^+$ *m/z*: 431.28641, found 431.58652.

Triethyl 2,2',2''-(10-(3-(3-(benzyloxy)-2-nitrobenzyloxy)propyl)-1,4,7,10-tetraazacyclododecane-1,4,7-triyl)triacetate

(54)

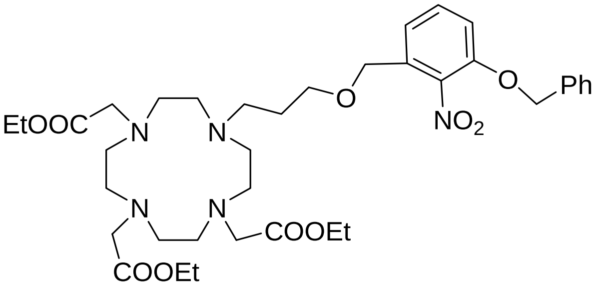

Compound **53** (3.0 g, 6.9 mmol) was taken up in 20 ml DMF (dry) with K_2CO_3 (2.4 g, 17.4 mmol). This was heated at 60 °C for 1 h. The RM was brought to RT and compound **45** (3.0 g, 7.8 mmol) dissolved in DMF was added dropwise to it. The contents were heated at 60 °C overnight. The RM was then filtered and the solvent was evaporated under vacuum. The residue obtained was dissolved in $CHCl_3$ and washed with water. The organic layer collected was dried under anhyd. Na_2SO_4 and evaporated under vacuum. This was purified by column chromatography using $MeOH/CH_2Cl_2$ (0.01-0.05:1) as the solvent mixture. The product (3.0 g, 52 %) was obtained with approximately 13% (0.4 g) of the tetra substituted side product.

^{1}H NMR (300 MHz, $CDCl_3$), δ ppm: 1.10 - 1.20 (m, 10 H), 1.49 - 1.72 (m, 2 H), 1.86 - 2.01 (m, 1 H), 2.14 - 2.50 (m, 8 H), 2.57 - 2.95 (m, 9 H), 3.09 (s, 2 H), 3.19 (s, 3 H), 3.29 - 3.43 (m, 3 H), 3.95 - 4.20 (m, 7 H), 4.42 (s, 2 H), 5.10 (s, 2 H), 6.89 (d, *J*=7.74 Hz, 1 H), 7.00 (d, *J*=8.50 Hz, 1 H), 7.18 - 7.35 (m, 6 H). (The integration of protons being reported with 13% of side product)
^{13}C NMR (75 MHz, D_2O), δ ppm: 13.96, 14.02, 25.9, 50.1, 50.3, 50.4, 50.7, 51.0, 51.3, 51.9, 55.1, 55.2, 55.6, 55.8, 61.5, 61.7, 68.7, 69.9, 71.0, 113.9, 120.5, 126.9, 128.1, 128.6, 131.2, 131.8, 135.5, 149.9, 173.4, 174.0.

ESI-MS calculated for $[C_{37}H_{55}N_5O_{10} + H]^+$ *m/z*: 730.4, found 730.4

triethyl 2,2',2''-(10-(3-(3-hydroxy-2-nitrobenzyloxy)propyl)-1,4,7,10-tetraazacyclododecane-1,4,7-triyl)triacetate

(55)

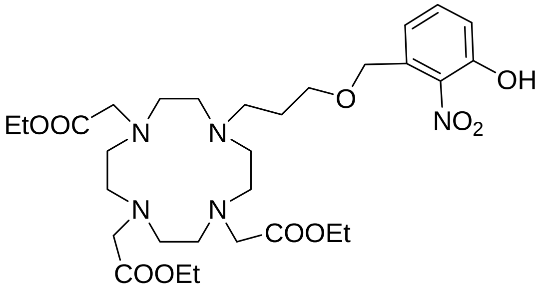

Compound **54** (2 g, 2.7 mmol) was dissolved in minimum amount of CH_2Cl_2 and added 20 ml of TFA to it. This was stirred overnight at room temperature. The TFA was evaporated and the residue obtained was suspended in water. The pH of water layer was increased to 7 and $CHCl_3$ added to it. The contents were washed with water and brine. The organic layer collected was dried under anhyd. Na_2SO_4 and evaporated under vacuum. This was purified by column chromatography using $MeOH/CH_2Cl_2$ (0.02-0.05:1) as the solvent mixture to obtain the product (0.92 g, 54%) with approximately 25% of the tetrasubstituted side product (0.29 g).

^{1}H NMR (300 MHz, $CDCl_3$), δ ppm: 0.76 - 0.91 (m, 2 H), 1.17 - 1.25 (m, 12 H), 1.56 - 1.72 (m, 2 H), 2.02 (s, 1 H), 2.17 - 2.54 (m, 10 H), 2.55 - 2.84 (m, 6 H), 3.10 (s, 2 H), 3.22 (s, 4 H), 3.35 - 3.49 (m, 3 H,) 3.97 - 4.29 (m, 8 H), 4.02 - 4.22 (m, 6 H), 4.49 (s, 2 H), 6.74 (d, *J*=7.37 Hz, 1 H), 7.21 (t, *J*=8.12, 7.74 Hz, 1 H), 7.33 (d, *J*=8.12 Hz, 1 H). (Integration of protons being reported with 25 % of the side product).

^{13}C NMR (75 MHz, $CDCl_3$), δ ppm: 14.0, 25.5, 29.5, 50.0, 51.0, 53, 55.5, 56, 61.5, 61.8, 69.5, 118.0, 119.0, 131.5, 132.0, 138.0, 152.0, 173.5, 174.0.

ESI-MS calculated for $[C_{30}H_{49}N_5O_{10} + H]^+$ *m/z*: 640.35505, found 640.35522.

triethyl 2,2',2''-(10-(3-(3-(2-morpholino-2-oxoethoxy)-2-nitrobenzyloxy)propyl)-1,4,7,10-tetraazacyclododecane-1,4,7-triyl)triacetate

(56)

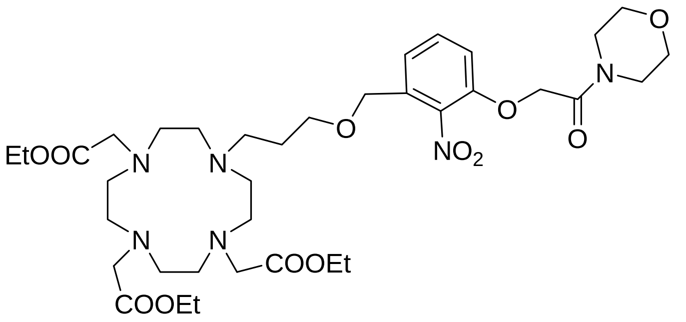

Compound **55** (0.9 g, 1.4 mmol) and K_2CO_3 (3.5 mmol, 0.48 g) was taken up in 10 ml DMF (dry) and heated for 30 min at 75 °C. The RM was cooled to RT and compound **52** (0.57 g, 2.8 mmol) dissolved in DMF was added to it. The contents were again heated at 75 °C for 1 h. It was then filtered and evaporated under vacuum. The residue obtained was re-dissolved in $CHCl_3$ and washed with water and brine. The organic layer collected was dried under anhyd. Na_2SO_4 and evaporated under vacuum. It was then purified by column chromatography using $MeOH/CH_2Cl_2$ (0.08-0.1:1) as the solvent mixture to obtain the pure product (0.5 g, 50 %).

^{1}H NMR (300 MHz, $CDCl_3$), δ ppm: 1.04 (t, *J*=7.18 Hz, 9 H), 1.40 - 1.59 (m, 2 H), 1.99 - 2.42 (m, 11 H),, 2.43 - 2.77 (m, 6 H), 2.89 - 3.18 (m, 6 H), 3.18 - 3.30 (m, 3 H), 3.31 - 3.41 (m, 4 H), 3.41 - 3.51 (m, 4 H), 3.83 - 4.10 (m, 6 H), 4.30 (s, 2 H), 4.66 (s, 2 H), 6.81 (d, *J*=7.55 Hz, 1 H), 6.95 (d, *J*=8.31 Hz, 2 H), 7.15 - 7.28 (m, 1 H).

^{13}C NMR (75 MHz, $CDCl_3$), δ ppm: 13.9, 25.7, 42.1, 45.5, 49.8, 50.6, 50.8, 51.8, 55.0, 55.6, 61.4, 61.6, 66.4, 66.6, 67.9, 68.5, 69.5, 113.5, 120.9, 131.3, 131.8, 140.0, 149.2, 165.1, 173.3, 173.8

ESI-MS: calculated for $[C_{36}H_{58}N_6O_{12}+H]^+$ *m/z*: 767.41855, found 767.41857

triethyl 2,2',2''-(10-(3-(2-amino-3-(2-morpholino-2-oxoethoxy)benzyloxy)propyl)-1,4,7,10-tetraazacyclododecane-1,4,7-triyl)triacetate

(57)

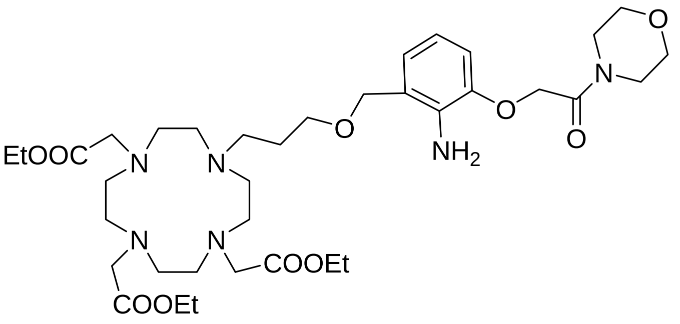

Compound **56** (0.47 g, 0.6 mmol) was dissolved in MeOH with Pd-C (10%, w/w) as the catalyst. Ammonium formate (0.035 g, 0.6 mmol) was added to it and the mixture was stirred in a Parr apparatus at 1 atm H_2 for 2 h. It was then filtered and the solvent was evaporated under vacuum to obtain the product (0.4 g, 89%). This was used as such for the next reaction without further purifications.

^{1}H NMR (300 MHz, $CDCl_3$), δ ppm: 0.61 - 0.82 (m, 2 H), 1.13 - 1.13 (m, 9 H), 1.82 (br. s., 2 H), 2.15 - 2.44 (m, 4 H), 2.52 - 2.67 (m, 8 H), 2.76 - 2.92 (m, 4 H), 3.18 - 3.28 (m, 9 H), 3.49 - 3.58 (m, 8 H), 3.95 - 4.07 (m, 6 H), 4.35 (s, 2 H), 4.60 (s, 2 H), 6.46 (t, *J*=7.93 Hz, 1 H), 6.58 - 6.68 (m, 2 H).

^{13}C NMR (75 MHz, D_2O), δ ppm: 13.7, 29.2, 41.8, 43.6, 45.0, 47.0, 49.5, 50.3, 51.3, 51.9, 52.7, 54.3, 54.6, 55.5, 60.4, 65.8, 66.2, 67.5, 71.0, 112.4, 116.4, 136.2, 145.3, 165.0, 166.4.

ESI-MS calculated for $[C_{36}H_{60}N_6O_{10} + H]^+$ *m/z*: 737.4, found 737.5

2,2',2''-(10-(3-((3-oxo-3,4-dihydro-2H-benzo[b][1,4]oxazin-5-yl)methoxy)propyl)-1,4,7,10-tetraazacyclododecane-1,4,7-triyl)triacetic acid

(58)

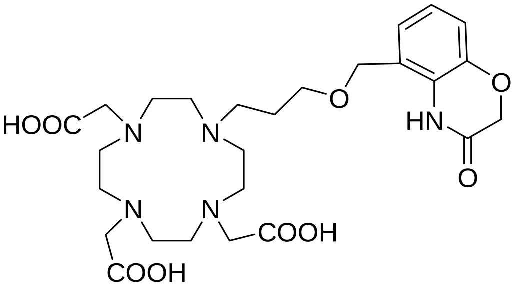

Compound **57** (0.4 g, 0.5 mmol) was dissolved in 5 ml EtOH. KOH (0.1 g, 1.8 mmol) dissolved in 3 ml of H_2O was added at 0 °C. The RM was stirred for 1 h at RT. It was then evaporated and purified by RP-HPLC (method C) to obtain the pure product as solid (0.14 g, 50%).

^{1}H NMR (300 MHz, D_2O), δ ppm: 1.91 (br. s., 2 H), 2.95 - 3.23 (m, 14 H), 3.23 - 3.32 (m, 4 H), 3.42 (br. s., 2 H), 3.47 (br. s., 2 H), 3.51 - 3.58 (m, 2 H), 3.68 (s, 2 H), 4.47 (s, 4 H), 6.91 (s, 3 H).

^{13}C NMR (75 MHz, D_2O), δ ppm: 23.6, 49.1, 49.3, 49.4, 50.5, 51.2, 55.0, 55.4, 66.4, 67.3, 68.9, 116.7, 123.9, 124.1, 124.4, 124.6, 143.6, 167.5, 170.9, 174.1.

ESI-MS calculated for $[C_{26}H_{39}N_5O_9 + H]^+$ *m/z*: 566.3, found 566.2

3-(2-amino-3-(benzyloxy)benzyloxy)propan-1-ol

(59)

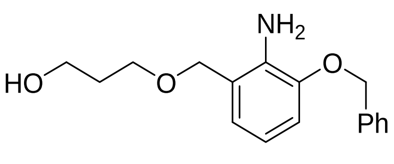

Compound **44** (1.4 g, 4.4 mmol) was taken in 21.0 ml acetic acid. To this iron powder (70 mesh) was added and the contents were vigorously stirred at 50 °C for 15 min. The yellow color of the heterogeneous mixture turned to dark brown. This was then filtered through celite pad and washed with ethylacetate. The solvent was evaporated and dissolved in ethylacetate and extracted with water. The organic layer collected was dried under anhydrous Na_2SO_4 and evaporated under vacuum. The residue obtained was purified by column chromatography using ethylacetate/hexane (0.2:1) as the solvent mixture to obtain the product as solid (1.0 g, 79%).

^{1}H NMR (300 MHz, $CDCl_3$), δ ppm: 1.78 - 1.87 (m, 2 H), 3.58 (t, *J*=6.04 Hz, 2 H), 3.70 (t, *J*=6.04 Hz, 2 H), 4.55 (s, 2 H), 5.07 (s, 2 H), 6.64 - 6.72 (m, 1 H), 6.73 - 6.80 (m, 1 H), 6.86 (d, *J*=7.93 Hz, 1 H), 7.34 - 7.48 (m, 5 H).

^{13}C NMR (75 MHz, $CDCl_3$), δ ppm: 31.9, 60.1, 67.3, 70.3, 71.5, 111.7, 117.0, 122.1, 127.2, 127.7, 128.3, 135.6, 136.8, 146.3.

di-tert-butyl 2,2'-(2-(benzyloxy)-6-((3-hydroxypropoxy)methyl)phenylazanediyl)diacetate (60)

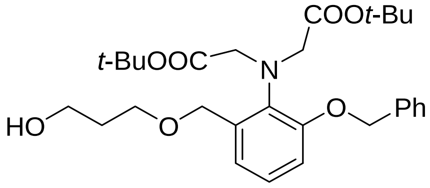

Compound **59** (3.7 g, 12.9 mmol), proton sponge (11.0 g, 51.6 mmol) and KI (0.2 g, 1.3 mmol) were taken up in 70 ml MeCN (dry) and refluxed for 3 h. The RM was then cooled down and *tert*-butyl bromoacetate (7.5 ml, 51.6 mmol) was added to it. The contents were refluxed for 5 days. The RM was then filtered and evaporated. The residue obtained was re-dissolved in toluene and filtered again. The evaporated residue was then purified by column chromatography using ethylacetate/hexane (0.3:1) as the solvent mixture to obtain the product (3.6 g, 54%) co-eluted with proton sponge (1.0 g). Some of the unused reactant was also recovered (0.7 g, 19%) at ethyacetate/hexane (0.4-0.5:1) solvent mixture with traces of co-eluted proton sponge.

^{1}H NMR (300 MHz, $CDCl_3$), δ ppm: 1.41 (s, 18 H), 1.82 - 1.95 (m, 2 H), 3.77 (s, 8 H), 4.93 (s, 2 H), 5.10 (s, 2 H), 6.87 (dd, *J*=7.93, 1.51 Hz, 1 H), 7.04 - 7.17 (m, 2 H), 7.35 - 7.52 (m, 5 H).

^{13}C NMR (75 MHz, $CDCl_3$), δ ppm: 28.4, 32.6, 44.7, 57.9, 62.2, 69.9, 70.3, 70.6, 80.9, 112.2, 121.2, 125.8, 126.9, 127.7, 128.3, 128.9, 137.4, 137.5, 139.8, 156.9, 170.8.

ESI-MS: calculated for $[C_{29}H_{41}NO_7 + Na]^+$ *m/z*: 538.29558, found 538.29557

di-tert-butyl 2,2'-(2-(benzyloxy)-6-((3-bromopropoxy)methyl)phenylazanediyl)diacetate

(61)

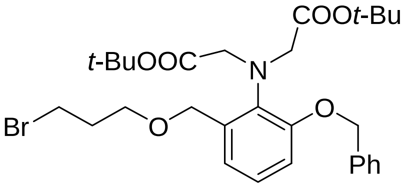

Compound **60** (3.0 g, 5.8 mmol) and PPh_3 (3.0 g, 11.6 mmol) was dissolved in CH_2Cl_2 and cooled to 0 °C. CBr_4 (4.0 g, 12.2 mmol) was added in small lots. After complete addition, the RM was stirred at RT for 2 h. The solvent was evaporated and the residue obtained was purified by column chromatography using ethylacetate/hexane (0.05:1) as the solvent mixture to obtain the pure product (3.0 g, 88%).

^{1}H NMR (300 MHz, $CDCl_3$), δ ppm: 1.30 (s, 18 H), 1.99 - 2.11 (m, 2 H), 3.43 (t, *J*=6.80 Hz, 2 H), 3.56 (t, *J*=5.85 Hz, 2 H), 3.70 (s, 4 H), 4.79 (s, 2 H), 4.97 (s, 2 H), 6.71 - 6.77 (m, 1 H), 6.93 - 7.05 (m, 2 H), 7.18 - 7.33 (m, 3 H), 7.33 - 7.40 (m, 2 H).

^{13}C NMR (75 MHz, $CDCl_3$), δ ppm: 27.5, 30.2, 32.6, 56.9, 67.4, 69.2, 69.7, 79.8, 111.3, 120.3, 125.9, 126.8, 127.3, 128.0, 136.4, 138.9, 155.9, 169.8.

ESI-MS: calculated for $[C_{29}H_{40}BrNO_6 + Na]^+$ *m/z*: 600.19312 found, 600.19276

tri-tert-butyl 2,2',2''-(10-(3-(3-(benzyloxy)-2-(bis(2-tert-butoxy-2-oxoethyl)amino)benzyloxy)propyl)-1,4,7,10-tetraazacyclododecane-1,4,7-triyl)triacetate

(62)

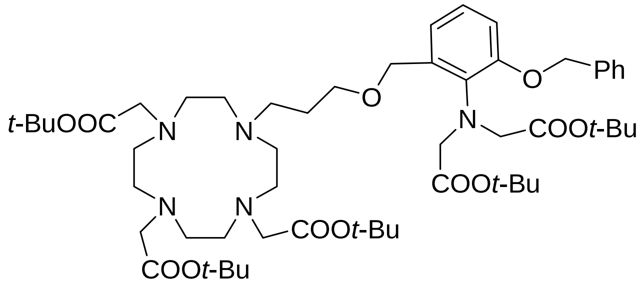

Tris-*tert*-Bu-DO3A (2.0 g, 4.0 mmol) and K_2CO_3 (1.8 g, 13 mmol) was taken in 12 ml DMF (dry) and heated at 60 °C for 1 h. The reaction mixture was brought to room temperature and compound **61** (3.0 g, 5.2 mmol) dissolved in DMF was added to it. The contents were kept for heating at 60 °C overnight. The reaction mixture was then filtered and evaporated under vacuum. The residue was re-dissolved in $CHCl_3$ and washed with water. The organic layer was dried under anhydrous. Na_2SO_4 and evaporated to the yellow oil. This was purified by column chromatography using $MeOH/CH_2Cl_2$ (0.05:1) as the solvent mixture to obtain the pure product as light yellow fluffy solid (2.2 g, 55%).

^{1}H NMR (300 MHz, $CDCl_3$), δ ppm: 1.30 (s, 18 H), 1.33 - 1.42 (m, 27 H), 1.62 - 1.75 (m, 2 H), 2.14 - 2.51 (m, 11 H), 2.61 - 2.94 (m, 7 H), 2.94 - 3.20 (m, 6 H), 3.45 (t, *J*=5.85 Hz, 2 H), 3.68 (s, 4 H), 4.77 (s, 2 H), 5.01 (s, 2 H), 6.77 (dd, *J*=7.93 Hz, 1 H), 6.90 - 6.96 (m, 1 H), 6.99 - 7.06 (m, 1 H), 7.23 - 7.42 (m, 5 H).

^{13}C NMR (75 MHz, $CDCl_3$), δ ppm: 28.0, 28.17, 28.20, 50.5, 52.0, 53.7, 56.0, 56.7, 57.7, 69.1, 69.7, 70.4, 80.6, 82.6, 82.9, 111.7, 120.3, 126.7, 127.5, 128.1, 128.8, 136.9, 137.2, 139.9, 156.6, 170.5, 172.9, 173.7.

ESI-MS: calculated for $[C_{55}H_{89}N_5O_{12} + 2H]^{2+}$ *m/z*: 506.83266, found 506.83263

tri-tert-butyl 2,2',2''-(10-(3-(2-(bis(2-tert-butoxy-2-oxoethyl)amino)-3-hydroxybenzyloxy)propyl)-1,4,7,10-tetraazacyclododecane-1,4,7-triyl)triacetate

(63)

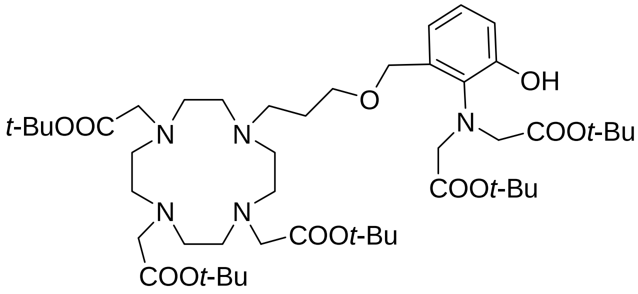

Compound **62** (2.2 g, 2.1 mmol) was dissolved in 10 ml ethanol (dry) with suspended $Pd(OH)_2$ (50% wet, 10% w/w) and stirred in a Parr apparatus under H_2 atmosphere (3 atm) for 5 h. The RM was then filtered and the solvent was evaporated to obtain the product as yellow solid (95%, 1.8 g).

^{1}H NMR (300 MHz, $CDCl_3$), δ ppm: 1.20 (br. s., 45 H), 1.53 (br. s., 1 H), 1.84 (br. s., 1 H), 2.00 - 2.37 (m, 5 H), 2.43 - 2.72 (m, 8 H), 2.75 - 3.02 (m, 6 H), 3.07 (s, 2 H), 3.20 - 3.35 (m, 4 H), 3.37 - 3.66 (m, 7 H), 4.31 - 4.46 (m, 2 H), 6.55 - 6.70 (m, 2 H), 6.77 - 6.92 (m, 1 H).

^{13}C NMR (75 MHz, $CDCl_3$), δ ppm: 27.6, 27.7, 27.8, 27.9, 31.0, 47.5, 49.8, 50.1, 50.4, 51.9, 52.3, 52.7, 54.9, 55.5, 56.1, 56.2, 56.3, 56.7, 67.0, 67.6, 68.9, 69.4, 69.5, 81.4, 81.9, 82.2, 82.5, 116.4, 119.9, 120.1, 127.3, 127.4, 135.3, 137.8, 138.0, 155.0, 169.7, 170.1, 172.3, 172.5, 173.2.

ESI-MS: calculated for $[C_{48}H_{83}N_5O_{12} + 2H]^{2+}$ *m/z*: 461.80919, found 461.80924

tri-tert-butyl 2,2',2''-(10-(3-(2-(bis(2-tert-butoxy-2-oxoethyl)amino)-3-(2-morpholino-2-oxoethoxy)benzyloxy)propyl)-1,4,7,10-tetraazacyclododecane-1,4,7-triyl)triacetate

(64)

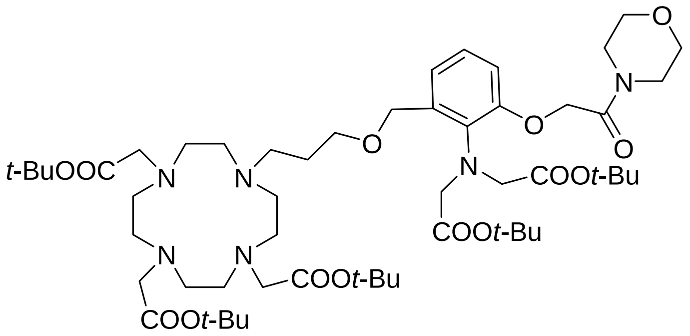

NaH (0.02 g, 0.54 mmol, 60% emulsion in oil) was suspended in freshly distilled THF (5 ml) and cooled down to -5° C. After 15 min, compound **63** (0.5 g, 0.54 mmol) dissolved in minimum amount of THF (dry) was added. The reaction mixture was stirred for 20 minutes and compound **52** (0.45 g, 2.2 mmol) was added to it while the temperature was maintained at -5 °C. After 5 min NaH (0.02 g, 0.54 mmol) was again added and the RM was finally stirred at the same temperature for another 30 min. The completion of reaction was monitored by ESI-MS. The reaction was quenched by addition of water. The product was extracted in $CHCl_3$ from the reaction mixture, dried under anhydrous Na_2SO_4 and evaporated to yellow oil. This was purified by column chromatography using $MeOH/CH_2Cl_2$ (0.08-0.1:1) as the solvent mixture to obtain the product (0.35g, 62%).

^{1}H NMR (300 MHz, $CDCl_3$), δ ppm: 1.32 (s, 18 H), 1.34 - 1.42 (m, 27 H), 1.61 - 1.75 (m, 2 H), 2.18 - 2.50 (m, 9 H), 2.65 - 2.91 (m, 5 H), 2.97 - 3.18 (m, 5 H), 3.40 - 3.47 (m, 2 H), 3.48 - 3.53 (m, 2 H), 3.54 - 3.68 (m, 11 H), 3.72 (s, 4 H), 4.71 (s, 2 H), 4.76 (s, 2 H), 6.80 (d, *J*=7.93 Hz, 1 H), 6.95 (d, *J*=7.55 Hz, 1 H), 7.03 (t, *J*=7.74 Hz, 1 H).

^{13}C NMR (75 MHz, $CDCl_3$), δ ppm: 26.7, 27.7, 27.87, 27.98, 42.1, 45.5, 50.2, 50.7, 51.8, 53.4, 55.7, 56.4, 57.1, 66.6, 66.7, 67.4, 68.8, 69.3, 80.3, 82.3, 82.7, 112.0, 120.9, 126.3, 136.9, 139.2, 155.6, 166.5, 170.2, 172.5.

ESI-MS calculated for $[C_{54}H_{92}N_6O_{14}+Na]^+$ *m/z*: 1071.7 found 1071.8

2,2',2''-(10-(3-(2-(bis(carboxymethyl)amino)-3-(2-morpholino-2-oxoethoxy)benzyloxy)propyl)-1,4,7,10-tetraazacyclododecane-1,4,7-triyl)triacetic acid

(L^8)

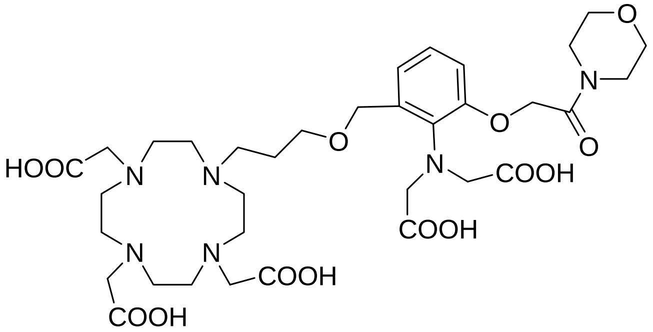

Compound **61** (0.3 g, 0.28 mmol) was dissolved in minimum amount of CH_2Cl_2 and 15 ml of TFA added to it. The RM was stirred at room temperature overnight. TFA was evaporated under vacuum and the residue obtained was purified by RP-HPLC (method C) to obtain the pure product (0.14 g, 65 %).

^{1}H NMR (300 MHz, D_2O), δ ppm: 1.88 (br. s., 2 H), 2.77 - 3.03 (m, 8 H), 3.12 - 3.19 (m, 4 H), 3.20 - 3.33 (m, 6 H), 3.34 - 3.44 (m, 6 H), 3.46 - 3.63 (m, 8 H), 3.67 (s, 2 H), 3.94 (s, 4 H), 4.62 (s, 2 H), 4.88 (s, 2 H), 6.81 (dd, *J*=7.46, 4.44 Hz, 2 H), 7.12 (t, *J*=7.84 Hz, 1 H).

^{13}C NMR (75 MHz, D_2O), δ ppm: 21.9, 41.3, 44.0, 47.6, 48.8, 50.4, 50.9, 52.6, 55.3, 58.8, 64.8, 65.2, 65.4, 66.9, 69.6, 112.9, 121.9, 128.4, 133.1, 134.3, 152.9, 165.4, 169.1, 173.4, 173.9.

ESI-MS calculated for $[C_{34}H_{52}H_6O_{14} - H]^{2-}$ *m/z*: 383.16980, found 383.16981

ESI-MS of **GdL^8**: calculated for $[C_{34}H_{49}GdN_6O_{14} + H]^+$ 922.2 found 922.3 with isostopic distribution.

ethyl 2-(2-bromoethoxy)acetate

(65)

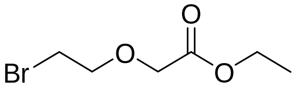

Bromoethanol (2.1 ml, 30.2 mmol) was taken up in CH_2Cl_2 (50 ml). Rhodium (II) acetate dimer powder (0.15 g, 0.33 mmol) was under ice. After 5 min, the ice bath was removed and ethyldiazoacetate (3.5 ml, 33.2 mmol) dissolved in 25 ml of CH_2Cl_2 was added dropwise to it. After complete addition, the RM was stirred for 2 h. It was then filtered through celite pad and evaporated under vacuum. The residue obtained was purified by column chromatography using ethylacetate/hexane (0.05-0.1:1) to get the product as transparent oil (4.7 g, 75%).

^{1}H NMR (300 MHz, $CDCl_3$), δ ppm: 1.24 (t, *J*=7.18 Hz, 3 H), 3.47 (t, *J*=6.23 Hz, 2 H), 3.85 (t, *J*=6.23 Hz, 2 H), 4.10 (s, 2 H), 4.18 (q, *J*=14.16, 7.18 Hz, 2 H).

^{13}C NMR (75 MHz, $CDCl_3$), δ ppm: 14.1, 29.9, 60.9, 68.4, 71.4, 170.0.

ESI-MS: calculated for $[C_6H_{11}BrO_3 + Na]^+$ *m/z*: 232.97838, found 232.97834

2,2',2''-(10-(3-(2-(bis(carboxymethyl)amino)-3-(2-(carboxymethoxy)ethoxy)benzyloxy)propyl)-1,4,7,10-tetraazacyclododecane-1,4,7-triyl)triacetic acid

(L^9)

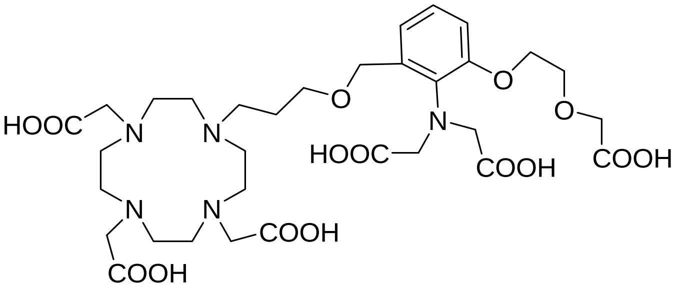

NaH (0.012 g, 0.3 mmol, 60% emulsion in oil) was taken in freshly distilled THF (5 ml) and cooled down to - 5° C. After 15 min, compound **63** (0.28 g, 0.3 mmol) dissolved in minimum amount of THF (dry) was added to it. The reaction mixture was stirred for 20 minutes and compound **65** (0.45 g, 1.2 mmol) was added to it while the temperature was maintained at -5 °C. After 5 min, NaH (0.02 g, 0.54 mmol) was again added to it and the reaction mixture was finally stirred at the same temperature for another hour. The completion of reaction was monitored by ESI-MS. The reaction was quenched by addition of water. This was then evaporated and the contents were re-dissolved in small amount of CH_2Cl_2 and cooled down under ice-salt bath. HBr-AcOH (5 ml) was added to it and the reaction mixture was stirred at RT for 5 h. The acid was evaporated under vacuum. The residue obtained was re-dissolved in water and pH was increased to 7 by 1 N NaOH. This was then purified by RP-HPLC (method C) to obtain the product as solid (0.057 g, 25%).

^{1}H NMR (300 MHz, D_2O), δ ppm: 1.94 (br. s., 2 H), 2.96 (s, 8 H), 3.13 - 3.26 (m, 6 H), 3.26 - 3.33 (m, 4 H), 3.34 - 3.40 (m, 2 H), 3.40 - 3.48 (m, 2 H), 3.54 - 3.63 (m, 3 H), 3.73 (br. s., 2 H), 3.86 - 3.93 (m, 2 H), 4.01 - 4.10 (m, 3 H), 4.14 (s, 2 H), 4.16 - 4.22 (m, 2 H), 4.72 (s, 2 H), 6.84 (d, *J*=7.36 Hz, 1 H), 7.01 (d, *J*=8.31 Hz, 1 H), 7.23 (t, *J*=7.84 Hz, 1 H).

^{13}C NMR (75 MHz, $CDCl_3$), δ ppm: 22.8, 48.4, 48.5, 49.7, 51.3, 51.8, 53.4, 56.2, 59.7, 67.6, 67.9, 69.4, 70.8, 114.3, 122.1, 130.1, 131.8, 133.8, 153.4, 173.4, 174.3, 174.6.

ESI-MS: calculated for $[C_{32}H_{49}N_5O_{15} - H]^{2-}$ 370.65398 found 370.65416

ESI-MS: calculated for compound **66**: $[C_{54}N_{93}N_5O_{15} + H]^+$ *m/z:* 1052.7, found 1052.9

ESI-MS of **Gd-L^9:** calculated for $[C_{32}H_{46}GdN_5O_{15} + H]^+$ *m/z:* 897.2 found 897.3

methyl 8,8,9,9-tetramethyl-3-oxo-1-phenyl-2,7-dioxa-4-aza-8-siladecane-5-carboxylate

(67)

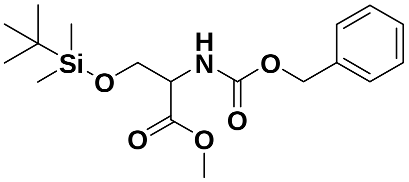

N-Carbobenzyloxy-L-serine methyl ester (4.0 g, 16 mmol) with imidazole (1.4 g, 20.8 mmol) was taken in DMF (dry) and stirred for 10 min. *tert*-butyldimethylsilyl chloride (3.1 g, 20.8 mmol) was added and the RM was stirred at RT for 3 h. The solvent was evaporated and the residue obtained was purified by column chromatography using ethylacetate/hexane (1:9) to obtain the pure product as oil (5.3 g, 92%).

^{1}H NMR (400 MHz, $CDCl_3$), δ ppm: 0.02 (s, 6 H), 0.86 (s, 9 H), 3.76 (s, 3 H), 3.85 (d, *J*=9.92 Hz, 1 H), 4.07 (d, *J*=9.92 Hz, 1 H), 4.44 (d, *J*=8.65 Hz, 1 H), 5.14 (s, 2 H), 7.29 - 7.44 (m, 5 H).

^{13}C NMR (100 MHz, $CDCl_3$), δ ppm: -5.7, -5.6, 18.1, 25.6, 52.3, 55.9, 63.6, 66.9, 128.10, 128.13, 136.2, 155.9, 170.9

ESI-MS: calculated for $[C_{18}H_{29}NO_5Si + H]^+$ *m/z*: 368.18878, found 368.18856

Compound **70** was synthesized according to reported procedure [184]

methyl 6-(benzyloxycarbonylamino)-2,2,3,3,17,17-hexamethyl-7,15-dioxo-4,16-dioxa-8,14-diaza-3-silaoctadecane-13-carboxylate

(71)

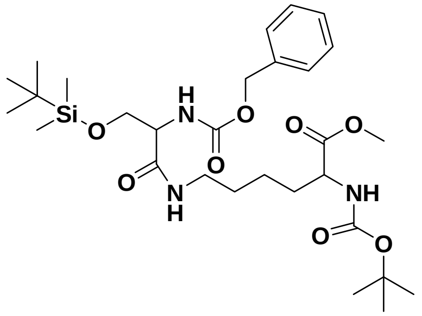

Compound **67** (3.0 g, 8.2 mmol) was dissolved in 15 ml of THF:MeOH:H2O (3:2:2) and LiOH (0.3 g, 12.3 mmol) was added. The RM was stirred for 3 h and the completion of reaction was monitored by ESI-MS. The pH of the solution was decreased to 7 by the addition of 3 N HCl. The solvent was evaporated and the crude product (**68**) obtained was dried under vacuum. This was re-dissolved in 5 ml of DMF (dry) and compound **70** (4.2 g, 10.7 mmol), NMM (2.5 ml, 23.5 mmol), HOBt (1.7 g, 12.8 mmol) was also added under N_2. The RM was heated at 60 °C for 1 h and EDC (12.84 mmol, 2.5 g) was added. The reaction mixture was then stirred at same temperature overnight. DMF was evaporated and the residue was re-dissolved in $CHCl_3$ and extracted with water. The collected organic layer was dried with anhydrous Na_2SO_4 and evaporated under vacuum. The residue obtained was purified by column chromatography using 15-20% ethylacetate in hexane as the solvent mixture to obtain the product (0.35g, 62%).

^{1}H NMR (400 MHz, $CDCl_3$), δ ppm: 0.00 (s, 6 H), 0.82 (s, 9 H), 1.25 - 1.32 (m, 2 H), 1.38 (s, 9 H), 1.41 - 1.48 (m, 2 H), 1.51 - 1.63 (m, 1 H), 1.66 - 1.78 (m, 1 H), 3.07 - 3.27 (m, 2 H), 3.59 (dd, *J* = 7.12, 9.66 Hz, 1 H), 3.65 (s, 3 H), 3.94 (dd, *J* = 3.56 Hz, 1 H), 4.06 - 4.26 (m, 2 H), 5.05 (s, 2 H), 5.71 (br. s., 1 H), 6.59 (br. s., 1 H), 7.18 - 7.38 (m, 5 H).

^{13}**C NMR** (100 MHz, $CDCl_3$), δ ppm: -5.76, 17.9, 22.4, 25.6, 28.1, 28.9, 31.9, 28.9, 52.0, 53.1, 55.7, 63.1, 66.8, 79.6, 135.9, 155.3, 155.9, 169.9, 173.0.

ESI-MS: calculated for $[C_{29}H_{49}N_3O_8Si + Na]^+$ *m/z*: 618.31811, found 618.31814

methyl 6-(2-(benzyloxycarbonylamino)-3-hydroxypropanamido)-2-(tert-butoxycarbonylamino)hexanoate

(72)

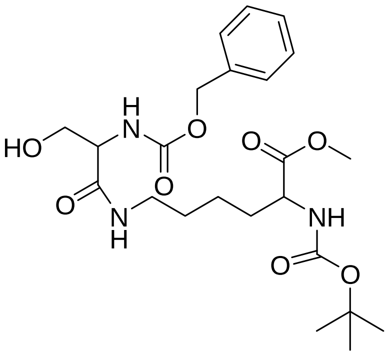

Compound **71** (2.5 g, 4.2 mmol) was dissolved in 10 ml of THF:TBAF (1:1) and the reaction mixture was stirred for 4 h. The solvents were evaporated and the obtained residue was washed with water, saturated NaHCO3 and brine. The organic layer collected was dried under anhydrous NaSO4 and evaporated under vacuum. The crude product obtained was purified by column chromatography using 20-30% ethylaceate in hexane as the solvent mixture to obtain the pure product (72) (1.6 g, 80%)

^{1}**H NMR** (400 MHz, $CDCl_3$), δ ppm: 1.29 - 1.36 (m, 2 H), 1.41 (s, 9 H), 1.53 - 1.69 (m, 2 H), 1.68 - 1.79 (m, 1 H), 3.10 - 3.33 (m, 2 H), 3.61 - 3.75 (m, 4 H), 3.94 - 4.07 (m, 1 H), 4.22 (br. s., 2 H), 5.10 (s, 2 H), 7.29 - 7.36 (m, 5 H).

^{13}**C NMR** (100 MHz, $CDCl_3$), δ ppm: 22.3, 28.2, 28.6, 31.8, 38.8, 52.2, 53.2, 54.8, 55.8, 62.6, 67.1, 79.9, 127.9, 128.2, 128.4, 135.9, 155.5, 156.6, 170.8, 173.3.

methyl 13-(benzyloxycarbonylamino)-2,2,19-trimethyl-4,12,16-trioxo-3,15,17-trioxa-5,11-diazaicosane-6-carboxylate

(73)

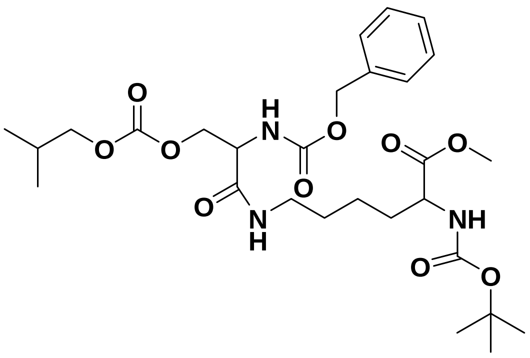

Compound 72 (1.0 g, 2.1 mmol) was dissolved in 25 ml CH_2Cl_2 containing pyridine (0.4 ml, 4.6 mmol) and kept in acetone bath. *Iso*-Bu chloroformate (0.55 ml, 4.2 mmol) dissolved in 5 ml of CH_2Cl_2 and added slowly. The reaction mixture was stirred at RT for 3-4 h. the product formed was extracted in organic layer by washing RM with water, saturated $NaHCO_3$ and brine. The organic layer extracted was dried under Na_2SO_4 and evaporated under vacuum. The residue was purified by column chromatography using 15-20% ethylacetate in hexane to obtain the pure product (0.72 g, 60%).

^{1}H NMR (400 MHz, $CDCl_3$), δ ppm: 0.92 (d, *J*=6.61 Hz, 6 H), 1.29 - 1.38 (m, 2 H), 1.41 (s, 9 H), 1.45 - 1.54 (m, 2 H), 1.54 - 1.68 (m, 1 H), 1.68 - 1.84 (m, 1 H), 1.87 - 2.00 (m, 1 H), 3.11 - 3.33 (m, 2 H), 3.71 (s, 3 H), 3.89 (d, *J*=6.61 Hz, 2 H), 4.18 - 4.27 (m, 1 H), 4.27 - 4.37 (m, 1 H), 4.42 - 4.56 (m, 2 H), 5.11 (s, 2 H), 7.28 - 7.40 (m, 5 H).

^{13}C NMR (100 MHz, $CDCl_3$), δ ppm: 18.4, 21.9, 27.3, 27.9, 28.4, 29.3, 31.6, 38.7, 51.8, 52.8, 53.6, 66.6, 66.9, 74.1, 79.5, 127.7, 127.9, 128.1, 135.5, 154.5, 155.1, 155.8, 168.1, 172.9.

ESI-MS: calculated for $[C_{24}H_{43}N_3O_{10} + K]^+$ *m/z*: 620.25800, found 620.25790.

methyl 13-amino-2,2,19-trimethyl-4,12,16-trioxo-3,15,17-trioxa-5,11-diazaicosane-6-carboxylate

(74)

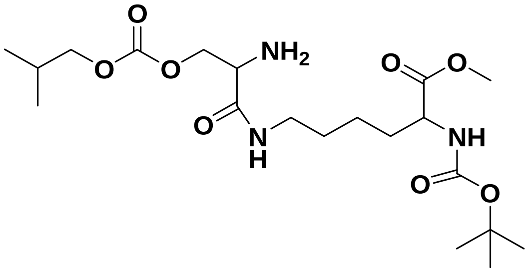

Compound **73** (0.5 g, 0.86 mmol) was dissolved in MeOH with Pd-C catalyst (10%, w/w) and stirred for 5 h in a Parr apparatus under 3 atm H_2 pressure. The reaction mixture was filtered and the solvent evaporated under vacuum to obtain the product in quantitative yields which was used as such without further purifications.

^{1}H NMR (400 MHz, $CDCl_3$), δ ppm: 0.85 (d, *J*=6.10 Hz, 6 H), 1.32 - 1.39 (m, 12 H), 1.44 - 1.54 (m, 2 H), 1.56 - 1.67 (m, 2 H), 1.83 - 1.93 (m, 1 H), 3.06 - 3.32 (m, 2 H), 3.64 (s, 3 H), 3.84 (d, *J*=5.85 Hz, 2 H), 4.09 - 4.32 (m, 1 H), 4.32 - 4.70 (m, 2 H).

^{13}C NMR (100 MHz, $CDCl_3$), δ ppm: 20.0, 23.8, 28.8, 29.48, 28.5, 30.8, 33.1, 33.3, 40.5, 43.1, 53.4, 54.0, 54.3, 54.6, 67.7, 75.8, 80.5, 80.9, 155.9, 156.3, 156.8, 168.1, 174.7, 177.2.

ESI-MS: calculated for $[C_{20}H_{37}N_3O_8 + Na]^+$ *m/z*: 470.24729, found 470.24704.

2-amino-6-(3-hydroxy-2-(5-(2-oxo-hexahydro-1H-thieno[3,4-d]imidazol-4-yl)pentanamido)propanamido)hexanoic acid

(L^{10})

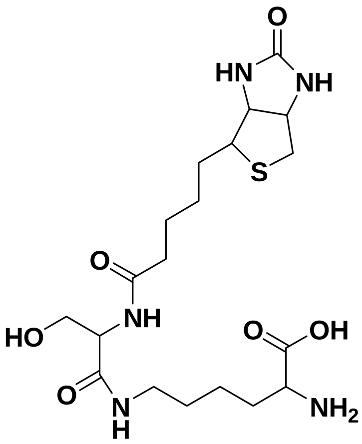

Compound **74** (0.14 g, 0.3 mmol) was dissolved in 4 ml DMF (dry). Biotin (0.95 g, 0.4 mmol) and DIEA (0.14 ml, 0.7 mmol) was added under N_2. The RM was stirred at RT for 1 h under N_2. HATU (0.18 g, 0.4 mmol) was then added and the contents were stirred overnight. The formation of product (**75**) was confirmed by ESI-MS. DMF was evaporated and the residue obtained was re-dissolved in 10 ml of THF:MeOH:H_2O (3:2:2) and LiOH (0.4 mmol, 0.011 g) was added. The RM was stirred at RT for 3 h and TFA (10 ml) was added. This was then stirred for another 3 h. The solvents were evaporated and the obtained residue was purified by RP-HPLC to obtain the pure product (0.03 g, 24%).

^{1}H NMR (400 MHz, D_2O), δ ppm: 1.28 - 1.44 (m, 4 H), 1.46 - 1.57 (m, 3 H), 1.57 - 1.74 (m, 3 H), 1.75 - 1.92 (m, 2 H), 2.32 (t, *J*=7.38 Hz, 2 H), 2.74 (d, *J*=12.97 Hz, 1 H), 2.96 (dd, *J*=5.09 Hz, 1 H), 3.12 - 3.26 (m, 2 H), 3.27 - 3.35 (m, 1 H), 3.70 (p.t, *J*=6.61, 5.60 Hz, 1 H), 3.79 (d, *J*=5.60 Hz, 2 H), 4.31 (t, *J*=5.59 Hz, 1 H), 4.39 (dd, *J*=4.58, 7.88 Hz, 1 H), 4.57 (dd, *J*=4.83, 7.88 Hz, 1 H).

^{13}C NMR (100 MHz, D_2O), δ ppm: 24.6, 27.8, 30.5, 30.7, 30.9, 32.9, 38.0, 41.85, 42.6, 57.4, 58.2, 63.2, 64.0, 64.9, 168.2, 174.6, 177.4, 180.0.

ESI-MS: calculated for $[C_{19}H_{33}N_5O_6Si + H]^+$ *m/z*: 460.22243, found 460.22251

methyl 2-(benzyloxycarbonylamino)-3-bromopropanoate

(76)

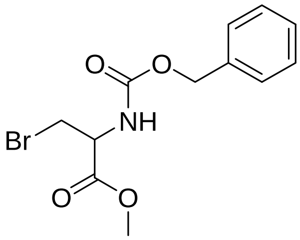

N-Carbobenzyloxy-L-serine methyl ester (2 g, 8 mmol) was taken up in 50 ml DMF (dry) and PPh_3 (4 g, 16 mmol) was added to it. N-bromosuccinimide (2.8 g, 16 mmol) was added in small lots to the homogenous solution obtained. The RM was stirred for 30 min at 50 °C. Heating bath was then removed and 2 ml of MeOH was added to quench the reaction. 100 ml of ether was added to it and the mixture was extracted with water. The organic layer collected was dried over anhydrous Na_2SO_4 and concentrated under vacuum. The residue obtained was purified by column chromatography using 25 % ethylacetate in hexane as the solvent mixture to obtain the product (2.1 g, 84%).

^{1}H NMR ($CDCl_3$, 400 MHz), δ (ppm): 3.4-3.7 (m, 5H); 4.57-4.62 (m, 1H); 4.91 (s, 2H); 5.49-5.58 (m, 1H); 7.07-7.28 (m, 5H).

^{13}C NMR ($CDCl_3$, 100 MHz), δ (ppm) 33.6; 53.0; 54.2; 67.2; 128.0; 128.2; 128.4; 139.5; 159.5; 169.2.

ESI-MS: calculated for $[C_{12}H_{14}BrNO_4 + H]^+$ *m/z*: 317.0, found 317.3

methyl 2-(benzyloxycarbonylamino)-3-(1,4,7,10-tetraazacyclododecan-1-yl)propanoate

(77)

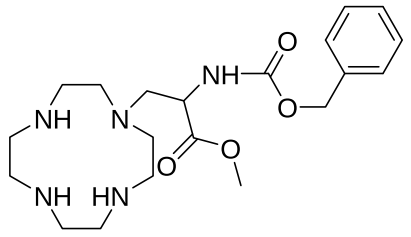

Cyclen (5.0 g, 29 mmol) was taken up in 100 ml of toluene and compound **76** (2.0 g, 6.5 mmol) dissolved in 25 ml of toluene was added to it dropwise. The reaction mixture was stirred for 18 h. The toluene was evaporated and the contents were dissolved in $CHCl_3$ (100 ml) and washed with water (4*75 ml). The collected organic layer was dried under anhydrous. Na_2SO_4 and evaporated to obtain the product with some unreacted cyclen. The product could be purified on silica or alumina column; however this leads to loss of yield because of the high polarity of the product and reactant. To avoid yield loss, the mixture obtained was used as such for the next reaction and purified in the next step.

ESI-HRMS calculated for $[C_{20}H_{33}N_5O_4 +H]^+$; m/z 408.2605 found 408.2607.

tri-tert-butyl 2,2',2''-(10-(2-(benzyloxycarbonylamino)-3-methoxy-3-oxopropyl)-1,4,7,10-tetraazacyclododecane-1,4,7-triyl)triacetate

(78)

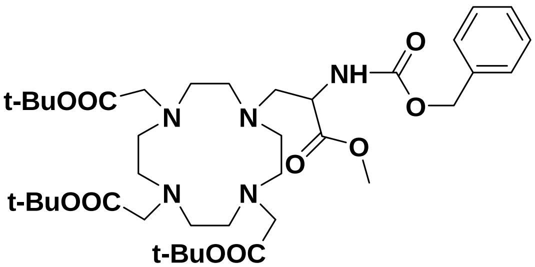

A solution of **77** (4.1 g, 24.0 mmol), sodium carbonate (6.4 g, 60.0 mmol) was taken up in 70 ml MeCN (dry) and heated at 60 °C for 30 min. The RM was cooled down and *tert–*

butylbromoacetate (14.2 ml, 96 mmol) in MeCN (25 ml) was dropwise added. The RM was then stirred at 60°C for 6 h. It was then filtered, washed with MeCN and evaporated under vacuum. The obtained residue was re-dissolved in CH_2Cl_2 and extracted with water. The organic layer was dried under anhydrous Na_2SO_4 and evaporated to yellow oil. This was purified by column chromatography (5% MeOH/CH_2Cl_2) to give **78** as light yellow solid (3.5 g, 72%).

^{1}H NMR (300 MHz, CDCl3), δ ppm: 1.21 - 1.34 (m, 27 H), 1.76 - 2.49 (m, 9 H), 2.50 - 3.38 (m, 15 H), 3.55 (s, 3 H), 4.23 - 4.48 (m, 1 H), 4.66 (br. s., 1 H), 4.87 - 5.16 (m, 1 H), 7.07 - 7.24 (m, 5 H).

^{13}C NMR (75 MHz, CDCl3), δ ppm: 27.9, 47.8, 49.6, 51.6, 53.1, 55.1, 56.5, 57.6, 66.9, 81.5, 81.7, 128.0, 128.3, 128.5, 137.2, 142.9, 169.7, 170.1, 172.3.

ESI-HRMS calculated for $[C_{38}H_{63}N_5O_{10}+H]^+$; m/z 750.4647 found 750.4641.

2-(benzyloxycarbonylamino)-3-(4,7,10-tris(2-tert-butoxy-2-oxoethyl)-1,4,7,10-tetraazacyclododecan-1-yl)propanoic acid

(79)

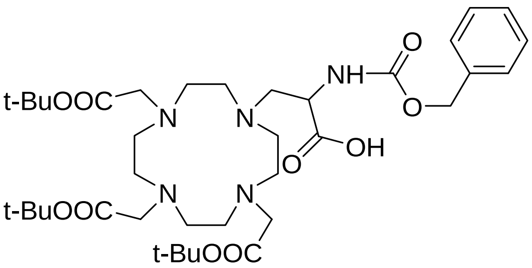

Compound **78** (0.5 g, 0.7 mmol) was dissolved in 6 ml of THF:MeOH:H_2O (3:2:2) and LiOH (1 mmol, 0.024 g) was added. The RM was stirred at RT for 3-4 h. The pH of the solution was decreased to 7 by addition of 3 N HCl. The solvents were evaporated and the crude product was used as such for the next reaction.

^{1}H NMR (300 MHz, $CDCl_3$), δ ppm: 1.31 - 1.47 (m, 27 H), 2.00 - 3.17 (m, 18 H), 3.23 - 3.51 (m, 4 H), 3.51 - 3.75 (m, 2 H), 3.94 (br. s., 1 H), 4.90 - 5.15 (m, 2 H), 7.14 -7.41 (m, 5 H).

^{13}C NMR (75 MHz, $CDCl_3$), δ ppm: 27.99, 28.05, 28.17, 31.2, 46.6, 47.2, 47.9, 50.9, 51.3, 51.4, 51.6, 51.8, 52.3, 52.7, 54.0, 54.4 54.7, 55.8, 56.2, 56.7, 60.4, 66.0, 66.1, 81.4, 81.8, 82.1, 127.5, 127.8, 128.4, 136.8, 155.9, 171.6, 174.1, 174.5.

ESI-MS calculated for $[C_{37}H_{61}N_5O_{10}+H]^+$ *m/z* 736.4, found 736.3

tri-tert-butyl 2,2',2''-(10-(2-amino-3-methoxy-3-oxopropyl)-1,4,7,10-tetraazacyclododecane-1,4,7-triyl)triacetate

(80)

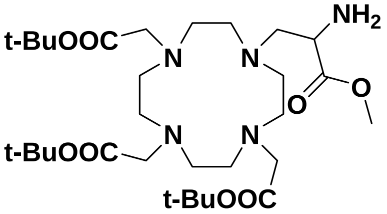

Compound **79** (1.5 g, 2.0 mmol) was dissolved in MeOH with Pd-C (10%, w/w) and stirred for 5 h in a Parr apparatus under 3 atm H_2 pressure. The reaction mixture was filtered and the solvent was evaporated under vacuum to obtain the crude product as yellow solid. This was purified by column chromatography using 5-10% MeOH in CH_2Cl_2 to get pure product as light yellow solid (0.74 g, 60%).

^{1}H NMR (400 MHz, $CDCl_3$), δ ppm: 1.38 - 1.41 (m, 18 H), 1.43 - 1.47 (m, 9 H), 1.99 - 2.25 (m, 7 H), 2.31 - 2.47 (m, 4 H), 2.57 - 2.76 (m, 3 H), 2.78 - 2.92 (m, 4 H), 3.11 - 3.27 (m, 4 H), 3.27 - 3.38 (m, 2 H), 3.58 - 3.67 (m, 1 H), 3.70 (s, 3 H).

^{13}C NMR (100 MHz, $CDCl_3$), δ ppm: 28.21, 28.25, 30.0, 49.1, 50.8, 52.6, 52.7, 53.2, 53.9, 55.9, 56.2, 56.5, 82.4, 82.6, 82.7, 173.10, 173.4, 176.0.

2,2',2''-(10-(2-carboxy-2-(5-(2-oxo-hexahydro-1H-thieno[3,4-d]imidazol-4-yl)pentanamido)ethyl)-1,4,7,10-tetraazacyclododecane-1,4,7-triyl)triacetic acid

(L^{12})

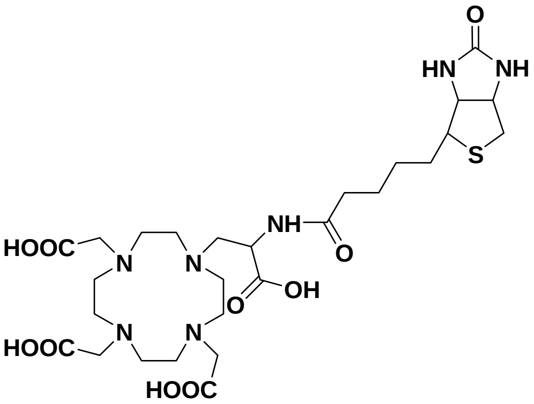

80 (0.25g, 0.4 mmol), D-Biotin (1.0 g, 0.4 mmol), HOBt (0.06 g, 0.44 mmol), N-methyl morpholine (0.085ml, 0.8 mmol) were taken up in 8 ml of DMF (dry) and stirred under N_2 for 1 h. After 1 h, EDC (0.85 mg, 0.44 mmol) was added. The RM was stirred at RT for 12 h. Formation of the intermediate product (**81**) was confirmed by ESI-MS. The crude **81** was subjected to global deprotection, first with 2 eq of LiOH (THF/MeOH /H_2O, 3:2:2) and then with 10 ml of TFA (neat). After TFA evaporation, the crude residue was re-dissolved in CH_2Cl_2 and evaporated 3 times and then repeated with methanol to completely evaporate TFA. The residue obtained was purified by preparative RP-HPLC using method C to give the final ligand, $\mathbf{L^{12}}$ as off white solid (0.11 g, 41%).

^{1}H NMR (400 MHz, D_2O), δ (ppm): 1.25 - 1.37 (m, 2 H), 1.41 - 1.57 (m, 3 H), 1.57 - 1.70 (m, 1 H), 2.10 - 2.28 (m, 2 H), 2.62 - 2.69 (m, 1 H), 2.76 - 3.02 (m, 7 H), 3.07 - 3.29 (m, 10 H), 3.31 (s, 1 H), 3.40 (br. s., 3 H), 3.47 - 3.56 (m, 1 H), 3.56 - 3.70 (m, 3 H), 3.70 - 3.86 (m, 2 H), 4.26 - 4.35 (m, 2 H), 4.45 - 4.52 (m, 1 H).

^{13}CNMR (100 MHz, D_2O), δ (ppm): 22.7, 25.5, 25.7, 25.9, 26.0, 33.1, 33.3, 37.6, 44.9, 45.5, 47.1, 48.0, 48.9, 49.1, 49.4, 49.8, 52.0, 53.1, 53.3, 54.3, 54.6, 58.1, 59.9, 163.3, 174.0, 174.1, 174.50, 174.53, 175.0.

ESI-MS: calculated for $[C_{27}H_{45}N_7O_{10}S - H]^-$ *m/z* 658.3, found 658.3.

ESI-MS of **Gd-L^{12}**: calculated for $[C_{27}H_{42}GdN_7O_{10}S – H]^-$ *m/z* 813.2, found 813.1

ESI-MS of **Eu-L^{12}**: calculated for $[C_{27}H_{42}EuN_7O_{10}S – H]^-$ *m/z* 808.2, found 808.1

benzyl 3-hydroxypropyl(methyl)carbamate

(82)

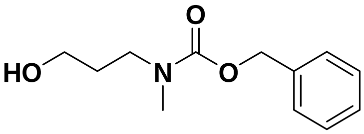

N-methyl 3-propanol (10 mmol, 0.948 ml) was dissolved in 50 ml Dioxane/water (1:1) and taken in three neck round bottom flask fitted with pH meter. N-carbobenzyloxy chloride (13 mmol, 1.8 ml) added to it in small lots by addition funnel while maintaining the pH at 10 with the addition of 3.5 M KOH solution. After the complete addition the RM was stirred for 1 h. To this, 200 ml of diethyl ether was added and the mixture was extracted with water (2 x 75 ml), satuarted. $NaHCO_3$ (2 x 75 ml) and then washed with brine. The organic layer collected was dried over anhydrous Na_2SO_4 and evaporated to get colourless oil. This oil was purified by column chromatography using 40 % ethylacetate in hexane to obtain the final product as oil (1.8 g, 82%).

^{1}H NMR (400 MHz, $CDCl_3$), δ ppm: 1.66 - 1.80 (m, 2 H), 2.92 (s, 3 H), 3.44 (t, 2 H), 3.57 (t, 2 H), 5.14 (s, 2 H), 7.28 - 7.39 (m, 5 H).

^{13}CNMR (100 MHz, $CDCl_3$), δ ppm: 29.6, 33.9, 45.1, 58.2, 67.2, 127.7, 127.9, 128.4, 136.5, 157.3.

ESI-HRMS: calculated for $[C_{12}H_{17}NO_3 + H]^+$ *m/z*: 246.11006, found 246.11004

benzyl 3-bromopropyl(methyl)carbamate

(83)

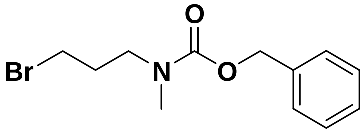

Compound **81** (7.7 mmol, 1.74 g) and PPh3 (15.4 mmol, 4.1 g) were dissolved in CH_2Cl_2 (dry). CBr_4 (15.4 mmol, 5.4 g) was added in small lots and reaction and reaction mixture was stirred for an hour at room temperature. The solvent was evaporated and obtained residue was purified by column chromatography using 15% ethyacetate in hexane to obtain the colourless oil (1.7g, 80%).

^{1}H NMR (400 MHz, $CDCl_3$), δ ppm: 2.04 - 2.18 (m, 2 H), 2.96 (s, 3 H),3.33 - 3.48 (m, 4 H), 5.14 (s, 2 H), 7.31 - 7.42 (m, 5 H).

^{13}CNMR (100 MHz, $CDCl_3$), δ ppm: 30.2, 30.3, 30.6, 30.9, 34.3, 34.7, 46.9, 47.6, 66.7, 127.5, 127.6, 128.1, 136.5, 155.9.

ESI-HRMS: calculated for $[C_{12}H_{16}BrNO_2 + Na]^+$ *m/z*: 308.02566, found 308.02560

tri-tert-butyl 2,2',2''-(10-(3-((benzyloxycarbonyl)(methyl)amino)propyl)-1,4,7,10-tetraazacyclododecane-1,4,7-triyl)triacetate

(84)

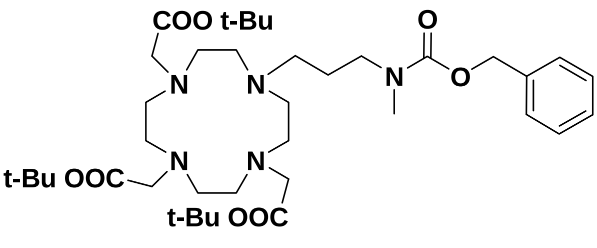

Tris-*tert*-Bu-DO3A (1.8 g, 3.5 mmol) and K_2CO_3 (1.6 g, 11.5 mmol) were taken in 25 ml MeCN (dry) and stirred at 70°C for 1 h. After 1 h, RM was removed from heating and **83** (1.4 g, 4.6

mmol) was added slowly. After complete addition the RM was stirred at 70°C overnight. It was then filtred and solvent was evaporated under vaccum. The obatined residue was dissolved in CH_2Cl_2 and extracted with water. The organic layer was dried under anhydrous Na_2SO_4 and evapoarted to get yellow oil. The obtained oil was purified by column chromatography using 5-10% MeOH in CH_2Cl_2 to the final product as solid (1.4 g, 55%).

^{1}H NMR (400 MHz, $CDCl_3$), δ ppm: 1.21 (s, 9 H), 1.25 (s, 18 H), 1.34 - 1.57 (m, 2 H), 2.00 – 2.31 (m, 9 H), 2.38 - 2.75 (m, 9 H), 2.75 - 3.19 (m, 9 H), 5.09 - 5.15 (m, 2 H), 7.04 - 7.20 (m, 5 H).

^{13}CNMR (100 MHz, $CDCl_3$), δ ppm: 24.3, 28.4, 27.5, 27.6, 33.8, 34.4, 46.7, 47.1, 50.0, 51.2, 53.4, 55.4, 56.1, 66.6, 82.2, 127.4, 127.7, 128.2, 136.4, 155.7, 173.4.

ESI-MS: calculated for $[C_{38}H_{65}N_5O_8 + H]^+$ *m/z*: 720.49059, found 720.49125

tri-tert-butyl 2,2',2''-(10-(3-(methylamino)propyl)-1,4,7,10-tetraazacyclododecane-1,4,7-triyl)triacetate

(85)

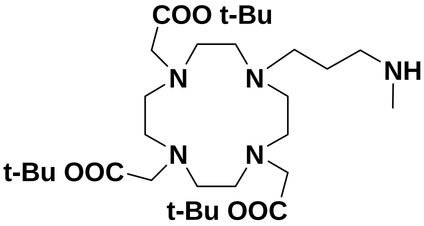

Compound **83** (1.0g, 1.4 mmol) and Pd-C (10%, w/w) were taken up in MeOH and kept for stirring under H_2 (3 atm) in a Parr apparatus for 6 h. The RM was then filtred through a pad of celite and the solvent evaporated to light yellow solid. The product was obtained in quantitaive yields and was used as such for the next recation without further purification.

^{1}H NMR (250 MHz, MeOD), δ ppm: 1.51 (s, 9 H), 1.57 (s, 16 H), 1.95 - 2.12 (m, 2 H), 2.21 (s, 3 H), 2.28 - 2.51 (m, 5 H), 2.57 - 2.91 (m, 11 H), 2.99 - 3.09 (m, 2 H), 3.11 - 3.32 (m, 4 H).

^{13}CNMR (62 MHz, MeOD), δ ppm: 22.9, 28.4, 28.6, 31.1, 33.9, 50.1, 56.9, 57.7, 83.3, 83.6, 174.4, 175.2.

ESI-HRMS: calculated for $[C_{30}H_{59}N_5O_6 + H]^+$ *m/z*: 586.45381, found 586.45350

2,2',2"-(10-(3-(N-methyl-5-(2-oxo-hexahydro-1H-thieno[3,4-d]imidazol-4-yl)pentanamido)propyl)-1,4,7,10-tetraazacyclododecane-1,4,7-triyl)triacetic acid

(L^{13})

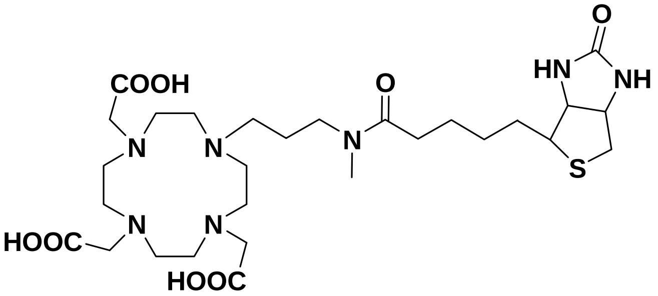

Compound **85** (0.3 g, 0.5 mmol,), D-Biotin (0.15 g, 0.6 mmol,), PyBrop (0.3 g, 0.6 mmol,) were taken up in 10 ml CH_2Cl_2 (dry) and kept for stirring at 0°C for 30 min. DIEA (0.3ml, 1.54 mmol) was added dropwise while maintaing the reaction mixture at 0°C. After complete addition the reaction mixture was kept for stirring at RT for 24 h. The formation of product (86) was confirmed by ESI-MS. The RM was then evaporated and the residue obtained was subjected to global deprotection by addition of 15 ml TFA (neat). This was stirred at room temperature for 12 h and then evaporated under vacuum. To remove the TFA completely, the residue obtained was redissolved in CH_2Cl_2 (2 x 25 ml) and methanol (2 x 25 ml) and evaporated to dry. This was purified by RP-HPLC using method C to obtain the final ligand L^{13}, as solid (0.16 g, 50 %).

^{1}H NMR (400 MHz, D_2O), δ ppm: 1.29 - 1.41 (m, 2 H), 1.43 - 1.61 (m, 3 H), 1.61 - 1.72 (m, 1 H), 1.90 (br. s., 2 H), 2.31 - 2.40 (m, 2 H), 2.66 - 2.73 (m, 1 H), 2.83 (s, 1 H), 2.87 - 2.95 (m, 1 H), 2.95 - 3.17 (m, 12 H), 3.17 - 3.38 (m, 12 H), 3.39 - 3.49 (m, 2 H), 3.49 - 3.61 (m, 2 H), 3.66 - 3.76 (m, 2 H), 4.30 - 4.38 (m, 1 H), 4.48 - 4.57 (m, 1 H).

^{13}CNMR (100 MHz, D_2O), δ ppm: 23.1, 26.1, 26.6, 29.4, 29.5, 29.8, 33.7, 34.5, 35.1, 37.4, 41.4, 46.6, 49.0, 50.5, 51.0, 51.2, 52.4, 53.1, 55.7, 57.0, 57.4, 61.8, 63.6, 166.8, 175.47, 175.52, 177.6, 177.9.

ESI-MS of **Gd-L^{13}**: calculated for $[C_{28}H_{46}GdN_7O_8S + H]^+$ *m/z:* 797.2, found 797.1 with appropriate isotopic distribution.

ESI-MS of **Eu-L^{13}**: calculated for $[C_{28}H_{46}EuN_7O_8S + H]^+$ *m/z:* 792.2, found 792.1 with appropriate isotopic distribution.

Appendix 1

NMR-spectra of the final ligands and the important intermediates

Appendix 1

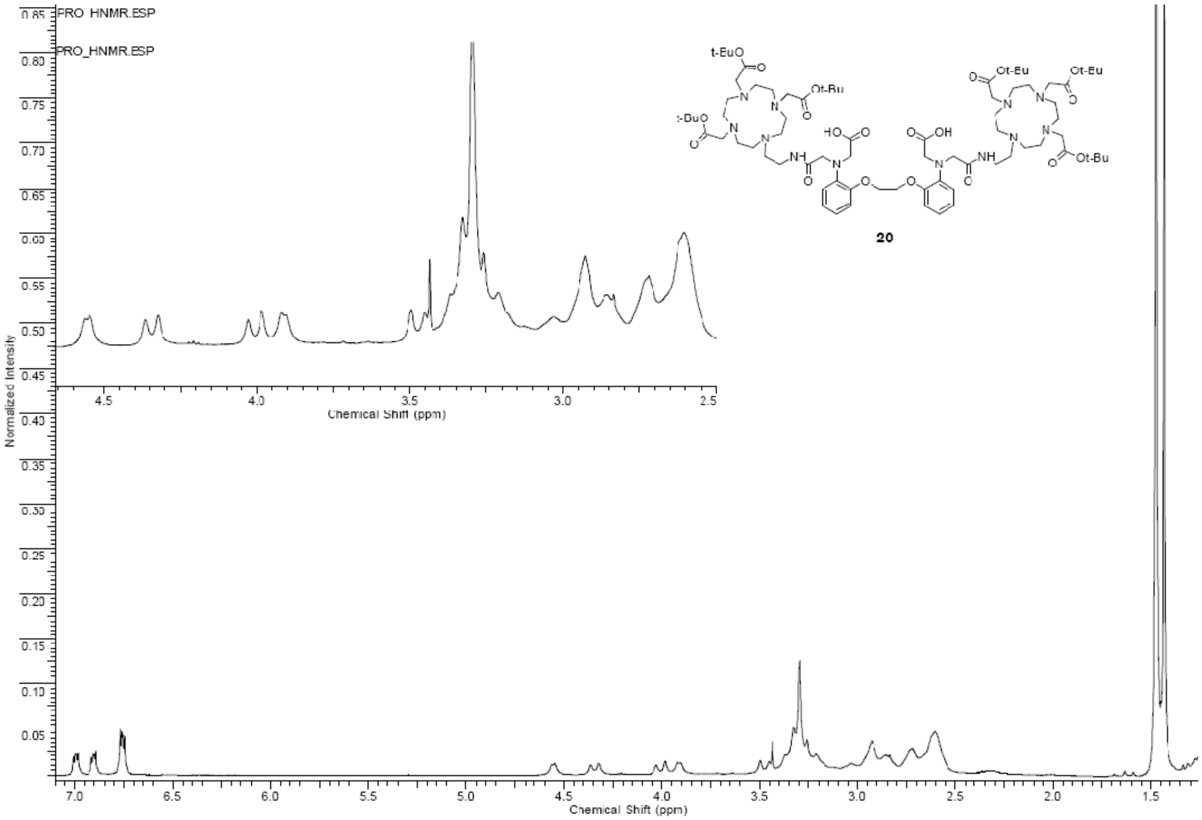

PRO_HNMR.ESP
PRO_HNMR.ESP
Normalized Intensity
0.85
0.80
0.75
0.70
0.65
0.60
0.55
0.50
0.45
0.40
0.35
0.30
0.25
0.20
0.15
0.10
0.05
4.5
4.0
3.5
3.0
2.5
Chemical Shift (ppm)
7.0
6.5
6.0
5.5
5.0
4.5
4.0
3.5
3.0
2.5
2.0
1.5
Chemical Shift (ppm)
t-BuO
Ot-Bu
t-BuO
HO
O
OH
NH
N
Ot-Bu
Ot-Bu
Ot-Bu
20

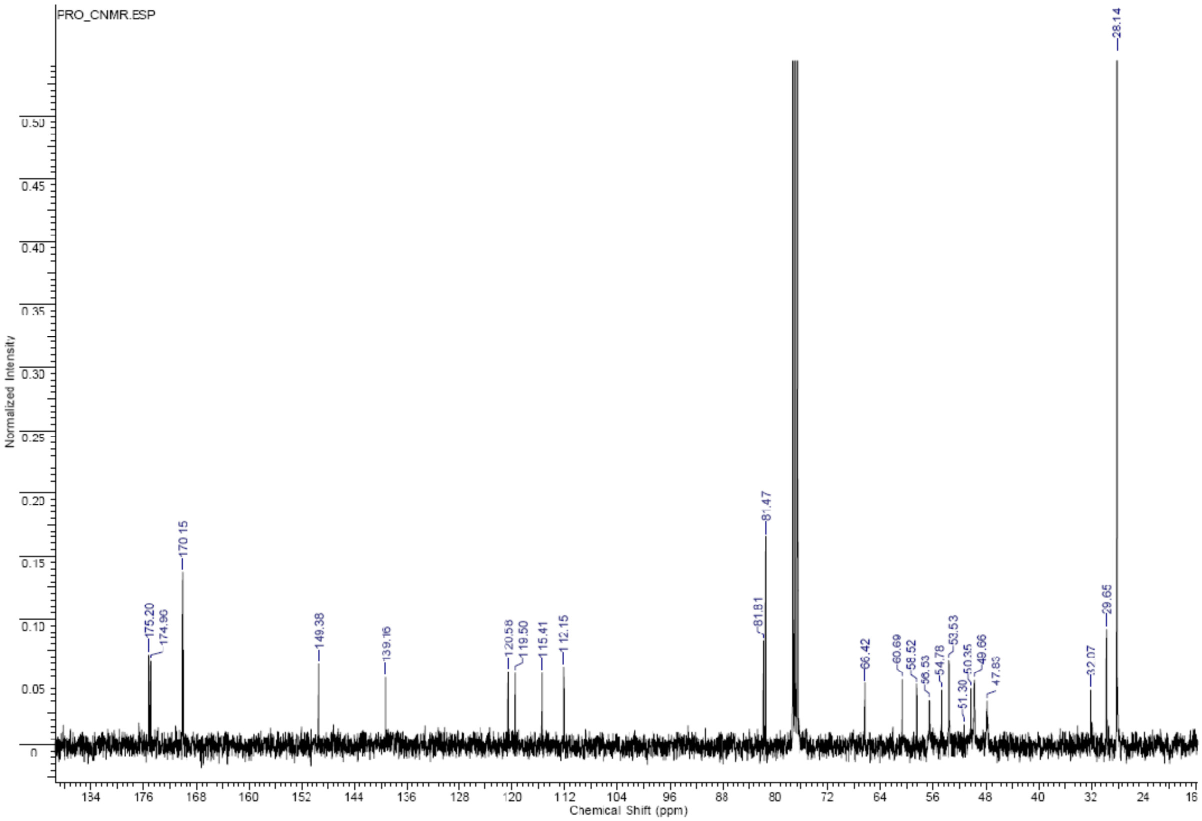

PRO_CNMR.ESP
Normalized Intensity
0.50
0.45
0.40
0.35
0.30
0.25
0.20
0.15
0.10
0.05
0
175.20
174.90
170.15
149.38
139.16
120.58
119.50
115.41
112.15
81.81
81.47
66.42
60.69
58.52
56.53
54.78
53.53
51.30
50.35
49.66
47.83
32.07
29.65
28.14
184
176
168
160
152
144
136
128
120
112
104
96
88
80
72
64
56
48
40
32
24
16
Chemical Shift (ppm)

Appendix 1

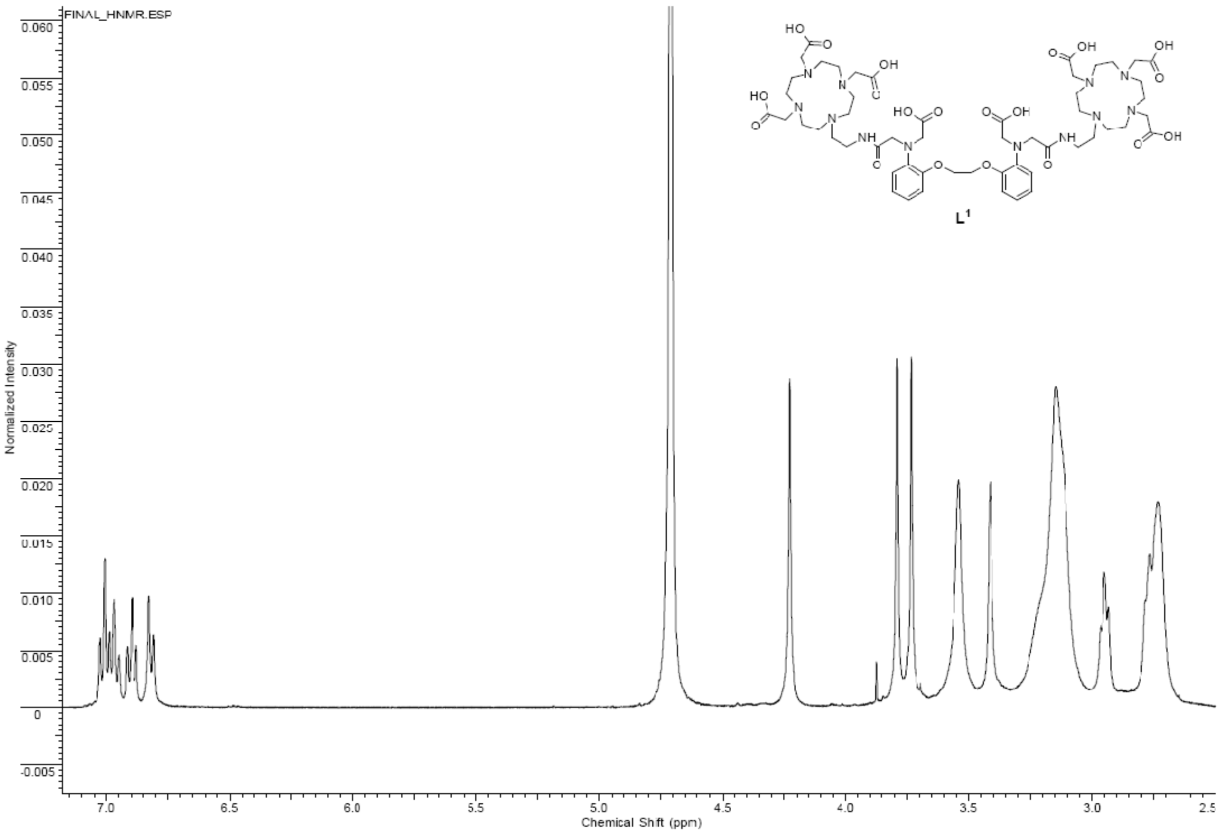
FINAL_HNMR.ESP
Normalized Intensity
Chemical Shift (ppm)
L1
0.060
0.055
0.050
0.045
0.040
0.035
0.030
0.025
0.020
0.015
0.010
0.005
0
-0.005
7.0
6.5
6.0
5.5
5.0
4.5
4.0
3.5
3.0
2.5

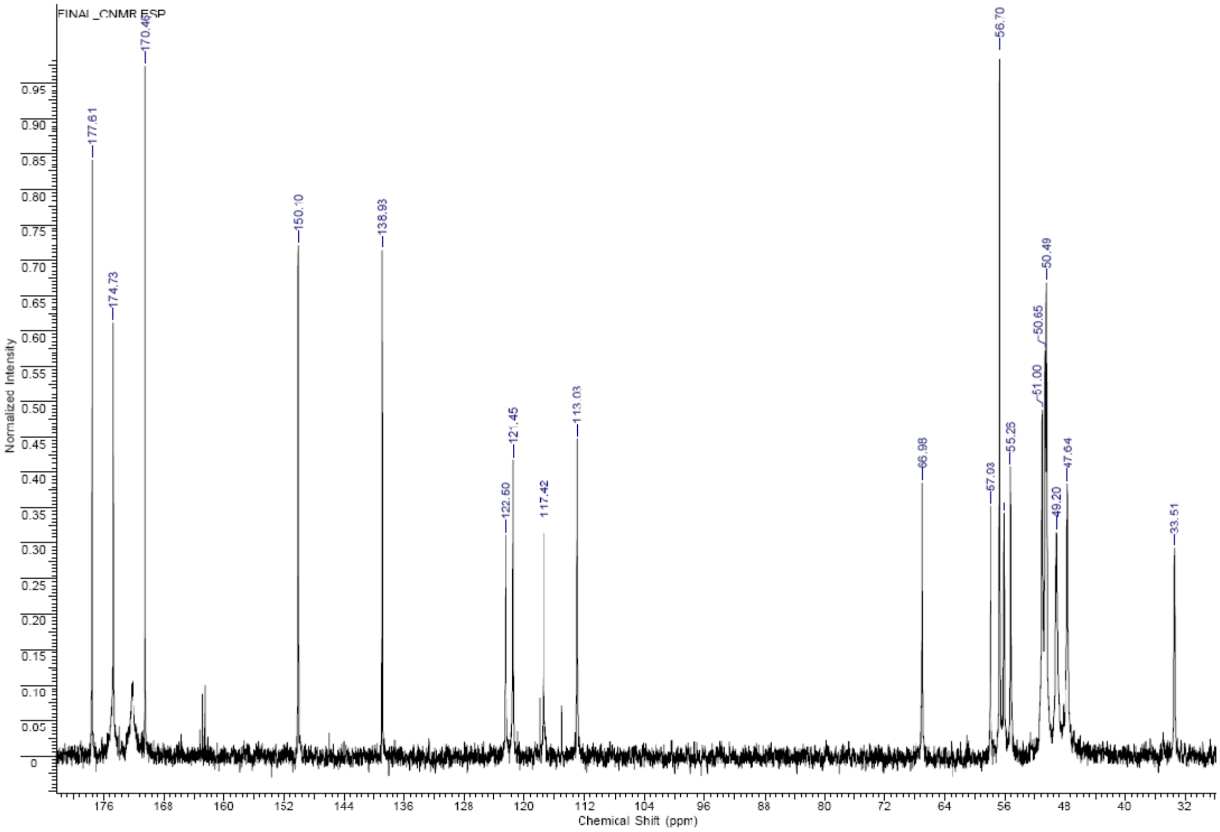
FINAL_CNMR.ESP
Normalized Intensity
Chemical Shift (ppm)
177.61
174.73
170.46
150.10
138.93
122.60
121.45
117.42
113.03
66.98
57.03
56.70
55.28
51.00
50.65
50.49
49.20
47.64
33.51
176
168
160
152
144
136
128
120
112
104
96
88
80
72
64
56
48
40
32

Appendix 1

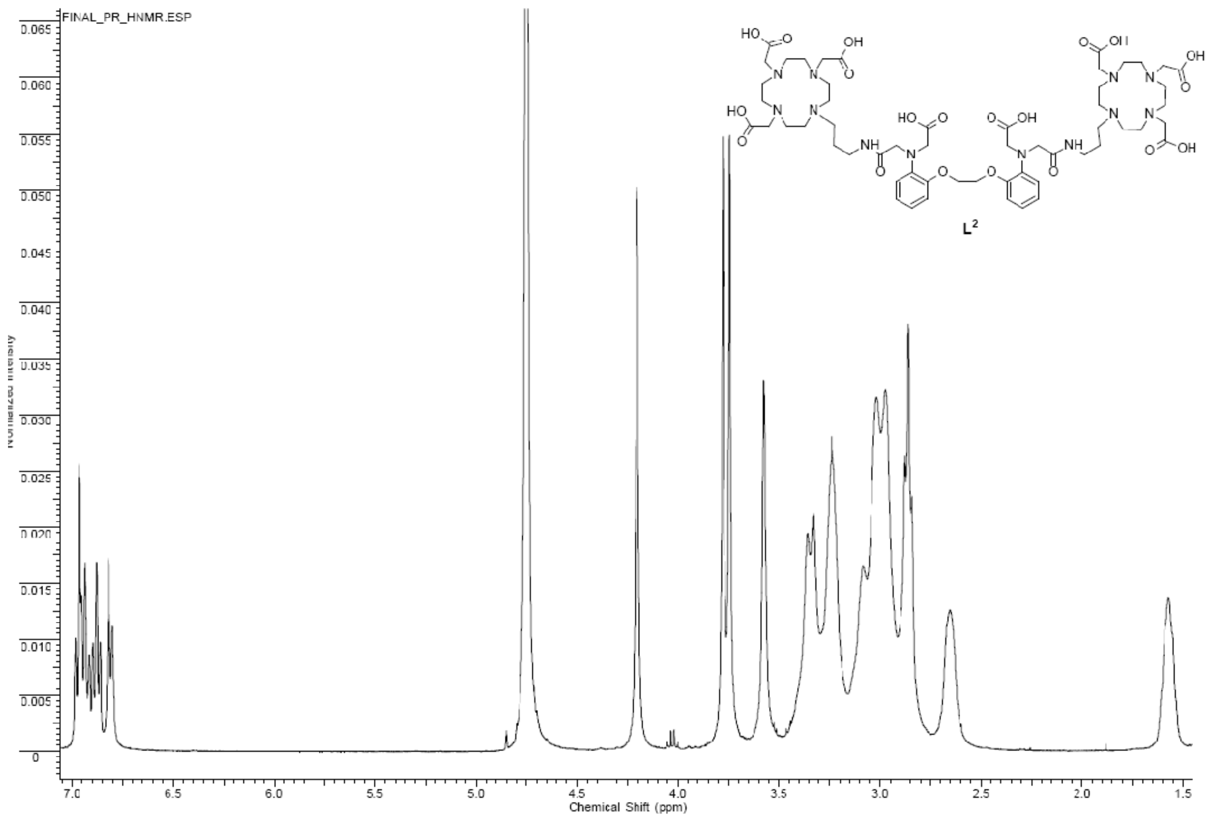
FINAL_PR_HNMR.ESP
Normalized Intensity
0.065
0.060
0.055
0.050
0.045
0.040
0.035
0.030
0.025
0.020
0.015
0.010
0.005
0
7.0
6.5
6.0
5.5
5.0
4.5
4.0
3.5
3.0
2.5
2.0
1.5
Chemical Shift (ppm)
HO
O
OH
N
NH
L2

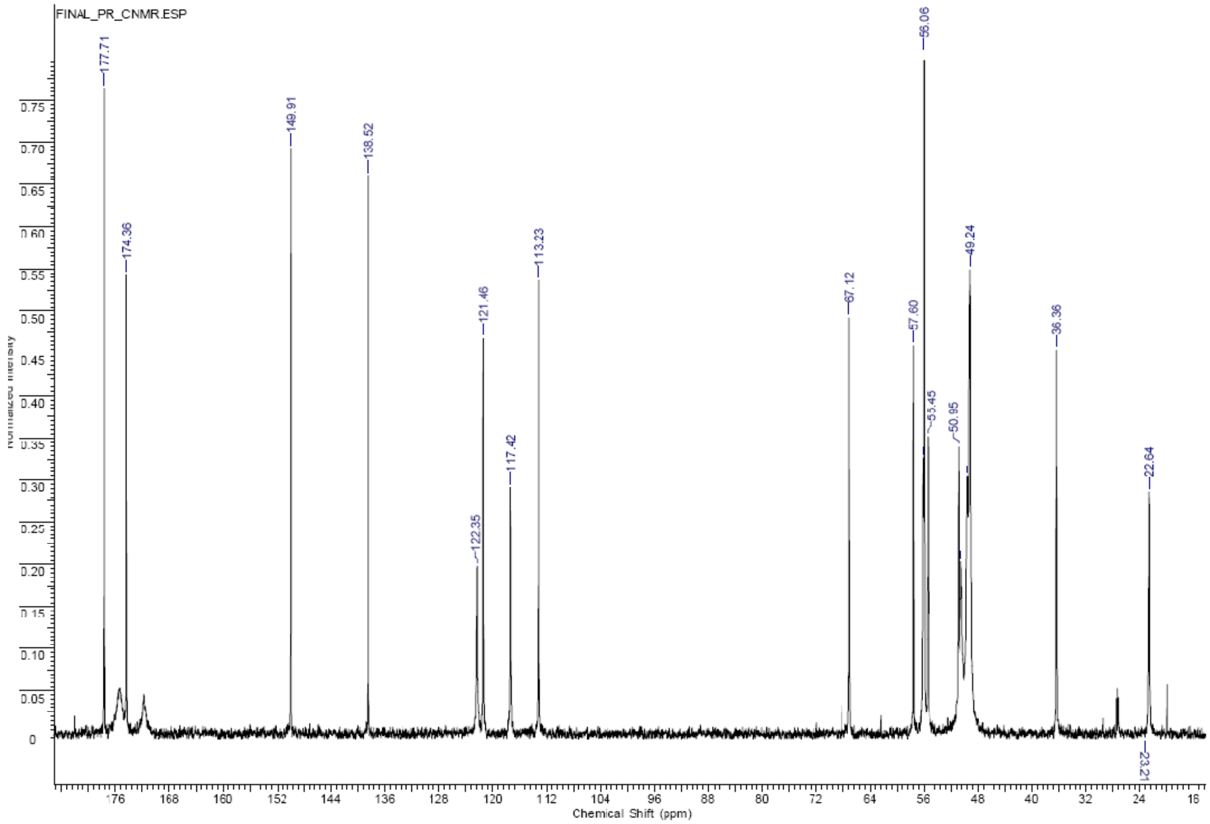
FINAL_PR_CNMR.ESP
Normalized Intensity
0.75
0.70
0.65
0.60
0.55
0.50
0.45
0.40
0.35
0.30
0.25
0.20
0.15
0.10
0.05
0
177.71
174.36
149.91
138.52
122.35
121.46
117.42
113.23
67.12
57.60
56.06
55.45
50.95
49.24
36.36
22.64
23.21
176
168
160
152
144
136
128
120
112
104
96
88
80
72
64
56
48
40
32
24
16
Chemical Shift (ppm)

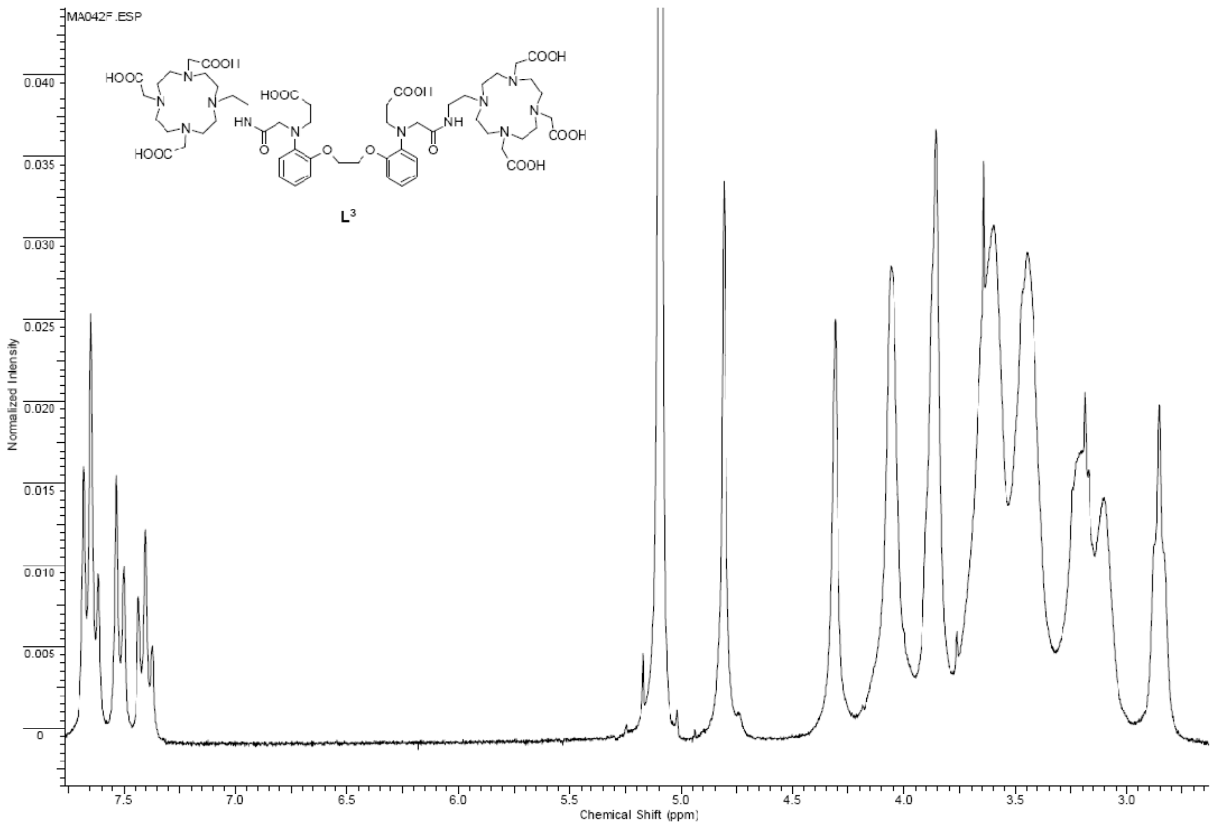
MA042F.ESP
HOOC
COOH
HOOC
COOH
COOH
HOOC
HN
NH
O
O
COOH
HOOC
COOH
L^3
Normalized Intensity
0.040
0.035
0.030
0.025
0.020
0.015
0.010
0.005
0
7.5
7.0
6.5
6.0
5.5
5.0
4.5
4.0
3.5
3.0
Chemical Shift (ppm)

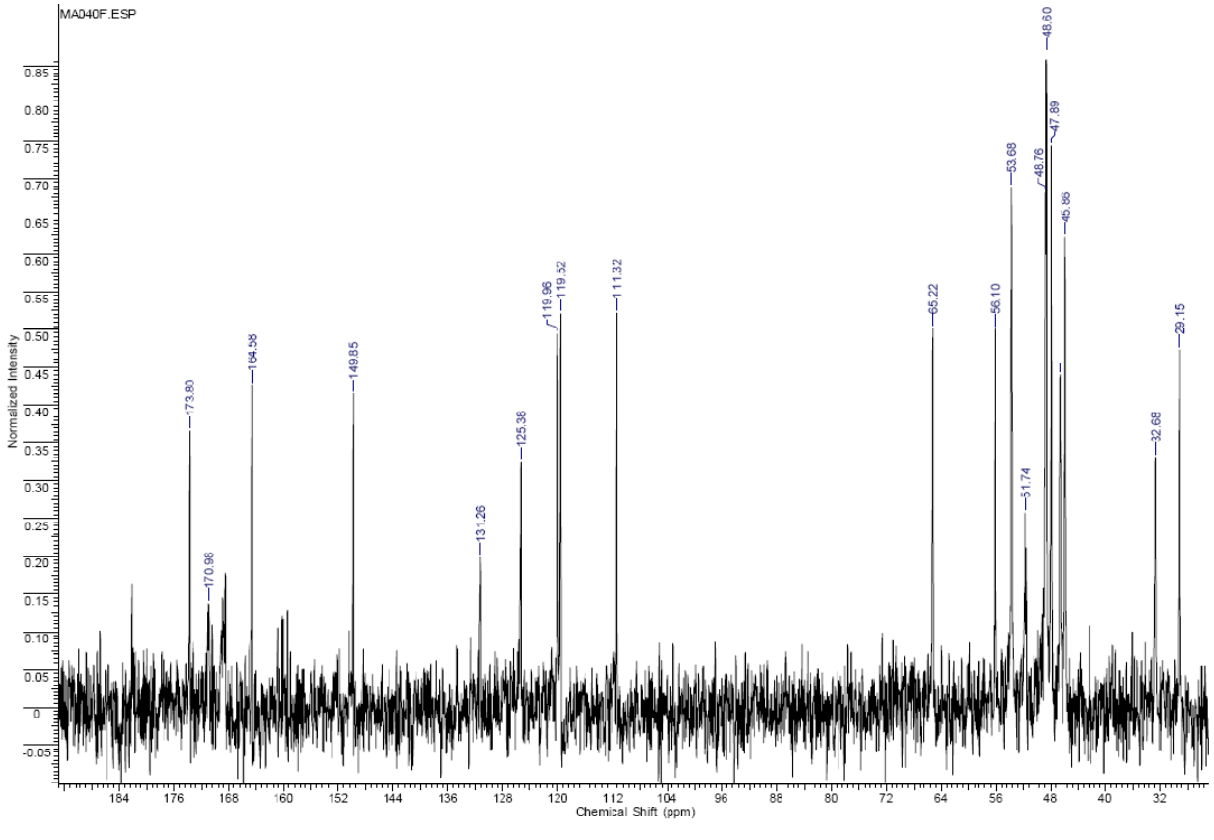
MA040F.ESP
Normalized Intensity
0.85
0.80
0.75
0.70
0.65
0.60
0.55
0.50
0.45
0.40
0.35
0.30
0.25
0.20
0.15
0.10
0.05
0
-0.05
173.80
170.96
164.58
149.85
131.26
125.38
119.96
119.52
111.32
65.22
56.10
53.68
51.74
48.76
48.60
47.89
45.86
32.68
29.15
184
176
168
160
152
144
136
128
120
112
104
96
88
80
72
64
56
48
40
32
Chemical Shift (ppm)

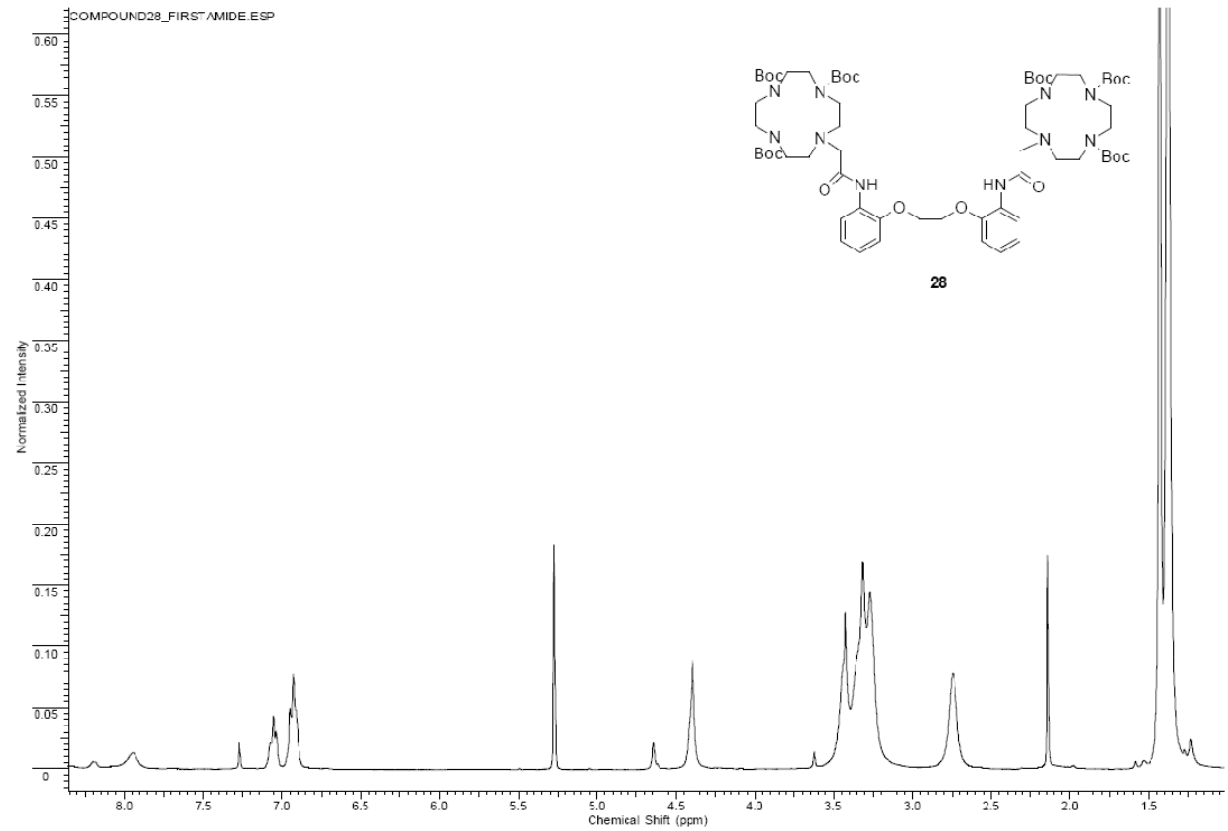
COMPOUND28_FIRSTAMIDE.ESP
Normalized Intensity
0
0.05
0.10
0.15
0.20
0.25
0.30
0.35
0.40
0.45
0.50
0.55
0.60
8.0
7.5
7.0
6.5
6.0
5.5
5.0
4.5
4.0
3.5
3.0
2.5
2.0
1.5
Chemical Shift (ppm)
Boc
N
NH
HN
O

28

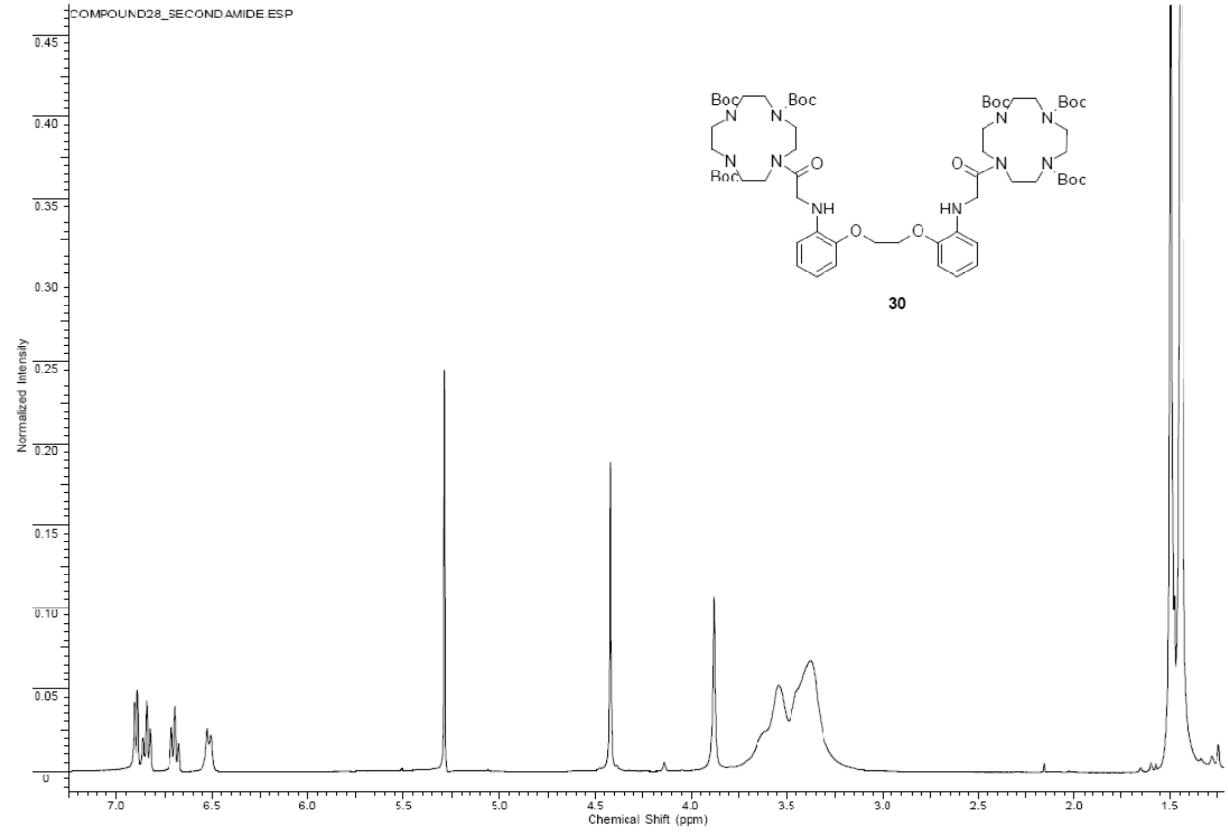
COMPOUND28_SECONDAMIDE.ESP
Normalized Intensity
0
0.05
0.10
0.15
0.20
0.25
0.30
0.35
0.40
0.45
7.0
6.5
6.0
5.5
5.0
4.5
4.0
3.5
3.0
2.5
2.0
1.5
Chemical Shift (ppm)
Boc
N
NH
HN
O

30

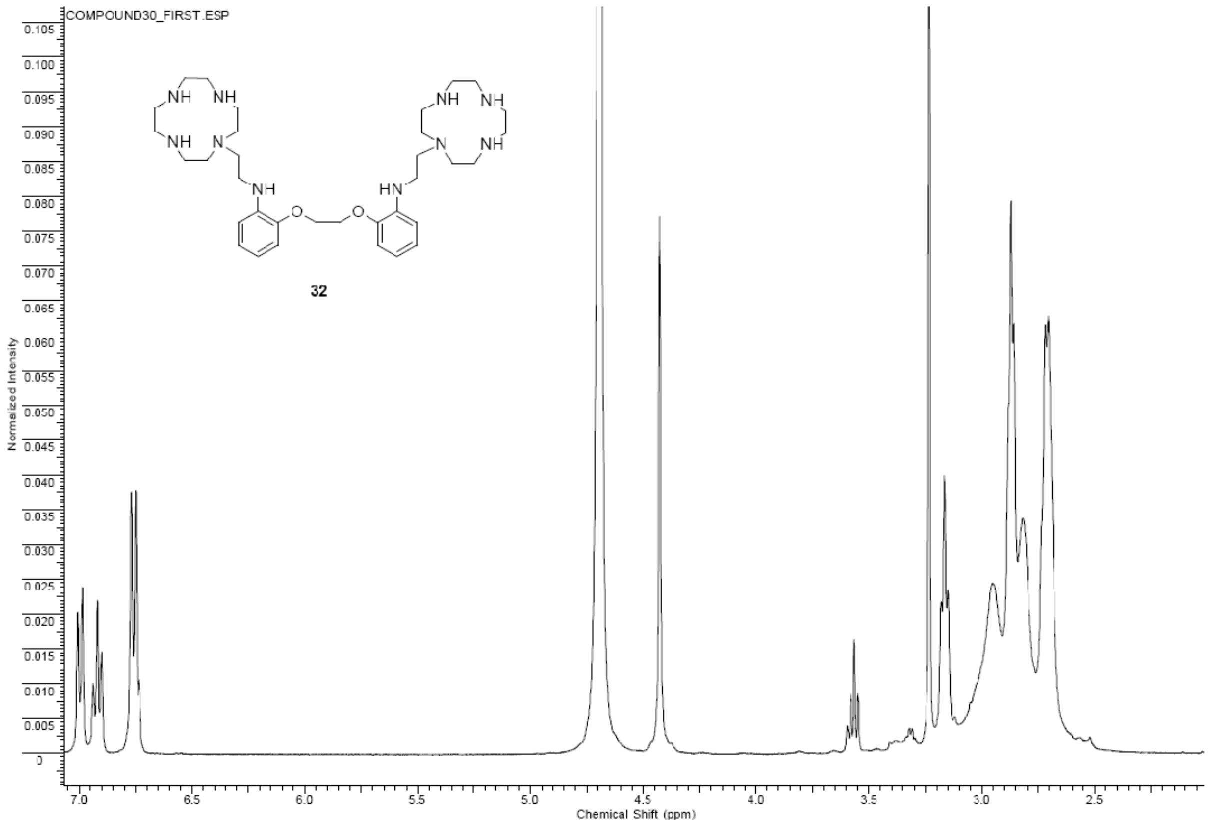
COMPOUND30_FIRST.ESP
NH
N
O
32
Normalized Intensity
0.105
0.100
0.095
0.090
0.085
0.080
0.075
0.070
0.065
0.060
0.055
0.050
0.045
0.040
0.035
0.030
0.025
0.020
0.015
0.010
0.005
0
7.0
6.5
6.0
5.5
5.0
4.5
4.0
3.5
3.0
2.5
Chemical Shift (ppm)

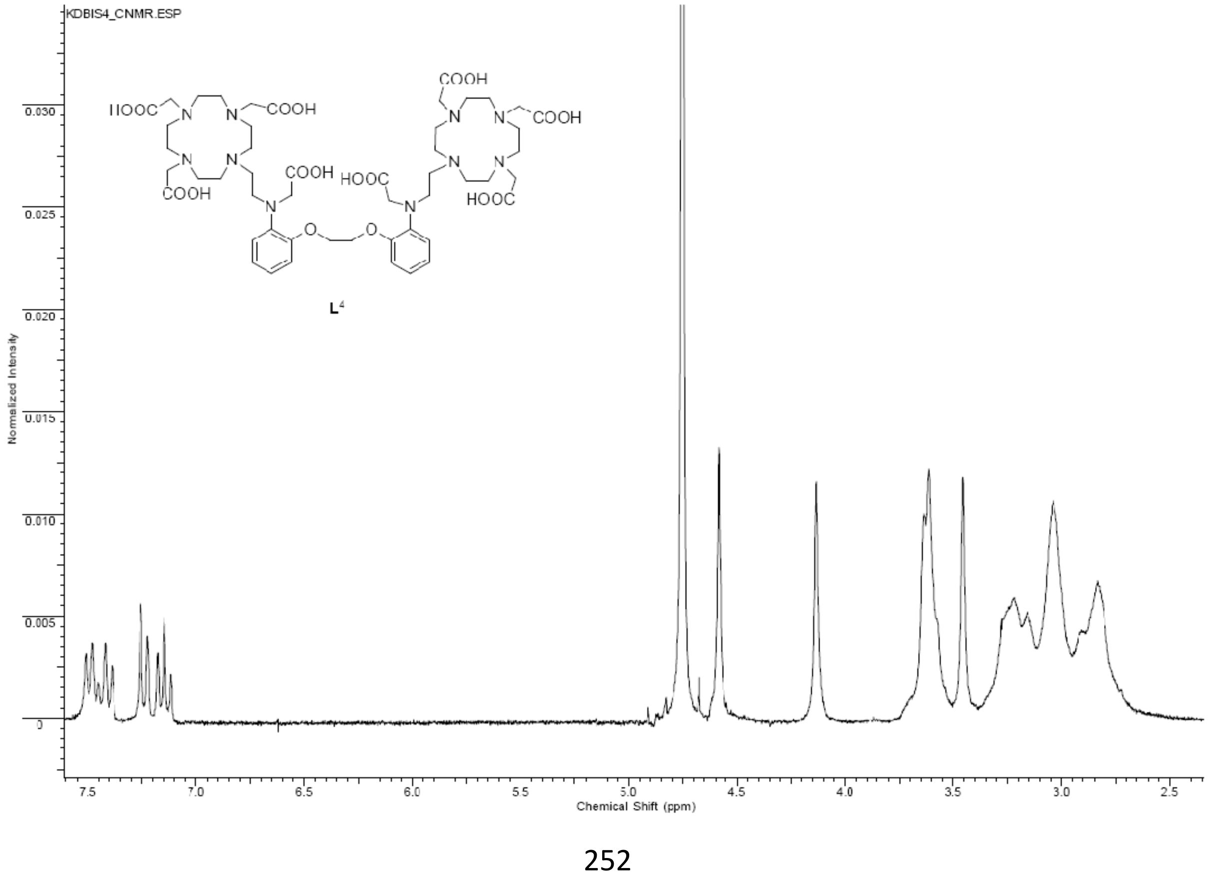
KDBIS4_CNMR.ESP
HOOC
COOH
N
O
L^4
Normalized Intensity
0.030
0.025
0.020
0.015
0.010
0.005
0
7.5
7.0
6.5
6.0
5.5
5.0
4.5
4.0
3.5
3.0
2.5
Chemical Shift (ppm)

Appendix 1

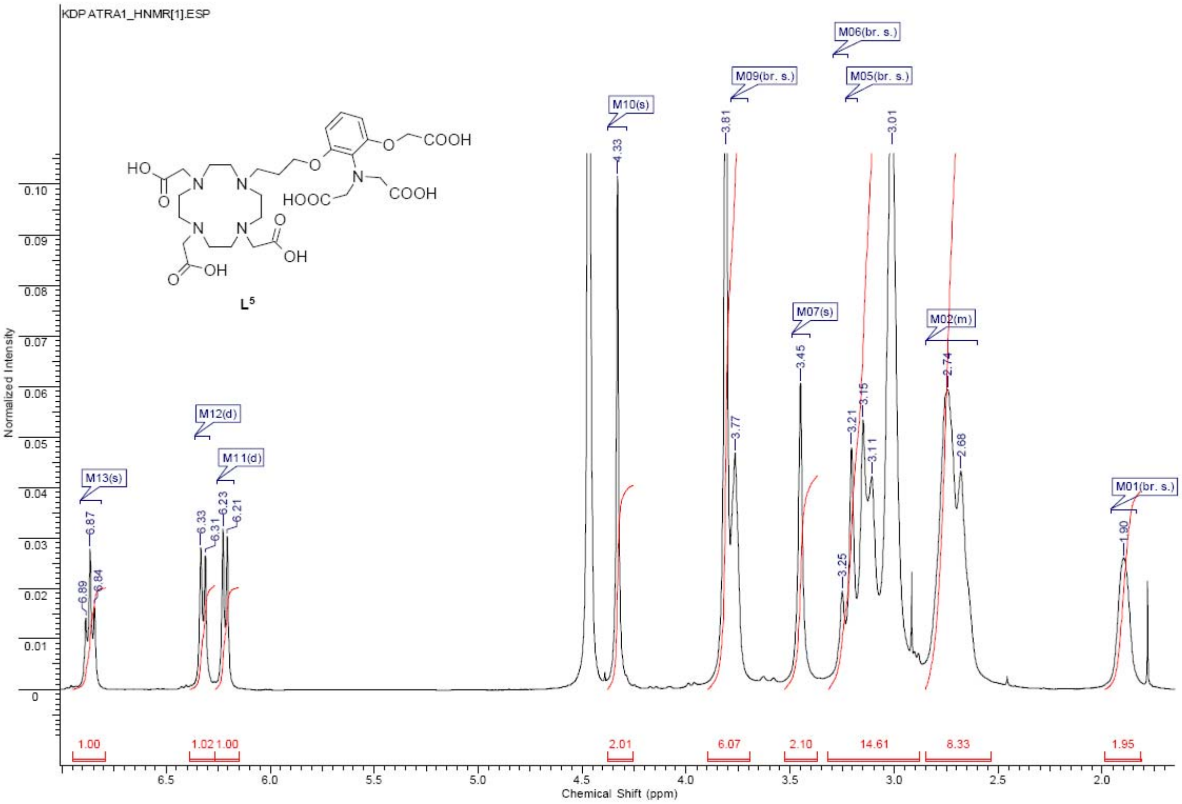
KDPATRA1_HNMR[1].ESP
L5
HO
COOH
HOOC
OH
N
O
M13(s)
M12(d)
M11(d)
M10(s)
M09(br. s.)
M07(s)
M06(br. s.)
M05(br. s.)
M02(m)
M01(br. s.)
6.89
6.87
6.84
6.33
6.31
6.23
6.21
4.33
3.81
3.77
3.45
3.25
3.21
3.15
3.11
3.01
2.74
2.68
1.90
1.00
1.02
1.00
2.01
6.07
2.10
14.61
8.33
1.95
Normalized Intensity
Chemical Shift (ppm)

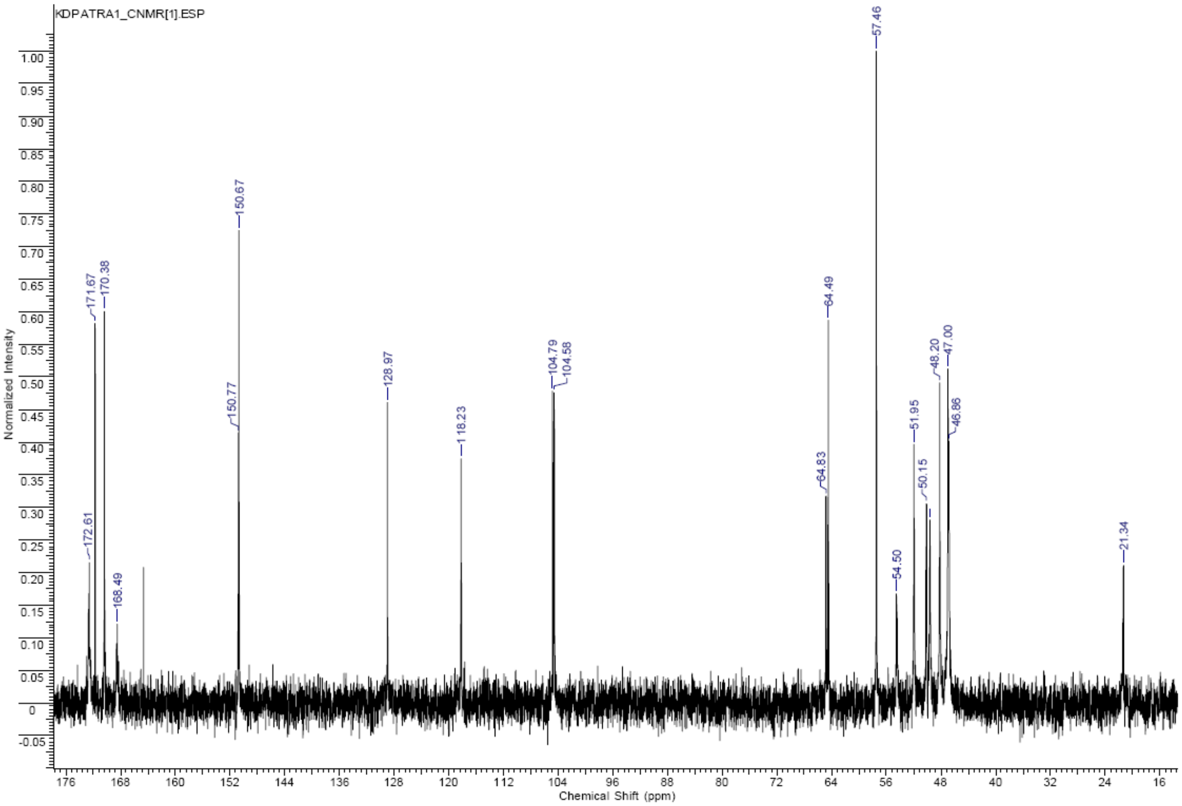
KDPATRA1_CNMR[1].ESP
172.61
171.67
170.38
168.49
150.77
150.67
128.97
118.23
104.79
104.58
64.83
64.49
57.46
54.50
51.95
50.15
48.20
47.00
46.86
21.34
Normalized Intensity
Chemical Shift (ppm)

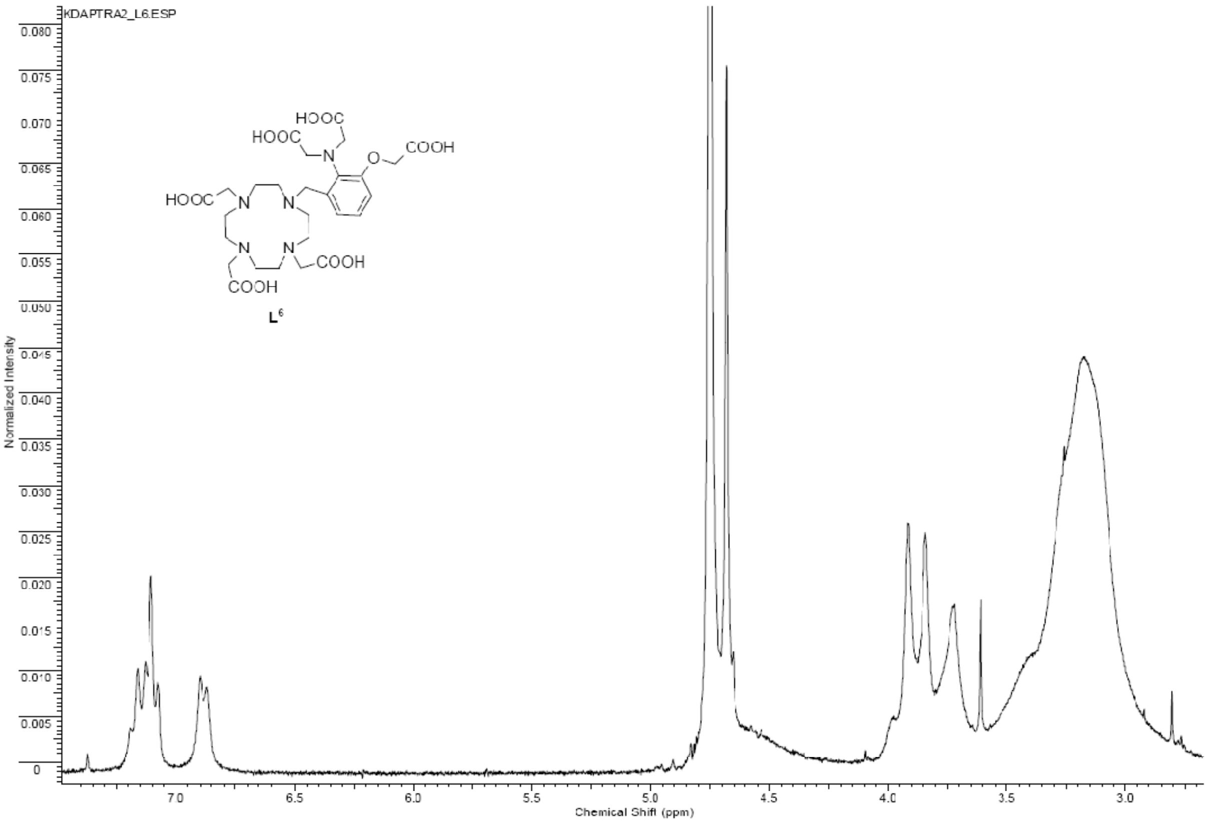
KDAPTRA2_L6.ESP
HOOC
HOOC
N
O
COOH
HOOC
N
N
N
N
COOH
COOH
L6
Normalized Intensity
0.080
0.075
0.070
0.065
0.060
0.055
0.050
0.045
0.040
0.035
0.030
0.025
0.020
0.015
0.010
0.005
0
7.0
6.5
6.0
5.5
5.0
4.5
4.0
3.5
3.0
Chemical Shift (ppm)

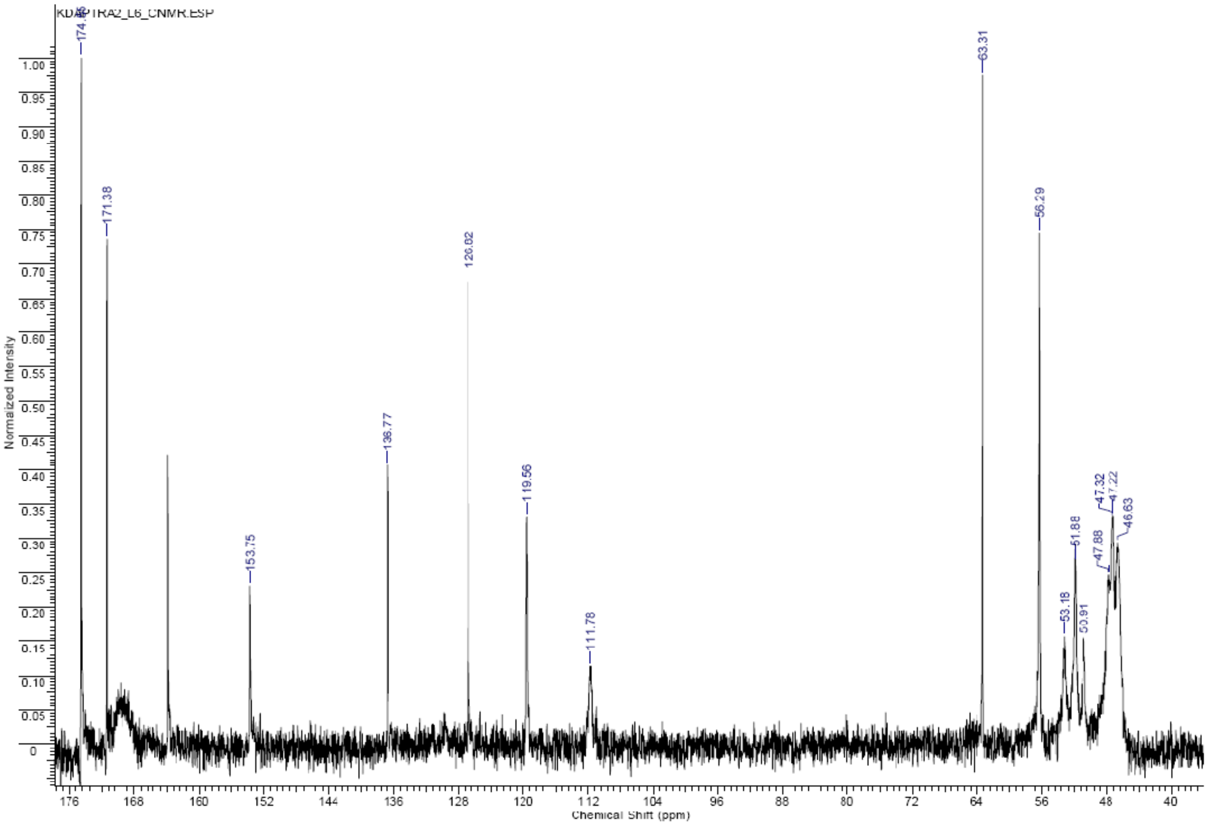
KDAPTRA2_L6_CNMR.ESP
174.45
171.38
153.75
136.77
126.02
119.56
111.78
63.31
56.29
53.18
51.88
50.91
47.88
47.32
47.22
46.63
Normalized Intensity
1.00
0.95
0.90
0.85
0.80
0.75
0.70
0.65
0.60
0.55
0.50
0.45
0.40
0.35
0.30
0.25
0.20
0.15
0.10
0.05
0
176
168
160
152
144
136
128
120
112
104
96
88
80
72
64
56
48
40
Chemical Shift (ppm)

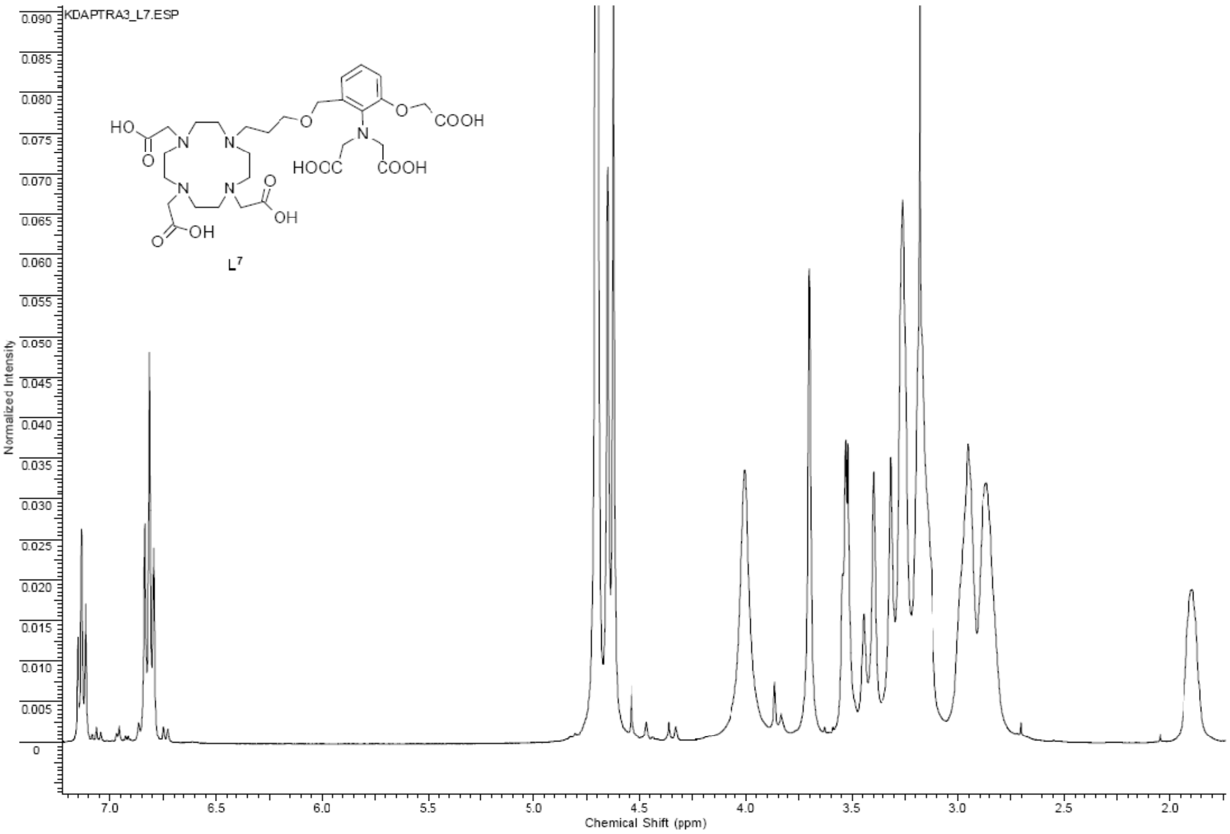
KDAPTRA3_L7.ESP
HO
O
N
N
N
N
O
OH
O
OH
O
O
COOH
N
HOOC
COOH
L⁷
Normalized Intensity
0.090
0.085
0.080
0.075
0.070
0.065
0.060
0.055
0.050
0.045
0.040
0.035
0.030
0.025
0.020
0.015
0.010
0.005
0
7.0
6.5
6.0
5.5
5.0
4.5
4.0
3.5
3.0
2.5
2.0
Chemical Shift (ppm)

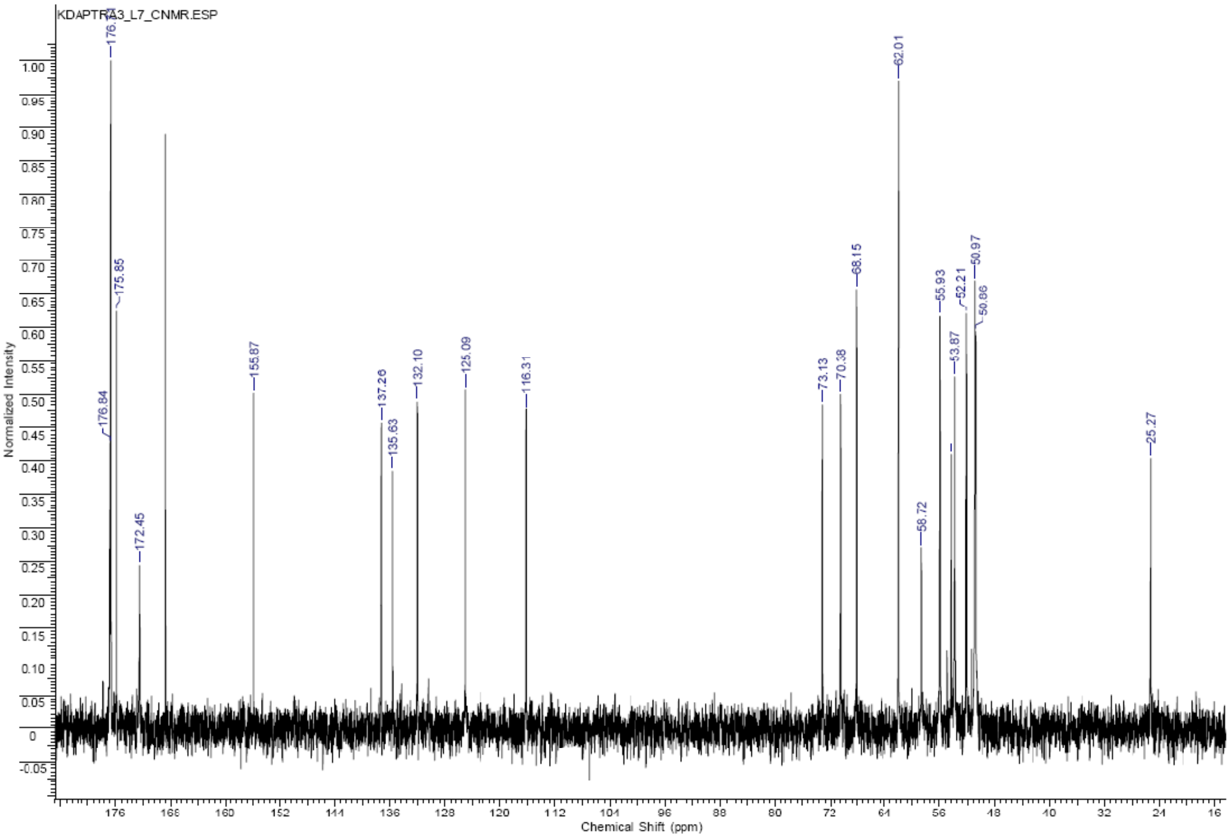
KDAPTRA3_L7_CNMR.ESP
176.
176.84
175.85
172.45
155.87
137.26
135.63
132.10
125.09
116.31
73.13
70.38
68.15
62.01
58.72
55.93
53.87
52.21
50.97
50.86
25.27
Normalized Intensity
1.00
0.95
0.90
0.85
0.80
0.75
0.70
0.65
0.60
0.55
0.50
0.45
0.40
0.35
0.30
0.25
0.20
0.15
0.10
0.05
0
-0.05
176
168
160
152
144
136
128
120
112
104
96
88
80
72
64
56
48
40
32
24
16
Chemical Shift (ppm)

Appendix 1

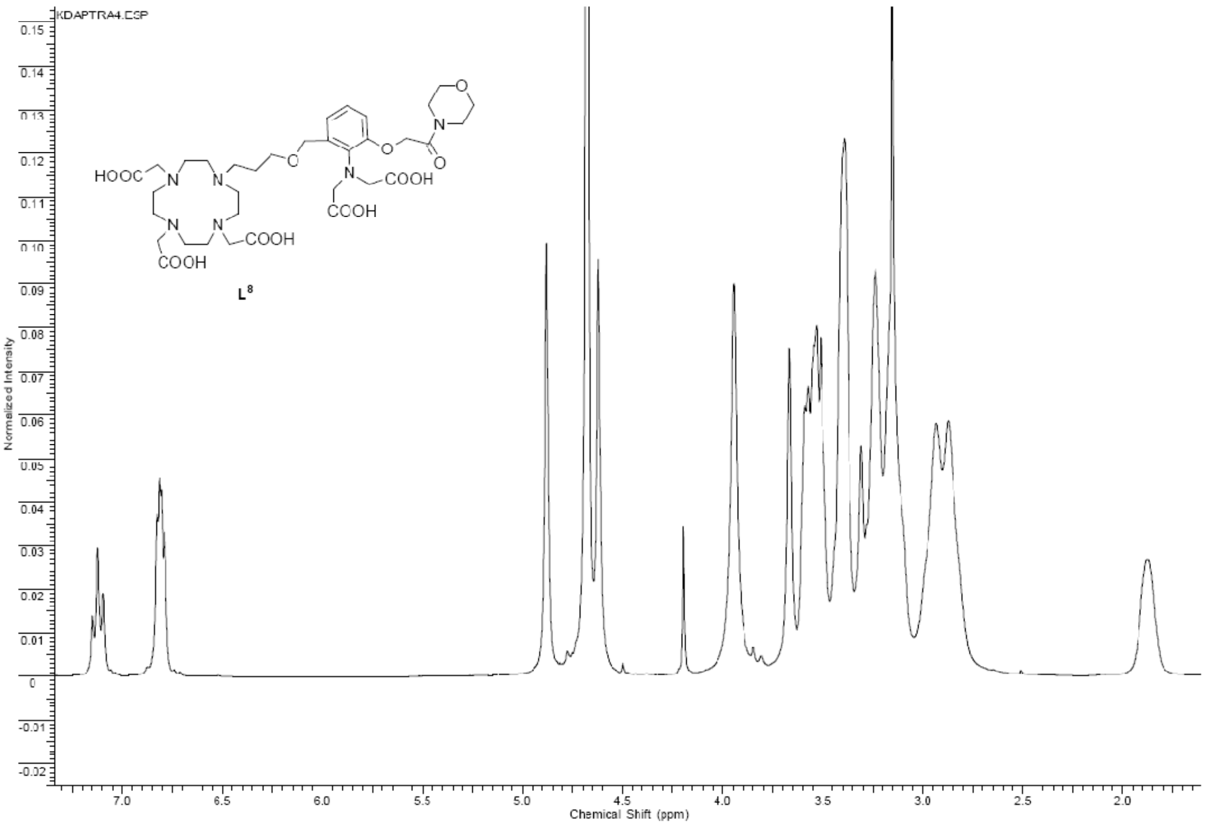
KDAPTRA4.ESP
HOOC
COOH
COOH
COOH
COOH
N
O
L8
Normalized Intensity
Chemical Shift (ppm)
7.0
6.5
6.0
5.5
5.0
4.5
4.0
3.5
3.0
2.5
2.0
0.15
0.14
0.13
0.12
0.11
0.10
0.09
0.08
0.07
0.06
0.05
0.04
0.03
0.02
0.01
0
-0.01
-0.02

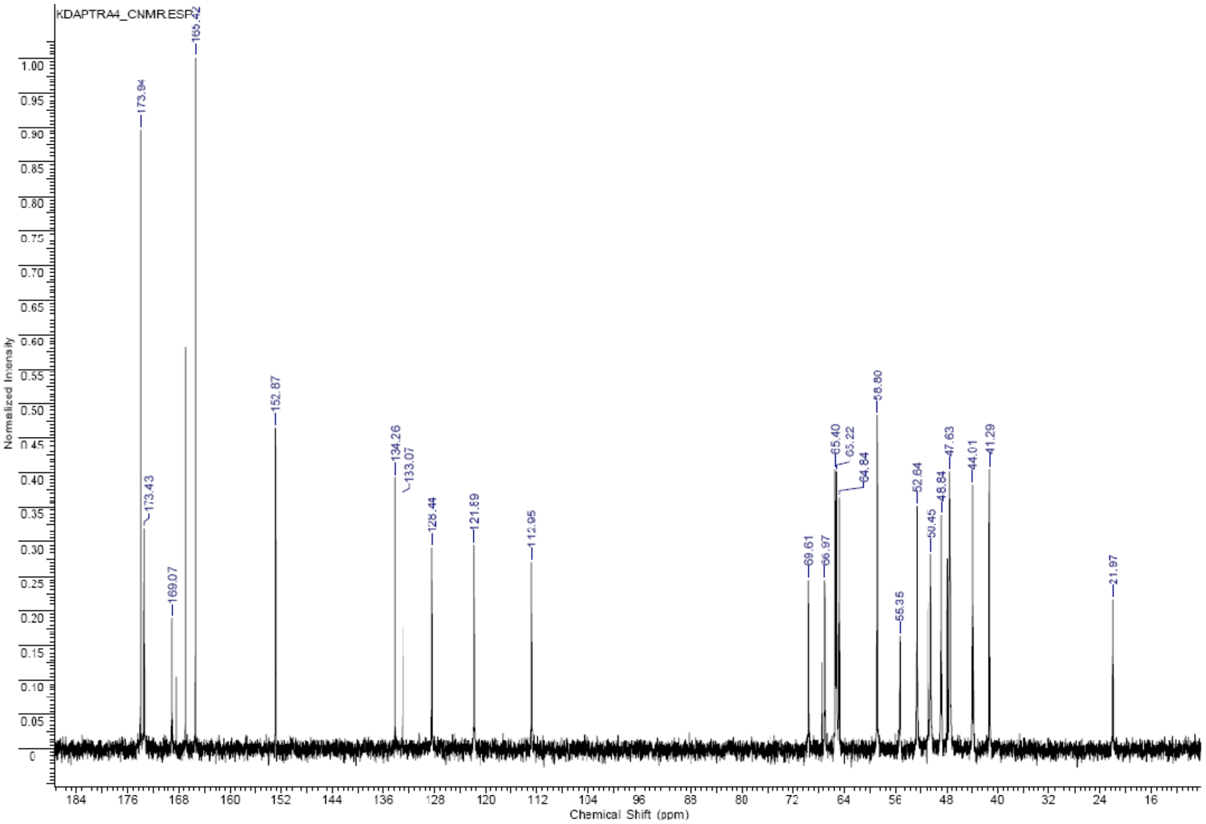
KDAPTRA4_CNMR.ESP
165.42
173.94
173.43
169.07
152.87
134.26
133.07
128.44
121.89
112.95
69.61
66.97
65.40
65.22
64.84
58.80
55.35
52.64
50.45
48.84
47.63
44.01
41.29
21.97
Normalized Intensity
Chemical Shift (ppm)
184
176
168
160
152
144
136
128
120
112
104
96
88
80
72
64
56
48
40
32
24
16

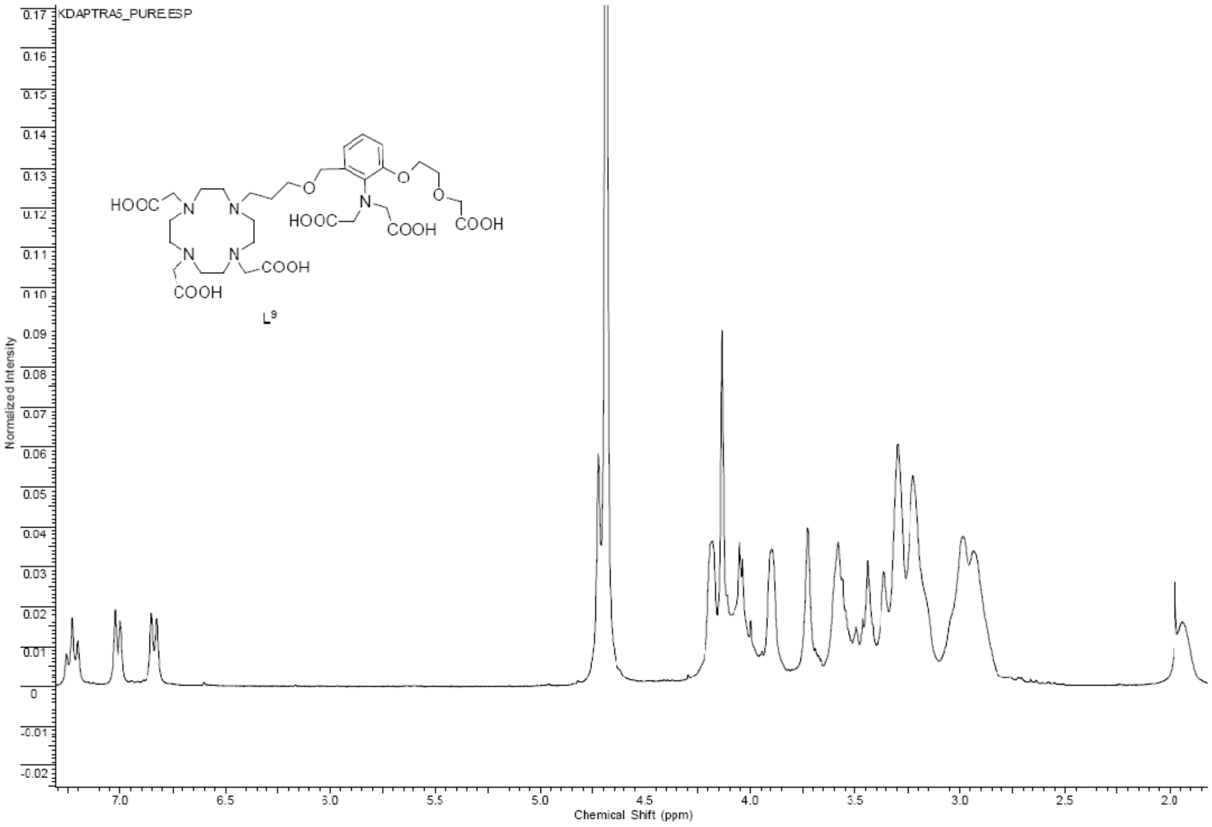
KDAPTRAS_PURE.ESP
Normalized Intensity
0.17
0.16
0.15
0.14
0.13
0.12
0.11
0.10
0.09
0.08
0.07
0.06
0.05
0.04
0.03
0.02
0.01
0
-0.01
-0.02
7.0
6.5
6.0
5.5
5.0
4.5
4.0
3.5
3.0
2.5
2.0
Chemical Shift (ppm)
HOOC
N
N
N
N
COOH
COOH
O
O
O
HOOC
N
COOH
COOH
L9

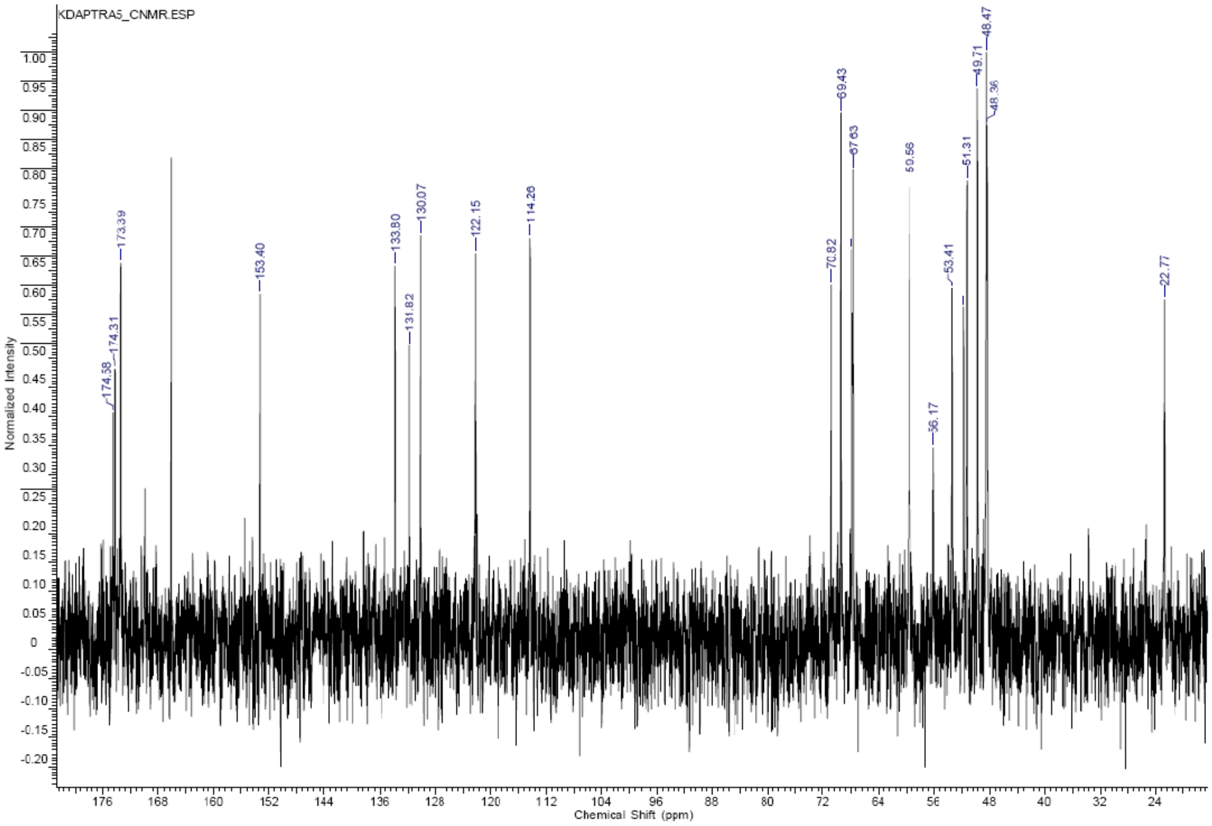
KDAPTRAS_CNMR.ESP
Normalized Intensity
1.00
0.95
0.90
0.85
0.80
0.75
0.70
0.65
0.60
0.55
0.50
0.45
0.40
0.35
0.30
0.25
0.20
0.15
0.10
0.05
0
-0.05
-0.10
-0.15
-0.20
174.58
174.31
173.39
153.40
133.80
131.82
130.07
122.15
114.26
70.82
69.43
67.63
59.56
56.17
53.41
51.31
49.71
48.47
48.36
22.77
176
168
160
152
144
136
128
120
112
104
96
88
80
72
64
56
48
40
32
24
Chemical Shift (ppm)

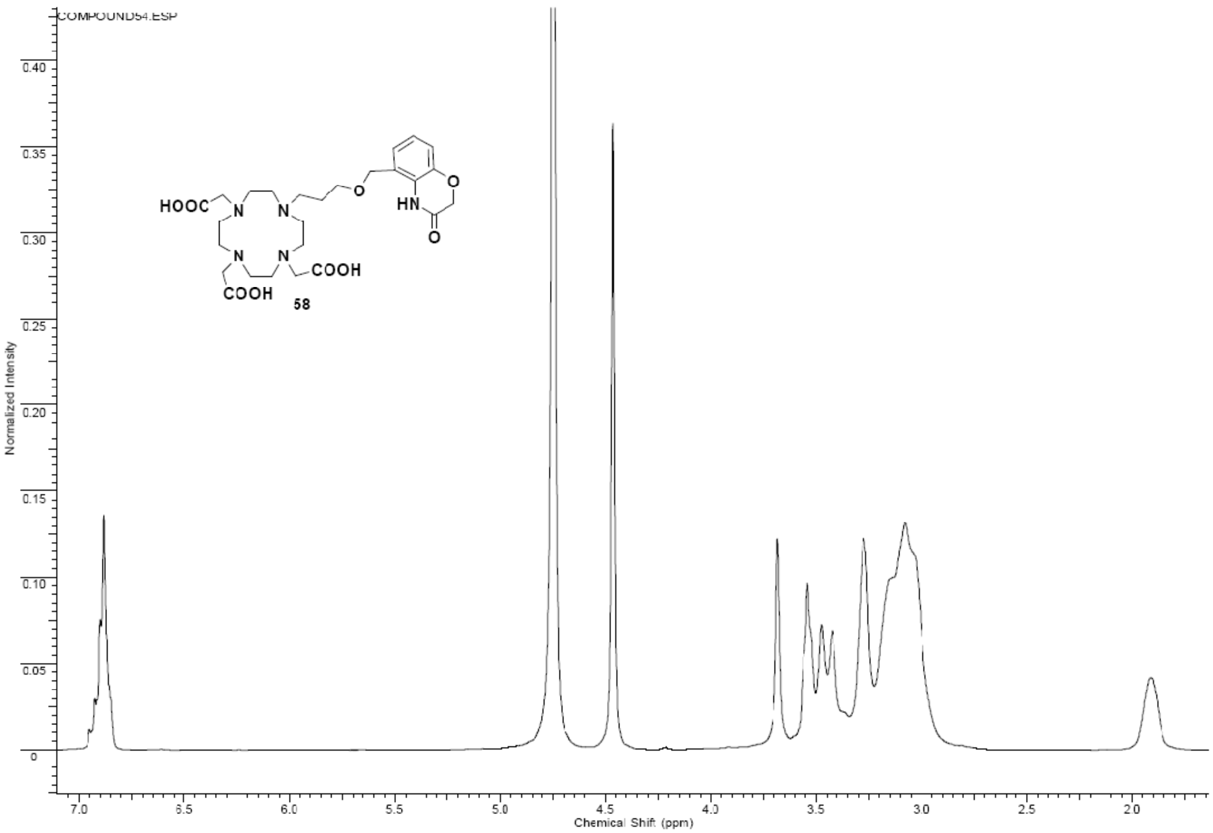
COMPOUND54.ESP
HOOC
N
N
N
N
COOH
COOH
O
HN
O
O
58
Normalized Intensity
0.40
0.35
0.30
0.25
0.20
0.15
0.10
0.05
0
7.0
6.5
6.0
5.5
5.0
4.5
4.0
3.5
3.0
2.5
2.0
Chemical Shift (ppm)

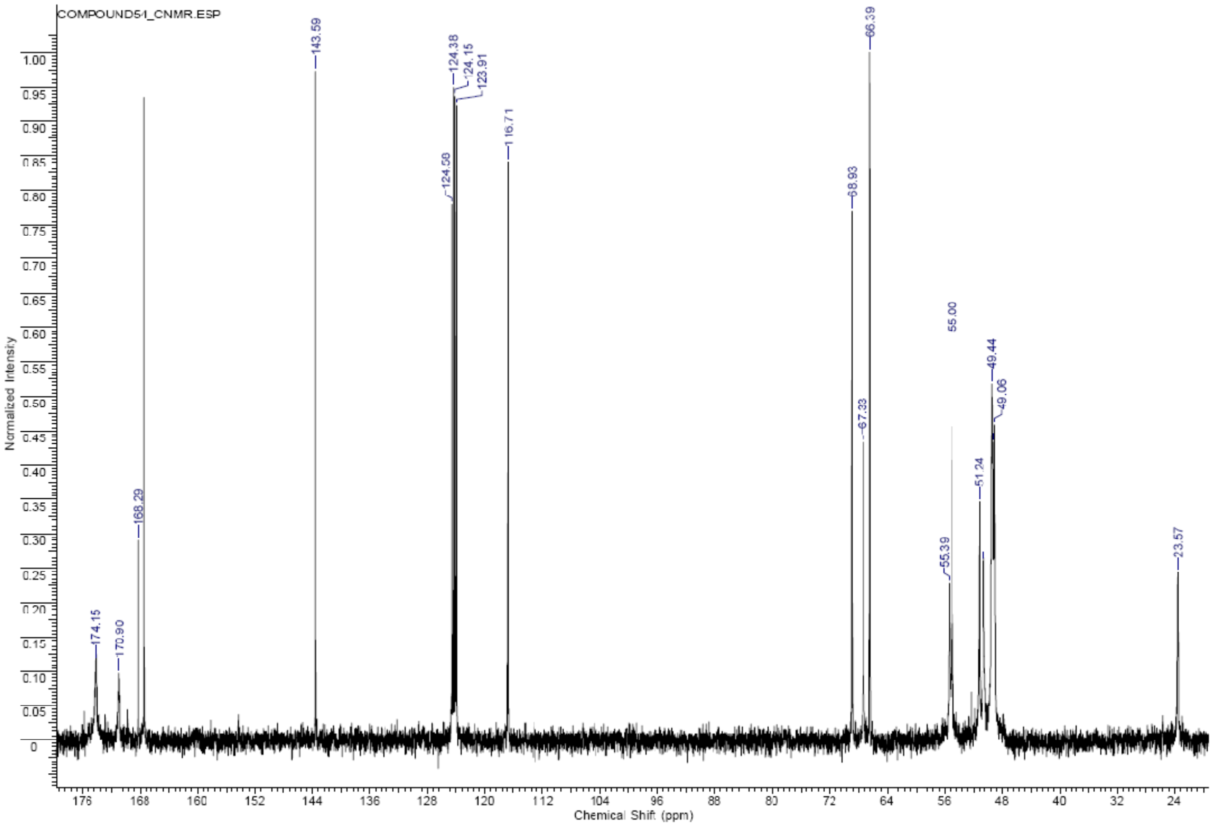
COMPOUND54_CNMR.ESP
143.59
124.38
124.15
123.91
124.58
116.71
66.39
68.93
67.33
55.00
55.39
51.24
49.44
49.06
23.57
168.29
174.15
170.90
Normalized Intensity
1.00
0.95
0.90
0.85
0.80
0.75
0.70
0.65
0.60
0.55
0.50
0.45
0.40
0.35
0.30
0.25
0.20
0.15
0.10
0.05
0
176
168
160
152
144
136
128
120
112
104
96
88
80
72
64
56
48
40
32
24
Chemical Shift (ppm)

Appendix 1

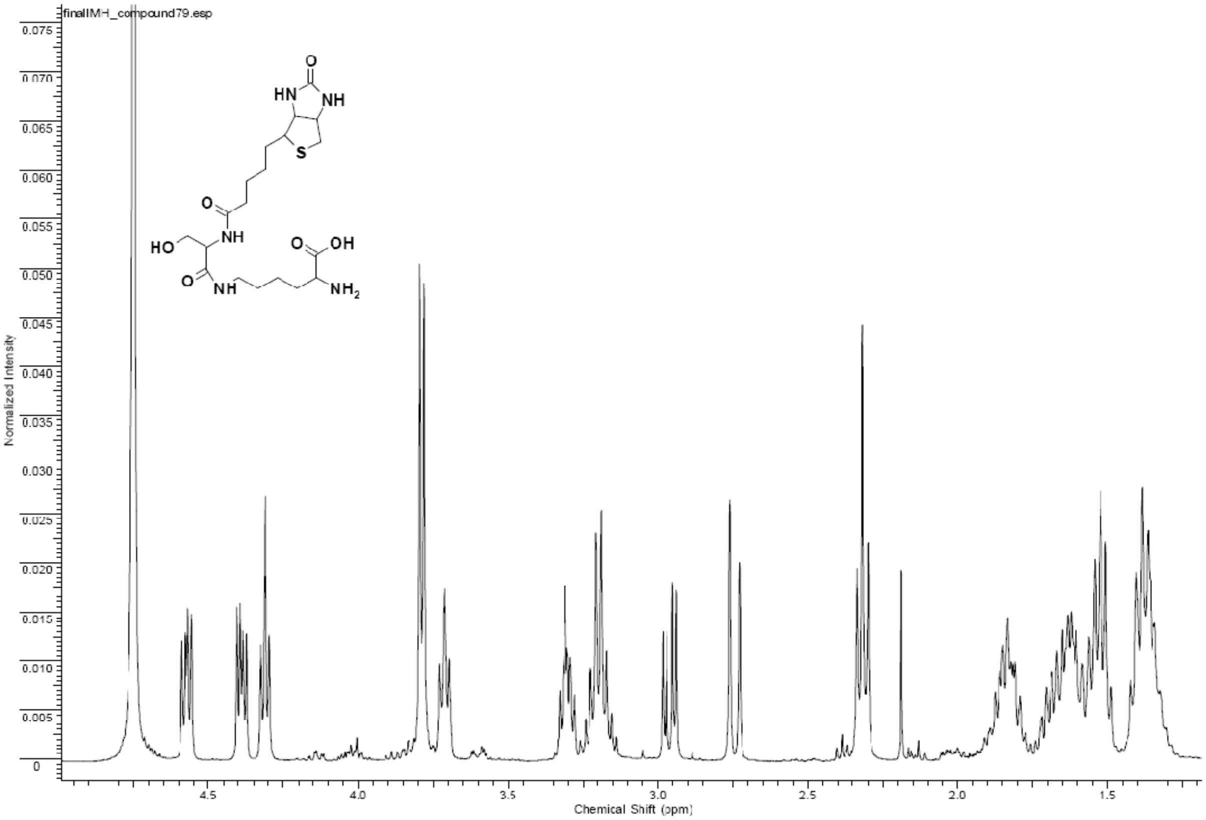
finalIMH_compound79.esp
Normalized Intensity
Chemical Shift (ppm)
0.075
0.070
0.065
0.060
0.055
0.050
0.045
0.040
0.035
0.030
0.025
0.020
0.015
0.010
0.005
0
4.5
4.0
3.5
3.0
2.5
2.0
1.5
O
HN
NH
S
O
NH
HO
O
OH
O
NH
NH2

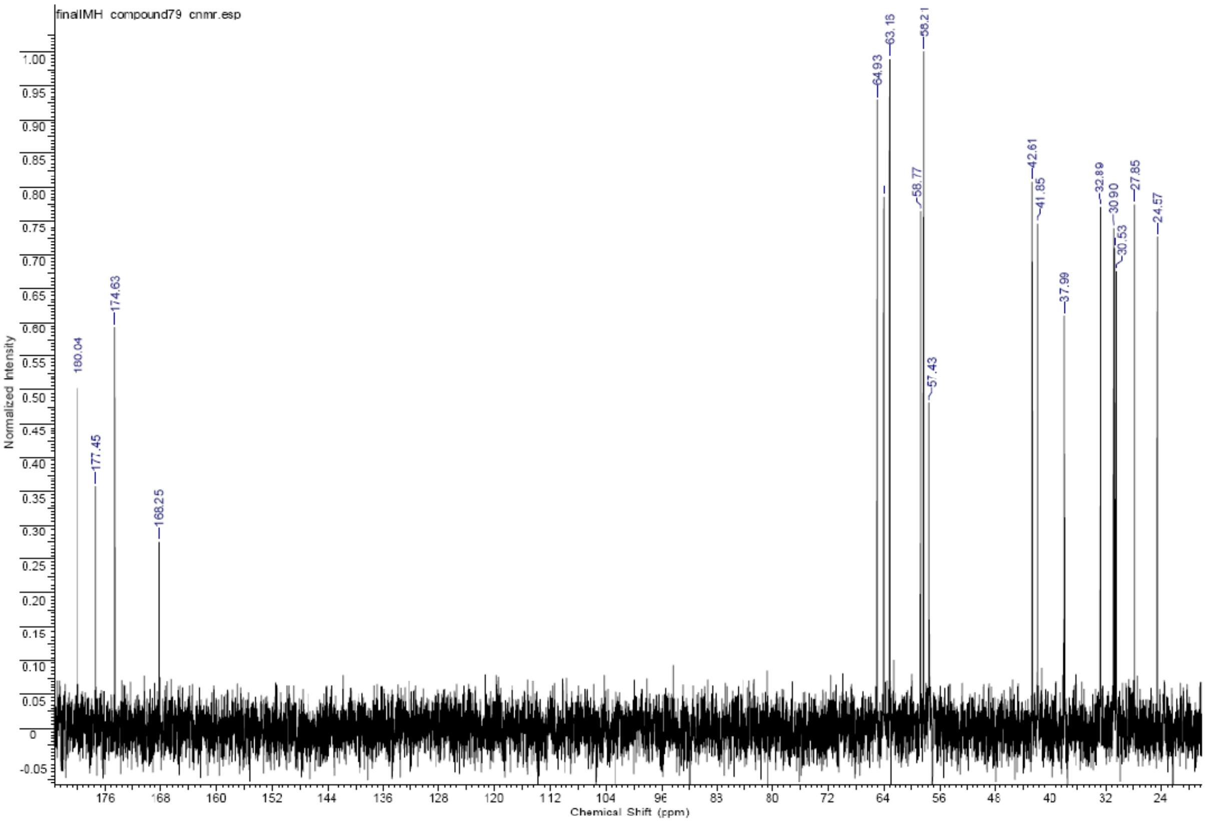
finalIMH_compound79_cnmr.esp
Normalized Intensity
Chemical Shift (ppm)
180.04
177.45
174.63
168.25
64.93
63.16
58.77
58.21
57.43
42.61
41.85
37.99
32.89
30.90
30.53
27.85
24.57
1.00
0.95
0.90
0.85
0.80
0.75
0.70
0.65
0.60
0.55
0.50
0.45
0.40
0.35
0.30
0.25
0.20
0.15
0.10
0.05
0
-0.05
176
168
160
152
144
136
128
120
112
104
96
88
80
72
64
56
48
40
32
24

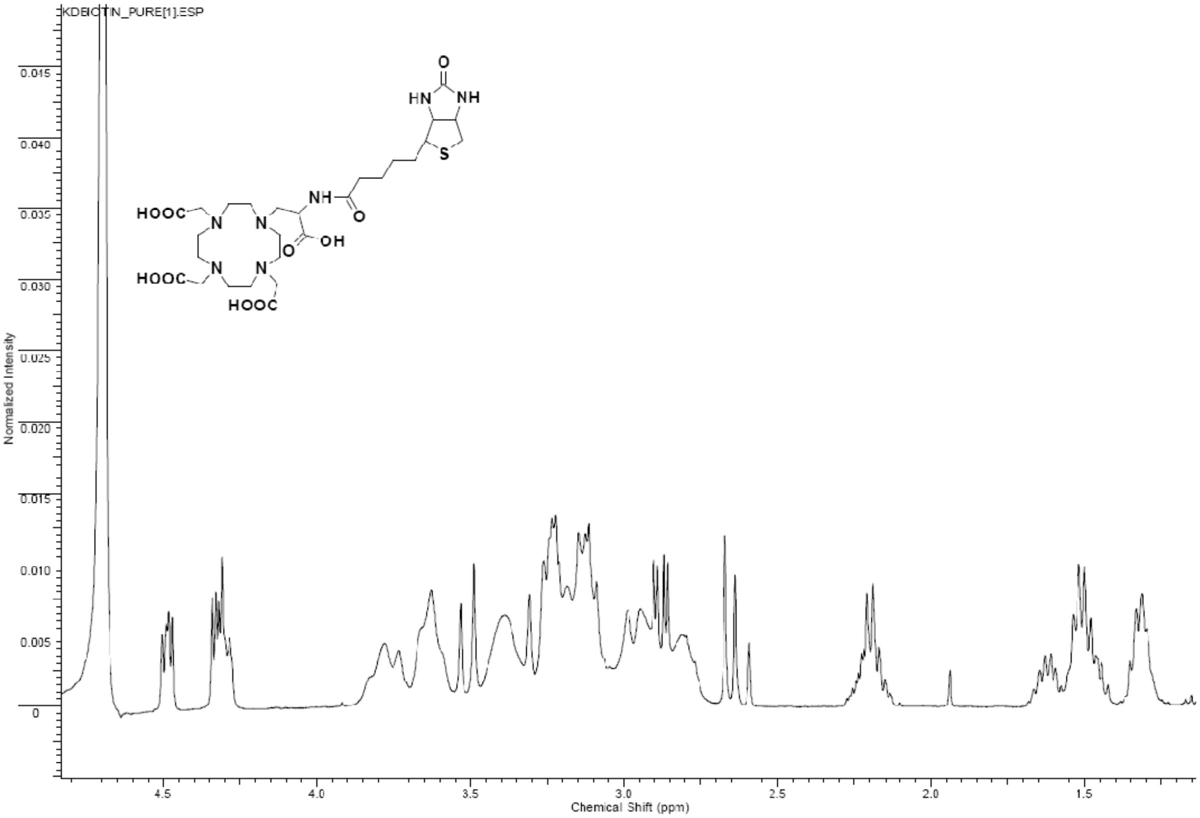
KDBIOTIN_PURE[1].ESP
Normalized Intensity
0.045
0.040
0.035
0.030
0.025
0.020
0.015
0.010
0.005
0
Chemical Shift (ppm)
4.5
4.0
3.5
3.0
2.5
2.0
1.5
HOOC
N
N
N
N
HOOC
HOOC
NH
O
OH
O
HN
NH
O
S

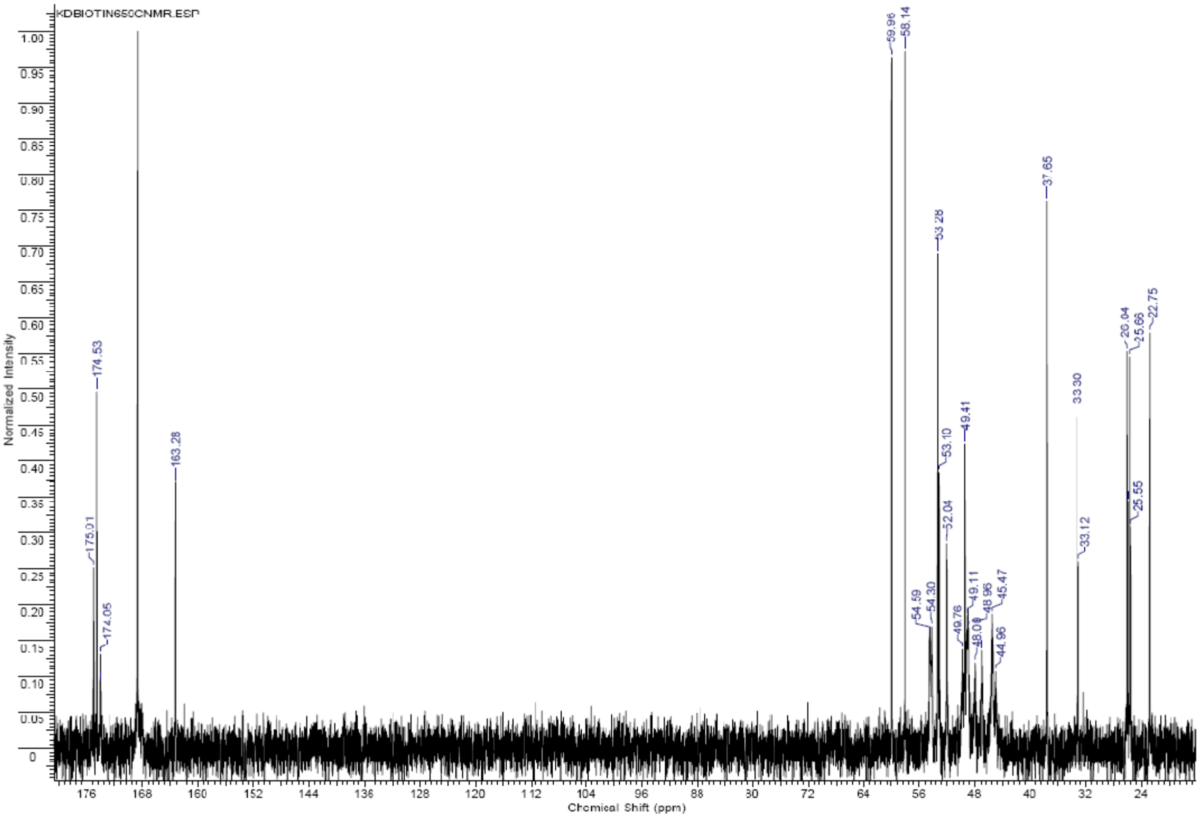
KDBIOTIN650CNMR.ESP
Normalized Intensity
1.00
0.95
0.90
0.85
0.80
0.75
0.70
0.65
0.60
0.55
0.50
0.45
0.40
0.35
0.30
0.25
0.20
0.15
0.10
0.05
0
175.01
174.53
174.05
163.28
59.96
58.14
54.59
54.30
53.28
53.10
52.04
49.76
49.41
49.11
48.96
48.08
45.47
44.96
37.65
33.30
33.12
26.04
25.66
25.55
22.75
Chemical Shift (ppm)
176
168
160
152
144
136
128
120
112
104
96
88
80
72
64
56
48
40
32
24

Appendix 1

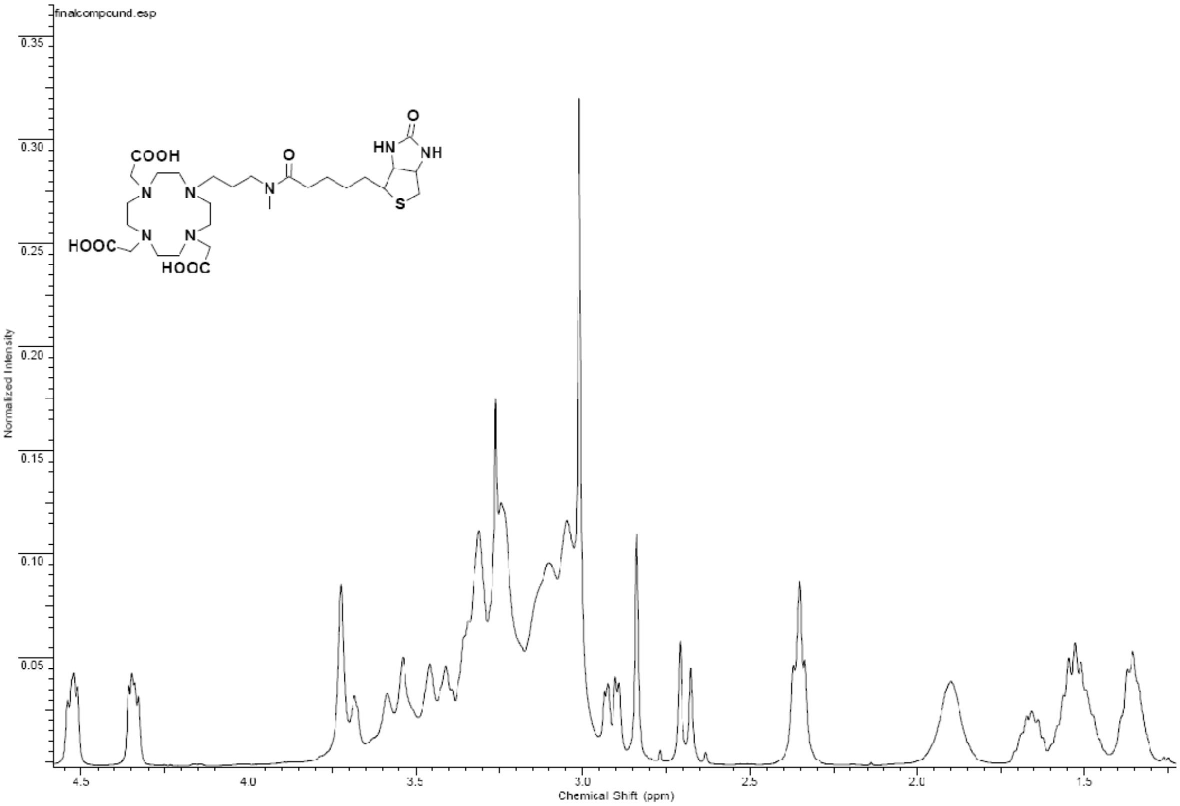
finalcompound.esp
Normalized Intensity
0.35
0.30
0.25
0.20
0.15
0.10
0.05
COOH
N
N
N
N
HOOC
HOOC
O
N
HN
NH
O
S
4.5
4.0
3.5
3.0
2.5
2.0
1.5
Chemical Shift (ppm)

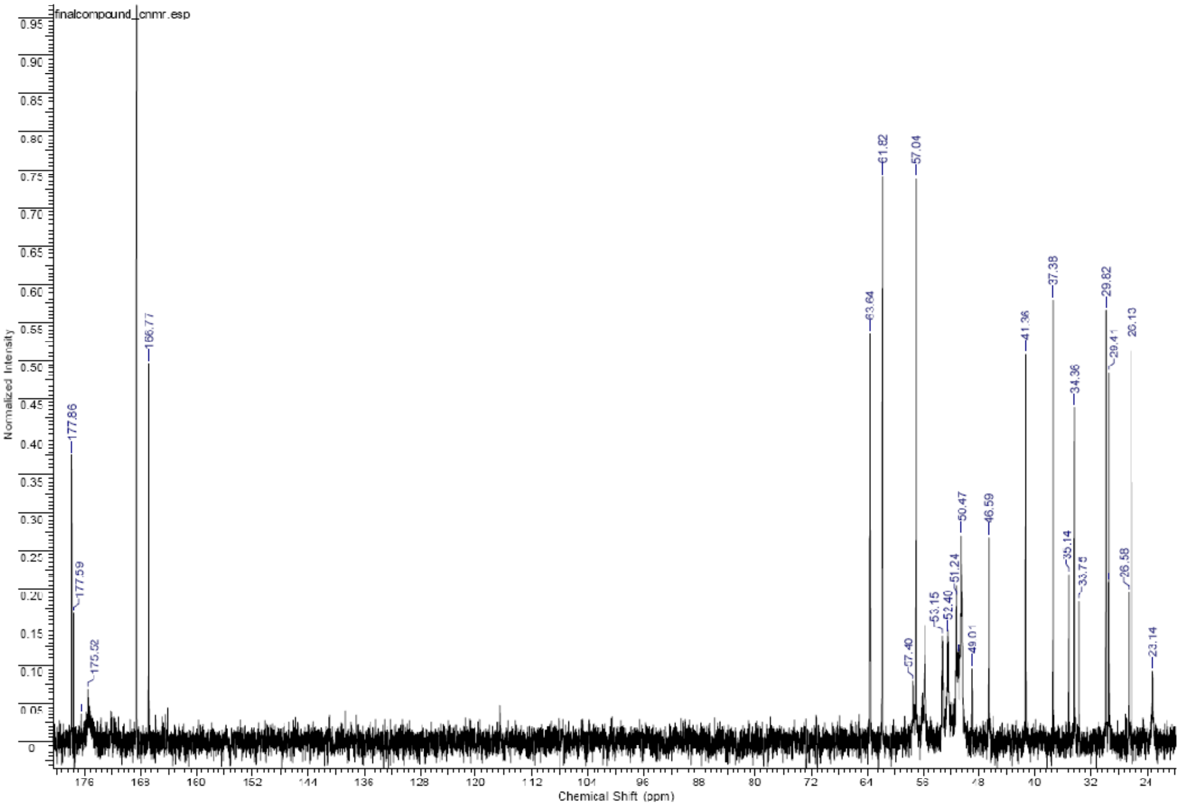
finalcompound_cnmr.esp
Normalized Intensity
0.95
0.90
0.85
0.80
0.75
0.70
0.65
0.60
0.55
0.50
0.45
0.40
0.35
0.30
0.25
0.20
0.15
0.10
0.05
0
177.86
177.59
175.52
166.77
63.64
61.82
57.04
57.40
53.15
52.40
51.24
50.47
49.01
46.59
41.36
37.38
35.14
34.36
33.75
29.82
29.41
26.58
26.13
23.14
176
168
160
152
144
136
128
120
112
104
96
88
80
72
64
56
48
40
32
24
Chemical Shift (ppm)

Appendix 2

Appendix 2

Table A1. Fitted parameters of **Gd_2L^1** in the absence of Ca^{2+}. The underlined parameters were fixed during the fitting.

Parameter	Gd_2L^1
k_{ex}^{298} [10^6 s^{-1}]	2.4±0.2
$\Delta H^\ddagger$ [kJ mol^{-1}]	43.6±3.3
$\Delta S^\ddagger$ [J $mol^{-1}K^{-1}$]	+23.5
$A/\hbar$ [10^6 rad s^{-1}]	$\underline{-3.8}$
τ_{RO}^{298} [ps]	349±47
E_R [kJ mol^{-1}]	24±1
τ_V^{298} [ps]	20.6±2.7
E_V [kJ mol^{-1}]	$\underline{1}$
Δ^2[10^{20} s^{-2}]	0.46±0.10
D^{298}_{GdH} [$10^{-10}m^2s^{-1}$]	25±3
E_{DGdH} [kJ mol^{-1}]	30±2
δg_L^2 [10^{-1}]	2.7±0.7
$\tau_{RH}^{298}/\ \tau_{RO}^{298}$	0.76±0.12
r_{GdO} [Å]	$\underline{2.5}$
r_{GdH} [Å]	$\underline{3.1}$
$r_{GdHouter}$ [Å]	$\underline{3.6}$
$\chi(1+\eta^2/3)^{1/2}$ [MHz]	$\underline{7.58}$
q	$\underline{0.4}$
q_{2nd}	$\underline{1}$
$\tau_M{}^{298}{}_{2nd}$ [ps]	$\underline{50}$

ΔH^{298}_{2nd} [kJ mol^{-1}]	35
r^{2nd}_{GdH} [Å]	3.5
r^{2nd}_{GdO} [Å]	4.1

Table A2. Variable temperature reduced transverse and longitudinal ^{17}O relaxation rates of Gd_2L^1 in the absence of Ca^{2+}, c(Gd^{3+})=51.8 mM, pH=7, P_m=4.00·10^{-4} at 11.75 T. Reference was acidified H_2O, pH=3.4.

t / °C	T / K	1000/T / K^{-1}	P_m	T_1 (Gd)/s	T_1 (ref)/s	T_2(Gd)/s	T_2(ref)/s	ln(1/T_{1r})	ln(1/T_{2r})
			(*10^{-4})	(*10^{-3})	(*10^{-3})	(*10^{-3})	(*10^{-3})		
3.75	276.9	3.61	4.0	2.93	3.65	2.09	3.29	12.03	12.98
10.45	283.6	3.53	4.0	3.74	4.51	2.02	4.66	11.64	13.46
16.65	289.8	3.45	4.0	4.26	5.66	2.04	5.70	11.88	13.57
25.45	298.6	3.35	4.0	5.65	7.06	2.3	6.74	11.39	13.44
35.45	308.6	3.24	4.0	7.03	8.92	2.75	8.88	11.23	13.35
46.75	319.9	3.13	4.0	9.07	1.16	3.42	1.18	10.99	13.16
59.25	332.4	3.01	4.0	12.0	1.45	4.83	1.43	10.47	12.75
70.55	343.7	2.91	4.0	14.5	1.75	6.37	1.72	10.27	12.42

Table A3. Variable temperature reduced transverse and longitudinal ^{17}O relaxation rates of Gd_2L^1 in the presence of 1M Ca^{2+}, c(Gd^{3+})=45.6 mM, pH=7, P_m=5.41·10^{-4} at 11.75 T. Reference was acidified 1M $CaCl_2$.

t / °C	T / K	1000/T / K^{-1}	P_m	T_1 (Gd)/s	T_1 (ref)/s	T_2(Gd)/s	T_2(ref)/s	ln(1/T_{1r})	ln(1/T_{2r})

			(*10^{-4})	(*10^{-3})	(*10^{-3})	(*10^{-3})	(*10^{-3})		
4.25	277.4	3.60	5.41	2.56	4.14	1.36	4.08	12.38	13.71
10.55	283.7	3.52	5.41	2.86	5.06	1.39	4.93	12.25	13.77
17.95	291.1	3.44	5.41	3.78	6.16	1.46	5.97	12.09	13.77
24.85	298.0	3.36	5.41	4.05	7.24	1.45	6.76	11.94	13.81
34.15	307.3	3.25	5.41	5.23	9.16	1.67	8.94	11.76	13.71
50.35	323.5	3.09	5.41	6.98	12.9	1.95	11.7	11.44	13.58
65.25	338.4	2.96	5.41	8.85	16.6	2.48	15.9	11.16	13.35

Table A4. Fitted parameters of Gd_2L^1 in the presence of 1M Ca^{2+}. The underlined parameters were fixed during the fitting.

Parameter	Gd_2L^1 + Ca^{2+}
k_{ex}^{298} [10^6 s^{-1}]	7.5±1.6
$\Delta H^{\ddagger}$ [kJ mol^{-1}]	$\underline{43.6}$
$\Delta S^{\ddagger}$ [J $mol^{-1}K^{-1}$]	+33.0
$A/\hbar$ [10^6 rad s^{-1}]	$\underline{-3.8}$
τ_{RO}^{298} [ps]	1152±243
E_R [kJ mol^{-1}]	21±6
τ_V^{298} [ps]	0.13±0.02
E_V [kJ mol^{-1}]	$\underline{1}$
Δ^2[10^{20} s^{-2}]	0.50±0.05
δg_L^2 [10^{-2}]	$\underline{2.1}$
r_{GdO} [Å]	$\underline{2.5}$

r_{GdH} [Å]	3.1
r_{GdHouter} [Å]	3.5
$\chi(1+\eta^2/3)^{1/2}$ [MHz]	7.58
q	0.7
q_{2nd}	1
$\tau_{M}{}^{298}{}_{2nd}$ [ps]	50
$\Delta H^{298}{}_{2nd}$ [kJ mol^{-1}]	35
$r^{2nd}{}_{\mathrm{GdH}}$ [Å]	3.5
$r^{2nd}{}_{\mathrm{GdO}}$ [Å]	4.1

Appendix 3

X-ray crystallography

Appendix 3

Crystal 1: crystallized with five water molecules (not shown in the figure)

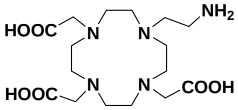

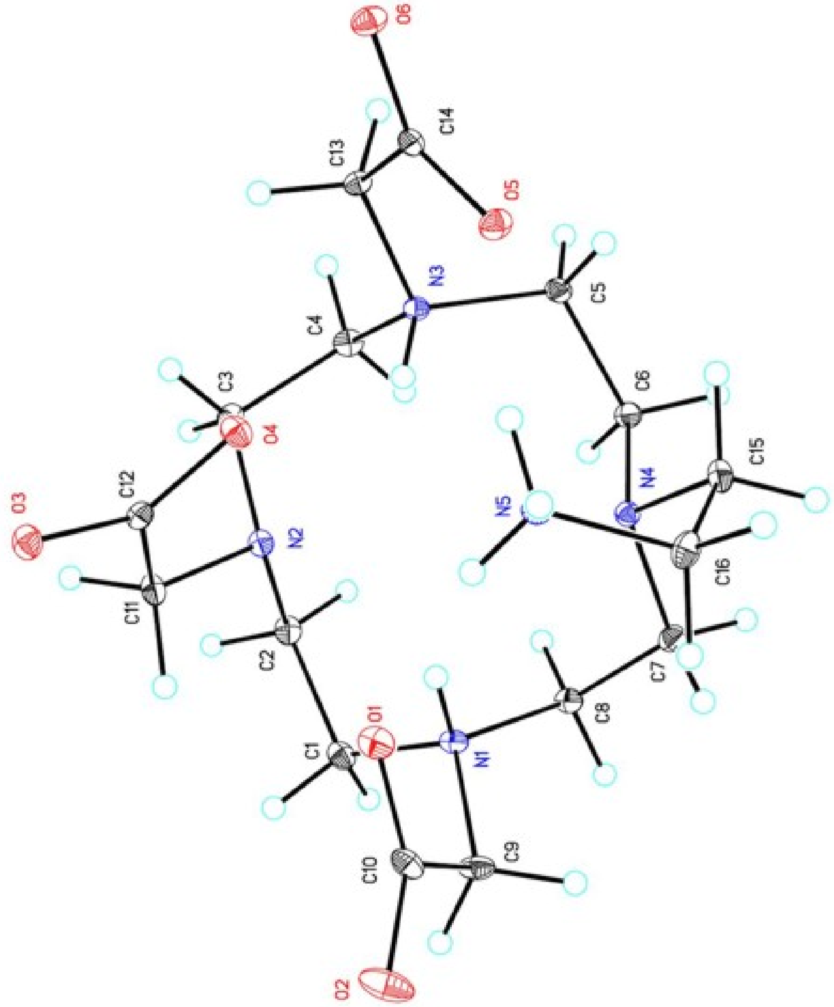

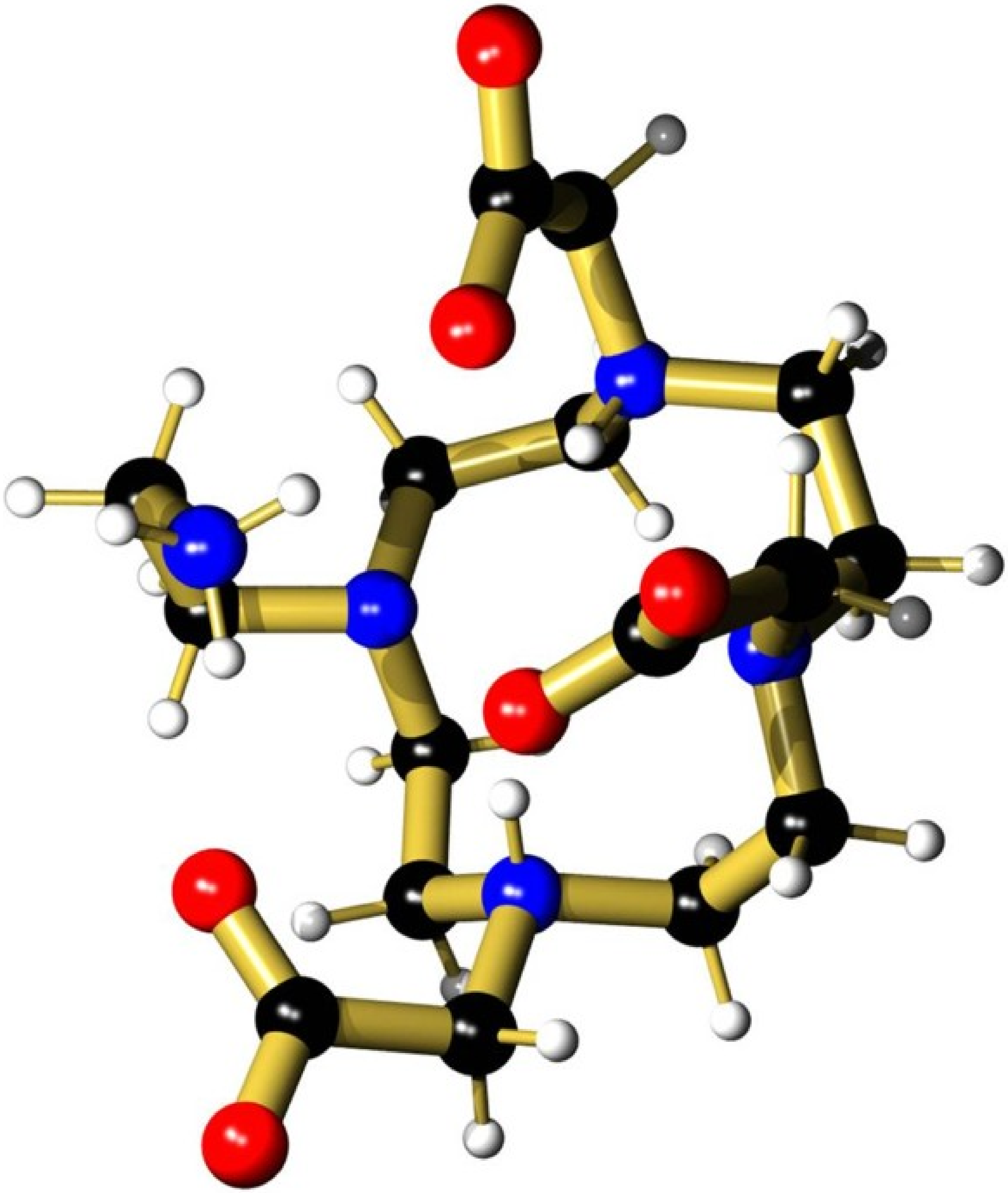

Crystal 2:

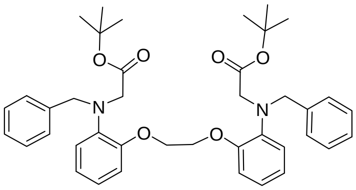
O
O
N
O
O
O
O
N

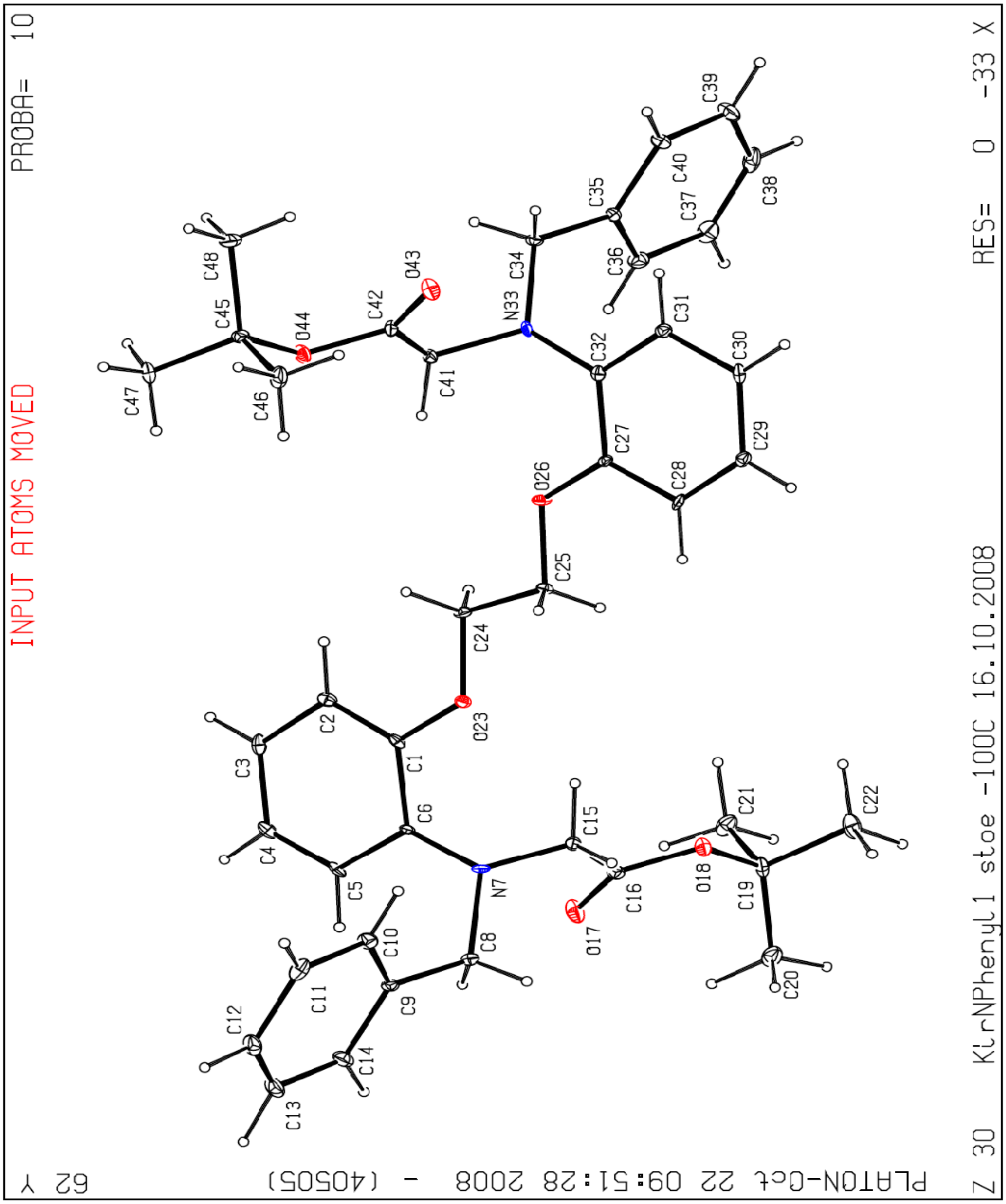
PROBA= 10
INPUT ATOMS MOVED
RES= 0 -33 X
KirNPhenyL1 stoe -100C 16.10.2008
PLATON-Oct 22 09:51:28 2008 - (40505)
Z 30
62 Y
C1
C2
C3
C4
C5
C6
N7
C8
C9
C10
C11
C12
C13
C14
C15
C16
O17
O18
C19
C20
C21
C22
O23
C24
C25
O26
C27
C28
C29
C30
C31
C32
N33
C34
C35
C36
C37
C38
C39
C40
C41
C42
O43
O44
C45
C46
C47
C48

Appendix 3

Crystal 3:

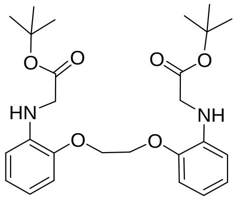

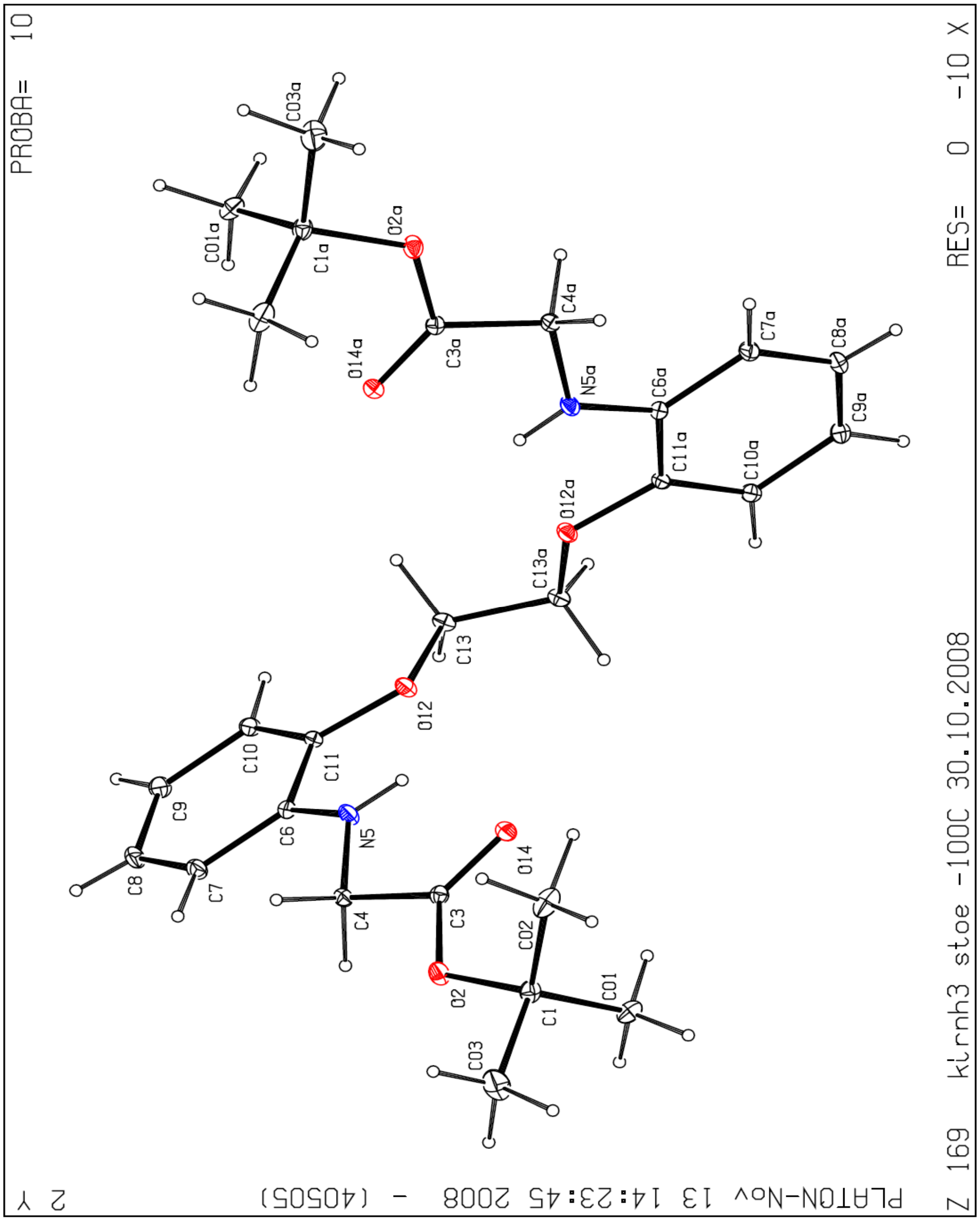

Crystal 4: Cystal with four four water molecules (shown in red)

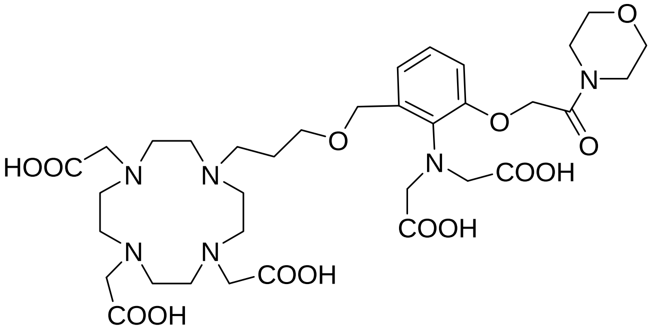

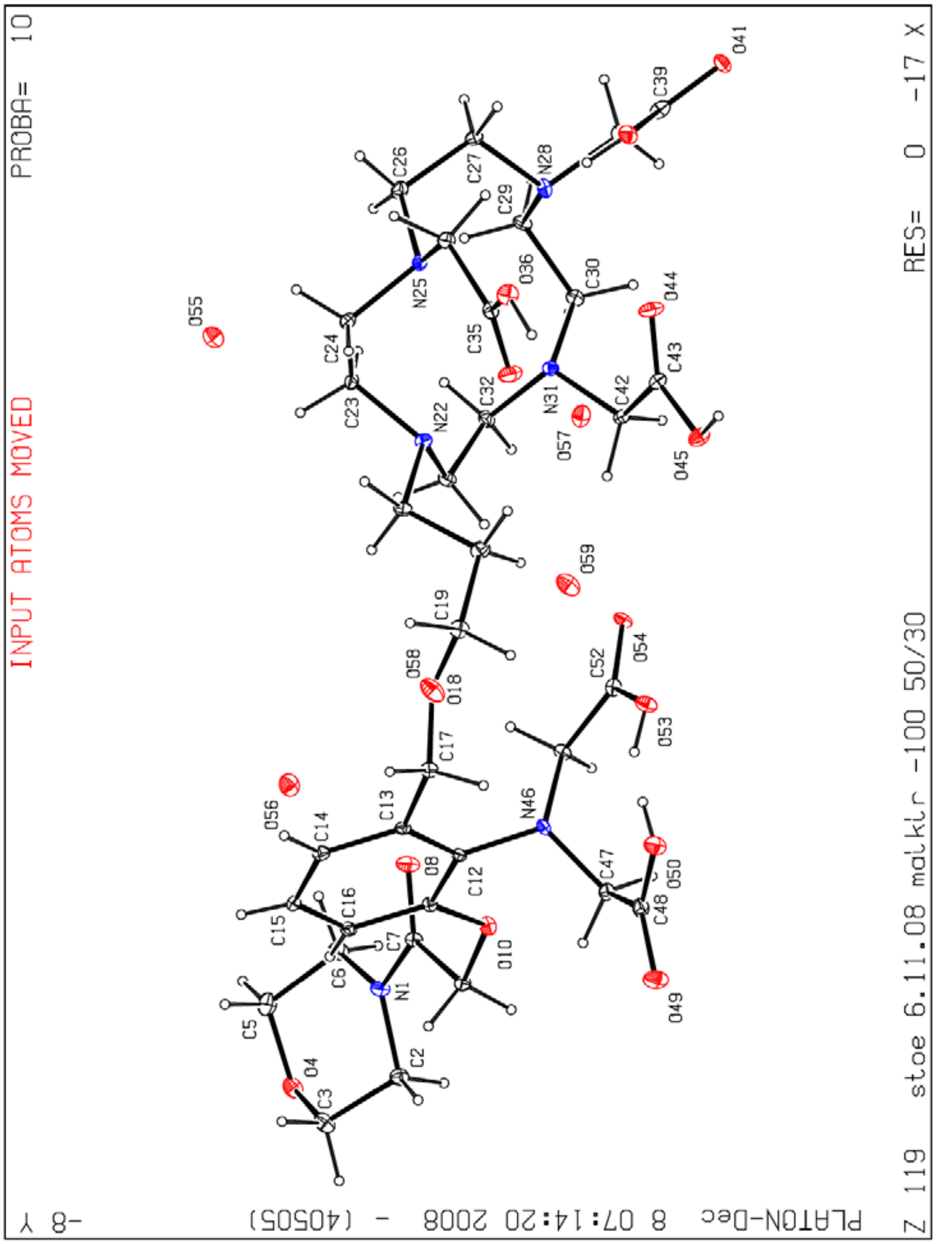

H. References

1. Bushong, S.C. (1996). Magnetic Resonance Imaging-Physical and Biological Principles, Second Edition (Mosby).
2. Haacke, E.M., Brown, R.W., Thompson, M.R., and Venkatesan, R. (1999). Magnetic Resonance Imaging - Physical Principles and Sequence Design (Willey-Liss).
3. Buxton, R.B. (2002). Introduction to Functional Magnetic Resonance Imaging - Principles and Techniques (Cambridge University Press).
4. Kemp, W. Organic Spectroscopy, Third Edition (Macmillan).
5. Peters, J.A., Huskens, J., and Raber, D.J. (1996). Lanthanide induced shifts and relaxation rate enhancements. Progress in Nuclear Magenetic Resonance Spectroscopy *28*, 283-350.
6. Merbach, A.E., and Toth, E. eds. The Chemistry of Contrast Agents in Medical Magentic Resonance Imaging, First Edition (John Wiley).
7. Helm, L. (2006). Relaxivity in paramagnetic systems: Theory and mecahnisms. Prog. Nuc. Mag. Res. Spect. *49*, 45-64.
8. Bloembergen, N. (1957). Proton Relaxation Times in Paramagnetic Solutions. J. Chem. Phys. *27*, 572-573.
9. Solomon, I. (1955). Relaxation Processes in a System of Two Spins Phys. Rev. *99*, 559-565.
10. Ayant, Y., Belorizky, E., Aluzon, J., and Gallice, J. (1975). Calcul des densités spectrales résultant d'un mouvement aléatoire de translation en relaxation par interaction dipolaire magnétique dans les liquides. J. de Physique *36*, 991-1004.
11. Ayant, Y., Belorizky, E., Fries, P., and Rosset, J. (1977). Effet des interactions dipolaires magnétiques intermoléculaires sur la relaxation nucléaire de molécules polyatomiques dans les liquides. J. de Physique *38*.
12. Freed, J.H. (1978). Dynamic effects of pair correlation functions on spin relaxation by translational diffusion in liquids. II. Finite jumps and independent T1 processes. J. Chem. Phys. *68*, 4034-4037.
13. Hwang, L.-P., and Freed, J.H. (1975). Dynamic effects of pair correlation function on spin relaxation by translationaldiffucion in liquids. . J. Chem. Phys. *63*, 4017-4025.
14. Fries, P.H., and Belorizky, E. (2007). Relaxation theory of the electronic spin of a complexed paramagnetic metal ion in solution beyond the redfield limit. J. Chem. Phys. *126*, 1-7.
15. Bloembergen, N., and Morgan, L.O. (1961). Proton Relaxation Times in Paramagnetic Solutions: Effect of Electron Spin Relaxation. J. Chem. Phys. *34*, 842-850.
16. Strijkers, G.J., Mulder, W.J., van Tilborg, G.A., and Nicolay, K. (2007). MRI contrast agents: current status and future perspectives. Anticancer Agents Med Chem *7*, 291-305.
17. Pankhurst, Q.A., Connoly, J., Jones, S.K., and Dobson, J. (2003). Applications of magnetic nanoaparticles in biomedicine. Journal of Physics D; Applied Physics *36*, R167-R181.

18. Jun, Y.W., Lee, J.H., and Cheon, J. (2008). Chemical design of nanoparticle probes for high-performance magnetic resonance imaging. Angew Chem Int Ed Engl *47*, 5122-5135.
19. Koenig, S.H., and Kellar, K.E. (1995). Theory of 1/T1 and 1/T2 NMRD profiles of solutions of magnetic nanoparticles. Magn Reson Med *34*, 227-233.
20. Bulte, J.W., Brooks, R.A., Moskowitz, B.M., Bryant, L.H., Jr., and Frank, J.A. (1999). Relaxometry and magnetometry of the MR contrast agent MION-46L. Magn Reson Med *42*, 379-384.
21. Bowen, C.V., Zhang, X., Saab, G., Gareau, P.J., and Rutt, B.K. (2002). Application of the static dephasing regime theory to superparamagnetic iron-oxide loaded cells. Magn Reson Med *48*, 52-61.
22. Medintz, I.L., Uyeda, H.T., Goldman, E.R., and Mattoussi, H. (2005). Quantum dot bioconjugates for imaging, labelling and sensing. Nat Mater *4*, 435-446.
23. Weissleder, R., Lee, A.S., Fischman, A.J., Reimer, P., Shen, T., Wilkinson, R., Callahan, R.J., and Brady, T.J. (1991). Polyclonal Human Immunoglobulin G Labeled with Polymeric Iron Oxide:Antibody MR Imaging. Radiol. *181*, 245-249.
24. He, L., Musick, M.D., Nicewarner, S.R., Salinas, F.G., Benkovic, S.J., Natan, M.J., and Keating, C.D. (2000). Colloidal Au-Enhanced Surface Plasmon Resonance for Ultrasensitive Detection of DNA Hybridization. J. Am. Chem. Soc. *922*, 9071-9077.
25. Sonnichsen, C., Reinhard, B.M., Liphardt, J., and Alivisatos, A.P. (2005). A molecular ruler based on plasmon coupling of single gold and silver nanoparticles. Nat Biotechnol *23*, 741-745.
26. Medarova, Z., Pham, W., Farrar, C., Petkova, V., and Moore, A. (2007). In vivo imaging of siRNA delivery and silencing in tumors. Nat. Med *13*, 372-377.
27. Weissleder, R., Moore, A., Mahmood, U., Bhorade, R., Benveniste, H., Chiocca, E.A., and Basilion, J.P. (2000). In vivo magnetic resonance imaging of transgene expression. Nat. Med *6*, 351-354.
28. Woods, M., Woessner, D.E., and Sherry, A.D. (2006). Paramagnetic lanthanide complexes as PARACEST agents for medical imaging. Chem Soc Rev *35*, 500-511.
29. Sherry, A.D., and Woods, M. (2008). Chemical exchange saturation transfer contrast agents for magnetic resonance imaging. Annu Rev Biomed Eng *10*, 391-411.
30. Chan, K.W.-Y., and Wong, W.-T. (2007). Small moelcular gadolinium(III) complexes as MRI contrast agents for diagnostic imaging. Coord. Chem. Rev. *251*, 2428-2451.
31. Hendrick, R.E., and Haacke, E.M. (1993). Basic physics of MR contrast agents and maximization of image contrast. J Magn Reson Imaging *3*, 137-148.
32. Dardzinski, B.J., Schmithorst, V.J., Holland, S.K., Boivin, G.P., Imagawa, T., Watanabe, S., Lewis, J.M., and Hirsch, R. (2001). MR imaging of murine arthritis using ultrasmall superparamagnetic iron oxide particles. Magn Reson Imaging *19*, 1209-1216.
33. Aime, S., Barge, A., Cabella, C., Crich, S.G., and Gianolio, E. (2004). Targeting cells with MR imaging probes based on paramagnetic Gd(III) chelates. Curr Pharm Biotechnol *5*, 509-518.
34. Mulder, W.J.M., Strijkers, G.J., Griffioen, A.W., Bloois, L.v., Molema, G., Storm, G., Koning, G.A., and Nicolay, K. (2004). A Liposomal System for Contrast-Enhanced Magnetic Resonance Imaging of Molecular Targets. Bioconj. Chem. *4*, 799-806.

35. Kang, H.W., Josephson, L., Petrovsky, A., Weissleder, R., and Bogdanov, A. (2002). Magnetic Resonance Imaging of Inducible E-Selectin Expression in Human Endothelial Cell Culture. Bioconj. Chem. *13*, 122-127.
36. Tilborg, G.A.F.v., Mulder, W.J.M., Deckers, N., Storm, G., Reutelingsperger, C.P.M., Strijkers, G.J., and Nicolay, K. (2006). Annexin A5-Functionalized Bimodal Lipid-Based Contrast Agents for the Detection of Apoptosis. Bioconj. Chem. *17*, 741-749.
37. Winter, P.M., Caruthers, S.D., Kassner, A., Harris, T.D., Chinen, L.K., Allen, J.S., Lacy, E.K., Zhang, H., Robertson, J.D., Wickline, S.A., and Lanza, G.M. (2003). Molecular imaging of angiogenesis in nascent Vx-2 rabbit tumors using a novel alpha(v)beta3-targeted nanoparticle and 1.5 tesla magnetic resonance imaging. Cancer Res *63*, 5838-5843.
38. Moats, R.A., Fraser, S.E., and Meade, T.J. (1997). A “Smart” Magnetic Resonance Imaging Agent That Reports on Specific Enzymatic Activity. Angew Chem Int Ed Engl *36*, 726-728.
39. Louie, A.Y., Huber, M.M., Ahrens, E.T., Rothbacher, U., Moats, R., Jacobs, R.E., Fraser, S.E., and Meade, T.J. (2000). In vivo visualization of gene expression using magnetic resonance imaging. Nat Biotechnol *18*, 321-325.
40. Nivorozhkin, A.L., Kolodziej, A.F., Caravan, P., Greenfield, M.T., Lauffer, R.B., and McMurry, T.J. (2001). Enzyme-Activated Gd3+ Magnetic Resonance Imaging Contrast Agents with a Prominent Receptor-Induced Magnetization Enhancement. Angew Chem Int Ed Engl *40*, 2903-2906.
41. Lowe, M.P. (2004). Activated MR Contrast Agents. Curr Pharm Biotechnol *5*, 519-528.
42. Chauvin, T., Durand, P., Bernier, M., Meudal, H., Doan, B.T., Noury, F., Badet, B., Beloeil, J.C., and Toth, E. (2008). Detection of enzymatic activity by PARACEST MRI: a general approach to target a large variety of enzymes. Angew Chem Int Ed Engl *47*, 4370-4372.
43. Kalman, F.K., Woods, M., Caravan, P., Jurek, P., Spiller, M., Tircso, G., Kiraly, R., Brucher, E., and Sherry, A.D. (2007). Potentiometric and relaxometric properties of a gadolinium-based MRI contrast agent for sensing tissue pH. Inorg Chem *46*, 5260-5270.
44. Ali, M.M., Woods, M., Caravan, P., Opina, A.C., Spiller, M., Fettinger, J.C., and Sherry, A.D. (2008). Synthesis and relaxometric studies of a dendrimer-based pH-responsive MRI contrast agent. Chemistry *14*, 7250-7258.
45. Aime, S., Barge, A., Botta, M., Howard, J.A.K., Kataky, R., Lowe, M.P., Moloney, J.M., Parker, D., and Sousa, A.S.d. (1999). Dependence of the relaxivity and luminescence of gadolinium and europium amino-acid complexes on hydrogencarbonate and pH. Chem. Commun., 1047-1048.
46. Bruce, J.I., Dickins, R.S., Govenlock, L.J., Gunnlaugsson, T., Lopinski, S., Lowe, M.P., Parker, D., Peacock, R.D., Perry, J.J.B., Aime, S., and Botta|, M. (2000). The Selectivity of Reversible Oxy-Anion Binding in Aqueous Solution at a Chiral Europium and Terbium Center: Signaling of Carbonate Chelation by Changes in the Form and Circular Polarization of Luminescence Emission. J. Am. Chem. Soc. *122*, 9674-9684.
47. Lowe, M.P., Parker, D., Reany, O., Aime, S., Botta, M., Castellano, G., Gianolio, E., and Pagliarin, R. (2001). pH-dependent modulation of relaxivity and luminescence in macrocyclic gadolinium and europium complexes based on reversible intramolecular sulfonamide ligation. J Am Chem Soc *123*, 7601-7609.

48. Lowe, M.P., and Parker, D. (2000). Controllable pH modulation of lanthanide luminescence by intramolecular switching of the hydration state. Chem. Commun., 707-708.
49. Lowe, M.P., and Parker, D. (2001). pH Switched sensitisation of europium(III) by a dansyl group. Inorg. Chim. Acta *317*, 163-173.
50. Aime, S., Botta, M., Crich, S.G., Giovenzana, G., Palmisanod, G., and Sisti, M. (1999). A macromolecular Gd(iii) complex as pH-responsive relaxometric probe for MRI applications. Chem. Commun., 1577-1578.
51. Hovland, R., Gløgård, C., Aasen, A.J., and Klaveness, J. (2001). Gadolinium DO3A derivatives mimicking phospholipids;preparation and in vitro evaluation as pH responsive MRI contrast agents. J. Chem. Soc., Perkin Trans. 2 *2*, 929-933.
52. Laus, S., Sour, A., Ruloff, R., Toth, E., and Merbach, A.E. (2005). Rotational dynamics account for pH-dependent relaxivities of PAMAM dendrimeric, Gd-based potential MRI contrast agents. Chemistry *11*, 3064-3076.
53. Toth, E., Bolskar, R.D., Borel, A., lez, G.G., Helm, L., Merbach, A.E., Sitharaman, B., and Wilson, L.J. (2004). Water-Soluble Gadofullerenes: Toward High-Relaxivity, pH-Responsive MRI Contrast Agents. J Am Chem Soc *127*, 799-805.
54. Hartman, K.B., Laus, S., Bolska, R.D., Muthupillai, R., Helm, L., Toth, E., Merbach, A.E., and Wilson, L.J. (2008). Gadonanotubes as Ultrasensitive pH-Smart Probes for Magnetic Resonance Imaging. Nano lett. *8*, 415-419.
55. Li, W.-h., Fraser, S.E., and Meade, T.J. (1999). A Calcium-Sensitive Magnetic Resonance Imaging Contrast Agent. J. Am. Chem. Soc. *121*, 1413-1414.
56. Li, W.H., Parigi, G., Fragai, M., Luchinat, C., and Meade, T.J. (2002). Mechanistic studies of a calcium-dependent MRI contrast agent. Inorg Chem *41*, 4018-4024.
57. Attwell, D., and Iadecola, C. (2002). The neural basis of functional brain imaging signals. Trends Neurosci *25*, 621-625.
58. Atanasijevic, T., Shusteff, M., Fam, P., and Jasanoff, A. (2006). Calcium-sensitive MRI contrast agents based on superparamagnetic iron oxide nanoparticles and calmodulin. Proc Natl Acad Sci U S A *103*, 14707-14712.
59. Jasanoff, A. (2007). MRI contrast agents for functional molecular imaging of brain activity. Curr Opin Neurobiol *17*, 593-600.
60. Hanaoka, K., Kikuchi, K., Urano, Y., and Nagano, T. (2001). Selective sensing of zinc ions with a novel magnetic resonance imaging contrast agent. J. Chem. Soc., Perkin Trans. 2, 1840-1843.
61. Zhang, X.A., Lovejoy, K.S., Jasanoff, A., and Lippard, S.J. (2007). Water-soluble porphyrins as a dual-function molecular imaging platform for MRI and fluorescence zinc sensing. Proc Natl Acad Sci U S A *104*, 10780-10785.
62. Major, J.L., Parigi, G., Luchinat, C., and Meade, T.J. (2007). The synthesis and in vitro testing of a zinc-activated MRI contrast agent. Proc Natl Acad Sci U S A *104*, 13881-13886.
63. van Zijl, P.C., Jones, C.K., Ren, J., Malloy, C.R., and Sherry, A.D. (2007). MRI detection of glycogen in vivo by using chemical exchange saturation transfer imaging (glycoCEST). Proc Natl Acad Sci U S A *104*, 4359-4364.

64. Zhou, J., Payen, J.F., Wilson, D.A., Traystman, R.J., and van Zijl, P.C. (2003). Using the amide proton signals of intracellular proteins and peptides to detect pH effects in MRI. Nat Med *9*, 1085-1090.
65. Zhang, S., Winter, P., Wu, K., and Sherry, A.D. (2001). A novel europium(III)-based MRI contrast agent. J Am Chem Soc *123*, 1517-1518.
66. Aime, S., Barge, A., Delli Castelli, D., Fedeli, F., Mortillaro, A., Nielsen, F.U., and Terreno, E. (2002). Paramagnetic lanthanide(III) complexes as pH-sensitive chemical exchange saturation transfer (CEST) contrast agents for MRI applications. Magn Reson Med *47*, 639-648.
67. Zhang, S., Trokowski, R., and Sherry, A.D. (2003). A paramagnetic CEST agent for imaging glucose by MRI. J Am Chem Soc *125*, 15288-15289.
68. Trokowski, R., Zhang, S., and Sherry, A.D. (2004). Cyclen-based phenylboronate ligands and their Eu3+ complexes for sensing glucose by MRI. Bioconjug Chem *15*, 1431-1440.
69. Damadian, R. (1971). Tumor detection by nuclear magnetic resonance. Science *171*, 1151-1153.
70. Ogawa, S., Lee, T.M., Nayak, A.S., and Glynn, P. (1990). Oxygenation-sensitive contrast in magnetic resonance image of rodent brain at high magnetic fields. Magn Reson Med *14*, 68-78.
71. Ogawa, S., Tank, D.W., Menon, R., Ellermann, J.M., Kim, S.G., Merkle, H., and Ugurbil, K. (1992). Intrinsic signal changes accompanying sensory stimulation: functional brain mapping with magnetic resonance imaging. Proc Natl Acad Sci U S A *89*, 5951-5955.
72. Bandettini, P.A., Wong, E.C., Hinks, R.S., Tikofsky, R.S., and Hyde, J.S. (1992). Time course EPI of human brain function during task activation. Magn Reson Med *25*, 390-397.
73. Kwong, K.K., Belliveau, J.W., Chesler, D.A., Goldberg, I.E., Weisskoff, R.M., Poncelet, B.P., Kennedy, D.N., Hoppel, B.E., Cohen, M.S., Turner, R., and et al. (1992). Dynamic magnetic resonance imaging of human brain activity during primary sensory stimulation. Proc Natl Acad Sci U S A *89*, 5675-5679.
74. Fox, P.T., and Raichle, M.E. (1985). Stimulus rate determines regional brain blood flow in striate cortex. Ann Neurol *17*, 303-305.
75. Mintun, M.A., Fox, P.T., and Raichle, M.E. (1989). A highly accurate method of localizing regions of neuronal activation in the human brain with positron emission tomography. J Cereb Blood Flow Metab *9*, 96-103.
76. Buxton, R.B. (2002). Introduction to Functional Magnetic Resonance Imaging-Principles and Techniques (Cambridge University Press).
77. Iannetti, G.D., and Wise, R.G. (2007). BOLD functional MRI in disease and pharmacological studies: room for improvement? Magn Reson Imaging *25*, 978-988.
78. Logothetis, N.K. (2007). The ins and outs of fMRI signals. Nat Neurosci *10*, 1230-1232.
79. Logothetis, N.K. (2008). What we can do and what we cannot do with fMRI. Nature *453*, 869-878.
80. Frahm, J., Dechent, P., Baudewig, J., and Merboldt, K.D. (2004). Advances in functional MRI of the human brain. Prog. Nuc. Mag. Res. Spect. *44*, 1-32.
81. Logothetis, N.K., Pauls, J., Augath, M., Trinath, T., and Oeltermann, A. (2001). Neurophysiological investigation of the basis of the fMRI signal. Nature *412*, 150-157.

82. Logothetis, N.K., and Pfeuffer, J. (2004). On the nature of the BOLD fMRI contrast mechanism. Magn Reson Imaging *22*, 1517-1531.
83. Logothetis, N.K., and Wandell, B.A. (2004). Interpreting the BOLD signal. Annu Rev Physiol *66*, 735-769.
84. Shulman, R.G., and Rothman, D.L. (1998). Interpreting functional imaging studies in terms of neurotransmitter cycling. Proc Natl Acad Sci U S A *95*, 11993-11998.
85. Attwell, D., and Laughlin, S.B. (2001). An energy budget for signaling in the grey matter of the brain. J Cereb Blood Flow Metab *21*, 1133-1145.
86. Nehlig, A., and Coles, J.A. (2007). Cellular pathways of energy metabolism in the brain: is glucose used by neurons or astrocytes? Glia *55*, 1238-1250.
87. Jakovcevic, D., and Harder, D.R. (2007). Role of astrocytes in matching blood flow to neuronal activity. Curr Top Dev Biol *79*, 75-97.
88. Iadecola, C., and Nedergaard, M. (2007). Glial regulation of the cerebral microvasculature. Nat Neurosci *10*, 1369-1376.
89. Haydon, P.G., and Carmignoto, G. (2006). Astrocyte control of synaptic transmission and neurovascular coupling. Physiol Rev *86*, 1009-1031.
90. Roy, C.S., and Sherrington, C.S. (1890). On the Regulation of the Blood-supply of the Brain. J Physiol *11*, 85-158 117.
91. Buxton, R.B., Uludag, K., Dubowitz, D.J., and Liu, T.T. (2004). Modeling the hemodynamic response to brain activation. Neuroimage *23 Suppl 1*, S220-233.
92. Norris, D.G. (2006). Principles of magnetic resonance assessment of brain function. J Magn Reson Imaging *23*, 794-807.
93. Kandel, E.R., Schwartz, J.H., and Jessel, T.M. eds. Priniciples of Neural Science, Fourth Edition (McGraw-Hill).
94. Tsien, R.Y. (1989). Fluorescent probes of cell signaling. Annu Rev Neurosci *12*, 227-253.
95. Tsien, R.Y. (1998). The green fluorescent protein. Annu Rev Biochem *67*, 509-544.
96. Miyawaki, A. (2005). Innovations in the imaging of brain functions using fluorescent proteins. Neuron *48*, 189-199.
97. Mao, T., O'Connor, D.H., Scheuss, V., Nakai, J., and Svoboda, K. (2008). Characterization and subcellular targeting of GCaMP-type genetically-encoded calcium indicators. PLoS ONE *3*, e1796.
98. Knopfel, T., Diez-Garcia, J., and Akemann, W. (2006). Optical probing of neuronal circuit dynamics: genetically encoded versus classical fluorescent sensors. Trends Neurosci *29*, 160-166.
99. Denk, W., Delaney, K.R., Gelperin, A., Kleinfeld, D., Strowbridge, B.W., Tank, D.W., and Yuste, R. (1994). Anatomical and functional imaging of neurons using 2-photon laser scanning microscopy. J Neurosci Methods *54*, 151-162.
100. Denk, W., Strickler, J.H., and Webb, W.W. (1990). Two-photon laser scanning fluorescence microscopy. Science *248*, 73-76.
101. Duemani Reddy, G., Kelleher, K., Fink, R., and Saggau, P. (2008). Three-dimensional random access multiphoton microscopy for functional imaging of neuronal activity. Nat Neurosci *11*, 713-720.
102. Helmchen, F., and Waters, J. (2002). Ca2+ imaging in the mammalian brain in vivo. Eur J Pharmacol *447*, 119-129.

103. Salome, R., Kremer, Y., Dieudonne, S., Leger, J.F., Krichevsky, O., Wyart, C., Chatenay, D., and Bourdieu, L. (2006). Ultrafast random-access scanning in two-photon microscopy using acousto-optic deflectors. J Neurosci Methods *154*, 161-174.
104. Nicholson, C., Bruggencate, G.T., Steinberg, R., and Stockle, H. (1977). Calcium modulation in brain extracellular microenvironment demonstrated with ion-selective micropipette. Proc Natl Acad Sci U S A *74*, 1287-1290.
105. Nicholson, C., ten Bruggencate, G., Stockle, H., and Steinberg, R. (1978). Calcium and potassium changes in extracellular microenvironment of cat cerebellar cortex. J Neurophysiol *41*, 1026-1039.
106. Nicholson, C. (1980). Modulation of extracellular calcium and its functional implications. Fed Proc *39*, 1519-1523.
107. Mody, I., and Heinemann, U. (1986). Laminar profiles of the changes in extracellular calcium concentration induced by repetitive stimulation and excitatory amino acids in the rat dentate gyrus. Neurosci Lett *69*, 137-142.
108. Rusakov, D.A., and Fine, A. (2003). Extracellular Ca2+ depletion contributes to fast activity-dependent modulation of synaptic transmission in the brain. Neuron *37*, 287-297.
109. Cohen, J.E., and Fields, R.D. (2004). Extracellular calcium depletion in synaptic transmission. Neuroscientist *10*, 12-17.
110. Egelman, D.M., and Montague, P.R. (1998). Computational properties of peri-dendritic calcium fluctuations. J Neurosci *18*, 8580-8589.
111. Egelman, D.M., and Montague, P.R. (1999). Calcium dynamics in the extracellular space of mammalian neural tissue. Biophys J *76*, 1856-1867.
112. Rusakov, D.A., Kullmann, D.M., and Stewart, M.G. (1999). Hippocampal synapses: do they talk to their neighbours? Trends Neurosci *22*, 382-388.
113. King, R.D., Wiest, M.C., and Montague, P.R. (2001). Extracellular calcium depletion as a mechanism of short-term synaptic depression. J Neurophysiol *85*, 1952-1959.
114. Rusakov, D.A. (2001). The role of perisynaptic glial sheaths in glutamate spillover and extracellular Ca(2+) depletion. Biophys J *81*, 1947-1959.
115. King, R.D., Wiest, M.C., Montague, P.R., and Eagleman, D.M. (2000). Do extracellular Ca2+ signals carry information through neural tissue? Trends Neurosci *23*, 12-13.
116. Berridge, M.J., Lipp, P., and Bootman, M.D. (2000). The versatility and universality of calcium signalling. Nat Rev Mol Cell Biol *1*, 11-21.
117. Berridge, M.J., Bootman, M.D., and Roderick, H.L. (2003). Calcium signalling: dynamics, homeostasis and remodelling. Nat Rev Mol Cell Biol *4*, 517-529.
118. Augustine, G.J., Santamaria, F., and Tanaka, K. (2003). Local calcium signaling in neurons. Neuron *40*, 331-346.
119. Sinha, S.R., Wu, L.G., and Saggau, P. (1997). Presynaptic calcium dynamics and transmitter release evoked by single action potentials at mammalian central synapses. Biophys J *72*, 637-651.
120. Adams, S.R., Grynkiewicz, J.P.Y.K.G., Minta, A., and Tsien, R.Y. (1988). Biologically useful chelators that release Ca2+ upon illumination. J Am Chem Soc *110*, 3212-3220.
121. Beeby, A., Clarkson, I.M., Dickins, R.S., Faulkner, S., Parker, D., Royle, L., Sousa, A.S.d., Williams, J.A.G., and Woods, M. (1999). Non-radiative deactivation of the excited states

of europium, terbium and ytterbium complexes by proximate energy-matched OH, NH and CH oscillators: an improved luminescence method for establishing solution hydration states. J. Chem. Soc., Perkin Trans. 2 *2*, 493-503.

122. Tsien, R.Y. (1980). New calcium indicators and buffers with high selectivity against magnesium and protons: design, synthesis, and properties of prototype structures. Biochemistry *19*, 2393-2404.
123. Albin, M., Farber, G.K., and Horrocks, W.D. (1984). Europium(III) luminescence excitation spectroscopy. A species-specific method for the quantitation of lanthanide ion binding to chelating agents. Complexes of (1,2-ethanediyldioxy)diacetate. Inorg Chem *23*, 1648-1651.
124. Geier, G., and Jørgensen, C.K. (1971). High-resolution visible spectroscopy of two europium (III) ethylenediaminetetra-acetates differing in one molecule of ligated water. Chem Phys Lett *9*, 263-265.
125. Tóth, É., Dhubhghaill, O.M.N., Besson, G., Helm, L., and Merbach, A.E. (1999). Coordination equilibrium - a clue for fast water exchange on potential magnetic resonance imaging contrast agents? Magn Reson Chem *37*, 701-708.
126. Yerly, F., Dunand, F.A., Tóth, É., Figueirinha, A., Kovács, Z., Sherry, A.D., Geraldes, C.F.G.C., and Merbach, A.E. (2000). Spectroscopic Study of the Hydration Equilibria and Water Exchange Dynamics of Lanthanide(III) Complexes of 1,7-Bis(carboxymethyl)-1,4,7,10-tetraazacyclododecane (DO2A). Eur. J. Inorg. Chem *1000*, 1001-1006.
127. Congreve, A., Parker, D., Gianolio, E., and Botta, M. (2004). Steric control of lanthanide hydration state: fast water exchange at gadolinium in a mono-amide 'DOTA' complex. Dalton Trans, 1441-1445.
128. Frey, S.T., and Jr., W.D.H. (1995). On correlating the frequency of the 7F0 → 5D0 transition in Eu3+ complexes with the sum of 'nephelauxetic parameters' for all of the coordinating atoms. Inorg Chim Acta *229*, 383-390.
129. Caravan, P. (2006). Strategies for increasing the sensitivity of gadolinium based MRI contrast agents. Chem Soc Rev *35*, 493-576.
130. Lebduskova, P., Hermann, P., Helm, L., Toth, E., Kotek, J., Binnemans, K., Rudovsky, J., Lukes, I., and Merbach, A.E. (2007). Gadolinium(III) complexes of mono- and diethyl esters of monophosphonic acid analogue of DOTA as potential MRI contrast agents: solution structures and relaxometric studies. Dalton Trans, 493-501.
131. Lebduskova, P., Sour, A., Helm, L., Toth, E., Kotek, J., Lukes, I., and Merbach, A.E. (2006). Phosphinic derivative of DTPA conjugated to a G5 PAMAM dendrimer: an 17O and 1H relaxation study of its Gd(III) complex. Dalton Trans, 3399-3406.
132. Powell, D.H., Dhubhghaill, O.M.N., Pubanz, D., Helm, L., Lebedev, Y.S., Schlaepfer, W., and Merbach, A.E. (1996). Structural and Dynamic Parameters Obtained from 17O NMR, EPR, and NMRD Studies of Monomeric and Dimeric Gd3+ Complexes of Interest in Magnetic Resonance Imaging: An Integrated and Theoretically Self-Consistent Approach. J Am Chem Soc *118*, 9333-9346.
133. Laus, S., Ruloff, R., Toth, E., and Merbach, A.E. (2003). GdIII complexes with fast water exchange and high thermodynamic stability: potential building blocks for high-relaxivity MRI contrast agents. Chemistry *9*, 3555-3566.

134. Que, E.L., and Chang, C.J. (2006). A smart magnetic resonance contrast agent for selective copper sensing. J Am Chem Soc *128*, 15942-15943.
135. Somjen, G.J. (2004). Ions in the Brain - Normal Function, Seizures, and Stroke (Oxford University Press).
136. Veloso, D., Guynn, R.W., Oskarsson, M., and Veech, R.L. (1973). The concentrations of free and bound magnesium in rat tissues. Relative constancy of free Mg 2+ concentrations. J Biol Chem *248*, 4811-4819.
137. Di Terlizzi, R., and Platt, S. (2006). The function, composition and analysis of cerebrospinal fluid in companion animals: part I - function and composition. Vet J *172*, 422-431.
138. Reany, O., Gunnlaugsson, T., and Parker, D. (2000). Selective signalling of zinc ions by modulation of terbium luminescence. Chem. Commun., 473-474.
139. Kay, A.R. (2003). Evidence for chelatable zinc in the extracellular space of the hippocampus, but little evidence for synaptic release of Zn. J Neurosci *23*, 6847-6855.
140. Yamaguchi, Y. (2000). Lecticans: organizers of the brain extracellular matrix. Cell Mol Life Sci *57*, 276-289.
141. Ham, R.G. (1965). Clonal Growth of Mammalian Cells in a Chemically Defined, Synthetic Medium. Proc Natl Acad Sci U S A *53*, 288-293.
142. Bottenstein, J.E. (1985). Cell Culture in the Neurosciences (NewYork and London: Plenum Press).
143. Aime, S., Barge, A., Botta, M., Howard, J.A.K., Kataky, R., Lowe, M.P., Moloney, J.M., Parker, D., and Sousa, A.S.d. (1999). Dependence of the relaxivity and luminescence of gadolinium and europium amino-acid complexes on hydrogencarbonate and pH. Chem. Commun. *11*, 1047-1048.
144. Tour, O., Adams, S.R., Kerr, R.A., Meijer, R.M., Sejnowski, T.J., Tsien, R.W., and Tsien, R.Y. (2007). Calcium Green FlAsH as a genetically targeted small-molecule calcium indicator. Nat Chem Biol *3*, 423-431.
145. Lutza, M., Pursiainena, J., and Akselab, R. (2005). Facile Syntheses of Novel Acyclic Polycarboxylic Acids. Z. Naturforsch., 408-412.
146. Dhingra, K., Maier, M.E., Beyerlein, M., Angelovski, G., and Logothetis, N.K. (2008). Synthesis and characterization of a smart contrast agent sensitive to calcium. Chem Commun (Camb), 3444-3446.
147. Kristensson, K., and Olsson, Y. (1971). Retrograde axonal transport of protein. Brain Res *29*, 363-365.
148. LaVail, J.H., and LaVail, M.M. (1972). Retrograde axonal transport in the central nervous system. Science *176*, 1416-1417.
149. Kobbert, C., Apps, R., Bechmann, I., Lanciego, J.L., Mey, J., and Thanos, S. (2000). Current concepts in neuroanatomical tracing. Prog Neurobiol *62*, 327-351.
150. Koretsky, A.P. (2004). New developments in magnetic resonance imaging of the brain. NeuroRx *1*, 155-164.
151. Koretsky, A.P., and Silva, A.C. (2004). Manganese-enhanced magnetic resonance imaging (MEMRI). NMR Biomed *17*, 527-531.
152. Lee, J.H., and Koretsky, A.P. (2004). Manganese enhanced magnetic resonance imaging. Curr Pharm Biotechnol *5*, 529-537.

153. Silva, A.C., Lee, J.H., Aoki, I., and Koretsky, A.P. (2004). Manganese-enhanced magnetic resonance imaging (MEMRI): methodological and practical considerations. NMR Biomed *17*, 532-543.
154. Pautler, R.G., Silva, A.C., and Koretsky, A.P. (1998). In vivo neuronal tract tracing using manganese-enhanced magnetic resonance imaging. Magn Reson Med *40*, 740-748.
155. Watanabe, T., Natt, O., Boretius, S., Frahm, J., and Michaelis, T. (2002). In vivo 3D MRI staining of mouse brain after subcutaneous application of MnCl2. Magn Reson Med *48*, 852-859.
156. Aoki, I., Wu, Y.J., Silva, A.C., Lynch, R.M., and Koretsky, A.P. (2004). In vivo detection of neuroarchitecture in the rodent brain using manganese-enhanced MRI. Neuroimage *22*, 1046-1059.
157. Chang, S.L., LoTurco, J.J., and Nisenbaum, L.K. (2000). In vitro biocytin injection into perinatal mouse brain: a method for tract tracing in developing tissue. J Neurosci Methods *97*, 1-6.
158. Horikawa, K., and Armstrong, W.E. (1988). A versatile means of intracellular labeling: injection of biocytin and its detection with avidin conjugates. J Neurosci Methods *25*, 1-11.
159. Hymes, J., and Wolf, B. (1996). Biotinidase and its roles in biotin metabolism. Clin Chim Acta *255*, 1-11.
160. Wilbur, D.S., Hamlin, D.K., Vessella, R.L., Stray, J.E., Buhler, K.R., Stayton, P.S., Klumb, L.A., Pathare, P.M., and Weerawarna, S.A. (1996). Antibody fragments in tumor pretargeting. Evaluation of biotinylated Fab' colocalization with recombinant streptavidin and avidin. Bioconjug Chem *7*, 689-702.
161. Mock, D.M., Lankford, G.L., Widness, J.A., Burmeister, L.F., Kahn, D., and Strauss, R.G. (1999). Measurement of circulating red cell volume using biotin-labeled red cells: validation against 51Cr-labeled red cells. Transfusion *39*, 149-155.
162. Pispa, J. (1965). Animal biotinidase. Ann Med Exp Biol Fenn *43*, Suppl 5:1-39.
163. Suchy, S.F., McVoy, J.S., and Wolf, B. (1985). Neurologic symptoms of biotinidase deficiency: possible explanation. Neurology *35*, 1510-1511.
164. Zaffanello, M., Zamboni, G., Fontana, E., Zoccante, L., and Tato, L. (2003). A case of partial biotinidase deficiency associated with autism. Child Neuropsychol *9*, 184-188.
165. Tsao, C.Y., and Kien, C.L. (2002). Complete biotinidase deficiency presenting as reversible progressive ataxia and sensorineural deafness. J Child Neurol *17*, 146.
166. Heller, A.J., Stanley, C., Shaia, W.T., Sismanis, A., Spencer, R.F., and Wolf, B. (2002). Localization of biotinidase in the brain: implications for its role in hearing loss in biotinidase deficiency. Hear Res *173*, 62-68.
167. Wilbur, D.S., Chyan, M.K., Pathare, P.M., Hamlin, D.K., Frownfelter, M.B., and Kegley, B.B. (2000). Biotin reagents for antibody pretargeting. 4. Selection of biotin conjugates for in vivo application based on their dissociation rate from avidin and streptavidin. Bioconjug Chem *11*, 569-583.
168. Wilbur, D.S., Hamlin, D.K., Chyan, M.K., Kegley, B.B., and Pathare, P.M. (2001). Biotin reagents for antibody pretargeting. 5. Additional studies of biotin conjugate design to provide biotinidase stability. Bioconjug Chem *12*, 616-623.

169. Wilbur, D.S., Pathare, P.M., Hamlin, D.K., Stayton, P.S., To, R., Klumb, L.A., Buhler, K.R., and Vessella, R.L. (1999). Development of new biotin/streptavidin reagents for pretargeting. Biomol Eng *16*, 113-118.
170. Wilbur, D.S., Pathare, P.M., Hamlin, D.K., and Weerawarna, S.A. (1997). Biotin reagents for antibody pretargeting. 2. Synthesis and in vitro evaluation of biotin dimers and trimers for cross-linking of streptavidin. Bioconjug Chem *8*, 819-832.
171. Sabatino, G., Chinol, M., Paganelli, G., Papi, S., Chelli, M., Leone, G., Papini, A.M., De Luca, A., and Ginanneschi, M. (2003). A new biotin derivative-DOTA conjugate as a candidate for pretargeted diagnosis and therapy of tumors. J Med Chem *46*, 3170-3173.
172. Urbano, N., Papi, S., Ginanneschi, M., De Santis, R., Pace, S., Lindstedt, R., Ferrari, L., Choi, S., Paganelli, G., and Chinol, M. (2007). Evaluation of a new biotin-DOTA conjugate for pretargeted antibody-guided radioimmunotherapy (PAGRIT). Eur J Nucl Med Mol Imaging *34*, 68-77.
173. Mishra, A. (2007). Design, synthesis and Characterization of Novel Exogeneous Smart/bioresponsive Contrast Agents for Magnetic Resonance and Optical Imaging, der Eberhard-Karls-Universitaet Tuebingen, Tuebingen.
174. Green, N.M. (1963). Avidin. 1. The Use of (14-C)Biotin for Kinetic Studies and for Assay. Biochem J *89*, 585-591.
175. Artemov, D., Mori, N., Ravi, R., and Bhujwalla, Z.M. (2003). Magnetic resonance molecular imaging of the HER-2/neu receptor. Cancer Res *63*, 2723-2727.
176. Winter, P.M., Caruthers, S.D., Kassner, A., Harris, T.D., Chinen, L.K., Allen, J.S., Lacy, E.K., Zhang, H., Robertson, J.D., Wickline, S.A., and Lanza, G.M. (2003). Molecular imaging of angiogenesis in nascent Vx-2 rabbit tumors using a novel alpha(nu)beta3-targeted nanoparticle and 1.5 tesla magnetic resonance imaging. Cancer Res *63*, 5838-5843.
177. Artemov, D., Mori, N., Okollie, B., and Bhujwalla, Z.M. (2003). MR molecular imaging of the Her-2/neu receptor in breast cancer cells using targeted iron oxide nanoparticles. Magn Reson Med *49*, 403-408.
178. Zhu, W., Okollie, B., Bhujwalla, Z.M., and Artemov, D. (2008). PAMAM dendrimer-based contrast agents for MR imaging of Her-2/neu receptors by a three-step pretargeting approach. Magn Reson Med *59*, 679-685.
179. Hanaoka, K., Kikuchi, K., Terai, T., Komatsu, T., and Nagano, T. (2008). A Gd3+-based magnetic resonance imaging contrast agent sensitive to beta-galactosidase activity utilizing a receptor-induced magnetization enhancement (RIME) phenomenon. Chemistry *14*, 987-995.
180. Zech, S.G., Eldredge, H.B., Lowe, M.P., and Caravan, P. (2007). Protein binding to lanthanide(III) complexes can reduce the water exchange rate at the lanthanide. Inorg Chem *46*, 3576-3584.
181. Dhingra, K., Fouskova, P., Angelovski, G., Maier, M.E., Logothetis, N.K., and Toth, E. (2008). Towards extracellular Ca2+ sensing by MRI: synthesis and calcium-dependent 1H and 17O relaxation studies of two novel bismacrocyclic Gd3+ complexes. J Biol Inorg Chem *13*, 35-46.
182. Wong, W., and Li, C. (2005) (P.I. Appl., ed.), vol. CODEN: PIXXD2 WO 2005003105 A1 20050113.

183. We, W.-h., Tomohiro, T., Kodaka, M., and Okun, H. (2000). Selective Synthesis and Kinetic Measurement of 1:1 and 2:2 Cyclic Compounds Containing 1,4,7,10-Tetraazacyclododecane and Azobenzene Units. J Org Chem *65*, 8979-8987.

184. Patrice Talaga, Benezra, C., and Stampf, J.-L. (1990). Sterechemistry of the Michael Addition of Lysing derivatives to a-Methylene-y-butyrolactones. Biorg. Chem. *18*, 199-206.